UNIVERSIDAD
DE LA RIOJA

TESIS DOCTORAL

Título
Reducing uncertainty in solar radiation data to improve PV system simulations
Autor/es
Rubén Urraca Valle
Director/es
Francisco Javier Martínez de Pisón Ascacíbar, Andrés Sanz García y Fernando Jesús Antoñanzas Torres
Facultad
Escuela Técnica Superior de Ingeniería Industrial
Titulación
Departamento
Ingeniería Mecánica
Curso Académico

publicaciones.unirioja.es
E-mail: publicaciones@unirioja.es

UNIVERSITY OF LA RIOJA

DOCTORAL THESIS

Reducing uncertainty in solar radiation data to improve PV system simulations

---

Author:
Rubén URRACA VALLE

Supervisors:
Dr. Francisco Javier MARTÍNEZ DE PISÓN ASCACÍBAR
Dr. Andrés SANZ GARCÍA
Dr. Fernando ANTOÑANZAS TORRES

A thesis submitted in fulfillment of the requirements
for the degree of Doctor of Philosophy

in the

EDMANS Group
Department of Mechanical Engineering

September, 2018

To Thomas

Declaration of Authorship

I, Rubén URRACA VALLE, declare that this thesis titled, “Reducing uncertainty in solar radiation data to improve PV system simulations” and the work presented in it are my own. I confirm that:

- This work was done wholly or mainly while in candidature for a research degree at this University.
- Where any part of this thesis has previously been submitted for a degree or any other qualification at this University or any other institution, this has been clearly stated.
- Where I have consulted the published work of others, this is always clearly attributed.
- Where I have quoted from the work of others, the source is always given. With the exception of such quotations, this thesis is entirely my own work.
- I have acknowledged all main sources of help.

Signed:

Date:

Acknowledgements

I would like to start by acknowledging the support of my supervisors. Javi, who leads the EDMANS group and creates an excellent working atmosphere for PhD students. Andrés, who pushed me to start this PhD. Thank you for our long discussions and your meticulous but valuable comments. And Fernan, who showed me the path to start this PhD with his passion for solar energy when I was lost in a sea of doubt.

I don't want to forget the remaining members of the EDMANS group, Enrique, Alpha, Julio, and especially Javi. Thank you for listening to my complaints and for sharing your mountain madness for more than ten years. I am also indebted with the University of La Rioja for funding this research and my visiting stays with the FPI-UR 2014.

This journey wouldn't have been possible without the support of my family. Thank you four all your patience especially during the last months when this thesis took almost all my time. I would also like to thank the support of my friends, who encouraged me to hang out or go for a ride when I was tired and needed fresh air to clear my mind.

I would like to thank all the collaborators from the DWD, FMI, and Met Office. Special thanks to the JRC of Ispra where I spent two wonderful stays. Juan, Silvia, Irene, and Ana made that time flew during those months in Ispra. Finally, I would like to express my special gratitude to Thomas. He inspired me with his dedicated work and passion for developing PVGIS. He led us by example with his sustainable way of life. It is completely unfair that he won't be able to see the better world for which he fought so hard. Without him, this thesis wouldn't have been possible.

Abstract

PV system simulations are used to estimate the energy yield of new installations and assess the performance of PV materials in different regions. This thesis focuses on reducing the uncertainty of these simulations by quantifying and decreasing the uncertainty in solar radiation data, which currently accounts for around 50% of the total uncertainty.

Simulations seldom use solar radiation measurements due to the scarcity of ground sensors. However, the uncertainty in measurements is the basis of most solar radiation studies. We found that low-cost photodiodes present substantially larger uncertainties than thermopile pyranometers if they are inadequately calibrated. The uncertainty further increased due to operational failures, which were very common in regional and agricultural networks, leading to uncertainties in measurements higher than those of the best radiation databases. Moreover, these defects were not detected by the most widely used QC methods, such as the BSRN tests. Hence, we developed a new QC procedure, the BQC, that identified most operational defects and some equipment errors by analyzing the stability of the deviations between several radiation databases and measurements.

Solar radiation estimations are customarily used to assess PV systems due to their extensive spatiotemporal coverage and high resolution. We verified that databases from geostationary satellites, such as SARAH or NSRDB, should be preferred to assess the solar resource because they present the smallest bias and uncertainty. We have also evaluated the potential of reanalyses to complement satellite-based data in high latitudes. We confirmed that former ERA-Interim and MERRA reanalyses should be avoided, but we found that ERA5 and COSMO-REA6 are valid alternatives to satellite-based databases. These results validated the incorporation of both reanalyses in the online simulator PVGIS. However, users should take into account their limitations; primarily the strong dependence of their deviations on the atmospheric transmissivity due to the incorrect modeling of clouds. The analysis of the uncertainty propagation through PV simulations confirmed that SARAH should be preferred to assess PV systems in Central and South Europe, whereas it revealed that ERA5 is the best alternative in Northern Europe. We also found that cloud-related errors in reanalyses amplified the bias through the simulations. These amplifications should be accounted for selecting databases because their magnitude is sometimes larger than the bias of solar radiation estimations.

Resumen

Las simulaciones de sistemas fotovoltaicos sirven para estimar la producción en nuevas instalaciones y evaluar la eficiencia de los materiales en distintas zonas geográficas. El principal objetivo de esta tesis es la disminución de la incertidumbre en estas simulaciones a través de la reducción de la incertidumbre en los datos de radiación solar, ya que éstos aportan actualmente alrededor de un 50% de la incertidumbre total.

Las simulaciones no se suelen realizarse con mediciones de radiación solar debido a la escasez de estaciones con piranómetros. Sin embargo, la incertidumbre de estas mediciones es fundamental en la mayor parte de estudios de radiación solar. Hemos observado que la incertidumbre de los fotodiodos de silicio es muy superior a la de los piranómetros térmicos cuando no son calibrados adecuadamente. Esta incertidumbre puede ser incluso superior a la de las mejores bases de datos de radiación debido a la aparición de fallos operacionales en las estaciones, los cuales son muy comunes en redes regionales y agrícolas como SIAR. Los métodos de control de calidad más utilizados, como los que propone la BSRN, no son capaces de detectar este tipo de errores. Por tanto, hemos desarrollado un nuevo método de control de calidad, denominado BQC, que es capaz de detectar defectos operacionales y de equipo analizando la estabilidad de las desviaciones entre varias bases de datos de radiación y las mediciones del sensor.

Las simulaciones de sistemas fotovoltaicos utilizan generalmente estimaciones obtenidas a partir de imágenes de satélite debido a su alta resolución espacial y temporal. Hemos verificado que las bases de datos obtenidas a partir de satélites geoestacionarios, como SARAH y NSRDB, proporcionan los datos con el menor bias e incertidumbre. También hemos evaluado el potencial de los datos de reanálisis para complementar a los modelos de satélite en las regiones polares. Los resultados obtenidos confirman que no es recomendable el uso de versiones antiguas como ERA-Interim o MERRA, pero revelan que nuevos modelos como ERA5 o COSMO-REA6 son una alternativa válida. Estos resultados llevaron a la inclusión de ambas bases de datos en el simulador online PVGIS. Sin embargo, los usuarios de estos productos deben tener en cuenta sus limitaciones; especialmente la variación de sus errores con el grado de claridad del cielo debido a una deficiente predicción de nubes. El análisis de la propagación del bias en las simulaciones confirmó que SARAH es la mejor base de datos para modelar sistemas fotovoltaicos en la mayor parte de Europa, mientras que ERA5 es la mejor alternativa en el norte de Europa. Este estudio también reveló que los errores en la predicción de nubes amplifican el bias de los datos de reanálisis en las simulaciones. Estas amplificaciones son a veces superiores al bias de las estimaciones de radiación

solar por lo que deben ser consideradas al seleccionar bases de datos para la simulación de sistemas fotovoltaicos.

Contents

List of Figures

List of Tables

List of Abbreviations

AEMET	Agencia Estatal de Meteorología
BQC	Bias-based Quality Control method
BSRN	Baseline Surface Radiation Network
CI	confidence interval
CM SAF	Satellite Application Facility on Climate Monitoring
DWD	Deutscher Wetterdienst
ECMWF	European Centre for Medium-range Weather Forecast
EUMETSAT	European Organisation for the Exploitation of Meteorological Satellites
FMI	Finnish Meteorological Institute
GUM	Guide to the expression of Uncertainty in Measurement
HErZ/DWD	Hans-Ertel-Zentrum for weather research of DWD
JMA	Japan Meteorological Agency
LCOE	levelized cost of energy
LMT	Landbruksmeteorologisk Tjeneste
MFG	Meteosat First Generation
MSG	Meteosat Second Generation
NA	not available
NASA	National Aeronautics and Space Administration
NASA's GMAO	NASA's Global Modeling and Assimilation Office
NOAA	National Oceanic and Atmospheric Administration
NREL	National Renewable Energy Laboratory
NSRDB	National Solar Radiation Database
NWP	numerical weather prediction
PV	photovoltaic
PVGIS	Photovoltaic Geographical Information System
QC	quality control
RMIB	Royal Meteorological Institute of Belgium
RTM	radiative transfer model
SHMI	Swedish Meteorological and Hydrological Institute
SIAR	Servicio Integral de Asesoriamiento al Regante
WMO	World Meteorological Organization

List of Symbols

G	global irradiance	$\mathrm{W/m^2}$
B	beam irradiance	$\mathrm{W/m^2}$
D	diffuse irradiance	$\mathrm{W/m^2}$
R	reflected irradiance	$\mathrm{W/m^2}$
E	extraterrestrial irradiance	$\mathrm{W/m^2}$
G_{eff}	effective irradiance available for being converted into electrical current	$\mathrm{W/m^2}$
K_{CS}	clear-sky index	-
K_T	clearness index	-
K'_T	modified clearness index	-
K_N	beam transmittance	-
K_D	effective diffuse transmittance	-
K	diffuse ratio	-
T_{mod}	module temperature	°C
T_{amb}	ambient temperature	°C
WS	wind speed	m/s
P	power of a PV system	W
Y	energy yield of a PV system	kWh
w	window width of the BQC	days
n	parameter to adjust the level of restriction of the BQC	-
MBD	mean bias deviation	
$\widetilde{MBD}$	median bias deviation	
MAD	mean absolute deviation	
$\widetilde{MAD}$	median absolute deviation	
$RMSD$	root mean squared deviation	
$rMBD$	relative mean bias deviation	%
$rMAD$	relative mean absolute deviation	%
$rRMSD$	relative root mean squared deviation	%
u	uncertainty	%

Greek letters

θ_s	solar zenith angle	°
α_s	solar elevation angle	°
ϕ_s	solar azimuth angle	°
β	module inclination angle	°
θ	incidence angle of sun rays on an inclined plane	°
ϕ	orientation angle of an inclined plane	°
η	energy conversion efficiency of the PV module	-
ρ_g	surface albedo	-
ρ_c	cloud albedo	-
ρ	apparent albedo observed by spaceborne sensors	-

Superscripts

ref	reference value
tst	test value
mea	measured value
est	estimated value
$'$	variable normalized to STC

Subscripts

H	horizontal plane
N	plane always normal to sun rays
POA	plane of the array
STC	standard test conditions
DC	direct current
AC	alternating current
min	minutely/minute
h	hourly/hour
d	daily/day
m	monthly/month
y	annual/year

Chapter 1

Introduction

1.1 Background

The Paris Agreement aims to hold the increase in global average temperature below 2°C above pre-industrial levels, pursuing efforts to limit the increase to 1.5°C. The agreement came into force on 4th November 2016, but the Nationally Determined Contributions (NDCs) proposed by each country are still insufficient to meet Paris climate objectives. For instance, the European Union (EU) has set a binding target of a 40% cut in greenhouse emissions by 2030 with respect 1990, but carbon neutrality should be reached by the second half of the century to meet Paris targets.

The decarbonization of our energy supply is essential to achieve carbon neutrality since 68% of the world's CO_2 emissions currently come from burning fossil fuels for energy consumption [1]. More specifically, electricity generation produces 38% of the emissions accounting just for 18.5% of energy consumption [2]. Therefore, most countries are currently working on the development of carbon-free and renewable electricity sources that not only will have to increase their electricity production share but also provide the additional electricity required to electrify sectors such as transportation or heating. The EU target for 2030 specifies that 27% of the final energy consumption should be provided by renewables. This value was increased up to a 35% by the European Parliament [3]. The current share of renewables is 17% in the EU gross energy consumption and 29.6% in the EU electricity generated [4]. These statistics are similar in Spain with 17.3% of the energy consumed and 36.6% of the electricity generated produced by renewable energies.

The policies proposed by EU and Spain emphasize in a massive deployment of wind and solar energies. In this line, Spain's Commission of Experts has recently published a series of recommendations to generate 62% of the electricity from renewable sources by 2030 [5]. The report pointed out that almost all Spanish coal-fired power plants should be closed. The wind capacity of Spain should increase 35% including repowering old wind turbines. However, the major boost should come from solar energy, and more specifically from photovoltaics (PV). Spain does not plan to increase its thermal solar capacity by 2030 despite being a pioneering country in this technology. Solar thermal facilities can store the energy produced more easily, but their production is limited in regions with clouds or haze. Besides, solar thermal is currently more costly than solar PV excluding storage costs [6]. On the contrary, Spain's Commission of Experts foresees an increase of the PV capacity from the current 4.5 GW to 40-50 GW that corresponds to a rise in the electricity share from 3.1% to 26-28%.

Despite the Paris Agreement has accelerated the development of PV technology, solar PV was already one of the fastest growing industries. Solar energy took in 2017 for the 7th year in a row the largest share of new investments in renewable energies with 57% of the total investment (EUR 103.4 billion) [3]. The main reasons are the introduction of favorable policies such as feed-in tariffs (FITs) or net metering (NM) schemes, and the improved price competitiveness of solar technology. The price of PV panels sharply dropped over 85% between 2009-2017 in most mature markets [3], leaving the current costs of new PV systems around 1300 EUR/kWp. Hence, solar PV not only has become one of the cheapest renewable sources but also a competitive technology against traditional energy sources. The competitiveness of renewables is assessed with the grid parity concept. It occurs when the levelized cost of energy (LCOE) of PV generation is equal to or less than the price of purchasing energy power. Assessing grid parity is not simply because it varies geographically due to differences in the solar resource, installation costs, governmental regulations and electricity prices. However, several studies claim that PV has already hit grid parity in several markets, meaning that it is competitive without subsidies.

Grid parity is not reached simultaneously by utility-scale facilities and residential rooftop installations. The LCOE of the prior is compared with the wholesale electricity price whereas the LCOE of the latter is compared with the retail electricity price, which is substantially greater. Hence, residential PV should hit grid parity before utility-scale systems, despite its larger LCOE. This has already occurred in countries such as Germany (LCOE = 0.12 EUR/kWh) or Spain (LCOE = 0.067-0.1 EUR/kWh) [7], with retail electricity prices of 0.308 EUR/kWh and 0.208 EUR/kWh in 2017, respectively [8]. Another indicator of grid parity is that current FITs offered by the German government for new residential PV systems (~0.12 EUR/kWh) are well below the retail electricity price (0.308 EUR/kWh). One of the advantages of residential systems is that they provide a better match between generation and consumption as they bring the generation closer to the demand. Besides, residential systems help in the electrification of energy sectors such as transportation or heating. A study made by Huld et al. [1] highlighted that the space required by residential PV is not a limitation. Only a quarter of the total roof area suitable for PV over Europe would be needed to meet the EU 2030 target of a 35% share for renewables using residential PV alone.

Utility-scale facilities take advantage of the economy of scale showing lower LCOEs. Their global weighted LCOE was 0.08 EUR/kWh in 2017 [7] while the wholesale electricity price for Europe during the same year was on average 0.06 EUR/kWh [8]. Therefore, utility-scale PV is approaching grid parity as well. Grid parity of utility-scale PV can be assessed based on the latest renewable energy auctions, which are replacing FITs for installing new utility-scale PV capacity in most countries. Compared to FITs, auctions are a competitive scheme that establishes with a bidding system the electricity price and capacity installed from each technology. Electricity revenues set in latest auctions were typically below the wholesale electricity price. Some low-records bids in Saudi Arabia (0.0149 EUR/kWh) and Mexico (0.0148 EUR/kWh) were even under the LCOE of fossil-fuels based technologies. In Spain, solar PV obtained 3.9 GW during the last renewable energy auction compared to the 1.1 GW of wind energy. This energy will be sold at price market with a price floor of 0.032 EUR/kWh. Another indication that utility-scale PV is reaching grid parity in high irradiation regions is that Spain has even several subsidy-free projects in process accounting for 20 GW.

Future efforts to increase the penetration of solar PV should be oriented to keep with the cost reduction. Particular attention should be given to reduce balance-of-system (BoS) and soft costs, which currently account for around 50% of total costs. Efforts should be also made in improving the efficiency of PV materials. Crystalline silicon (c-Si) modules currently account for around 90% of the systems installed, with efficiencies around 16-20%. New researches not only focus on improving current c-Si materials but also on finding new materials with higher efficiency limits, lower production costs, and better integrability into buildings.

The main drawback for higher penetration of solar PV is the intermittency of the energy generated. This is a direct consequence of the variability of solar radiation. Different solutions are being explored such as the use of storage systems, the complementarity with other renewable sources [9], and the adaptation of electricity consumption patterns. Besides being intermittent, solar PV is highly unpredictable. The variability of solar radiation is composed by a deterministic component due to solar position changes and by a stochastic part caused by atmospheric processes such as cloud formation. These atmospheric stochastic processes are not easily predictable hindering the modeling of both solar radiation and energy produced by PV systems. Therefore, the development of accurate PV system models, and especially the estimation of the solar resource available at each site, is essential to reduce the uncertainty in PV system modeling and help in the deployment of solar PV globally.

1.2 Problem statement and motivation

Long-term predictions of the total energy yield (Y_{AC}) expected from new PV installations are one of the most important simulations made during the system lifetime. Yield predictions are made during the planning stage to select the best sites, evaluate the feasibility of the project, and calculate the cash flows. The uncertainty in the annual energy yield estimations is around 10% (80-95% level of confidence) [10, 11, 12, 13]. Reducing this uncertainty is fundamental to obtain more accurate bankable data and mitigate the financial risks. The uncertainty of yield predictions is primarily driven by the large uncertainty in solar radiation data, currently accounting for around 50% of total uncertainty [14, 11, 15, 13]. Yield predictions are made using solar radiation data from the past (at least 10 years) to estimate the solar resource during the system lifetime (next 20-30 years). Even though part of this uncertainty may be caused by long-term changes in the solar resource [16], most of it originates from solar resource assessment in past years. Either solar radiation measurements or estimations can be used. However, the variable routinely provided in both cases is the global horizontal irradiance (G_H), requiring the use of transposition models to calculate the irradiance in the plane of the array (G_{POA}) and increasing, even more, the uncertainty related to solar radiation data.

Solar radiation measurements are the most accurate source of radiation data for PV simulations when using high-quality and strictly-maintained sensors. This is the case of data from the Baseline Surface Radiation Network (BSRN) that reports annual uncertainties below ±2% with a 95% level of confidence [17]. However, long-term measurements are rarely available to make yield predictions. Pyranometers are installed at utility-scale facilities during the planning stage of the system, so measured data is generally not longer than one year. Measurements made by nearby weather stations can be also used, but stations measuring G_H are sparsely distributed. In practice, the use of solar radiation measurements for planning purposes is limited to correcting the bias of estimations with site-adaptation techniques [18].

Nonetheless, the uncertainty in solar radiation measurements is the basis for almost all solar radiation studies. Measurements can be used not only to directly feed PV system simulations but also to correct the bias of estimations, to validate modeling techniques [19], and to analyze climate trends [20], among others. The high quality of measurements is generally taken for granted by some users. However, the accuracy of measurements substantially decreases due to a poor placement of the stations, deficient maintenance or low-quality sensors such as photodiodes. All these factors introduce operational and equipment defects that increase the uncertainty in measured data. Moreover, most common quality control (QC) procedures cannot detect these defects as they introduce low-magnitude deviations that are plausible from a physical and even a statistical perspective. Therefore, developing more efficient QC methods to identify these types of defects and quantifying the real uncertainty in solar radiation measurements is essential to reduce the uncertainty in measured data.

Satellite-based databases are the most common choice to generate yield predictions because they allow evaluating the solar resource in almost every region in mid-latitudes with acceptable accuracy. They provide long-term and spatially continuous estimations of solar radiation with resolutions up to 3 km and 30 min [19]. Satellite-based estimations currently show biases below ±2% and annual uncertainties around ±5% due to the significant progress achieved during the last decades [19]. This is the reason because popular online PV simulators such as PVGIS, PVWatts or PV*SOL integrate satellite-based databases such as SARAH, NSRDB, and Meteonorm, respectively. However, these databases are derived from images taken by geostationary satellites, limiting their spatial coverage to the satellite field of view. Databases from different geostationary satellites can be combined to achieve global coverage at equatorial latitudes, but geostationary satellites cannot provide valid data in latitudes above ±65°. Besides, the quality of estimations decreases substantially near the edge of the satellite disk due to the shallow viewing geometries [21], and over snow-covered surfaces [22], among others. Therefore, other alternatives are being explored to assess the solar resource.

Atmospheric reanalyses, which are based on numerical weather prediction (NWP), have global coverage and similar temporal resolutions to satellite-based databases. NWP models estimate many other variables required to simulate PV systems such as ambient temperature and wind speed. This makes reanalyses an attractive alternative to satellite-based data because they could be used as the single source of climatic data to predict the expected energy yield in any part of the world. However, the accuracy of the most used reanalyses such as ERA-Interim or MERRA is substantially lower than that of satellite-based databases, mainly due to their coarse resolution (50-80 km) and incorrect modeling of clouds. These reanalyses show biases above 5% and large annual uncertainties, and their use for solar resource assessment is generally not recommended [23, 24]. Nonetheless, the advent of a new generation of reanalyses such as ERA5 or COSMO-REA6, with many improved features such as higher spatial resolutions (5-30 km), may reduce the accuracy gap between reanalysis and satellite-based databases. The new reanalyses may have the potential to complement satellite-based databases for simulating PV systems in regions not covered by geostationary satellites.

Radiation databases used for simulating PV systems are primarily chosen based on the bias and annual uncertainty in G_H. The bias in G_H is generally the most important indicator because it conveys proportionally to Y_{AC}. This is because simulation models are basically a series of multiplicative derating factors accounting for different types of loses [11]. The uncertainty in annual G_H also propagates directly to Y_{AC}, accounting for around 50% of the total uncertainty. Therefore, selecting radiation data with low uncertainty is also essential to increase the confidence of yield predictions. The interdependency between bias and uncertainty is generally ignored, but large intra-annual deviations in solar radiation data may amplify both bias and annual uncertainty through the modeling chain. These changes are caused by the dependence of some sub-models on the irradiance received by the panel. Cole et al. [25] estimated that intra-annual deviations may change the bias around ±2% through the simulations. However, a more accurate quantification of these effects is needed to improve the selection of radiation databases for PV system modeling.

1.3 Objectives

The main objective of the thesis is the reduction of the uncertainty in solar radiation data to enhance the confidence in yield predictions. The specific objectives focus on the reduction and quantification of uncertainty in solar radiation data:

1. Quantify uncertainty in solar radiation measurements, differentiating between the uncertainty of pyranometers due to equipment errors and the additional uncertainty added by operational defects. This objective includes the development of new QC procedures to detect low-magnitude defects, making possible to estimate the uncertainty added by each type of defect.

2. Quantify uncertainty of estimations from satellite-based and reanalysis databases. We will assess whether the latest reanalysis databases (ERA5 and COSMO-REA6) can close the accuracy gap with satellite-based data.

3. Compare the uncertainty and bias in annual G_H of solar radiation measurements and estimations under a common framework. More specifically, benchmark the uncertainty of estimations (satellite-based and reanalysis data), the uncertainty of measurements (thermopile and photodiode pyranometers) and the uncertainty added by operational errors.

The last objective is to analyze the propagation of uncertainty in solar radiation data through PV simulations to improve the selection of radiation databases for yield predictions. In this context, we also plan to evaluate the suitability of new reanalyses to complement satellite-based databases for simulating PV systems in Northern Europe.

Chapter 2

State of the art

2.1 Solar radiation measuring

The total amount of short-wave incoming irradiance [290 - 4000 nm] reaching the Earth's surface is known as global irradiance (G) or broadband irradiance. Global irradiance can be measured on any arbitrary plane, but it is routinely measured on a horizontal plane, also known as global horizontal irradiance (G_H). Three different components integrate G:

$$G = B + D + R \tag{2.1}$$

- Beam/direct irradiance (B). Solar radiation coming from the sun disk without interacting with the atmosphere. The quantity measured is the beam irradiance on a plane always normal to sun rays, or beam normal irradiance (B_N). It is the irradiance used by concentrating systems.
- Diffuse irradiance (D). Solar radiation scattered by aerosols (Mie scattering), atmospheric molecules (Rayleigh scattering) and clouds. The quantity measured is the diffuse irradiance on a horizontal plane, or diffuse horizontal irradiance (D_H).
- Reflected irradiance (R). Solar radiation reflected from the ground, sometimes treated as a fraction of diffuse irradiance. The quantity typically used is the ground albedo (ρ_g), a dimensionless coefficient that gives the fraction of G_H reflected by ground.

As the contribution of reflected irradiance on a horizontal plane is zero, the geometric relationship between the radiation components on a horizontal plane is:

$$G_H = B_H + D_H = B_N \cdot \cos\theta_s + D_H \tag{2.2}$$

where θ_s is the solar zenith angle and B_H the beam horizontal irradiance, i.e., the geometric projection of B_N on a horizontal plane.

The variable commonly measured at weather and radiometric stations is G_H because it includes the contribution of all radiation components. Besides, measuring G_H is easier than other components because it does not require moving parts in the radiometer. Diffuse and beam irradiances are only measured at specialized stations such as those from national services, while reflected irradiance measurements are even rarer. Therefore, several empirical models known as separation or decomposition models have been developed to obtain diffuse and beam irradiances from G_H. These models are not universal and increase the uncertainty of irradiance [26]. Reflected irradiance is generally estimated assuming an isotropic distribution of the irradiance and using an empirically-derived ρ_g value for each type of surface.

2.1.1 Radiometers

Instruments to measure solar radiation are known as radiometers. The two most common radiometers are pyranometers, which are used to measure global, diffuse or reflected irradiance, and pyrheliometers, which measure beam irradiance. The electrical signal of radiometers is related to the irradiance quantity measured with a calibration factor (inverse of responsivity). Besides, both radiometers can use two types of detectors: thermoelectric detectors (thermopiles), which produce an electrical signal based on a thermal difference, and photoelectric sensors (photodiodes), which produce an electrical signal based on the photovoltaic effect. The main characteristics of pyranometers, pyrheliometers, and other radiometers are outlined in the following sections.

Pyrheliometers

Pyrheliometers measure beam normal irradiance (B_N). Theoretically, B_N only includes sun rays not interacting with the atmosphere. This strict definition of B_N can be applied by solar modeling techniques but not by ground radiometers because it is not possible to determine if a photon coming from the sun disk has been scattered or not. Therefore, this definition is relaxed for measuring B_N by considering B_N as the radiation coming from a small disk centered around the sun. The magnitude of this disk is defined by the field of view (FOV) of the instrument. The World Meteorological Organization (WMO) [27] recommends that the FOV should not exceed 2.5° (half-angle), which is roughly 10 times larger than the sun disk to reduce tracking errors. Consequently, pyrheliometers measure not only irradiance coming from the sun but also that coming from the circumsolar region, i.e., the bright annulus around the sun. Significant deviations up to

2% can be found between pyrheliometers with different FOVs that should be taken into account when using B_N data from different instruments [19].

Absolute cavity radiometers (Fig. 2.1a) are the most accurate type of pyrheliometer. They are self-calibrating (absolute) instruments that compensate the thermal difference created by solar radiation with electrical power. They are not used for field measurements but to calibrate other radiometers. In this regard, the World Radiometric Reference (WRR) is defined by a group of absolute cavity radiometers known as the World Standard Group (WSG), which are maintained by the World Radiation Center (WRC) at Davos. Every terrestrial radiometer must be traceable to the WRR. For that, absolute cavity radiometers from national and institutional organizations are compared against the WSG every five years at International Pyrheliometer Comparisons (IPCs). These organizations use these radiometers to calibrate field instruments, which are then considered WRR-traceable.

FIGURE 2.1: Types of pyrheliometers.

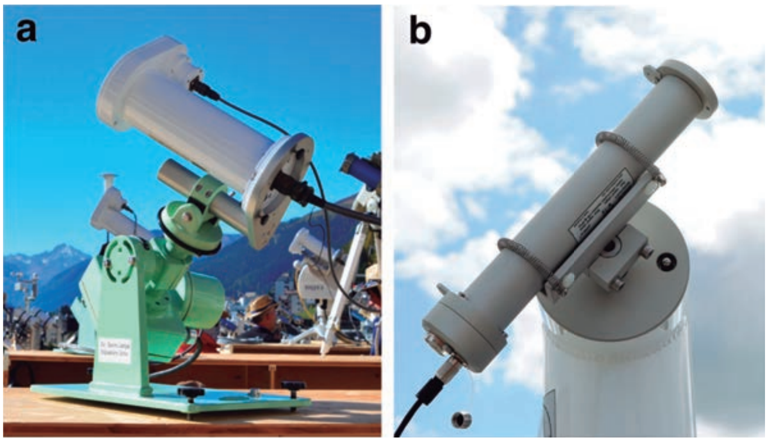

(a) Absolute cavity radiometer. Source: Silpakorn University (`http://www.calibrationsu.com`). (b) Field pyrheliometer (First class Middleton DN5). Source: Middleton Solar (`http://www.middletonsolar.com`).

Field pyrheliometers (Fig. 2.1b) include an automatic solar tracker to follow the sun path and an optical device to check the alignment of the instrument. Following WMO recommendations [27], all modern pyrheliometers should have a 2.5° FOV (half-angle). Both ISO and WMO establish different qualities of pyrheliometers. From highest to lowest quality, the Commission for Instruments and Methods of Observation (CIMO) guide [27] classifies pyrheliometers in (i) high quality and (ii) medium quality, while ISO 9060:1990 [28] distinguishes between (i) secondary standard, (ii) first class and (iii) second class. ISO highest quality is named secondary standard because absolute cavity radiometers are considered the primary standard. Pyrheliometers are calibrated using side-by-side measurements against a WRR-traceable absolute cavity radiometer, or against a WRR-traceable pyrheliometer [27].

Pyranometers

Pyranometers have a 360° FOV and are installed horizontally to measure global horizontal irradiance (G_H). The detector is protected from environmental factors with a dome (thermoelectric sensors) or a diffuser (photoelectric sensors). Pyranometers can be ventilated to reduce and prevent the accumulation of dust, snow and other particles over the instrument. Some ventilators include integrated heaters to help in melting snow and ice.

FIGURE 2.2: Types of pyranometers.

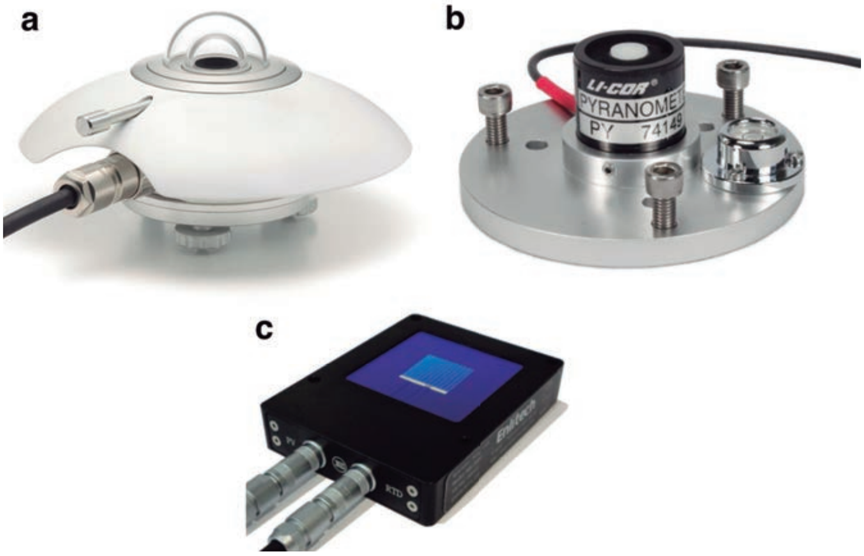

(a) Thermopile pyranometer (Hukseflux ISO 9060 secondary standard). Source: `http://ritmindustry.com`. **(b)** Photodiode pyranometer (LI-COR LI-200SZ). Source: `http://www.lpebumi.com`. **(c)** Solar reference cell (SRC-2020). Source: `http://solarmer.com`.

Pyranometers include either thermoelectric or photoelectric detectors. Thermoelectric pyranometers, or thermopiles (Fig. 2.2a), produce the highest-quality records and are the only one compliant with ISO-9060, which classifies them in (i) secondary standard (ii) first class and (iii) second class. The corresponding WMO quality levels are (i) high quality, (ii) medium quality, (iii) low quality. All-black pyranometers and black-and-white pyranometers are the most common thermopile pyranometers. The negative aspects of thermopile pyranometers are their high cost, the high maintenance required to keep their high-quality, and their slow temporal response (Table 2.1).

TABLE 2.1: Main features of thermopile and photodiode pyranometers.

	Thermopile	Photodiode
Principle	Thermolectric effect	Photovoltaic effect
Response time[a]	1-30 s	$\sim 1\ \mu$s
Spectral response	Flat response (96% broadband irrad.)	Wavelength dependent response (70-75% broadband irrad.)
Spectral range	300-3000 nm	400-1100 nm
ISO-9060	Compliant	Non Compliant
Cost	~2000 EUR	~300 EUR
Maintenance	High	Low
Use	High-quality stations ex. national agencies	Remote stations, secondary networks

[a] time to reach 95% of the final value.

Photodiodes and solar reference cells are the two main types of photoelectric pyranometers. Solar reference cells are used indoors for testing PV cells under solar simulators. They are made of the same material as the PV cell tested and are used to measure the exact amount of irradiance received by the cell. Photodiodes are the low-cost option to measure G_H outdoors. In addition, they require less maintenance and have lower affinity to soiling than thermopiles, which make them an attractive option for remote stations or agricultural networks. They are also used for real-time applications due to their fast response time. However, photodiodes have lower quality than thermopile pyranometers. They are not compliant with the ISO 9060:1990, mainly because they present a narrow [400 - 1100 nm] and wavelength dependent spectral response that accounts for 70-75% of broadband irradiance. Besides, other systematic errors such as the cosine error are more accentuated in photodiodes than in thermopiles (Subsection 2.1.2).

The most accurate method to obtain G_H is by adding independent measurements of diffuse and beam irradiance. Hence, one of the most common methods for calibrating pyranometers is by comparison with a standard pyrheliometer and a reference shaded pyranometer. If no reference pyranometers are available, pyranometers can be calibrated against a standard pyrheliometer by successively shading and unshading the pyranometer with a disk. Another common but less accurate method is to compare the pyranometer against another reference pyranometer either under natural or laboratory conditions. We refer to WMO [27] for more information on calibrating methods.

FIGURE 2.3: Types of shading mechanisms for measuring diffuse irradiance.

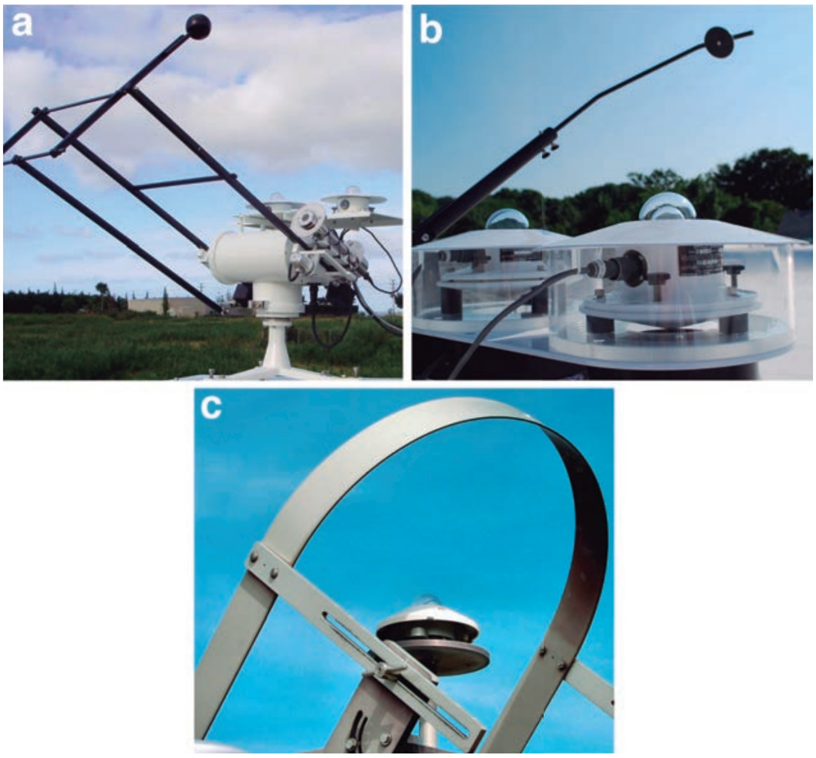

(**a**) Shading balls. Source: `https://www.niwa.co.nz`. (**b**) Shading discs. Source: `http://www.eppleylab.com`. (**c**) Shading ring/band. Source: `https://www.volker-quaschning.de`.

Shaded pyranometers Pyranometers installed horizontally can measure diffuse horizontal irradiance (D_H) by screening the beam irradiance with shading balls, shading disks or shading rings (Fig. 2.3). Shading balls and rings track the sun covering a small annulus around the sun disk, which similarly to pyrheliometers has an angle of around 2.5° (half angle). Shadow rings cover the whole daily sun path and have to be manually adjusted every other day. Besides, they screen part of the diffuse irradiance, so different corrections need to be applied to obtain valid measurements of diffuse irradiance.

Downwards pyranometers A pyranometer installed horizontally looking downwards measures reflected irradiance. The ground albedo (ρ_g) is obtained as the ratio between reflected and global horizontal irradiance.

Tilted pyranometers Pyranometers can be installed at any arbitrary inclination for measuring irradiance on an inclined plane, also known in the PV field as in-plane irradiance or plane-of-the-array irradiance (G_{POA}). In-plane irradiance is required for modeling inclined PV modules but is rarely measured at weather stations. This quantity is monitored just by some research organizations, and by utility-scale plants for planning and operational purposes. Thus, transposition models are commonly used to obtain in-plane irradiance from horizontal irradiance measurements.

Multi-pyranometers Multi-pyranometers measure simultaneously global, diffuse, and beam irradiance. They generally measure two of these variables and calculate the third one based on solar geometry. Some of the most used multi-pyranometers are RSIs, SPN1s or SCAPPs.

FIGURE 2.4: Types of multi-pyranometers.

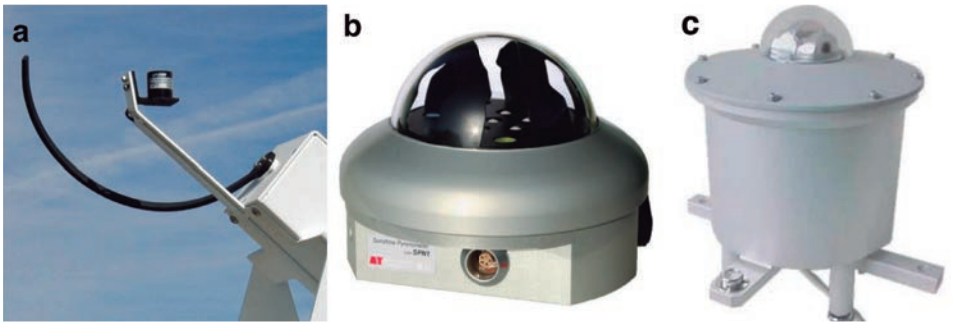

(**a**) RSI with a photoelectric detector. Source: `https://midcdmz.nrel.gov`. (**b**) SPN1 (Delta-T Devices, Ltd.). Source: `http://www.wind-pgc.com`. (**c**) SCAPP (DWD). Source: `https://www.wmo.int`.

Rotating shadowband irradiometers (RSIs) (Fig. 2.4a) are also known as rotating shadowband pyranometers or radiometers (RSPs or RSRs) [19]. A shadowband rotates around the detector, which measures diffuse irradiance when the shadowband blocks the detector and global irradiance in the remaining positions. There are two types of RSIs. *RSIs with continuous rotation* are the most extended ones. A shadowband rotates with a constant angular velocity (~1 Hz) while irradiance is recorded at a high frequency (~1 kHz), which makes necessary using photoelectric detectors. D_H and G_H are obtained through curve analysis algorithms. *RSIs with discontinuous rotation* only measure four points per rotation, one for measuring G_H and three for determining D_H. The shadowband remains immobile during each measurement, so the response time of the detectors is not an issue and thermoelectric sensors can be used. However, this increases the measurements uncertainty because the atmospheric conditions can change between measurements. Besides, using just four points per rotation makes critical the correct positioning of the shadowband.

SPN1 (Fig. 2.4b) measures D_H and G_H with seven thermopile detectors distributed in a hexagonal pattern under a particular shadow mask. For any sun position, at least one detector is shaded from the sun while at least another one is exposed to the sun. The minimum and the maximum readings of the detectors are used to derive D_H and G_H, respectively [19].

Scanning Pyrheliometer and Pyranometer (SCAPP) (Fig. 2.4c) is a low-cost instrument for measuring G_H and D_H using a photoelectric detector [29]. It was developed by DWD and manufactured by Siggelkow, and it is currently used operationally at few DWD stations.

Other sensors

All radiometers mentioned above measure the broadband short-wave irradiance. Measurements of irradiance received at a particular short-wave range can be made with sunphotometers, whereas the irradiance received by at each short-wave band, i.e., the solar spectrum, is measured with spectrometers or spectroradiometers. Sunphotometers are used to determine the atmospheric turbidity or the aerosol optical depth, among others. Spectral measurements can be made of either direct or global irradiance. They give valuable information about the composition of the atmosphere because each atmospheric component absorbs and scatters radiation at a specific wavelength. For instance, the solar spectrum is used to assess PV materials because each technology has a particular wavelength dependent response whereas the solar spectrum varies spatially and temporally. Therefore, the performance of PV materials may improve or worsen at some regions due to these spectral effects [30].

Apart from the short-wave irradiance emitted by the sun, the Earth also emits long-wave or thermal irradiance in the infrared range [3000 - 300000 nm] that is measured with pyrgeometers. Pyrgeometers can be installed upwards or downwards to measure downwelling or upwelling long-wave irradiance, respectively. For instance, long-wave measurements are useful for correcting the thermal offset of pyranometers. The sum of short-wave and long-wave irradiances is known as total irradiance and is measured by a pyrradiometers. Pyrradiometers are composed of a short-wave and a long-wave radiometer because there are no materials with constant responsivity from 300 to 300000 nm. The difference between total downwelling and upwelling irradiance is known as net irradiance and is measured by net radiometers. Similarly to pyrradiometers, net radiometers are composed of four independent instruments. These quantities are very relevant for studying the global energy balance.

2.1.2 Uncertainty in solar radiation measurements

Measuring surface irradiance is technically more difficult than other meteorological variables such as temperature or precipitation, making solar radiation measurements more prone to errors and increasing their uncertainty [31, 32]. Uncertainty varies depending on the quantity to be measured. B_N measurements present the lowest uncertainty, especially if they come from absolute cavity radiometers. G_H and D_H measurements have larger uncertainties because measuring diffuse irradiance is more complex than recording beam irradiance alone. Besides, pyrheliometers track the sun keeping the incidence angle barely constant, which eliminates the cosine error. The uncertainty of D_H is somewhat larger than that of G_H due to the tracking and shading systems required for measuring diffuse irradiance. For instance, the BSRN uncertainty targets with a 95% level of confidence for 1-min measurements are 0.5% or 1.5 W/m^2 for B_N, 2% or 5 W/m^2 for G_H, and 2% or 3 W/m^2 for D_H [17].

Measuring errors are classified according to WMO [33] in *systematic errors* that add a bias in measurements, *random errors* that are symmetrically distributed around zero and cause the variance of measurements, *large errors* that are mainly caused by malfunctions of the devices and errors in data acquisition and processing, and *micrometeorological errors* that refer to incoherences of the ground records compared to the surrounding regions. However, the most extended classification is the one proposed by Younes et al. [34], who differentiated between *equipment* and *operational* defects based on the source of the error. This classification applies to errors in both pyrheliometers and pyranometers. However, in the following paragraphs, we focus on measuring errors in pyranometers because they are the most extended type of sensors at weather stations.

Equipment errors

Equipment errors originate from the limitations of pyranometers and constitute the own uncertainty of the sensor. Equipment errors are inherent to the type of pyranometer and its calibration. Thus, they persist if the same sensor is installed at different sites, although some equipment errors can worsen under specific climatic conditions. The most common equipment errors are:

- Directional response (cosine error): responsivity variation with the incidence angle. Larger errors are obtained at shallow incidence angles. The semi-spherical dome of thermopile pyranometers is designed to minimize this error. The diffusers of photodiode pyranometers are also designed with different shapes to approach the directional response of thermopile pyranometers, but their cosine error is generally larger.
- Non-linearity: responsivity variation with irradiance. It is measured as the deviation from the responsivity at 500 W/m^2 due to any change of irradiance from 100 to 1000 W/m^2.
- Spectral response: responsivity variation with the wavelength of incoming solar radiation. The spectral response is the main difference between thermopile and photodiode detectors. Thermopile detectors have a constant or flat response over the whole short-wave range (300-3000 nm). Conversely, photodiodes present a wavelength-dependent response over a narrower range (350-1100 nm) that represents around 70-75% of broadband short-wave irradiance.
- Temperature response: responsivity variation with temperature. Thermopile detectors present a more non-linear dependence with temperature than photodiode sensors. Temperature dependence can be corrected if the pyranometer includes a temperature sensor.
- Zero offset A (dark offset): long-wave energy loss that produces negative measurements at night. It only affects thermopile detectors. Dark offsets can be mitigated by ventilating the pyranometers and can be corrected using long-wave irradiance measurements from collocated pyrgeometers.
- Zero offset B: variation in the output due to changes in the pyranometer body temperature. They are specified as the change due to a variation of ambient temperature of 5 K/h. Zero offset B can be corrected by anti-series arrangement of a second sensor not exposed to sunlight.
- Stability: responsivity drifts. They are usually evaluated in annual terms and may require to adjust the calibration constant.

Equipment errors depend on the type of detector (thermopile or photodiode) and the quality of the sensor, which is mainly related to its price. The consequences of equipment errors can be aggravated if the pyranometer is not calibrated correctly. Calibrating a pyranometer not only consists on finding the calibration constant (inverse of responsivity), which transforms the electric output of the pyranometer into irradiance. Some of the abovementioned errors introduce systematic deviations that can be corrected with empirical correction factors. Thus, the calibration constant is not strictly a constant but depends on many factors such as incidence angle, temperature, irradiance, and long-wave irradiance, among others. Corrections must be applied taking into account the specific climatic conditions of the site. Besides, sensors should be re-calibrated periodically to correct responsivity drifts.

The uncertainty values specified by manufacturers can be only assumed if the pyranometer has been properly calibrated. Several authors have studied the individual uncertainty added by each of the previous equipment errors. Driesse et al. [35, 36], Driesse and Zaaiman [37] evaluated linearity, spectral response, temperature dependence and directional response of photodiode and thermopile pyranometers indoors and outdoors. Sengupta et al. [38] also evaluated errors due to the narrow spectral response of photodiode pyranometers. Reda [39] estimated the contribution of equipment errors in the final uncertainty of pyranometers following the Guide to the expression of Uncertainty in Measurement (GUM). The overall uncertainty in thermopile pyranometers has been evaluated by comparison with collocated reference instruments [40, 41]. Photodiodes have also been extensively analyzed due to the appealing features of these sensors. Geuder et al. [42], Wilbert et al. [43], Al-Rasheedi et al. [44] estimated the uncertainty in RSIs with photoelectric detectors by comparison with reference thermopile detectors. They found that the uncertainty of uncorrected photodiodes doubles that of those with adequate corrections for cosine error, temperature dependence, and spectral response. On the contrary, the uncertainty of adequately corrected photodiodes is just slightly larger than most thermopile pyranometers.

A comparison of uncertainty estimates provided by each of these authors is hindered by the different temporal resolution of the data. Uncertainty decreases with a decreasing temporal resolution due to the compensation of systematic deviations. Uncertainty intervals can be calculated with different levels of confidence, though a 95% confidence level is generally used. Finally, the uncertainty may increase due to the particular climatic conditions at the site where the estimation was made. For instance, a high frequency of low solar elevation situations or cloudy situations may aggravate some equipment errors such as the cosine error increasing the total uncertainty of the sensors.

Operational errors

The uncertainty in measurements can increase due to operation-related issues. Operational errors depend on the location of the sensors, the operation conditions (e.g., maintenance protocols), and the influence of external factors. However, they are independent of the quality of the pyranometer. Operational errors involve different factors such as shading by nearby objects, accumulation of dew, frost, snow or dust (soiling) on the sensors, incorrect leveling of the pryanometer, station shut-downs, electric fields in the vicinity of cables, and any failure in the ancillary equipment (data logger, sun trackers, data processing system), among others [34].

Operational errors can be prevented by selecting adequate sites, using high-quality equipment and implementing strict maintenance protocols. Pyranometers should be installed at locations with a horizon free of obstacles and far from any potential source of dust or pollution. In addition, ventilating the pyranometers reduces the accumulation of snow, dew or dust. Besides, pyranometers should be inspected and cleaned at least every day. We refer to McArthur [17] for more detailed information about site selection and maintenance protocols.

2.1.3 Quality control

The best QC strategy is to minimize the number of defects by using high-quality equipment and following strict measurement guidelines. Time series with defects can be corrected, and those with gaps can be reconstructed, but the resulting values will not reach the quality of valid measurements. Defects can still arise even with stringent protocols. Thus, applying QC procedures is essential to identify and remove those records from the time series.

WMO [33] proposed a classification of QC procedures between basic and extended QC according to their automation level and the point of the data flow where the QC method is applied. *Basic QC*, also known as technical control, includes different automatic tests to detect gross errors, analyze the time consistency of the data (rates of change), and the consistency between variables. Basic QC tests are directly applied at weather stations either to raw signals (level I data) or processed values (level II data, 1-10 min averages). *Extended QC* includes more elaborated methods applied at data processing centers of meteorological agencies or directly by end users. They are generally semi-automatic tests that require expert decision to determine whether the value flagged is a true defect. The majority of QC methods for solar radiation measurements in the literature fall within this group. Some of these methods are developed by meteorological agencies to guarantee the quality of their data. For example, the BSRN tests

[45], NREL SERI QC [46] or the QC tests of the Royal Meteorological Institute of Belgium (RMIB) [32]. Other scientists and organizations have also proposed their alternative methodologies such is the case of the AQC web service [47], the web-based service from MINES ParisTech [48], or the MESoR project [49], among others.

A second classification of QC procedures can be made according to their restriction level. More restrictive methods detect a higher number of defects at the expense of reducing the degree of automation because they require expert decision to remove flagged samples. Ohmura et al. [50] enumerated five groups of QC procedures or levels, organized from less to more restrictive as follows: 1) physically possible ranges, 2) extremely rare ranges, 3) across quantities relationships, 4) model comparison, 5) time series examination.

1) Physically possible and 2) Extremely rare ranges Range checks verify if measurements fall within a particular interval defined by physically or statistically possible limits. They are the most widely used QC method, being included by most QC procedures as the first stage of quality level [51, 49, 46, 52, 32, 45]. The least restrictive intervals are those based on physically possible limits. The upper limit is usually set as a function of the extraterrestrial irradiance while the lower one generally lies between -4 to 0 W/m^2 [51, 49, 52]. Statistical ranges are more restrictive than physical ranges because they flag possible but unlikely samples. They are sometimes calculated similarly to physical ranges, but including an empirical or statistical coefficient that narrows the interval. The lower limit can be increased by using the clearness index (K_T) or the modified clearness index (K'_T) [53], e.g., discarding samples with $K_T < 0.03$ [48]. Climatological values are also used to adapt the intervals to the conditions of the site [52].

Range checking can also evaluate the time consistency of the data, i.e., the rate of change between two consecutive samples. These checks have to be applied with high temporal resolution data as the correlation between the adjacent samples increases with the sampling rate [32]. However and compared to other meteorological variables, the plausible rate of change of surface irradiance can be very high due to clouds motion reducing the number of errors detected by these checks. For instance, WMO [33] specifies that rates of change for G_H values should be below 800 W/m^2 for sub-minutely data, and below 1000 W/m^2 for 2- to 10-min data. A variant of consistency checking is persistence tests, which flag either constant or highly variable values based on the standard deviation of consecutive samples.

3) Across quantities relationships The BSRN recommends to measure redundant variables (G_H, D_H, B_N) and employ redundant instruments for measuring the same variable to reduce the uncertainty of measurements. The majority of QC procedures include consistency tests based on solar geometry relationships [51, 45, 32, 49] when G_H, D_H, and B_N are simultaneously measured. Across quantities relationships can also be applied with dimensionless indexes such as the clearness index (K_T), the beam transmittance ($K_N = B_H/E_H$), the effective diffuse transmittance ($K_D = D_H/E_H$), or the diffuse ratio ($K = G_H/D_H$). Some QC procedures use these indexes in envelope tests that analyze the whole time series in the $K - K_T$ and $K_N - K_T$ spaces [34, 32, 46, 54] instead of applying range tests. The detection of errors with envelope tests is generally performed by inspecting visually the plots generated, but it can be semi-automatized by setting empirical or statistical limits in the dimensionless spaces.

The relationship between solar radiation and other variables such reflected irradiance, long-wave irradiance or sunshine duration can also be analyzed. For instance, sunshine duration has been widely used to quality control solar radiation because it has been historically measured at many weather stations [32, 31]. In this line, one of the most obvious relationships between sunshine duration and irradiance is the definition of sunshine duration given by WMO: time during which $B_N > 120$ W/m^2.

4) Model comparisons Range tests discussed so far can be narrowed by using estimations from solar radiation models to define the interval limits. The upper limit can be made more restrictive with estimations from clear-sky models such as ESRA model [48, 32], Page model [34] or Bird model [49, 32]. These estimations are made under clean atmospheric conditions setting aerosols and water vapor to 0 or Linke turbidity to 1, including a weighting coefficient of around 1.1 [32, 55]. The lower limit can be increased with the estimations for overcast conditions (Page overcast-sky model [34]) or by using the Rayleigh limit [56].

Measurements can be directly compared against estimations instead of using them to narrow range tests. For instance, empirical models can be applied when other variables besides solar radiation are measured at the weather station [47]. The drawback is that empirical models present their own uncertainty, which can be sometimes greater than the uncertainty added by some of the defects. Estimations can also be obtained by spatial interpolations from nearby stations, also known as spatial consistency tests [32]. These tests can be applied at low-lying areas where the spatial variability of surface irradiance is low. Besides, they should be applied with averaged data (daily or monthly) because the instantaneous atmospheric conditions vary in small distances.

5) Time series examination The most reliable QC procedure is the visual examination of the time series. None of the methods described can replace an expert eye. The visual inspection of instantaneous time series is useful to detect defects such as snow, shadows or soiling. Inspecting monthly time series is more appropriate to find calibration drifts. Nonetheless, inspecting the complete time series of each variable at each location is very time-consuming. Thus, graphical methods requiring visual inspection are only used to analyze doubtful cases or as a complementary tool to evaluate the flags generated. For instance, the detection of defects with envelope tests is based on finding unusual patterns in the $K-K_T$ and K_N-K_T spaces. Another example is the QC procedure proposed by Moreno-Tejada et al. [57], which consists of plotting color-coded BSRN quality flags during one year of data (daily observations vs. days of the year). Visual inspection was also proposed by Ineichen [58] to detect timestamp issues. Ineichen's method analyzes the symmetry between morning and afternoon samples by plotting G_H and B_N against the sin of α_S under clear-sky days. If the timestamp is correct, morning and afternoon samples lie over the same line.

2.2 Solar radiation modeling

Measurements from ground radiometers are the most accurate source of surface irradiance data when high-quality equipment and strict protocols are used. However, the acquisition, operation, and maintenance costs of these stations are high. Thus, ground measurements are sparsely distributed, even those of G_H which is the quantity routinely monitored at weather stations from meteorological agencies. The number of reliable measurements obtained with high-quality and well-maintained equipment is even more scarce. Besides, the temporal coverage of ground measurements is sometimes insufficient for specific applications and may contain long periods of missing values. Therefore, different estimation methods have been developed to generate long-term and spatially-uniform estimates of the solar resource.

According to their spatial coverage, solar radiation models are classified into point and spatial estimations. *Point estimations* have been historically used as they are computationally less demanding. Solar radiation is estimated from other meteorological measurements using empirical, statistical, or physical approaches. The inputs and sometimes the own model are adapted to the particular conditions of the location assessed to reduce the estimation errors. However, point estimations have similar constraints to ground measurements because they are representative of a small area around the estimation site. On the other hand, *spatial or gridded estimations* are spatially-continuous estimates of surface irradiance in the form of irradiance maps. They cover large areas, even the whole globe, and span several years. This makes them the most widely used option for solar resource assessment. The most representative examples are satellite-based models, atmospheric reanalyses and interpolation techniques [23, 59]. A general overview of the most common modeling approaches will be given in the following sections.

2.2.1 Point estimations

Empirical models

Empirical models estimate G_H from other meteorological variables commonly measured at weather stations such as precipitation and temperature. Some of them include additional deterministic variables such as geographical and solar geometry parameters, and other less common ones such as aerosol content, cloud coverage and the concentration of atmospheric gases [60]. Regardless of the inputs selected, two distinct group of models are differentiated: parametric models, which are analytic expressions based on a finite number of parameters, and statistical models, which encompass a diverse group of generally non-linear techniques from statistics, artificial intelligence, and machine learning fields.

Parametric models are the simplest estimation methods and have been historically used since early 20^{th} century to estimate solar radiation. Given the fact that the extraterrestrial irradiance (E) can be calculated deterministically, most empirical models attempt to predict the atmospheric transmissivity, i.e., the relation between E_H and G_H, from meteorological variables. Parametric models are classified according to variable correlated with solar radiation. Models using sunshine duration or cloud cover generally produce the most accurate estimations due to their high correlation with atmospheric transmissivity [60]. Models based on sunshine duration derive from the Angström-Prescott equation [61, 62] and comprise one of the largest groups. Some examples of models based on cloud cover are those proposed by Black [63] and Supit and van Kappel [64]. Despite the high correlation of sunshine duration and cloud cover with atmospheric transmissivity, these variables are measured by few weather stations and may contain multiple gaps due to the necessity of human intervention in the measurement process. Therefore, other models have been proposed incorporating more extensively measured variables, particularly temperature and precipitation. Two of the most well-known temperature-based models are the ones proposed by Bristow and Campbell [65] and Hargreaves and Samani [66]. Examples of precipitation-based models are those proposed by de Jong and Stewart [67] and Liu and Scott [68]. With the spread of automatic stations, other meteorological variables such as wind speed or relative humidity have also been used [69]. The reader is referred to recent literature [60, 69] for further information about parametric models.

Parametric models generally present a low generalization capacity because they have to be locally calibrated to obtain acceptable estimations. Besides, the use of simple linear correlations limits the accuracy of the predictions obtained. *Statistical models* emerged in the late 90s to overcome some of these limitations, combining several input variables in more complex non-linear relationships. Different techniques have been tested to estimate solar radiation: artificial neural networks (ANN) [70, 71, 72, 73], support vector machines (SVM) [74, 75, 76], regression trees [77] or fuzzy logic [78], among others. Besides, meta-heuristics such as genetic algorithms (GA) [79, 80] have been used to optimize and automate the calibration of these techniques.

The main shortcoming of both parametric and statistical models in particular, and point estimations in general, is that the estimations are only valid in a small area around the location of the predictions. What is worse, the majority of empirical models present similar or greater errors than other modeling techniques such as satellite-based models even at the own location of the point estimation [59]. This is mainly due to the low correlation between meteorological variables such as temperature, precipitation or humidity with the atmospheric transmissivity. Despite models based on sunshine or cloud cover show lower estimation errors, their use is constrained by the few stations measuring these variables. Overall, empirical models currently have historical interest, and their use for solar resource assessment should be generally avoided [19].

Clear-sky models

One of the fundamental parts in solar radiation models is the knowledge the irradiance under clear conditions, which is the practical upper limit of surface irradiance. Clear-sky models are extensively included by estimation (solar resource assessment) and forecasting models. For instance, most satellite-based models calculate cloud properties from satellite images and combine this information with the clear-sky irradiance to obtain surface irradiance. Some examples of clear-sky models implemented by current satellite-based databases are REST2 (NSRDB-PSM) [81], McClear (MACC-RAD) [82], MAGIC (SARAH-2) [83], and SOLIS (SolarGIS) [84]. Similarly, clear-sky models are used for short-term forecastings coupled with cloud predictions from satellite images and sky imagers [85]. Clear-sky models are also the basis for the calculation of the clear-sky index (K_{CS}), which is a common estimator of the atmospheric transmissivity used by many applications such as quality control methods, decomposition models [26], or baseline forecasting models, among others.

Clear-sky models can be broadly classified into empirical and physical [86]. Empirical models are simplified parameterizations of the atmospheric attenuation that provide analytical expressions to estimate clear-sky irradiance using some atmospheric components as inputs. On the other hand, physical models include radiative transfer models (RTM) to simulate the attenuation of the irradiance throughout the different layers of the atmosphere. They provide a more detailed analysis of the atmospheric processes and can easily integrate the effects of the different atmospheric components. However, physical models are computationally more expensive and require a more detailed description of the atmospheric constituents. MAGIC [83], McClear [87], and SOLIS [88] are examples of physical models based on the libRadtran equations [89].

Some physical models (MAGIC or McClear) implement a hybrid approach that combines the benefits of empirical and physical approaches. RTM calculations are made with a limited set of atmospheric conditions and saved into look-up tables (LUTs). The clear-sky irradiance is then obtained by interpolating in the LUTs with the actual atmospheric conditions. This approach considerably reduces the computation cost of physical models enabling their implementation at large-scale geographical information systems (GIS). Some variations of these models are also able to predict all-sky irradiance by solving radiative transfer equations under all type of conditions when supplied with information of cloud properties; such is the case of FARMS and McCloud model. Both clear-sky and all-sky models are the basis of satellite imagery since they can produce gridded datasets when using as inputs satellite-derived estimates of cloud properties and other atmospheric components.

2.2.2 Spatial estimations

Satellite-based models

Satellite-based methods have reached a high degree of maturity and are becoming the most common option to evaluate solar radiation [18, 19]. They provide consistent estimations since the 1980s with resolutions up to 15 min and a few kilometers. Models can employ images from either geostationary or polar-orbiting satellites.

Geostationary satellites orbit in the equatorial plane synchronous with Earth's rotation providing continuous coverage of a specific terrestrial region. They orbit high enough (~36000 km) to gather a full-disk view, but the FOV usable for solar radiation modeling is limited to around 65° due to the shallow viewing angles in higher latitudes. Different organizations have launched several series of meteorological geostationary satellites: GOES-West (135°W) and GOES-East (75°W) from the National Oceanic and Atmospheric Administration (NOAA), Meteosat Prime (0°) and Meteosat East (41.5°E) from the European Organisation for the Exploitation of Meteorological Satellites (EUMETSAT), Elektro (76°E) from ROSCOSMOS, INSAT (70-95°E) from the Indian Space Research Organization (ISRO), Fengyun-2 (105°E) from China's National Satellite Meteorological Centre, and GMS/Himawari (140°E) from Japan Meteorological Agency (JMA), among others. Global coverage at mid and low latitudes can be achieved by combining images from different geostationary satellites as their FOV overlap. However, no geostationary satellites cover latitudes above 65° (Fig. 2.5). Thus, irradiance estimations derived from geostationary images show high temporal resolution (15-30 min) but limited spatial coverage.

Figure 2.5: Spatial coverage of several geostationary satellites.

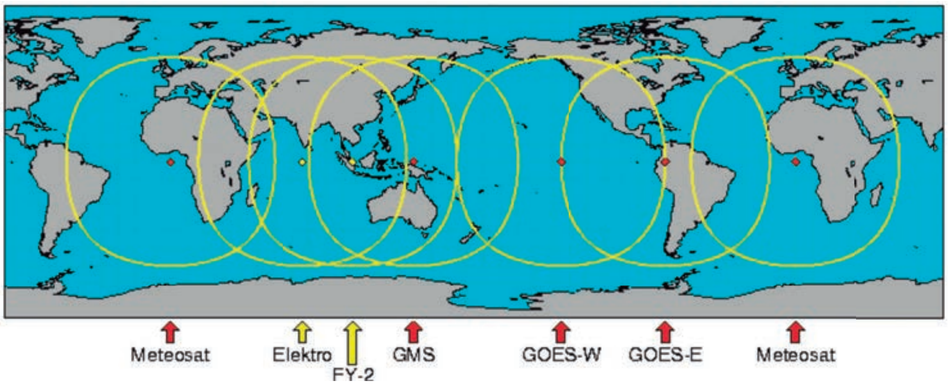

Source: UCAR/NCARR (`https://www.rap.ucar.edu`).

Polar-orbiting satellites scan the whole Earth every day. They are placed at sun-synchronous orbits at an altitude of around 700-800 km. Thus, each satellite crosses the equator at a constant local solar time throughout the year keeping constant the illumination conditions during the scanning process. In the equatorial region, each polar-orbiting satellite produces just two observations, one diurnal and another complementary observation 12 h later at night. Some examples of meteorological polar-orbiting satellites are Metop series from EUMETSAT and NOAA series. Currently, several polar-orbiting satellites from different organizations are available and distributed at different observation nodes, providing images at different diurnal times. However, the number of diurnal images is too low to produce sub-daily estimations. Contrary to geostationary satellites, estimations derived from polar-orbiting satellites have global coverage, but their temporal resolution is limited to daily coverage. The scan swatch of each satellite is around 3000 km, and the orbits overlap with increasing latitude. Therefore, polar-orbiting satellites provide higher spatial resolutions in the polar region, which by contrast is poorly covered by geostationary satellites.

FIGURE 2.6: Spatial coverage of a sun-synchronous polar-orbiting satellite.

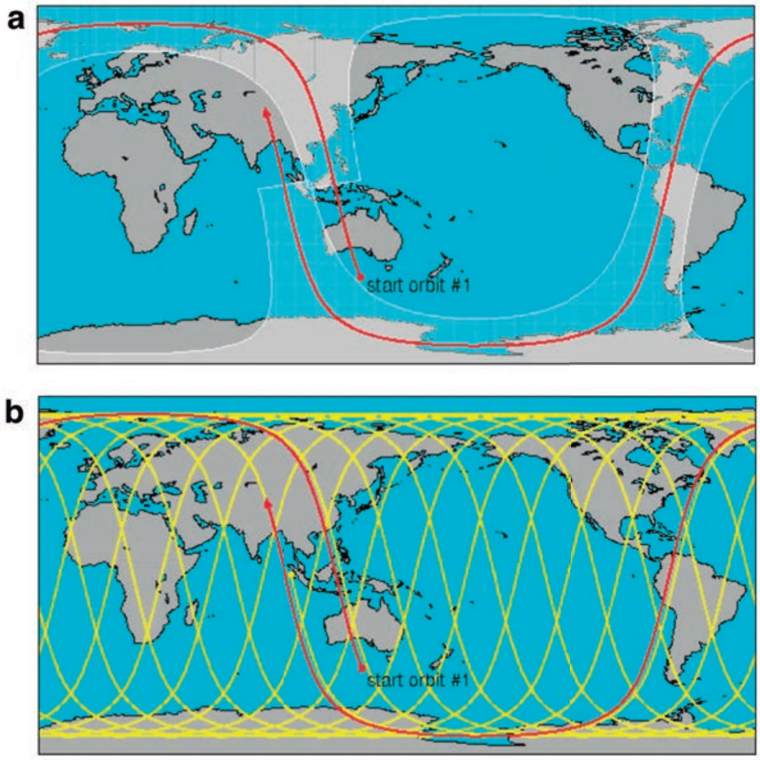

(**a**) Ground path of one revolution of a polar-orbiting satellite. (**b**) Ground paths of all the revolutions made by a polar-orbiting satellite during one day. Source: UCAR/NCARR (`https://www.rap.ucar.edu`).

Regardless of the type of satellite selected, surface irradiance can be estimated from the reflected irradiance measured by satellites with three types of modeling approaches: empirical, semi-empirical, and physical models [19]. *Empirical models* have been historically used due to their low computational cost, facilitating the processing of satellite images at the beginning of the satellite imagery era. G_H is calculated from the reflectance recorded by the satellite visible channels using empirical correlations. The most widespread empirical model is Heliosat [90, 91, 92], further improved with the release of Heliosat-2 [93] and Heliosat-3 [88]. In a first stage, Heliosat-based models calculate the cloud index, i.e., the normalized atmospheric reflectance seen by the satellite:

$$cloud\ index = \frac{\rho - \rho_g}{\rho_c - \rho_g} \tag{2.3}$$

where ρ is the reflectance recorded by the satellite, the minimum reflectance is the ground albedo (ρ_g), and the maximum reflectance is the cloud albedo (ρ_c). Different empirical and statistical correlations are then used to estimate the atmospheric transmissivity from the cloud index [94, 95]. The first empirical models calculated the clearness index (K_T) and combined it with the extraterrestrial irradiance to obtain G_H as follows:

$$K_T = a \cdot cloud\ index + b \tag{2.4}$$

where a and b are two statistically derived coefficients. Newest empirical models calculate the clear-sky index (K_{CS}) instead of the K_T, and then combined it with predictions from clear-sky models as:

$$K_{CS} \approx 1 - cloud\ index \tag{2.5}$$

One of the shortcomings of empirical models is that they only estimate G_H. Thus, empirical decomposition models are required to calculate diffuse and direct irradiance from G_H, increasing the uncertainty of the estimations. Besides, pure empirical models can exploit neither the newest estimations of atmospheric constituents (mainly water vapor and aerosols) nor the information provided by infrared channels. Therefore, most satellite-based models have evolved to a semi-empirical approach by including physical computations.

Semi-empirical models mostly implement the Heliosat-based approach. They still estimate the cloud index with an empirical approach, and the main change from pure empirical models is that they include RTMs in the clear-sky model. One of the most common choices is to use physical clear-sky models based on LUTs to reduce the computational cost. Semi-empirical models generally provide both G_H and its components, while physical clear-sky models can include newest estimations of aerosols and water vapor. Still, these models cannot include information from infrared channels that are useful in detecting snow and calculating specific cloud properties besides the cloud index.

Physical models solve radiative-transfer equations at the different layers of the atmosphere. They are the most computationally intensive models and require precise knowledge of the atmospheric composition. In turn, they can take advantage not only of new ancillary datasets but also of the information provided by all channels of the new satellites. Physical models are classified into broadband and spectral, depending if they solve for the whole short-wave spectrum or each spectral band, respectively. According to the modeling approach, they can also be classified into one-step or two-step models. One-step models derive ground observations directly from satellite observations with RTMs. Two-step models first calculate cloud properties, aerosol, and water vapor from satellite observations and then use these estimations to derive G_H with RTMs. Some of the new satellite-based databases have already switched to a fully physical approach thanks to the advances in the computational field. However, the majority of the methods keep a semi-empirical approach since semi-empirical models are computationally less intensive and can integrate more easily data from oldest satellite versions. This facilitates the production of long-term and stable databases from the 80s demanded in the analysis of climate trends.

Databases generated with modeling approaches mentioned above can be classified into climatological or operational depending on the end use of the data. *Climatological datasets* are the result of processing long periods of satellite images with the same model and set of inputs. They are particularly designed for the analysis of climate trends [96] with the objective of keeping a high temporal consistency. In contrast, *operational products* provide almost real-time estimates prioritizing accuracy above temporal coverage or stability. Operational models are constantly evolving and may undergo upgrades in some of the inputs or in the model itself.

There is a wide number of satellite-based databases available. Databases based on geostationary satellites and using a semi-empirical modeling approach are the most common ones. Some examples include SARAH from CM SAF [97], HelioClim from MINES ParisTech and available via the SODA Service [98], HelioMont from MeteoSwiss [99], SOLEMI and DLR-ISIS datasets from the DLR [100], the NASA/GEWEX Surface Radiation Budget (SRB) [101], and SolarGis [84]. The NSRDB from NREL [81] and MACC-RAD product based on the new Heliosat-4 from the MACC project and the Copernicus program [82] also used geostationary satellites but implementing a purely physical approach. One example of a database using polar-orbiting satellites is the CLARA series produced by CM SAF. The quality of satellite-based databases is generally validated against high-quality measurements by the own organizations producing the databases or by independent researchers: SARAH [102, 21, 22], CLARA [102, 103], NSRDB [81], HelioMont [99], HelioClim [104], MAC-RADD [82], or SolarGis [84] among others. The reader is referred to some recent reviews for a more detailed analysis of the available resources [105, 106, 107, 18].

Atmospheric reanalysis

Atmospheric reanalyses combine estimations from numerical weather prediction (NWP) models with ground and satellite observations [108]. The core of a reanalysis model is the data assimilation model, which uses past observations to limit and guide the predictions of a NWP model. This enables the extrapolation of the variables in space and time [109], generating a coherent set of atmospheric parameters that in some databases exceeds 100 variables. Reanalysis estimations cover the whole Earth (global reanalysis) from the stratosphere to the ground with temporal resolutions up to hourly and spatial resolutions around 30-80 km. Variables assimilated (analyzed fields) typically include air temperature, wind speed, pressure, or relative humidity, but the NWP model also produces a vast list of parameters that are not directly observed and are just outputs of the NWP model (forecast fields). This is the case of the incoming short-wave irradiance, which is obtained with a RTM that simulates the attenuation of the irradiance from the top of the atmosphere to the ground. The quality of surface radiation estimations depends on the RTM used and on the elements that attenuate the irradiance. Note that global reanalyses do not generally assimilate cloud, aerosol, or water vapor data, increasing the uncertainty around the surface irradiance estimates [110, 111].

Reanalysis products can be classified into two groups, global and regional, reflecting their different spatial extent. Global reanalyses are the most common type. Some of the currently available datasets are ERA-Interim [112] from the European Centre for Medium-range Weather Forecast (ECMWF), MERRA-2 from NASA's Global Modeling and Assimilation Office (NASA's GMAO), JRA-55 [113] from JMA, and CFSR [114] from National Centers for Environmental Prediction (NCEP). The ECMWF has recently released the first batch (2010-2016) of the new ERA5 [115], which will replace ERA-Interim by the end of 2019. On the other hand, regional reanalyses cover a specific region of the Earth with higher spatial resolutions (5-10 km). They are generated with a regional NWP model in a high-resolution grid that uses global reanalysis estimates as boundary conditions. Some examples are COSMO-REA6 [116] produced for Europe by the Hans-Ertel-Centre for Weather Research of Deutscher Wetterdienst (HErZ/DWD), the NARR (NCEP) [117] for North America, and the ASR [118] produced by the Polar Research Group for the Arctic.

The two most widely used reanalyses are probably ERA-Interim and MERRA with several validations published about their surface irradiance values. The quality of ERA-Interim has been evaluated against ground stations in Europe [23], Spain [59], and the Eastern Mediterranean [119]. ERA-Interim was also compared against CM SAF satellite-based products

[120, 23], and the CERES-EBAF dataset [119]. Most validations of NASA's GMAO reanalyses [121, 111, 122] focused on the former MERRA [123] as the new MERRA-2 was fully released in 2016. Only a few works have already assessed the changes in surface irradiance data from MERRA to MERRA-2 [124, 125]. Boilley and Wald [24] directly compared MERRA and ERA-Interim. We refer to Wang and Zeng [126], Decker et al. [127], and Zhang et al. [109] for more general validations that compare global reanalysis from different organizations.

All these studies found high bias in G_H estimates from MERRA, MERRA-2, and ERA-Interim. The average bias worldwide was positive for MERRA and ERA-Interim [127, 109] with a strong overestimation over Europe, Asia, and North America. This positive bias was related to an underestimation of the cloud fraction [111, 109], although the opposite, small negative biases under clear-skies, was reported by Boilley and Wald [24]. The dependence of the bias on cloudiness evidences the limitations of reanalyses when modeling cloud patterns [120, 121, 119]. The biases under clear conditions were also related to aerosols and water vapor data [109], but it is generally a secondary defect compared to clouds. Some authors have attempted to correct these biases [111, 128], but there is no method able to make a posteriori corrections of the large and highly variable errors caused by poor modeling of clouds [24]. Hence, ERA-Interim and MERRA are generally not recommended for solar resource assessment [120, 24, 23, 59], and its use is limited to filling gaps in times series [23] or providing gross estimates in low-cloudiness areas [24]. New reanalysis databases such as ERA5 and COSMO-REA6 present many new features that may improve the accuracy of former reanalysis. However, their performance has still not been evaluated against high-quality ground measurements.

Interpolation methods

Interpolation or spatial prediction techniques are used to produce gridded estimations from point values. Two main groups are differentiated, deterministic (non-geostatistical) and geostatistical. Both groups predict the output variable at unknown locations by weighting the observations made at known sites, differing in the method used to calculate the weights.

Deterministic techniques compute the weights based on similarity and distance-related measurements using techniques such as splines, inverse distance weighting (IDW), linear models (LM), or radial basis functions (RBF). On the contrary, geostatistical techniques are based on the spatial autocorrelation of points to calculate the weights. The main geostatistical technique is kriging, which in turn a group of techniques. The most common implementations are ordinary kriging (OK) and universal kriging (UK). OK assumes an unknown constant mean throughout the area of study, whereas UK considers that an underlying trend exists, and thus, this trend can be modeled as a function of the spatial coordinates and additional explanatory variables.

Interpolation has been extensively applied not only with solar radiation but also with many other fields. A straight implementation is to interpolate ground measurements [129, 130], because these are the point values with the lowest uncertainty. Interpolation techniques such as UK can account for the influence of external variables such as altitude [129, 75], clear-sky estimations [130], continentality, or satellite-based estimates [131] to smooth the interpolation errors. Dahmani et al. [72] reported that interpolated values are valid in a radius of 30 km around the stations, and Urraca et al. [59] showed that satellite-based models improve interpolated measurements for distances greater than 20-30 km from the station. These values may be even lower in areas with high irradiance variability such as mountainous regions. Therefore, interpolated values from station measurements should be only used in regions with a high density of stations separated by no more than 30 km.

Interpolation can also be used with point estimations from empirical models, or with a combination of observed and estimated values to increase the density of point values [132, 133, 134, 135, 23]. However, this generally increases the uncertainty of predictions because the errors of empirical and interpolation models add up. Interpolating estimations from empirical methods is generally not recommended because these models obtained larger errors than satellite-based models even at the locations where the empirical model is calibrated. Another method when combining interpolation with other modeling techniques is to interpolate first the inputs (e.g., temperatures), and then apply the estimation technique with the interpolated inputs [136, 75]. However, these methodologies have the same constraints than interpolated values from empirical methods.

The most interesting application of interpolation is the downscaling of either the inputs or the final estimations from satellite-based or reanalysis models. For example, satellite-based databases frequently downscale aerosols or water vapor because ancillary datasets generally have coarser resolutions than satellite images [22]. Besides, the final estimations from satellite-based or reanalysis methods are downscaled to enhance their performance in some particular regions. For instance, digital elevation models (DEM) are used to improve the performance of spatial estimations in areas with steep irradiance gradients such as mountainous regions [137, 138].

2.3 PV system modeling

PV system modeling is required at different phases during the installation lifetime. Simulations have different time horizons at each project stage due to their different objectives. Long-term simulations (yield prediction) are made for planning utility-scale and residential systems, whereas simulations of the current state of the system and short-term forecasts are required during the operation of utility-scale plants. The uncertainty of solar radiation data is one of the main concerns in most simulations because it is generally the main contributor to the uncertainty of the predictions. The availability and accuracy of solar radiation data vary for each type of simulation as it depends on the time horizon, the project stage, and the size of the system.

Simulations of the current and future state of the systems are made during the operational stage of utility-scale facilities. The evaluation of the current state of the system, also known as performance assessment, serves to detect operational defects. It is made by comparing the expected and actual energy yields in terms of the performance ratio (PR). The uncertainty of solar radiation data in performance assessments is generally low because utility-scale plants typically have pyranometers to measure solar radiation on horizontal and inclined planes [13].

Short-term forecasts are required by plant managers to plan the electricity sale on the markets, and by grid operators to combine different energy sources with the demand. Intra-day and day-ahead forecasts are used to sell energy in the different electricity markets. Independently of the time horizon, two modeling approaches are differentiated: feed forecast irradiance into a PV simulation model or directly forecast the energy output using statistical techniques [139]. Short-term forecasts are the simulations with the largest uncertainty due to the highly unpredictable behavior of the atmospheric processes in the near future.

Predictions of the total energy yield produced during the system lifetime (next 20-30 years) are required for planning new PV installations. [10, 140]. Yield predictions serve to select the best sites, assess the feasibility of the project, and calculate cash flows and financial risks. Long-term yield predictions are made using solar radiation data from past years (reference period). Thereby, simulation models for yield prediction comprise [141] (i) the estimation of the solar resource in the reference period, (ii) the estimation of the energy yield in the reference period, and (iii) the estimation of the energy yield in the prediction period. Typically, solar radiation covering at least the last 10 years or typical meteorological years (TMYs) are used [15].

Many modeling tools are currently available to predict the total energy yield of PV systems. They can be classified into simple online simulators and advanced modeling tools. Online simulators provide quick estimations of the energy yield generally at no cost. These tools usually integrate solar radiation data from satellite-based databases, and other meteorological variables needed to simulate PV systems. Hence, online simulators only require a simple description of the PV system to obtain yield predictions (Fig. 2.7). For instance, they usually include a single "system loss" parameter instead of disaggregating the individual losses of each specific component. Therefore, online simulators are specially designed for non-expert users, such as potential buyers of rooftop installations that need rough estimates of the energy yield to calculate the size of the installation. Some examples include PVGIS [142] from the European Commission, PVWatts [143] from NREL, and PV*SOL online, among others.

Advanced simulation tools provide an extensive performance and financial analysis of new PV installations, requiring a more detailed description of the PV system. These models usually incorporate the possibility of using radiation measurements if available, reducing the uncertainty of the predictions. Some examples include the NREL's System Advisor Model (SAM), pvPlanner [144] from SolarGIS, PV*SOL [145] from Valentin Software, and PVsyst, among others. These tools are more widely used for feasibility and financial studies of large PV systems where the uncertainty of the predictions becomes increasingly critical. Both types of modeling tools were compared by Freeman et al. [146] finding large annual deviations in PVWatts up to a 15% whereas the errors of the three advanced simulation packages evaluated (SAM, PV*SOL, and PVsyst) typically remained within ±5%.

Simulations made for energy rating also share many parts with those made for yield prediction. Energy rating is an extension of power rating. PV modules have been traditionally rated and sold according to its power under standard test conditions (STC), i.e., the nominal power given in the product datasheet [147]. However, PV module efficiency varies at conditions different from those at STC due to changes in temperature, irradiance, solar spectrum, and angle of incidence. The actual energy produced by a PV system could be around 90% of that obtained under STC [30, 147]. These variations are geographically dependent and also change with the materials employed. Hence, energy rating studies also serve to assess the efficiency of PV materials under different climatic conditions [30, 148, 147]. A new standard, the IEC 61853, is in preparation to start rating and selling PV modules according to the energy produced. The IEC 61853 consists on four parts: (1) temperature and irradiance dependence, i.e., power rating, (2) angle of incidence and spectral losses, (3) PV system modeling, and (4) climatic datasets needed for energy rating.

FIGURE 2.7: Example of the type of inputs required by the online simulator software PVGIS.

Address: Eg.Ispra, Italy

Lat/Lon: Eg. 45.8 Eg. 8.61

Cursor:

Selected: Select location!

Elevation (m):

Use terrain shadows:

☑ Calculated horizon

☐ Upload horizon file

Choose File no file selected

PERFORMANCE OF GRID-CONNECTED PV

Solar radiation database*

PV technology* Crystalline silicon

Installed peak PV power [kWp]* 1

System loss [%]* 14

Fixed mounting options

Mounting position* Free-standing

Slope [°]* 35 ☐ Optimize slope

Azimuth [°]* 0 ☐ Optimize slope and azimuth

☐ **PV electricity price**

PV system cost (your currency)

Interest [%/year]

Lifetime [years]

Source: http://re.jrc.ec.europa.eu/pvg_tools/en/tools.html#PVP.

Even though both energy yield and yield prediction simulations share many steps, yield prediction considers all specific details such as electrical losses or the exact amount of irradiation at each location after discounting shading, soiling or snow losses. By contrast, energy rating simulations are independent of the specific details of the installation. Another difference is that yield predictions are evaluated in terms of the total energy yield (Y_{AC}) whereas energy rating studies are based on the annual module performance ratio (MPR), an indicator that compares the real performance of PV modules to that under STC during a whole year. This thesis is mainly focused on the selection of radiation data for yield predictions, but some of the conclusions drawn may also apply to energy rating studies as discussed in Subsection 5.4.4. In the following, the main parts of the simulation models used for yield prediction are described, most of which are part of energy rating as well.

2.3.1 Solar resource assessment

Most PV systems have modules at an angle to the horizontal plane to maximize the energy received by the panel. Panels are typically installed at a fixed inclination due to its simplicity and low cost. Tracking systems increase the energy produced at the expense of higher investment and more maintenance needs. In both cases, PV system simulations require the knowledge of G_{POA}, whereas both measured and estimated irradiance data are generally available on the horizontal plane. Even though utility-scale plants measure G_{POA} for monitoring purposes, these datasets are not longer than one year in the planning stage. Therefore, solar resource assessment in the reference period comprises two steps: (i) the estimation of the solar resource on the horizontal plane and (ii) the transposition of irradiance from the horizontal plane to the plane of the array.

Horizontal irradiance data

The simulation of PV systems requires horizontal irradiance data with a resolution of at least 1 h. The smallest uncertainty is obtained from measurements made at the installation site. However, pyranometers are installed during the pre-feasibility stage whereas solar radiation data should cover at least 10 years to reduce the uncertainty due to inter-annual variability. Another option is the use of measurements made at nearby weather stations, but stations measuring G_H are sparsely distributed. Therefore, gridded estimations are becoming the most common choice for solar resource assessment as they provide spatial estimations since the 1980s, allowing to simulate PV systems at almost any location. Satellite-based databases are integrated by some of the most popular online PV simulation tools such as PVGIS, PVWatts, pvPlanner, and PV*SOL, which use SARAH, NSRDB, SolarGIS, and Meteonorm, respectively. Atmospheric reanalyses based on NWP are another alternative that predicts not only irradiance quantities but also other meteorological variables required for PV system modeling. However, reanalyses have generally larger uncertainties than satellite-based databases and are less frequently used. In both cases, the resulting uncertainty is significantly larger than that obtained with solar radiation measurements. This loss of accuracy might be acceptable to analyze the feasibility of small rooftop installations, but it is inappropriate for planning large utility-scale facilities. Hence, pre-feasibility studies of utility-scale plants are generally made based on estimated data, but once the site has been selected, a pyranometer is installed at the new facility to correct the bias of estimated data using site-adaptation techniques [18]. At least, one year of measurements are required. This significantly reduces the uncertainty of yield predictions improving the accuracy of profitability assessments.

The transposition of irradiance data from the horizontal plane to the plane of the array requires separate modeling of beam and diffuse irradiance. As above-mentioned, new satellite-based databases based on a physical modeling approach already estimate both G_H and the radiation components. However, former empirical and semi-empirical methods only estimated G_H. Besides, the variable routinely measured at weather stations is G_H and measurements of B_H or D_H are scarce. In these cases, decomposition or separation models have to be used to calculate D_H and B_H from G_H. Most of these techniques originate from the model proposed by Liu and Jordan [149], which estimates the diffuse factor (K_D) from the K_T. An extensive validation of decomposition models can be found in Gueymard and Ruiz-Arias [26]. These models generally rely on empirical correlations and lack of spatial generalization. Therefore, solar radiation databases estimating both G_H and the radiation components should be preferably chosen to avoid the use of decomposition models.

Transposition model

G_{POA} is calculated from horizontal irradiance quantities by transposing each radiation component separately and subsequently adding them:

$$G_{\mathrm{POA}} = B_{\mathrm{POA}} + D_{\mathrm{POA}} + R_{\mathrm{POA}} \tag{2.6}$$

where B_{POA}, D_{POA}, and R_{POA} are the beam, diffuse, and reflected irradiance on the plane of the array, respectively. The beam irradiance is a deterministic variable that can be transposed based on solar geometry:

$$B_{\mathrm{POA}} = B_H \cdot \frac{\cos\theta}{\cos\theta_s} \tag{2.7}$$

where θ is incidence angle of the sun rays on an inclined plane. The contribution of R_{POA} is much more smaller than the other two components and is generally calculated assuming an isotropic distribution of reflected irradiance:

$$R_{\mathrm{POA}} = G_H \cdot \rho_g \cdot \frac{1 - \cos \beta}{2} \tag{2.8}$$

where β is the module inclination angle, and ρ_g is chosen based on the type of surface and is generally kept constant throughout the year. Intra-annual variations of ρ_g are usually neglected due to the lack of reflected irradiance measurements.

Most simulation tools used previous equations to calculate B_{POA} and R_{POA}, differing in the model used to transpose diffuse irradiance. These can be classified into isotropic or anisotropic. Isotropic models assume that diffuse irradiance comes equally from all sky dome so D_{POA} just depends on the portion of sky seen by the panel. Liu and Jordan [150] proposed one of the first isotropic models. However, the diffuse irradiance is the radiation scattered by atmospheric components such as clouds or aerosols, and it is therefore non-uniform through the sky. Anisotropic models consider that some parts of the sky, such as the circumsolar region or the horizon band, scatter more radiation than the rest of the sky. They generally do not consider the variations of diffuse irradiance associated to cloud cover. Extensive evaluations of both isotropic and anisotropic models can be found in the literature [151, 152, 153].

2.3.2 PV module model

Calculation of effective irradiance

The PV module do not use all the irradiance reaching the plane of the array to produce electricity. The fraction of G_{POA} available for being converted into electrical current is known as effective irradiance (G_{eff}). G_{eff} is obtained from G_{POA} by applying several derating factors accounting for different types of losses:

$$G_{\mathrm{eff}} = \left(f_{\mathrm{AOI}} \cdot f_{\mathrm{snow}} \cdot f_{\mathrm{soiling}} \cdot f_{\mathrm{shading}} \right) \cdot G_{\mathrm{POA}} \tag{2.9}$$

Shading losses (f_{shading}) can be caused either by external or internal shadows. External shading includes terrain shading and shadows produced by nearby objects such as trees or buildings. External shadows are more likely in residential PV than in utility-scale plants, as the location of the prior is constrained by that of the roof. Some of the newest satellite-based databases already account for losses due to terrain shading by using high-resolution DEMs. Besides, many modeling tools include the possibility to add horizon images from digital cameras for modeling shadows caused by both terrain and nearby objects (Fig. 2.8). Internal or inter-row shadows are more influential in utility-scale plants because the panels are generally installed at fixed structures distributed in several rows. Inter-row shading is minimized by increasing the distance between rows and by including backtracking algorithms in PV trackers. Inter-row shading is also modeled based on solar geometry, but the effects of partial shading in the energy production are not so easily predictable.

Figure 2.8: Horizon shading.

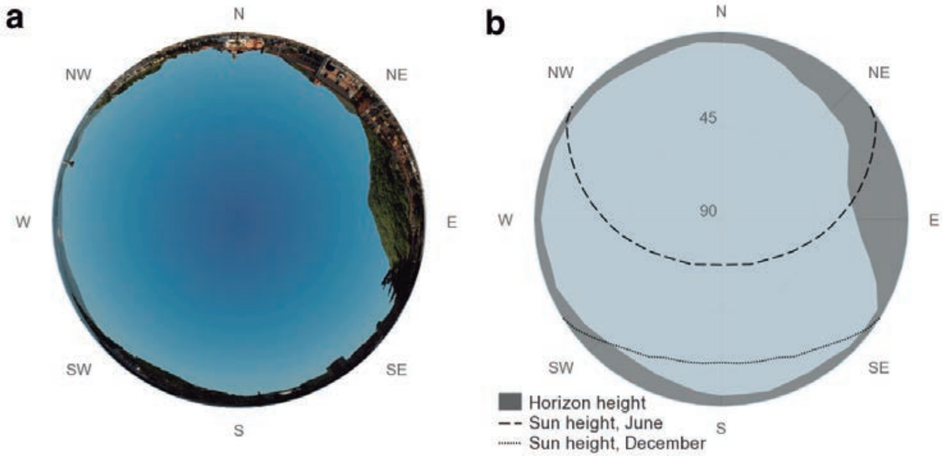

(a) Horizon image from a fisheye camera. **(b)** Sun elevations during the course of the year. Shaded areas depict sun elevations with external shading. Source: `http://re.jrc.ec.europa.eu/pvg_tools/en/tools.html#PVP`

The accumulation of soiling (f_{soiling}) and snow (f_{snow}) over the modules is characterized with experimental factors given the difficulties to develop physical models for both losses. Both defects are geographically dependent and increase with low maintenance and low inclination angles, conditions that prevent the self-cleaning of panels. Snow losses can reach up to a -10% in places with frequent snowfalls and low module inclination angles [12]. Soiling includes pollution, accumulation of dust or pollen, bird droppings, or the growth of lichen. It typically varies from -1 to -4%, exceeding -20% in arid locations [12]. Attempts to model soiling are currently being made based on rain and wind speed data, but they are hindered by the complex interdependencies between these variables. For instance, rain and wind speed favor the self-cleaning of panels, but some particular rain and wind speed events may bring additional loads of dust instead of cleaning the panels.

Angle of incidence (AOI) losses (f_{AOI}) account for the light reflected by PV modules at sharp incidence angles. P_{STC} already includes reflectivity losses at 90° because modules are rated using light perpendicular to the module surface. Hence, AOI losses account for the additional reflectivity at angles different from 90°. They depend on the inclination angle, the type of module surface, and the diffuse ratio because AOI losses are applied separately to diffuse and beam irradiances due to the different angles of incidence of each radiation component. AOI losses vary from -2 to -3% for modules using standard glass, but significant improvements have been found in modules using anti-reflective coating [147]

Module efficiency for conditions different from STC

PV modules are rated under STC, i.e., a irradiance level of 1000 W/m^2 distributed based on the standard solar spectrum (ASTM G173-03 AM 1.5) and a module temperature of 25 °C. The power produced under STC is known as nominal power (P_{STC}) and is reported in the product datasheet. However, the efficiency of the PV module under real conditions (η) varies from that under STC conditions (η_{STC}) due to changes in the irradiance level, ambient temperature, and solar spectrum:

$$\eta' = \frac{\eta}{\eta_{\mathrm{STC}}} = f_T \cdot f_G \cdot f_{\mathrm{spectral}} \tag{2.10}$$

where η' is the relative energy conversion efficiency. Both η_{STC} and η vary within 0.15-0.2 for newest c-Si modules whereas the annually averaged η' is around 0.8-0.95. The direct current module power (P_{DC}) is straightforwardly obtained as:

$$P_{\mathrm{DC}} = G_{\mathrm{eff}} \cdot \eta \cdot A_{\mathrm{mod}} \tag{2.11}$$

where A_{mod} is the total area of PV modules.

Spectral effects (f_{spectral}) account for variations in the module efficiency due to changes in the solar spectrum. These variations are geographically and temporally dependent. The surface solar spectrum depends on the atmospheric composition because gases and other atmospheric constituents absorb and scatter solar radiation at different wavelengths. The solar spectrum also changes with the solar position because it depends on the air mass (AM), i.e., the amount of atmosphere traversed by solar radiation. Variations in the solar spectrum are non-linear and affect each PV technology differently due to the particular spectral response of each material. Spectral effects are evaluated with indicators such as average photon energy (APE) or spectral mismatch (MM) using spectrally resolved irradiance. These data are measured only at a few research centers. However, they are increasingly being estimated by satellite-based databases thanks to the switch to physical modeling approaches. Hence, the number of studies evaluating spectral effects has increased during the latest years. For instance, Huld and Gracia Amillo [30] reported that annual spectral losses of c-Si modules varied from -5 to +2% over Europe, Asia, and Africa, being around +2% over most of Europe [148].

Variations in module efficiency due to irradiance (f_G) and temperature (f_T) effects are more substantial than those by spectral effects. In the same study, Huld and Gracia Amillo [30] reported annual efficiency variations due to temperature and irradiance from -15% to +5%. η remains stable at irradiances close to STC (1000 W/m^2) decreasing exponentially at low irradiance levels. On the contrary, η increases almost linearly with decreasing temperature. Module temperature is estimated from ambient temperature by taking into account the heating effect of irradiance and the cooling effect of wind.

Temperature and irradiance effects can be modeled together or separately. When modeled independently, temperature coefficients given in the product datasheet are used to account for temperature effects, and empirical models or irradiance curves are used to model irradiance effects. However, both effects are usually modeled together using either physical or empirical modeling approaches [154]. Physical models are based on the Shockley and Queisser diode equation and predict the whole I-V curve. They are also known as I-V models, and the most well-known examples are one-diode and two-diode models. I-V models require many inputs and have relatively high complexity, so their use is generally limited to research and theoretical studies. On the other hand, empirical models are simpler as they only predict the maximum power point (MPP). They are also known as MPP models and are usually developed by specialized PV laboratories to simulate the performance of PV modules at an industrial level. A set of power measurements, also known as power matrix, is made at different irradiance and temperature values under laboratory or field conditions. Then, the module power under any specific conditions is obtained by directly interpolating in the power matrix, or by fitting an empirical model.

Electrical losses

The final AC power (P_{AC}) of the installation is obtained by subtracting DC losses, inverter losses, AC losses, and taking into account the availability of the system:

$$P_{\text{AC}} = (f_{\text{mismatch}} \cdot f_{\text{cable,DC}} \cdot f_{\text{inverter}} \cdot f_{\text{cable,AC}} \cdot f_{\text{transformer}}) \cdot P_{\text{DC}} \qquad (2.12)$$

The total energy yield (Y_{AC}) is obtained by integrating P_{AC} over the period T under study:

$$Y_{\mathrm{AC}} = \int_{t=1}^{T} P_{\mathrm{AC}}(t)dt \tag{2.13}$$

If the calculations are made in terms of the specific power P' [W/Wp], Y_{AC} is obtained by multiplying P'_{AC} by the total nominal power installed instead of by A_{mod}.

Mismatch losses are caused by deviations of the real module power (measured power) from the nameplate power specified by the manufacturer. Most manufacturers have a nameplate power tolerance of ~5 Wp that results in yield variations of around 2.5% [13]. PV modules are connected in series, so the panel with the smallest real power limits the final current. This leads to losses of around -0.8% for production tolerances of ~5% [12]. Mismatch losses are larger on rooftop systems than in utility-scale plants, because the latter can measure and sort the panels according to the real power to mitigate the impact of mismatch. Mismatch losses can be aggravated by partial shading and other specific failures altering the power of a specific module.

Electrical losses include wiring losses in the DC side, inverter losses, wiring losses in the AC side, and transformer losses. Cable losses are generally small and below 1%. Inverter losses have been substantially reduced during the latest years due to the expansion of PV technology. New inverters can reach efficiencies up to 98.5%. These efficiencies depend on the size of the inverter, being around 95% for small inverters used in rooftop installations [12]. Transformer losses are also below 2% an are only applicable to utility-scale plants since residential systems are connected to low-voltage grids.

The availability is the percentage of the year during which the system produces electricity from the total time when production is possible. This percentage excludes periods with the sun below the horizon and shutdowns or reductions in the production by mutual agreement with grid operators. Hence, availability losses account for programmed stops (e.g., maintenance) and unexpected shutdowns of the station due to system failures. The availability of PV systems is around 95% under normal conditions [11], and it is generally smaller in residential systems than in utility-scale installations.

2.3.3 Long-term effects

The energy yield in the prediction period (next 20-30 years) is estimated from the energy yield in the reference period (past years) by accounting for long-term variation in the solar resource and changes in the module efficiency.

Module degradation is more accentuated during the first days of exposure of PV modules to light. This effect is known as light-induced degradation, and it is around a -2% after the initial 20 kWh/m^2 produced by c-Si modules [10]. Currently, it is up to manufactures to include this loss in the rated power of the modules [11]. The degradation stabilizes thereafter being around -0.5%/year for c-Si modules. Hence, manufacturers typically provide a double warranty for their products: 90% of the initial maximum power for the first 10 years, and 80% of the original maximum power for the next 10 years [12].

Simulations made for yield prediction commonly assume that the average irradiance in the predicting period does not significantly differ from the average irradiance in the reference period. However, the analysis of long-term surface radiation measurements has evidenced that climate trends in the solar resource do exist [20]. A decrease in surface solar radiation was observed globally from the 1950s to the 1980s (global dimming), whereas a partial recovery has been observed since then (global brightening). Müller et al. [16] reported a trend for the brightening period in Germany of +3.3 W/m^2/decade, which makes the current irradiance level about a 5% greater than the long-term average of the years 1951–2010. This recovery is most likely caused by a decrease in air pollution due to more effective regulations, and by a decrease in cloudiness due to an increase in anticyclonic activity [96]. Therefore, the use of long-term estimations/measurements from past years may lead to the underprediction of the solar resource in the next 20-30 years under the current scenario of global brightening. Müller et al. [10] recommended using radiation data only from the last 10 years to mitigate the effects of climate trends. Users might be tempted to correct solar radiation data for the next years with the current decadal trend, but this should be avoided because the magnitude or even the sign of climate trends may change again in the upcoming future. Nonetheless, climate trends should be accounted for the uncertainty analysis of yield prediction as they may partly explain the deviations observed. Estimating the uncertainty added by climate change in yield predictions complicates even more due to the opposite effects caused by temperature and irradiance in module efficiency. Climate change raises ambient temperature lowering the module efficiency, whereas irradiance raises as well improving both module efficiency and the total energy yield [155].

2.3.4 Uncertainty in PV simulations

Even the most detailed simulation software is useless without an uncertainty analysis of the predictions. Uncertainty estimations are especially required in yield predictions used as bankable data such is the case of yield certificates [14] because they set the risk of the investment. Different methods are used to calculate the uncertainty of PV simulations. One method is to compare predictions against yield measurements from power plants [12]. However, these data are usually not publicly available. An alternative is to calculate the uncertainty of each part of the simulation model separately and combine them. GUM proposes two different approaches to calculate the combined uncertainty. The first method consists of propagating the uncertainty from G_H to Y_{DC} by using the basic uncertainty propagation rules. This method assumes that simulation models are a series of independent multiplicative factors accounting from different losses that transform G_H into Y_{DC} [11, 13, 10]. The only part of the modeling chain that is not strictly a multiplicative factor is the transposition model, but it is usually treated as if it were. This method also assumes that the uncertainty of all factors is normally distributed. In multiplications, relative uncertainties (u) add in quadrature:

$$y = A \cdot x_1 \times B \cdot x_2 \quad \rightarrow \quad u(y) = \sqrt{u(x_1)^2 + u(x_2)^2} \tag{2.14}$$

Relative uncertainties are transformed to absolute uncertainties (U) and vice versa by $u(x) = U(x)/x$. Thus, the combined uncertainty in Y_{DC} is obtained as the quadratic sum of the relative uncertainties from the different sub-models and derating factors (f_n):

$$u(Y_{\mathrm{AC}}) = \sqrt{u(f_1)^2 + u(f_2)^2 + u(f_3)^2 + ... + u(f_n)^2} \tag{2.15}$$

The second method is based on Monte Carlo. The total uncertainty in Y_{DC} is obtained by running multiple simulations sampling from the uncertainty distributions of each sub-models. Monte Carlo generates the uncertainty distribution curve of Y_{DC} instead of a unique value with a specific level of confidence. Besides, Monte Carlo can be applied to non-normally distributed uncertainties. Examples of uncertainty studies using the Monte Carlo method include the studies made by Thevenard and Pelland [11], Hansen and Martin [156], and Müller et al. [15].

Similarly to uncertainty estimations of solar radiation data, the comparison of uncertainty estimations in yield predictions from the literature is hindered by the diversity of uncertainty definitions. Luckily, most uncertainty estimations of Y_{DC} are made in annual terms because this is the resolution of interest to assess the rates of return on investment. Besides, almost all studies follow GUM guidelines, differing on the level of confidence of the uncertainty estimations. GUM defines the expanded uncertainty as k times the standard deviation (sd) or standard uncertainty:

$$u = k \cdot sd \tag{2.16}$$

where k is the coverage factor that sets the level of confidence of the expanded uncertainty. For instance, coverage factors of 1, 1.28, and 1.96 give confidence levels of 66% (u_{66}), 80% (u_{80}), and 95% (u_{95}), respectively. The coverage factor method can be only used when variables are normally distributed, so several studies use Monte Carlo when normality is not fulfilled.

Uncertainty studies reported that solar radiation data not only was the most dominant factor in Y_{DC} [25, 157] but also the factor accounting for most of the uncertainty (around 50% of the total uncertainty [14, 11, 15, 13]). Müller et al. [10] estimated a total uncertainty (u_{66}) in Y_{DC} of ±8.1%, with a ±4.2% attributed to solar radiation data (±3% horizontal irradiance plus ±3% in the transposition model). Thevenard and Pelland [11] estimated a u_{66} in Y_{DC} of ±8.7% during the first year of the installation and a u_{66} = ±7.9% during the system lifetime. In this case, solar radiation data accounted for more than half of total uncertainty (±5%). GeoModel Solar [12] reported a u_{80} in Y_{DC} of ±4.6 and ±11.5% under low- and high-losses scenarios, respecteviely. In this case, ±4% and ±8% came from satellite-based databases, respectively. Richter et al. [13] compared the uncertainty in yield predictions (u_{95} = ±6-8%), which use solar radiation estimations, against that in performance assessments of utility-scale plants (u_{95} = ±2-5.3%), which use pyranometer measurements. The substantial differences between both types of simulations highlight the relevance of solar radiation data.

The two most important indicators when selecting radiation databases to simulate PV systems are the bias and annual uncertainty in G_H. As above-mentioned, the uncertainty in solar radiation data is the main driver of the uncertainty in yield predictions. However, the bias in G_H is even more influential, as if not corrected, the bias in G_H conveys proportionally to Y_{DC} [156]. This is because PV simulation models are virtually a series of multiplicative derating factors. For example, the biases in Y_{DC} obtained by Müller et al. [157] (+4.1%) and Müller et al. [10] (+3.7%) by comparing predicted and measured values of Y_{DC} were mainly driven by the bias in G_{POA} (4.9% and +2.9%, respectively). The interdependence between bias and uncertainty is generally ignored when choosing radiation databases. However, Cole et al. [25] suggested that intra-annual uncertainties in G_H may lead to additional systematic deviations in annual Y_{DC} of about a ±2%.

This implies that radiation databases with low bias and annual uncertainty may not always assure the best yield predictions. Quantifying more accurately the effects of large intra-annual deviations in radiation data on the simulation of PV systems would improve the selection of solar radiation databases.

Chapter 3

Data

3.1 Solar radiation measurements: weather stations

3.1.1 Global dataset

The Global dataset is exclusively composed of stations from the BSRN [158], which is a global radiometric network created to provide accurate reference data for validating satellite-based estimations and climate models [50]. It delivers 1-min records of G_H, B_N and D_H, covering the major climatic zones and following the highest-quality standards. BSRN stations are sparsely distributed. There are currently just 59 active BSRN stations, with a very low density of stations in regions such as Africa, South America, or Central Asia.

Figure 3.1: Locations of the BSRN stations included in the Global dataset.

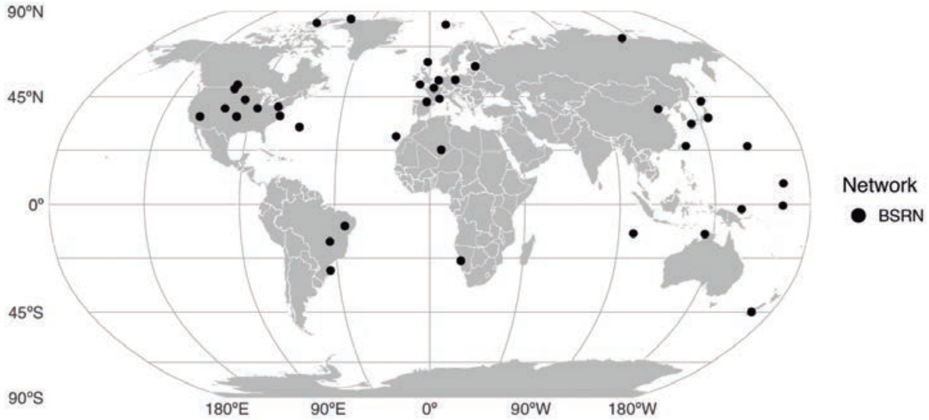

The Global dataset is composed of 41 BSRN stations that had more than 7500 h of G_H measurements for at least one year from 2010 to 2014 (Fig. 3.1). Stations in the Antarctic were excluded. All stations used secondary standard ventilated pyranometers: CM11, CM21, and CM22/CMP22 (Kipp&Zonen).

3.1.2 European dataset

The European dataset is composed of 334 weather stations that measure G_H and are homogeneously distributed over Europe (Fig. 3.2). In all cases, G_H was retrieved at the highest temporal resolution provided at no cost, from 2005 to 2015. The temporal resolution of data varies between networks (Table 3.1). Only those years with more than 7500 h of measurements were used in this study.

FIGURE 3.2: Locations of the weather stations included in the European dataset.

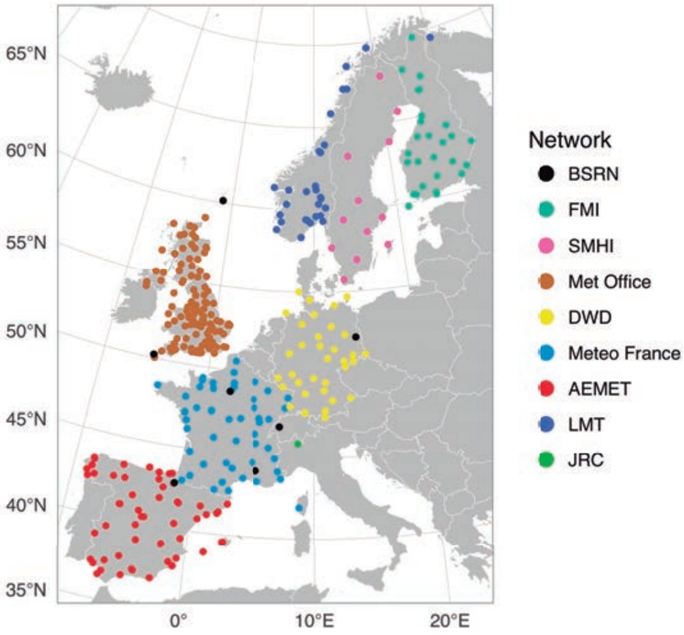

Most stations belong to national meteorological agencies (Table 3.1). In Sweden, the Swedish Meteorological and Hydrological Institute (SMHI) [159] measures G_H with CM11 (Kipp&Zonen) pyranometers before 2008, and with CM21 (Kipp&Zonen) pyranometers since then. In both cases, pyranometers were kept ventilated. In Finland, stations from the Finnish Meteorological Institute (FMI) [160] use CM11 (Kipp&Zonen) ventilated pyranometers. In the UK, data from the national weather service (Met Office) is accessible via Met Office Integrated Data Archive System (MIDAS). Before 2010, some stations used second class CM3 and CM5 (Kipp&Zonen)

Table 3.1: Description of the monitoring networks included in the European dataset

			Type of pyranometer[c]					
Network	Type[a]	Temporal resolution[b]	SS	FC	SC	Ph.	NR	**Total**
BSRN	rad.	1 min	7	-	-	-	-	**7**
FMI [FI]	met.	1 h (:00 LST)	27	-	-	-	-	**27**
SMHI [SE]	met.	1 h (:00 LST)	12	-	-	-	-	**12**
Met Office [UK]	met.	60 min (:30 UTC)	85	-	9	-	27	**121**
DWD [DE]	met.	1 h (:30 LST)	34	-	-	-	-	**34**
Météo France [FR]	met.	1 h (:30 LST/UTC)	49	-	-	-	-	**49**
AEMET [ES]	met.	1 d	55	-	-	-	-	**55**
LMT [NO]	agr.	1 h (:00 LST)	28	-	1	-	-	**29**
JRC-Ispra [IT]	res.	1 min	1	-	-	-	-	**1**
Total			-	-	**10**	-	**27**	**335**

[a] rad. = radiometric, met. = meteorological, agr. = agriculutral, eme. = emergencies.

[b] Values in brackets give interval midpoints. UTC = coordinated universal time, LST = local solar time.

[c] SS = secondary standard, FC = first class, SC = second class, Ph. = photodiode, NR = not reported.

pyranometers, but all measurements were made with CM11/CMP11 (Kipp&Zonen) pyranometers since then. In Germany, the Deutscher Wetterdienst (DWD) [161] freely offers station data via the Climate Data Center (CDC). Most DWD stations use secondary standard CM11 or CM21 pyranometers (Kipp&Zonen). In France, Météo France type 0 (synoptic network) and type 1 (automatic network) stations were used. Most stations belong to the synoptic network, but areas with low density of synoptic records, primarily the Alps and Pyrenees, were covered with type 1 stations. In Spain, stations from the national service, i.e., Agencia Estatal de Meterología (AEMET) [162], were used. All AEMET stations have ventilated secondary standard pyranometers. AEMET only provides daily means of G_H at no cost.

The Norwegian stations belong to the Landbruksmeteorologisk Tjeneste (LMT), which is a project run by the Norwegian Institute of Bioeconomy Research (NIBIO) for emergency services and agricultural research [163]. These stations are primarily located along the shoreline, which is characterized by narrow fjords cutting into high mountains. Most stations use secondary standard CM11/CMP11 (Kipp&Zonen) pyranometers, except for one station using a second class CM3 (Kipp&Zonen). The European dataset also includes some European BSRN stations (CNR, CAR, PAL, PAY, CAB, LIN, LER, and CAM), and the weather station from the Joint Research Center (JRC) at Ispra. The JRC station has a secondary standard CM11 (Kipp&Zonen) pyranometer, and the data can be freely accessed via

JRC [164].

FIGURE 3.3: Locations of the European weather stations used for PV simulations.

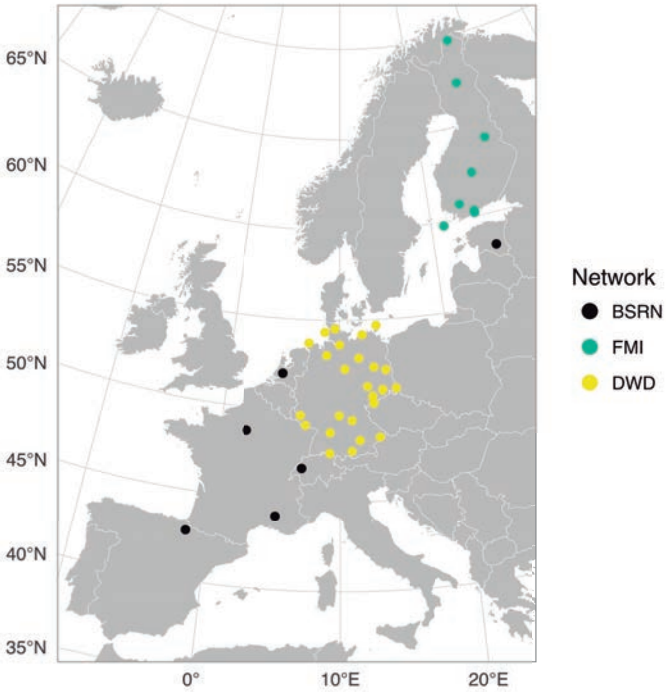

Solar radiation data used to simulate PV systems must have sub-daily resolution (preferably 1 h or higher) and include measurements of G_H and at least one radiation component (B_H or D_H) to avoid using separation models. Based on this, 39 weather stations from the European dataset which measure G_H and D_H with a resolution of at least 1 h were selected. Although some stations also record B_N, these data were not retrieved and B_H was calculated from G_H and D_H in all cases for homogenization. Stations selected belong to BSRN (6 stations), FMI (8 stations) and DWD (25 stations), covering most European latitudes. Years from 2010 to 2015 with more than 7500 h of simultaneous measurements of G_H and D_H were used. G_H and D_H were recorded with unshaded and shaded ventilated pyranometers, respectively. Most of them were secondary standard Kipp&Zonen pyranometers, except for DWD-2928, which had PRM2 (Sonntag) pyranometers (shaded and unshaded) from 2010 to 2013, and DWD-4336 & DWD-4393, which used a SCAPP for measuring D_H in 2010.

3.1.3 Spanish dataset

The Spanish dataset was composed of all Spanish weather stations that provide G_H measurements at no cost (Fig. 3.4). This results in a dataset comprised of 748 stations distributed in 9 networks: 1 global network, 2 national networks, and 6 regional networks. The dataset includes the BSRN station located at Cener, Pamplona (CNR). The two national networks are the national meteorological service (AEMET) and Servicio Integral de Asesoramiento al Regante (SIAR) [165], which is a national network created for irrigation planning. Note that some SIAR stations belong to the Spanish Ministry of Agriculture and some others to the regional governments. Thus, some differences may exist in the maintenance and calibration protocols. The regional networks are the meteorological agencies of Navarra (Meteo Navarra) [166], Cataluña (Meteocat) [167], País Vasco (Euskalmet) [168], and Galicia (MeteoGalicia) [169]. All Meteo Navarra stations belong to the Government of Navarra (GN), except for the station located at University of Pamplona (UPNA). The remaining regional networks are SIAR Rioja [170], the SIAR branch at La Rioja, and SOS Rioja [171], the emergencies network of the Government of La Rioja.

FIGURE 3.4: Locations of the weather stations included in the Spanish dataset.

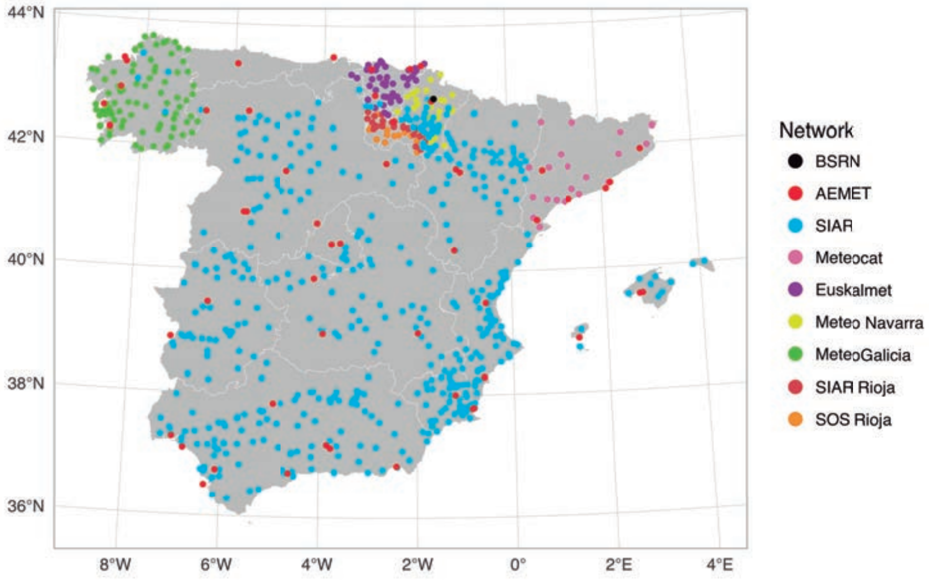

In all cases, G_H was downloaded from 2005 to 2013 at the highest temporal resolution provided at no cost (Table 3.2). The dataset contains only years with more than 7500 h of valid data. The number of years available

TABLE 3.2: Description of the monitoring networks included in the Spanish dataset.

			Type of pyranometer[c]					
Network	Type [a]	Temporal resolution [b]	SS	FC	SC	Ph.	NR	**Total**
BSRN	met.	1 min	1	-	-	-	-	**1**
AEMET	met.	1 d	53	-	-	-	-	**53**
SIAR	agr.	30 min (:00 UTC)	-	19	35	348	66	**468**
Meteo Navarra	met.	1 d	26	-	-	-	-	**26**
Meteocat	met.	1 d	-	15	-	5	-	**20**
Euskalmet	met.	10 min (:05 UTC)	43	-	-	-	-	**43**
MeteoGalicia	met.	10 min (:05 UTC)	1	21	34	27	1	**84**
SIAR Rioja	met.	1 h (:00 UTC)	-	-	21	-	-	**21**
SOS Rioja	eme.	1 h (:00 UTC)	-	12	-	-	4	**16**
Total			**124**	**67**	**90**	**380**	**71**	**732**

[a] rad. = radiometric, met. = meteorological, agr. = agriculutral, eme. = emergencies.

[b] Values in brackets give interval midpoints. UTC = coordinated universal time, LST = local solar time.

[c] SS = secondary standard, FC = first class, SC = second class, Ph. = photodiode, NR = not reported

varies between the stations. For each station, the information about the pyranometer model was collected, and sensors were accordingly classified as thermopile (285 stations) and photodiode pyranometers (386 stations) (Table 3.2).

3.2 Solar radiation estimations: radiation databases

3.2.1 Satellite-based models

SARAH

SARAH is a climate data record generated by CM SAF for Europe, Africa, and Asia using images from Meteosat geostationary satellites. SARAH implements a semi-empirical modeling approach. First, the effective cloud albedo or cloud index is calculated with a modified Heliosat algorithm using the broadband channel of MIVIRI instruments on-board MFGs (1983 - 2005) and the two narrow-band visible channels of SEVIRI instruments onboard MSGs (2006 - present). The cloud index defines the atmospheric transmissivity and is closely related to the clearness index ($K_{CS} \approx 1 - cloud\ index$), which is then combined with the clear-sky predictions of the all-sky model SPECMAGIC [172]. This is a variation of MAGIC clear-sky model [83] that includes spectrally resolved data. Both implement an efficient computational method based on LUTs to interpolate current atmospheric conditions on pre-computed RTM calculations.

Different versions of SARAH are currently available: SARAH-1 [173], SARAH-2 [174], and SARAH-East (SARAH-E) [21], an extension of SARAH-1 using images from Meteosat East (57°E). In this study we have used SARAH-1, SARAH-2, and SARAH PVGIS [142], a combination of SARAH-1 and SARAH-E. All versions have a spatial resolution of $0.05° \times 0.05°$. Although MSG satellites have a 15-min resolution, the temporal resolution of all versions is limited by that of MFG satellites (30 min). The specific characteristics of each version are:

- SARAH-1 (1983 - 2013). Hourly means are the weighted average of 30-min instantaneous values. Aerosol values are monthly climatologies from MACC reanalysis downscaled from its original resolution (∼120 km) to $0.5° \times 0.5°$. Water vapor data are monthly estimations from ERA-40 and ERA-Interim remapped to a grid of $0.25° \times 0.25°$.
- SARAH PVGIS (2005 - present). This version is a combination of SARAH-1 and SARAH-E produced almost operationally by the JRC for PVGIS calculations. It uses images from Meteosat Prime and Meteosat East satellites covering Europe, Africa, and most of Asia. The data is available for free from the PVGIS server: `http://re.jrc.ec.europa.eu/pvgis.html`. SARAH PVGIS produces hourly instantaneous irradiance by processing just one satellite image each hour. The spectrally resolved data is used by PVGIS to account for spectral effects on PV panels, but these data are not available for download. High aerosol values have been smoothed to account for the sensitivity of cloud index on high aerosol loads.
- SARAH-2 (1983 - 2013). SARAH-2 provides 30-min instantaneous irradiance and spectrally resolved irradiance. The calculation of hourly and daily means has been modified compared to SARAH-1. Water vapor has been adjusted to account for topographic effects. A correction of the cloud albedo has been implemented to account for slant viewing geometry effects, resulting in an improved performance at the edges of satellite images.

Hourly irradiance was downloaded for all the versions. SARAH datasets contain missing values provided as -1 at low solar elevation angles. The number of gaps is below 1 gap/d on a yearly average, but it increases in winter and high latitudes. Daily means calculated by CM SAF for SARAH-1 and SARAH-2 account for these missing values, so these values were additionally downloaded for validating SARAH-1 and SARAH-2 against weather stations. SARAH PVGIS does not provide daily means, so they had to be directly calculated from the hourly means containing missing values.

CM SAF operational product

CM SAF generates operational products of surface irradiance variables on a daily basis with a temporal delay of about 10 days, using images from Meteosat Prime geostationary satellites. The retrieval algorithm is based on a LUT approach as described in Müller et al. [83]. Two LUTs are used due to the different dominant processes when clouds are present. MAGIC clear-sky model [83] is used under clear sky, while under cloudy sky the measured reflected irradiance (TOA albedo) is related to the atmospheric optical depth based on precalculated LUTs using additional boundary conditions, e.g., surface albedo. Cloud masks are determined using multi-spectral information from SEVIRI instrument. Aerosol information is taken from the GADS/OPAC climatology using NCEP relative humidity to consider the effect of relative humidity. Water vapor data results from the analysis of the DWD global NWP model.

Daily and monthly data are available aggregated on a 15 km sinusoidal grid from the CM SAF data server. In the present study, the instantaneous hourly data of surface irradiance were used, which are available from the PVGIS server. The hourly means contain even more gaps (1-2 gap/d on yearly average) at low solar elevation angles than those of SARAH.

NSRDB

NSRDB is produced by NREL for the Americas using images from GOES-East (75°W) and GOES-West (135°W) geostationary satellites. The current version available is the Physical Solar Model (PSM) [81] and is the first NSRDB version based on a physical approach. In a first stage, cloud properties (cloud mask, cloud type, cloud height, or cloud optical depth, among others) are obtained with PATMOS-X cloud algorithm using data from the four channels of AVHRR instruments onboard GOES satellites. Then, two different RTMs are used to calculate surface radiation variables (G_H, D_H, B_N): REST2 under clear sky and FARMS under cloudy sky. A specific model was used under cloudy sky because the multiple absorption and scattering of clouds complicate radiative transfer processes. FARMS is based on pre-computed cloud transmittances and reflectances of irradiances obtained with the Rapid Radiative Transfer Model (RRTM). Aerosol data are obtained from a combination of MODIS satellite data with MERRA-2 reanalysis. The rest of ancillary variables such as water vapor are obtained from MERRA-2. NSRDB provides 30-min data with a spatial resolution of 0.038° × 0.038°, though in this study we have only used hourly values. Data for single locations or geographical areas are available from `https://nsrdb.nrel.gov`.

CLARA

CLARA is a climate data record generated by CM SAF based on observations from AVHRR instruments onboard NOAA and Metop polar-orbiting satellites. CLARA provides information on cloud properties, surface radiation (short-wave and long-wave), and surface albedo. AVHRR instruments have a spatial resolution close to 1 km at nadir, but data are archived and processed at a reduced resolution of ∼4 km, and the final results are averaged to a grid of 0.25° × 0.25°(∼25 km). The number of available polar-orbiting satellites carrying AVHRR instruments has significantly increased in recent years. Whereas only 1-2 satellites were available before 2000, 3-5 satellites are available since then. Sun-synchronous polar-orbiting satellites pass over equatorial regions twice per day, producing one diurnal observation and a complementary observation 12 h later at night. Each satellite is distributed at different observation nodes, so cloud properties are currently calculated with 3-5 diurnal images. Therefore, CLARA cannot produce sub-daily data, providing only daily and monthly values. A specific version of CLARA is available at the poles because orbits of polar-orbiting satellites overlap in high-latitudes increasing the number of diurnal observations.

Surface radiation quantities are obtained by combining MAGIC clear-sky model [83] with cloud screening products (cloudy or cloud-free conditions) and the TOA albedo derived from the two visible channels of AVHRR instruments. Aerosols values are taken from an aerosol climatology based on the Aerocom model median merged with Aeronet data. ERA-Interim estimations are used for water vapor. Two main versions have been produced: CLARA-A1 [175] and CLARA-A2 [176].

- CLARA-A1 (1982 to 2013). Data over bright surfaces (e.g., snow-covered areas and deserts) were set to missing due to their low quality.

- CLARA-A2 (1982 to 2015). The main change from CLARA-A1 is the extension of temporal coverage. Some minor changes are the use of an improved cloud detection method and the reduction of the number of values set to missing due to their low quality over some snow-covered areas.

Both versions are available from the CM SAF data server: `https://wui.cmsaf.eu/safira/action/viewProduktSearch?menuName=PRODUKT_SUCHE`.

3.2.2 Atmospheric reanalyses

ERA-Interim

ERA-Interim [112] is the 4th generation of global reanalysis products from ECMWF. This dataset is available almost operationally (with two months of delay) from 1979 to present. ERA-Interim uses a 12-h 4DVar data assimilation system. The NWP forecasting model is initialized at 00:00 and 12:00 UTC with a time step of 30 min, but the output frequency is 3 h for surface (2D) variables such as surface irradiance quantities. It uses climatological values for aerosols, carbon dioxide, trace gases, and ozone, and it takes prognostic information from the forecasting model for water vapor. The product has an overestimation of the irradiance at the top of the atmosphere of 2 W/m^2 [112].

The variable used for this study is the surface solar radiation downwards (SSRD) [J/m^2]. In particular, we retrieved steps 3, 6, 9 and 12 of the two daily forecasts performed at 00:00 and 12:00 UTC, where the step represents the number of hours from the beginning of the forecast. For accumulated variables such as SSRD, the value provided is the sum from the beginning of the forecast to the forecast step. Hence, some post-processing was required to obtain the 3-h means. Data can be ordered (for free but registration required) from `http://apps.ecmwf.int/datasets/data/interim-full-daily/levtype=sfc/`

ERA5

ERA5 is the new global climate reanalysis dataset from ECMWF (5th generation). The most substantial upgrades from ERA-Interim are the finer grid (31 km vs. 79 km), the higher temporal resolution (1-h vs. 3-h), the higher number of vertical levels (137 vs. 60), a new NWP model (IFS Cycle 41r2), and the increase of the amount of data assimilated. The data assimilation model is also a 12-h 4DVar. The dataset will cover from 1950 to near real-time, but at the time of writing only data from 2010 to 2016 is available.

The variable used is also SSRD [J/m^2], which is part of the forecast fields. Short forecasts are run at 06:00 and 18:00 UTC every day generating 18 forecast steps (up to 18 h) for each run. In this study, only steps 1 to 12 (the first 12 h) of each short forecast were used. Compared to ERA-Interim, the value provided for accumulated variables is the sum since

TABLE 3.3: Main features of the radiation databases.

Database	Organization	Spatial Coverage	Period	Spatial resolution[b]	Time resolution[c]	Type	Vertical levels	Variables
SARAH PVGIS	JRC	Eurasia, Africa 65°S - 65°N	2005 - present	$0.05° \times 0.05°$ 5 km	1 h (:50/:10 UTC)[d]	inst.	-	G_H, B_H
SARAH-1	CM SAF	Europe, Africa 65°S - 65°N	1983 - 2013	$0.05° \times 0.05°$ 5 km	1 h (:50/:10 UTC)[d]	avg.	-	G_H, B_H
SARAH-2	CM SAF	Europe, Africa 65°S - 65°N	1983 - 2015	$0.05° \times 0.05°$ 5 km	30 min (:50/:10 UTC)[d]	inst.	-	G_H, B_H
CM SAF Oper.	CM SAF	Europe, Africa 65°S - 65°N	2007 - present	$0.15° \times 0.15°$ 15 km	1 h (:55 UTC)	inst.	-	G_H, B_H
NSRDB PSM	NREL	Americas 20°S - 60°N	1998 - 2016	$0.038° \times 0.038°$ 4 km	30 min (:00 UTC)	inst.	-	G_H, B_H, D_H
CLARA-A1	CM SAF	Global	1982 - 2013	$0.25° \times 0.25°$ 25 km	1 d	avg.	-	G_H
CLARA-A2	CM SAF	Global	1982 - 2015	$0.25° \times 0.25°$ 25 km	1 d	avg.	-	G_H
ERA-Interim	ECMWF	Global	1979 - present	$0.75° \times 0.75°$ 81 km	3 h	avg.	60	G_H
ERA5	ECMWF	Global	1950 - present[a]	$0.28° \times 0.28°$ 31 km	1 h (:30 UTC)	avg.	137	G_H, B_H
MERRA-2	NASA's GMAO	Global	1980 - present	$0.625° \times 0.5°$ 50 km	1 h (:30 UTC)	avg.	72	G_H
COSMO-REA6	HErZ DWD	Europe	1995 - 2015	$0.055° \times 0.055°$ 6.2 km	15 min (:00 UTC)	inst.	40	B_H, D_H

[a] Preliminary release: 2010 - 2016.

[b] The second line shows the approximate spatial resolution in km at nadir.

[c] Values in brackets give the interval midpoint of average (avg.) values and the exact time of instantaneous (inst.) estimates.

[d] :50 until 2005 (MFG), :10 UTC since 2006 (MSG).

All databases can be accessed online at no cost.

the previous forecast step, e.g., the step 1 from 06:00 UTC forecast is the SSRD from 06:00 to 07:00 UTC. Therefore, mean hourly irradiances obtained from SSRD forecasts (accumulated radiation) are centered at half-hourly intervals, e.g., the step 1 from 06:00 UTC forecast gives the hourly mean irradiance centered at 06:30 UTC. Daily means were calculated by aggregating all steps from 00:00 to 23:59 UTC: steps 7-12 initialized at 18:00 UTC of the previous day (values centered at 00:30-5:30 UTC), steps 1-12 initialized at 06:00 UTC of the corresponding day (values centered at 6:30-17:30 UTC), and steps 1-6 initialized at 18:00 UTC of the corresponding day (values centered at 18:30-23:30 (UTC). Instructions for download are found in `https://software.ecmwf.int/wiki/display/CKB/How+to+download+ERA5+data+via+the+ECMWF+Web+API`.

MERRA-2

MERRA-2 [177] is the second version of the Modern-Era Retrospective Analysis for Research and Applications (MERRA) produced by NASA's GMAO. MERRA-2 was created to replace the former MERRA reanalysis [123], solving the limitations of the latter in the assimilation of the newest sources of satellite data. The new version maintains the main features of its predecessor, such as the spatial and temporal resolutions and the 3DVar 6-h update cycle. The NWP model is initialized at 00:00, 06:00, 12:00, and 18:00 UTC, and it has an hourly resolution for surface irradiance variables. The most substantial upgrades in MERRA-2 are the use of a new version of the GEOS-5 atmospheric model [178] and the assimilation of aerosol data to analyze five aerosol species including black and organic carbon, dust, sea salt, and sulfates. The variable retrieved was the surface net downward shortwave flux (SWGNT) [W/m^2], and the value provided is the average of each forecast interval centered at 00:30, 1:30, 2:30, etc. Information about data access can be found at `https://gmao.gsfc.nasa.gov/reanalysis/MERRA-2/data_access/`

COSMO-REA6

COSMO regional reanalyses are developed by HErZ/DWD with a resolution of ∼6.2 km for Europe (COSMO-REA6) [116] and of ∼2 km for Germany (COSMO-REA2) [179]. The product is based on the implementation of a regional NWP model using ERA-Interim estimates as boundary conditions. The data assimilation system uses a continuous nudging scheme that makes possible the continuous assimilation of observations. This process is interrupted every 3 h (00:00, 03:00 UTC, ...) for updating lateral boundary conditions, every 6 h (00:00, 06:00, 12:00, 18:00 UTC) for snow analysis, and every 24 h (00:00 UTC) for sea surface temperature analysis and soil moisture analysis. The NWP model is the COnsortium for Small-Scale MOdelling (COSMO) limited-area model (LAM) [180], which is part of the DWD operational scheme. The radiation scheme is called each 15 min. It uses instantaneous distributions of clouds and water vapor, whereas aerosols are modeled with the Tanré climatology. This climatology is used because it is the standard input of the COSMO model, even though it is known to provide too high values of aerosols optical thickness over Europe [181]. The output resolution available for surface radiation is 15 min. Variables retrieved were instantaneous direct radiation (SWDIFDS_RAD) and instantaneous diffuse radiation (SWDIRS_RAD) [W/m^2], which correspond to B_H and D_H, respectively. Data can be downloaded from `ftp://ftp-rea.dwd.de/pub/REA/COSMO_REA6`.

3.3 Additional meteorological data

3.3.1 Rain data

Daily rainfall measurements from weather stations were downloaded to help in the analysis of samples flagged by the BQC.

3.3.2 Temperature and wind speed data

Ambient temperature (T_{amb}) and wind speed at module's height (WS_{mod}) are required to calculate PV module temperature (T_{mod}). Both variables were obtained from ERA-Interim reanalysis, which estimates 10 m E-W wind component ($WS_{10m,x}$), 10 m N-S wind component ($WS_{10m,y}$), and 2 m temperature (T_{2m}) with a spatial resolution of 0.75°×0.75° (~81 km) and temporal frequency of 3 h. T_{amb} was assume to be equal to T_{2m}. WS_{mod} was obtained by adding in quadrature the two wind components and using the power law [182] to estimate WS variation with height:

$$\begin{aligned} WS_{10m} &= \sqrt{(WS_{10m,x})^2 + (WS_{10m,y})^2} \\ WS_{\mathrm{mod}} &= WS_{\mathrm{10m}} \cdot \left(\frac{z_{\mathrm{mod}}}{10}\right)^{\alpha} \end{aligned} \tag{3.1}$$

where z_{mod} is the module's height and α is the power law index, an empirically derived coefficient that depends on terrain roughness and atmospheric stability. In this case, z_{mod} and α were assumed to be 2 m and 0.2, respectively. Linear interpolation was used to obtain hourly WS_{mod} and T_{amb} from the 3-h ERA-Interim estimates. In addition, T_{amb} data were downscaled using the procedure described in Huld and Pinedo [138] to account for local terrain variations.

Chapter 4

Methods

4.1 New quality control procedure: the BQC method

We propose a new semi-automatic QC method that combines model comparison and visual inspection techniques to detect low-magnitude errors in ground measurements. The procedure is referred to as the Bias-based Quality Control (BQC) method as it compares estimations from radiation databases, mainly satellite-based models, against measurements evaluating the stability of the deviations obtained. Specifically, the BQC analyzes groups of consecutive days with a window function flagging those groups in which the daily deviations of all radiation databases statistically differ from the typical values in that region and time of the year. All databases used must be temporally stable to achieve a proper characterization of the deviations. Besides, the BQC includes two color-coded plots to help in the inspection of the quality flags generated.

4.1.1 Calculation of the confidence intervals (CIs)

The first step is to find the typical range of daily deviations for each radiation database in each region analyzed and time of the year. This is done statistically by defining a confidence interval (CI) within which the daily deviations of each radiation database lie. The daily deviations are the difference between estimations and measurements of the variable X being analyzed:

$$deviation_d(X) = X_d^{est} - X_d^{mea} \tag{4.1}$$

The CIs are defined as the median absolute deviation ($\widetilde{MAD}$) around the median bias deviation ($\widetilde{MBD}$). They are calculated for each month of the year m (temporal averaging) and each spatial region sr sharing similar characteristics (spatial averaging):

$$
\begin{aligned}
CI_{m,sr}^{db} &= \widetilde{MBD}_{m,sr}^{db} \pm n \cdot \widetilde{MAD}_{m,sr}^{db} \\
& \qquad m \in (Jan, \ldots, Dec),\ sr \in spatial\ regions,\ db \in radiation\ databases
\end{aligned}
\tag{4.2}
$$

where n is a tuning parameter that weights the $\widetilde{MAD}$ in order to tune the restriction level of the QC method. The $\widetilde{MAD}$ around the median has proven to be a more robust method for detecting outliers than the traditional standard deviation around the mean [183]. The $\widetilde{MBD}$ and the $\widetilde{MAD}$ are obtained in two steps to increase the robustness of the method. First the $\widetilde{MBD}$ is calculated for all stations (st) and all months of the time series (m') as:

$$
\widetilde{MBD}_{m',st}^{db} = median_{m',st}^{db}(deviation_{d,st}^{db}(X)) \tag{4.3}
$$

These values are subsequently averaged again by grouping the months of the time series (m') in the twelve months of the year (m) (temporal averaging) and stations (st) in spatial regions (sr) (spatial averaging). This results in a unique set of twelve CIs per spatial group and radiation database:

$$
\begin{aligned}
\widetilde{MBD}_{m,sr}^{db} &= median_{m,sr}^{db}(\widetilde{MBD}_{m',st}^{db}) \\
\widetilde{MAD}_{m,sr}^{db} &= 1.4826 \cdot median_{m,sr}^{db}(|\widetilde{MBD}_{m',st}^{db}|)
\end{aligned}
\tag{4.4}
$$

The $\widetilde{MAD}$ includes a constant scale factor of 1.4286 that ensures the consistency of estimates for different sample sizes (Eq. 4.4). The use of this constant value and the median makes this statistic more independent of the sample size and more robust than the standard deviation [183].

The CIs in each spatial region should be calculated only with high-quality measurements if available. The BQC will analyze any station within the spatial region including the group of high-quality measurements. If any defect is found in this group, the CIs should be recalculated excluding those samples. Locations where radiation databases typically produce large deviations, such as snow-covered areas, small islands, or high mountains, should also be excluded from the calculation of the CIs. Besides, samples flagged at these locations should be examined carefully because the flags may be caused by deviations in the radiation database and not in the sensor (false alarm). If there are a sufficient number of stations where radiation databases show the same type of failure, they can be grouped in a specific spatial group.

4.1.2 Flagging samples with a window function

Having defined the CIs, a window function goes through the time series of each station flagging those groups of consecutive days where the daily deviations of all radiation databases are predominantly over or under the CI limits. The number of days analyzed by the window function each time is set with the window width (w) parameter. The distance between the first day of two consecutive windows is specified by the parameter *step*. Consecutive windows overlap because w is substantially larger than *step*.

FIGURE 4.1: Flowchart of the window function.

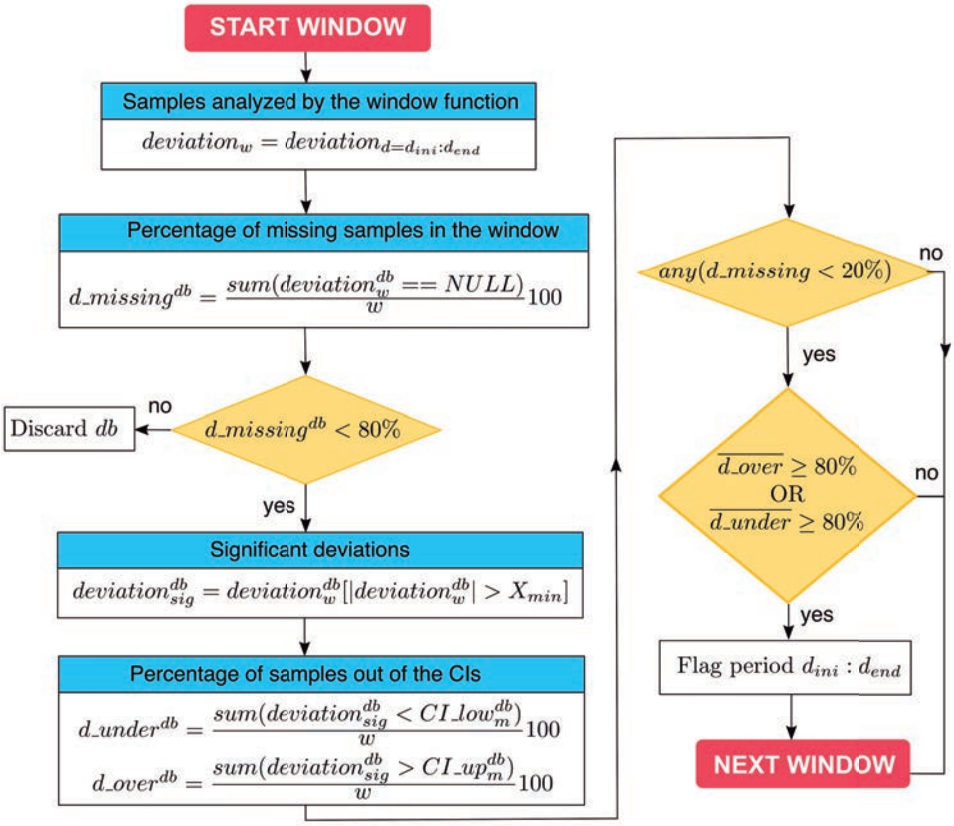

Notes: db = radiation database, d = day of the time series, d_{ini}, d_{end} = first and last days of the time series, respectively, $d\_missing$ = percentage of missing values, d_under, d_over = percentage of daily deviations under and over the CIs, CI = confidence intervals of the daily deviations, CI_low, CI_up = lower and upper limits of the CI, X variable analyzed, X_{min} minimum value of X to consider the deviations significant.

Each analysis of the window function (Fig. 4.1) starts with the calculation of the percentage of missing samples from each radiation database

($d\_missing^{db}$). Databases with more than 80% of missing values are discarded. Besides, at least one database should span almost the whole window ($d\_missing^{db} < 20\%$) to ensure that the analysis covers most of the variability within the window. In the remaining databases, the percentage of days with deviations over (d_over^{db}) or under (d_under^{db}) the CI limits are calculated and subsequently averaged ($\overline{d\_over}$, $\overline{d\_under}$). These percentages are calculated only with significant deviations ($deviation_{sig}$) larger than a threshold X_{min} to reduce the number of false alarms in cases with too narrow CIs (e.g., low irradiance months). All days within the window are flagged if more than 80% of the deviations are either over the CI upper limit ($\overline{d\_over} > 80\%$) or under the CI lower limit ($\overline{d\_under} > 80\%$).

4.1.3 Visual inspection of flagged samples

Figure 4.2: Example of the two color-coded plots generated by BQC for visual inspecting the flags.

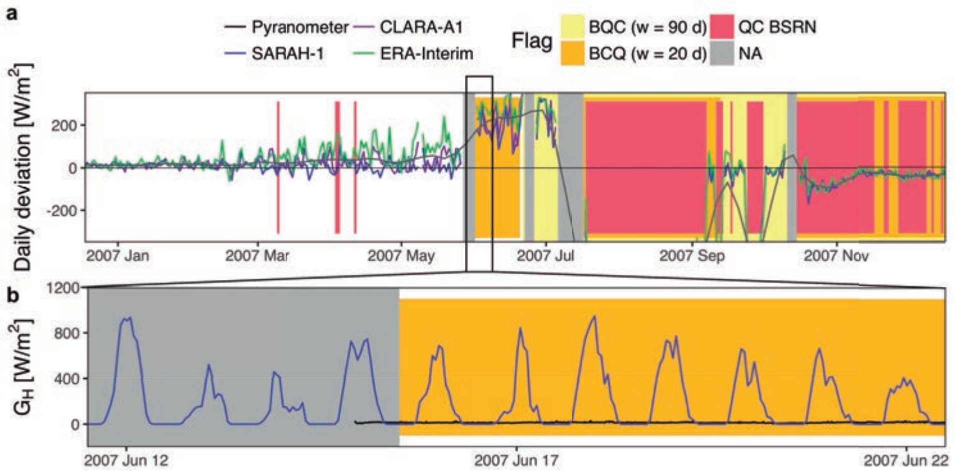

(a) Daily deviations (estimations - measurements) of the radiation databases. The gray line is a smoothed version of the deviations of the three databases. **(b)** Instantaneous G_H from SARAH-1 and the pyranometer.

The BQC automatically generates two plots to facilitate the visual inspection of the quality flags generated: (a) the time series of the daily deviations from all radiation databases, and (b), the time series of instantaneous irradiance from the sensor and radiation databases with sub-daily temporal resolution overlapped. Both plots include color-coded flags that shade those days flagged by the window function (yellow/orange flags) (Fig. 4.2). Additionally, a grey flag shows periods with missing samples, while a red flag indicates that the samples had not passed the BSRN "Extremely rare limits" and "Physically possible limits" (Eq. 4.5). The BSRN tests can be applied only to measurements with sub-daily temporal resolution. Even though the window function works with daily means, it is convenient to include at least one database with sub-daily resolution to generate plot b because this is the one that usually allows finding the cause of the error.

4.2 Pre-processing irradiance measurements

4.2.1 Quality control

Night samples (solar elevation < 0°) at weather stations with sub-daily resolution were set to 0 and subsequently quality controlled using the BSRN range tests [51]:

$$
\begin{aligned}
&\textit{Physically possible limits}: \\
&\qquad -4\ \mathrm{W/m^2} < G_H < E_N \cdot 1.5 \cdot \cos(\theta_s)^{1.2} + 100\ \mathrm{W/m^2} \\
&\qquad -4\ \mathrm{W/m^2} < D_H < E_N \cdot 0.95 \cdot \cos(\theta_s)^{1.2} + 50\ \mathrm{W/m^2} \\
&\textit{Extremely rare limits}: \\
&\qquad -2\ \mathrm{W/m^2} < G_H < E_N \cdot 1.2 \cdot \cos(\theta_s)^{1.2} + 50\ \mathrm{W/m^2} \\
&\qquad -2\ \mathrm{W/m^2} < D_H < E_N \cdot 0.75 \cdot \cos(\theta_s)^{1.2} + 30\ \mathrm{W/m^2}
\end{aligned}
\tag{4.5}
$$

Samples out of the physically possible and extremely rare limits were set to not available (NA). The daily means of European and Spanish weather stations were additionally quality controlled with the BQC. This method was not applied to the Global dataset due to the high-quality of BSRN data and to the geographical dispersion of these stations, which hinders the use of databases based on geostationary satellites to calculate the CIs. The BQC was implemented using SARAH PVGIS, CLARA-A2, and ERA-Interim, for the European dataset, and SARAH-1, CLARA-A1, and ERA-Interim, for the Spanish dataset. The BQC was applied only to G_H measurements because some of these databases (ERA-Interim, CLARA-A2, and CLARA-A1) do not estimate D_H and B_H.

Seven spatial regions were defined to quality control the European weather stations (Fig. 4.3): high latitudes above 65°N (14 stations), Norway below 65°N (23 stations), Finland and Sweden below 65°N (31 stations), Germany (35 stations), France along with the stations in North Italy and Switzerland (53 stations), the UK (123 stations), and Spain (55 stations). All stations available in each region were used to calculate the CIs. One group was roughly made for each country, making an additional split for stations above 65°N. This region presents particular conditions such as

Figure 4.3: Confidence intervals used to quality control the European weather stations.

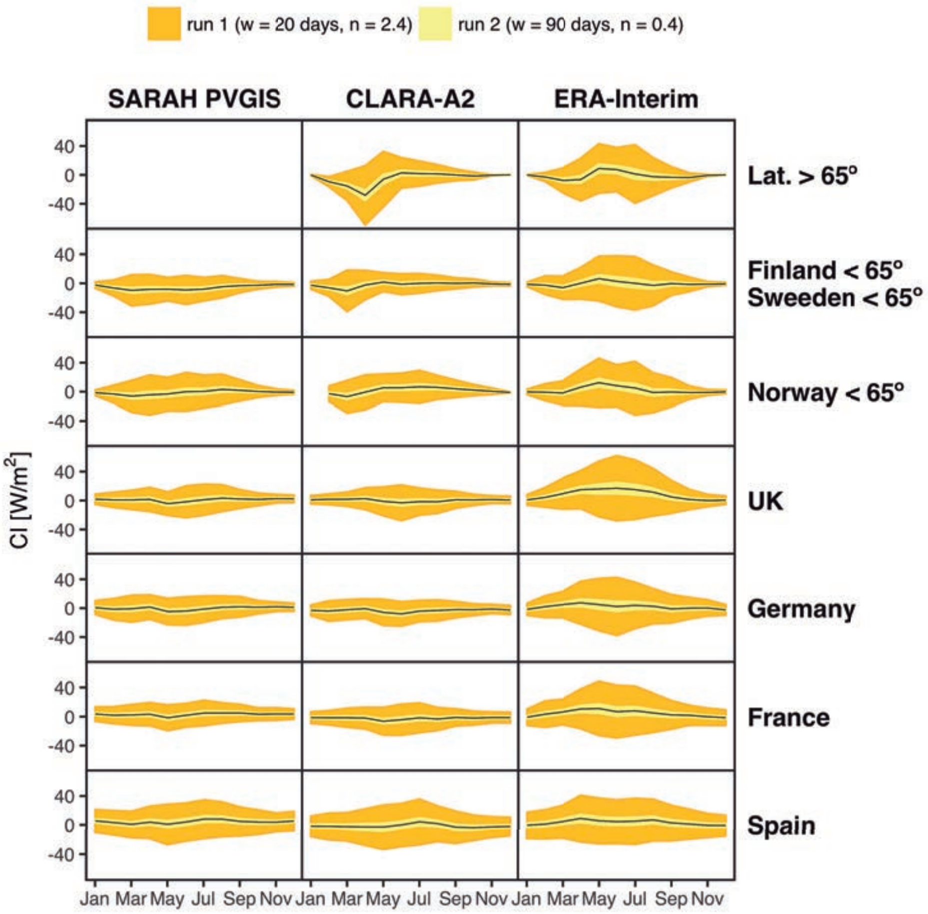

The black line represents the median.

seasonal snow, low viewing satellite angels, and low solar elevation angles in winter. Finland and Sweden below 65°N were grouped together to have a sufficient number of stations for obtaining robust CIs. An additional group could have been made for mountain stations due to the generally poor performance of radiation models there, but the number of stations was too low. These stations were analyzed with the CIs of their corresponding country, and they were treated as false alarms if flagged by the BQC.

The Spanish dataset was filtered out using the same CIs for all the stations (Fig. 4.4). The CIs were calculated using only AEMET stations to increase the robustness of the CIs because AEMET provides the highest-quality measurements among the Spanish networks analyzed.

FIGURE 4.4: Confidence intervals used to quality control the Spanish weather stations.

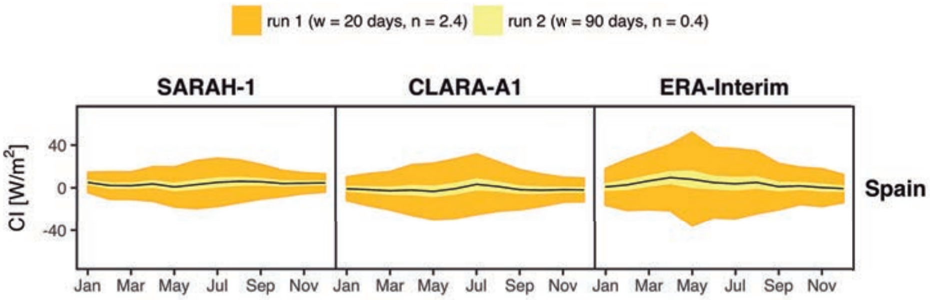

The black line represents the median.

The window function was run two times: (i) $w = 20$ d and $n = 2.4$, and (ii) $w = 90$ d and $n = 0.4$. In both cases, X_{min} was set to 5 W/m^2 or 5% to reduce the number of false alarms and *step* was set to 5 d to seep up the whole process (fast-moving filter). This configuration was determined after analyzing different combinations of w an n (Subsection 5.1.1). The first run looks for short-lived defects analyzing windows of 20 d, relaxing the level of restriction of the CIs ($n = 2.4$) to reduce the number of false alarms. The second run seeks for long-lasting deviations using windows of 90 d. Here, the CIs can be made more restrictive ($n = 2.4$) in order to detect low-magnitude defects such as shading or sensor miscalibrations.

Flagged samples were visually inspected and classified into true defects or false alarms using the two plots generated by the BQC. Defects were classified into the following groups: shading, soiling, snow/frost accumulation, time lags, diurnal values = 0, large errors, incorrect leveling, miscalibrations, and unknown causes. All samples with verified defects were set to NA for validating radiation databases, except for time lags whose effects disappear after aggregating the data to daily values.

4.2.2 Data aggregation

Daily means of G_H were calculated for all weather stations (Global, European, and Spanish) to homogenize the temporal resolution of the data. Hourly means were initially calculated for stations with sub-hourly resolution. In the case of 1-min data, 15-min averages were calculated if at least 5 min were available. Then hourly means were obtained if all four 15-min values were valid, following the procedure described in Roesch et al. [45]. In the case of resolutions between 5 min and 30 min, hourly means were directly calculated if all sub-hourly values were available. Finally, daily means were obtained by averaging all hourly values if at least 20 h were available. This threshold was elevated to 21 h for the dataset of 39 European stations used for the PV simulations. The same aggregation procedure was applied to calculate the daily means of D_H.

4.3 Pre-processing radiation databases

4.3.1 Data extraction

Radiation databases provide gridded estimations of surface irradiance as raster files. However, the exact values at the locations of weather stations are needed to evaluate the radiation databases against point measurements. For products with high spatial resolution (SARAH-1, SARAH PVGIS, CLARA-A1, CLARA-A2, NSRDB PSM, and COSMO-REA6), values used were those of the pixel containing the station location. For products with coarse resolution (MERRA2, ERA-Interim, and ERA5), the closest four pixels to the station location were interpolated using IDW. The spatial resolution of CLARA-A1 and CLARA-A2 is rather high (∼25 km) and similar to that of ERA5. However, CLARA was included in the high-resolution group because CLARA computations are made in a grid of ∼4 km and then averaged, so the output raster files already account for the spatial variability within each pixel.

4.3.2 Quality control

Reanalysis databases are obtained by assimilating satellite and ground observations and using a NWP model to extrapolate these observations in space and time, predicting many other unobserved variables such as surface radiation quantities. Assimilated observations are quality controlled, and the output of the forecast model is limited to a range of physically possible values. Thus, reanalysis data contain neither missing values nor inconsistencies. On the contrary, satellite-based databases may have some missing values due to either a real gap in satellite data or to the inability of the model to generate valid estimations under challenging conditions such as low solar elevation angles, slant viewing geometry, or bright surfaces. Therefore, satellite-based data with sub-daily resolution were quality controlled by setting night values to 0 and diurnal negative values to NA. Besides, missing values of SARAH-PVGIS and CM SAF operational at low solar elevation angles, which were provided as -1, were set to 0 to minimize their impact on the calculation of daily means. These values will still introduce a small negative bias in the daily averages of these databases that should be accounted for the interpretation of the results.

4.3.3 Data aggregation

Daily means of G_H, B_H and D_H for radiation databases with sub-daily resolution were obtained using the aggregation procedure described in Subsection 4.2.2 for station measurements.

4.4 Validation of radiation databases

Satellite-based databases and reanalyses were evaluated against quality-controlled measurements of the Global and European datasets. The main validation was made in Europe because this dataset has a dense network of weather stations covering the major European climates. A second validation was made against the Global dataset to corroborate the findings of the European validation and to evaluate the databases in other regions apart from Europe. In both cases, only the years of data from 2010 to 2014 with more than 310 valid daily samples were used. The specific databases and stations used for each validation were:

- European dataset (293 stations): four satellite-based databases (SARAH PVGIS, SARAH-2, CLARA-A2, and CM SAF Operational) and four reanalyses (ERA-Interim, ERA5, MERRA-2, and COSMO-REA6).
- Global dataset (41 stations): two satellite-based databases (SARAH PVGIS and NSRDB PSM) and three reanalyses (ERA-Interim, ERA5, and MERRA-2).

The variable evaluated was the daily G_H. Some of the radiation databases also estimate D_H and B_H, but these are not measured at all weather stations. Thus, they were validated only in the subset of 39 European weather stations used for simulating PV systems (Section 5.4). Although some databases and weather stations provide sub-daily data, we only evaluated the daily means of G_H because it was the highest resolution we could validate using all available weather stations. For instance, some databases and weather stations provide 1-h values, but they cannot be directly compared because hourly intervals are calculated differently by each monitoring network and radiation database. The validation of 1-h values requires 1-min measurements to calculate the hourly reference values with the same averaging intervals as those used by each radiation database. Besides, if the database provides instantaneous values instead of averages, just a few samples around the estimated value should be used. Thus, validating hourly G_H would have reduced the number of available stations drastically because only the BSRN provides 1-min data.

Radiation databases were evaluated based on the mean bias deviation (MBD), or simply the bias, the mean absolute deviation (MAD) and the root mean squared deviation (RMSD):

$$MBD = \frac{1}{N}\sum_{i=1}^{N}|X^{tst} - X^{ref}| \tag{4.6}$$

$$MAD = \frac{1}{N}\sum_{i=1}^{N}(X^{tst} - X^{ref}) \tag{4.7}$$

$$RMSD = \frac{1}{N}\sqrt{\sum_{i=1}^{N}(X^{tst} - X^{ref})^2} \tag{4.8}$$

where X_{text} is the test value, i.e., the estimations of daily G_H ($G_{H,d}^{est}$), X_{ref} the reference value, i.e., the measurements of daily G_H made at weather stations ($G_{H,d}^{mea}$), and N the total number of daily samples. The term deviation was used in lieu of error to stress that reference values (measurements) have their own uncertainty [184]. Relative metrics ($rMBD$, $rMAD$, and $rRMSD$) were obtained by dividing absolute metrics by annual average irradiance. All years of data had more than 310 valid samples per year, so validation metrics cover most of the inter-annual variability. This implies that biases reported are valid for other temporal resolutions because the bias is independent of the temporal resolution of the data if the number of missing values is low. This does not apply for absolute metrics such as MAD or $RMSD$ because absolute statistics increase with the temporal resolution of the estimations.

The performance of the models under different atmospheric conditions was evaluated with the monthly-aggregated $rMBD$ and with the density plots of daily relative deviations against the clearness index (K_T). The monthly-aggregated $rMBD$ was obtained by dividing the monthly-aggregated MBD by annual average irradiance, instead of by monthly average irradiance:

$$deviation_m(X)[\%] = \frac{X_m^{\text{est}} - X_m^{\text{mea}}}{X_y^{mea}} \cdot 100 \tag{4.9}$$

In this way, the monthly-aggregated $rMBD$ is independent of the seasonal variation of the solar resource and each value shows its real contribution to the annual *rMBD*. The same procedure was used to obtain the daily relative deviations:

$$deviation_d(X)[\%] = \frac{X_d^{\text{est}} - X_d^{\text{mea}}}{X_y^{mea}} \cdot 100 \tag{4.10}$$

The clearness index is the ratio between G_H and the extraterrestrial irradiance received on a horizontal plane (E_H):

$$K_{T,d} = \frac{G_{H,d}^{mea}}{E_{H,d}} \tag{4.11}$$

The K_T is a common indicator of the atmospheric transmissivity that varies from 0.1-0.2 under overcast conditions to 0.8-0.9 under clear conditions. The daily K_T was only calculated if $E_{H,d} > 1$ W/m^2 to prevent the inclusion of outliers in the K_T time series.

4.5 Estimation of uncertainty in solar radiation data

Previous sections dealt with the quality control of measurements and the validation of satellite-based and reanalysis estimations. The next step is to estimate the uncertainty of both measured and estimated G_H under a common framework. For measurements, we analyzed independently the uncertainty of pyranometers (equipment errors) and the uncertainty added by operational defects. We estimated the uncertainty of annual G_H because this is the temporal resolution used to calculate the uncertainty of PV yield predictions. We also reported daily uncertainties for consistency with previous sections and to facilitate the comparison of the results against other studies. The uncertainty analysis was made with the Spanish dataset because it presents the most favorable conditions to estimate the uncertainty statistically: it has a dense network of 732 stations with a high variety of pyranometers, and some Spanish stations showed several defects of different types facilitating the estimation of deviations added by operational errors.

For each factor analyzed (estimations, operational errors, and equipment errors), the annual relative deviation between the irradiance value being analyzed, i.e., the test value (X_{text}), and the irradiance value used as reference (X_{ref}) was obtained as:

$$deviation_y(X)[\%] = \frac{X_y^{tst} - X_y^{ref}}{X_y^{ref}} \cdot 100 \tag{4.12}$$

where X_y^{tst} and X_y^{ref} were calculated using the days with valid values for both test and reference variables. This prevents adding systematic deviations to annual deviations due to the presence of missing values in either test or reference variables. Variables used as test and reference varied depending of the factor analyzed (Subsections 4.5.1 to 4.5.3). Annual and daily uncertainties were calculated statistically from the distributions of annual and daily relative deviations, respectively (Subsection 4.5.4).

4.5.1 Uncertainty in estimations from radiation databases

The uncertainty in estimated irradiance was characterized using one geostationary satellite-based database (SARAH-1), one polar-orbiting satellite-based database (CLARA-A1), one regional reanalysis (COSMO-REA6), and two global reanalysis (ERA-Interim and ERA5). Similarly to the validation over Europe, the annual deviations of the estimations ($G_{H,y}^{est}$) were obtained as:

$$deviation_y^{db} = G_{H,y}^{est} - G_{H,y}^{aemet} \tag{4.13}$$

where the reference values ($G_{H,y}^{aemet}$) were the 53 quality-controlled AEMET stations to reduce the uncertainty of the validation. The analysis was limited to the period in which data from the five databases were simultaneously available (2010-2013).

4.5.2 Uncertainty added by operational errors

The uncertainty added by operational defects was estimated as the difference between measurements from stations with defects ($G_{H,y}^{mea}$) and SARAH-1:

$$deviation_y^{op-error} = G_{H,y}^{mea} - G_{H,y}^{sarah} \tag{4.14}$$

Annual deviations were calculated only at stations and years where defects occurred, independently of the duration of the defect. SARAH-1 was used as the reference due to the lack of collocated measurements to evaluate the magnitude of the operational errors.

4.5.3 Uncertainty of pyranometers (equipment errors)

The analysis of equipment errors was simplified to the comparison of 53 AEMET secondary standard pyranometers against 348 SIAR photodiodes. Sensors from the regional networks and other types of pyranometers (first class and second class) were excluded because they are sparsely distributed, so their inclusion would lead to additional uncertainties related

FIGURE 4.5: SIAR photodiodes separated by less than 20 km from an AEMET secondary standard pyranometer.

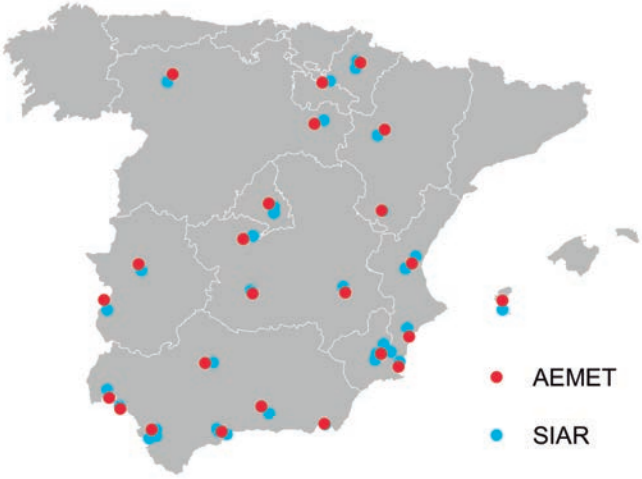

to the spatial location. AEMET uses ISO 9060 secondary standard pyranometers from Kipp & Zonen, which have an achievable uncertainty at 95% CI of ±3% and ±2% for hourly and daily values, respectively [19]. The uncertainty of annual values should be smaller due to the compensation of seasonal deviations, so we assumed an annual uncertainty of ±1.5%. SIAR photodiodes are the SP1110 model (Skye Instruments). Their datasheet specifies an absolute accuracy always better than 5% and most times under 3%, but it details neither the temporal resolution nor the confidence level of this value. Besides, field uncertainties of photodiodes depend on the empirical corrections applied for cosine error, spectral response, and thermal effects, among others. Thus, our goal is to roughly estimate the real uncertainty of SIAR photodiodes using AEMET secondary standards as reference. For that, we calculated the difference between SIAR photodiodes ($G_{H,y}^{siar-ph}$) and AEMET secondary standard ($G_{H,y}^{aemet-ss}$) in a group of 34 SIAR photodiodes that had an AEMET station in a radius of 20 km (Fig. 4.5).

$$deviation_y^{eq-error,ph} = G_{H,y}^{siar-ph} - G_{H,y}^{aemet-ss} \tag{4.15}$$

Operational errors were removed to evaluate the uncertainty of equipment errors alone. The analysis was restricted to the period 2007-2013 because most AEMET stations started in 2007. Besides, we only used SIAR and AEMET stations operating during all the years in this period to avoid including artificial trends in the comparison.

4.5.4 Estimation of uncertainty from the distributions of annual deviations

Annual deviations calculated in previous subsections included the uncertainties of both test and reference values. The uncertainty of test values alone was estimated statistically following the GUM guidelines: (i) remove the systematic part of deviations (bias), (ii) estimate the uncertainty of deviations statistically, and (iii) remove the uncertainty of reference values with the uncertainty propagation rules. GUM analyzes bias and uncertainty separately [185] because it considers that systematic errors can be detected and corrected. An example of this would be the use of site-adaptation techniques to eliminate the bias of radiation databases by comparing estimations against ground measurements [18]. Another example is the use of empirical correction factors during the calibration of pyranometers to remove systematic deviations of the sensors [186]. However, from the perspective of users of solar radiation data, the bias will generally be present in both measured and estimated data. Thus, we removed the bias from the deviations, but we kept it for the analysis reporting the results as $bias \pm u$.

The bias was characterized as the median bias deviation ($\widetilde{MBD}$) because the median is a more robust central measurement than the mean for non-normal distributions. The bias was only present in reference values when SARAH-1 was the reference, and it was directly removed to obtain the true bias in test values:

$$deviation = tst - ref \quad \rightarrow \quad bias^{tst} = bias^{deviation} + bias^{ref} \tag{4.16}$$

Uncertainty was estimated as the expanded uncertainty with a 95% confidence level (u_{95}). GUM defines this value as 1.96 times the standard deviation (coverage factor = 1.96), but we did not use this method because some of the variables were non-normally distributed. Instead, we calculated uncertainty statistically as the distance between the 95% CIs and the bias. The 95% CIs were defined by percentiles 2.5 ($p_{2.5}$) and 97.5 ($p_{97.5}$). The distance between the CIs and the bias (median) is not symmetric for non-normal distributions, so both negative (u^-) and positive (u^+) uncertainties were reported as:

$$\pm u_{95} = \begin{matrix} u^+ \\ u^- \end{matrix} = \begin{matrix} +(p_{97.5} - bias) \\ -(bias - p_{2.5}) \end{matrix} \tag{4.17}$$

The uncertainty of test values (u_y^{tst}) was obtained by removing the uncertainty of reference values with the functional relationships for uncorrelated uncertainties. All reference values had their own uncertainty because the true irradiance is never known. In case of subtractions, the absolute uncertainty of test and reference values add in quadrature:

$$y = x_1 \pm x_2 \quad \rightarrow \quad U(y) = \sqrt{U^2(x_1) + U^2(x_2))} \tag{4.18}$$

In our study, this rule also applies for relative uncertainties because the average value of the variables subtracted is the same. Hence, the uncertianty in test values is obtained as:

$$deviation = tst - ref \quad \rightarrow \quad u_y^{tst} = \sqrt{(u_y^{deviation})^2 - (u_y^{ref})^2} \tag{4.19}$$

The functional relationships were applied separately to u^+ and u^-. Daily uncertainties were obtained similarly to annual uncertainties but using daily differences ($deviation_d$ = $G_{H,d}^{tst}$ - $G_{H,d}^{ref}$) instead of annual ones.

4.6 PV system simulations

FIGURE 4.6: Flowchart of the procedure used to evaluate the suitability of radiation databases for simulating PV systems.

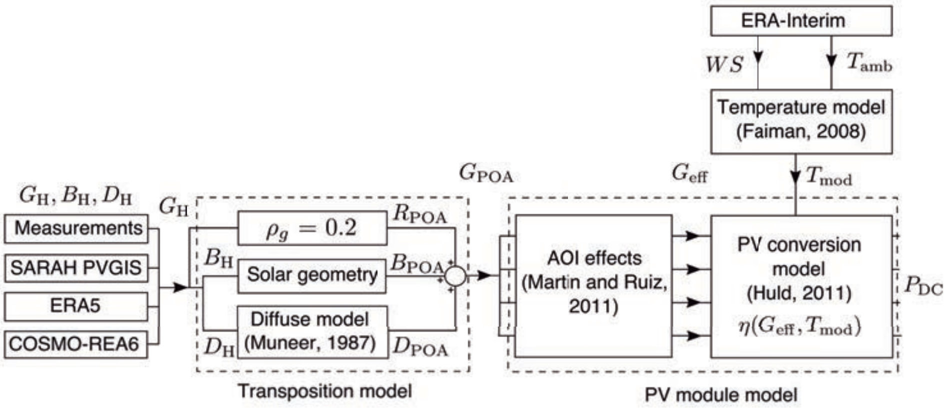

The simulation model is based on the one implemented by PVGIS.

The suitability of radiation databases for yield prediction studies was evaluated by comparing the results obtained with simulations based on estimated irradiance against those obtained with solar radiation measurements. The databases evaluated were those used by PVGIS: SARAH PVGIS, COSMO-REA6, and ERA5. The simulations were made at the locations of the 39 European weather stations that measure D_H, from 2010 to 2014.

The three radiation databases and all weather stations meet the requirements for simulating PV systems: (i) time resolution of at least 1 h, and (ii) availability of at least two out the three horizontal irradiance variables (G_H, D_H or B_H) to avoid the use of decomposition models. The simulation model implemented by PVGIS was used (Fig. 4.6). Ambient temperature and wind speed data were obtained from ERA-Interim (Subsection 3.3.2). The outputs stored were the hourly G_{POA} and the hourly module power (P_{DC}).

4.6.1 Transposition model

The transposition of irradiance from the horizontal plane to the plane of the array was made independently for each radiation component. B_{POA} was calculated from B_H using solar geometry relationships. R_{POA} was calculated assuming an isotropic distribution of reflected irradiance and a constant ground albedo ($\rho_g = 0.2$). D_{POA} was obtained using the anisotropic diffuse model proposed by Muneer [187], which accounts for the anisotropic diffuse irradiance coming from the horizon band and that from the circumsolar region. Muneer [187] proposed different equations for shaded and sunlit surfaces. The equation for shaded surfaces or sunlit surfaces under overcast situations is:

$$D_{POA} = D_H \cdot \left[\left(\frac{1+\cos\beta}{2} \right) + 0.25227 \cdot \left(\sin\beta - \beta\cdot\cos\beta - \pi\cdot\sin^2\!\left(\frac{\beta}{2}\right) \right) \right] \tag{4.20}$$

where β is the module inclination angle. For sunlit surfaces, Muneer's model further distinguishes between overcast and clear situations. The equation for sunlit surfaces under non-overcast situations is:

$$\begin{aligned} D_{POA} = D_H \cdot \Bigg[\Bigg(\left(\frac{1+\cos\beta}{2} \right) + \left(\sin\beta - \beta\cdot\cos\beta - \pi\cdot\sin^2\!\left(\frac{\beta}{2}\right) \right) \cdot \Bigg(0.00263 - \\ - 0.712 \cdot \frac{B_H}{E_H} - 0.6883 \cdot \left(\frac{B_H}{E_H} \right)^2 \Bigg) \Bigg) \cdot \left(1 - \frac{B_H}{E_H} \right) + \left(\frac{B_H}{E_H} \cdot \frac{\cos\theta}{\cos\theta_s} \right) \Bigg] \end{aligned} \tag{4.21}$$

and the following correction has to be applied for low solar elevation angles ($\alpha_s < 0.1$ rad):

$$D_{POA} = D_H \cdot \left[\left(\left(\frac{1+\cos\beta}{2}\right) + \left(\sin\beta - \beta\cdot\cos\beta - \pi\cdot\sin^2\left(\frac{\beta}{2}\right)\right)\cdot\left(0.00263 - 0.712\cdot\frac{B_H}{E_H} - 0.6883\cdot\left(\frac{B_H}{E_H}\right)^2\right)\right)\cdot\left(1-\frac{B_H}{E_H}\right) + \left(\frac{B_H}{E_H}\cdot\frac{\sin\beta\cdot\cos(\phi-\phi_s)}{0.1-0.008\cdot\alpha_s}\right)\right] \tag{4.22}$$

where ϕ is the module orientation and ϕ_s the solar azimuth angle. Muneer's model compares well with other transposition models [152]. The choice of inclined-plane model is not critical to the present study which investigates the effect of bias in the direct/diffuse irradiance. All models will predict a decrease in diffuse radiation with increasing inclination (as more and more of the sky will shine on the back of the plane), and an increase in direct radiation from horizontal up to an optimum angle which depends on latitude and the seasonal variation in climate. Reflected irradiance will also increase with the inclination, but its annual contribution is generally negligible when compared to the beam and diffuse components.

4.6.2 PV module model

The effective irradiance (G_{eff}) was calculated from G_{POA} by accounting only for AOI losses. Losses due to shading, accumulation of snow and soiling were also ignored because their impact is independent of the radiation database used.

Angle of incidence (AOI) effects

AOI losses were modeled with the method proposed by Martin and Ruiz [188], which is used in part 2 of the IEC 61853 standard on energy rating [189]. This models calculates the correction factor for beam ($f_{\mathrm{AOI,B}}$) and diffuse ($f_{\mathrm{AOI,D}}$) components separately:

$$f_{\mathrm{AOI},B} = \frac{1-\exp\left(-\cos\theta/a_r\right)}{1-\exp(-1/a_r)} \tag{4.23}$$

$$f_{\mathrm{AOI},D} = 1-\exp\left[\frac{-1}{a_r}\cdot\left(\frac{4}{3\pi}\cdot\left(\sin\beta+\frac{\pi-\beta-\sin\beta}{1+\cos\beta}\right) + (0.5a_r-0.154)\cdot\left(\sin\beta+\frac{\pi-\beta-\sin\beta}{1+\cos\beta}\right)^2\right)\right] \tag{4.24}$$

where a_r is an empirical coefficient. In this case, we used a value of $a_r = 0.16$ based on Martin and Ruiz [188]. Note that the expression for $f_{\mathrm{AOI,D}}$ only depends on β, so the reduction of the diffuse light is constant in time.

Model for PV power dependence on temperature and irradiance

The instantaneous power of PV modules at conditions different from those under STC depends on T_{mod}, G_{eff} and the solar spectrum. Spectral losses were neglected because only SARAH provided spectrally resolved irradiance. The dependence of the efficiency on temperature and irradiance was calculated with the model proposed by Huld et al. [190]:

$$\begin{aligned} P'_{\mathrm{DC}}(G'_{\mathrm{eff}}, T'_{\mathrm{mod}}) = G'_{\mathrm{eff}} \cdot \eta'(G'_{\mathrm{eff}}, T'_{\mathrm{mod}}) = G'_{\mathrm{eff}} \cdot \Big(1 + k_1 \cdot lnG'_{\mathrm{eff}} + k_2 \cdot ln^2 G'_{\mathrm{eff}} + \\ + k_3 \cdot T'_{\mathrm{mod}} + k_4 \cdot T'_{\mathrm{mod}} \cdot lnG'_{\mathrm{eff}} + k_5 \cdot T'_{\mathrm{mod}} \cdot ln^2 G'_{\mathrm{eff}} + k_6 \cdot (T'_{\mathrm{mod}})^2\Big) \end{aligned} \tag{4.25}$$

where the coefficients $k_1 \cdots k_6$ were those obtained by Huld et al. [190] for c-Si modules by fitting to measured power matrices. All variables in the model were normalized to STC as:

$$\begin{aligned} P'_{\mathrm{DC}} &= P_{\mathrm{DC}}/P_{\mathrm{STC}} && \text{with} && P_{\mathrm{STC}} = \text{nominal power} \\ G'_{\mathrm{eff}} &= G_{\mathrm{eff}}/G_{\mathrm{STC}} && \text{with} && G_{\mathrm{STC}} = 1000\,\mathrm{W/m^2} \\ T'_{\mathrm{mod}} &= T_{\mathrm{mod}} - T_{\mathrm{STC}} && \text{with} && T_{\mathrm{STC}} = 25°\mathrm{C} \end{aligned} \tag{4.26}$$

T_{mod} was calculated with the model proposed by Faiman [191]:

$$T_{\mathrm{mod}} = T_{\mathrm{amb}} + \frac{G_{\mathrm{POA}}}{u_0 + u_1 \cdot WS_{\mathrm{mod}}} \tag{4.27}$$

where u_0 and u_1 are the empirical coefficients reported by Koehl et al. [192] for c-Si modules. T_{amb} and WS_{mod} were derived from ERA-Interim estimates as described in Subsection 3.3.2.

4.7 Propagation of the bias in G_H through PV simulations

For each radiation database, the deviation between the simulations using estimated irradiance (subscript 'est') and the simulation using weather station measurements (subscript 'mea', reference simulation) was calculated:

$$deviation_d(X) = X_d^{\text{est}} - X_d^{\text{mea}} \qquad X \in (G_H, B_H, D_H, G_{\text{POA}}, P_{\text{DC}}) \tag{4.28}$$

This procedure gives the "true error" only for horizontal irradiance variables (G_H, B_H, D_H) because these are the only variables for which X^{mea} is actually measured data. In G_{POA} and P_{DC}, X^{mea} is the prediction obtained with the simulation based on ground measurement, so the deviations show the difference between predictions using estimated irradiance and predictions using ground measurements. Even though the simulations were made with hourly aggregated values, hourly deviations could not be calculated because hourly intervals were defined differently in radiation databases and weather stations. All simulations were made using c-Si modules with a nominal power of 1 kW (P_{STC} = 1 kW) and an inclination angle of 45° (β = 45°). The results are independent of P_{STC} because the simulations are evaluated with relative metrics.

The suitability of each radiation database for simulating PV systems was evaluated with the annual $rMBD$ of the daily deviations. The influence of the intra-annual distribution of the deviations in the propagation of the bias was also analyzed with the scatter plots of daily relative deviations against the clearness index. As for the validation of radiation databases, the relative daily deviations were obtained by dividing the absolute deviations by the annual averages instead of by the daily ones.

The use of relative metrics enables the comparison of the values obtained in the different steps of the simulation chain. Therefore, the propagation of the bias in the transposition model (Eq. 4.29) and the PV module model (Eq. 4.30) was straightforwardly calculated:

$$\begin{aligned} \Delta rMBD(\text{trans. model}) &= rMBD(G_{\text{POA}}) - rMBD(G_H) \\ \Delta deviation_d(\text{trans. model}) &= deviation_d(G_{\text{POA}}) - deviation_d(G_H) \end{aligned} \tag{4.29}$$

$$\begin{aligned} \Delta rMBD(\text{PVmod. model}) &= rMBD(P_{\text{DC}}) - rMBD(G_{\text{POA}}) \\ \Delta deviation_d(\text{PVmod. model}) &= deviation_d(P_{\text{DC}}) - deviation_d(G_{\text{POA}}) \end{aligned} \tag{4.30}$$

Note that in the present study, both positive and negative changes of the bias through the simulation have negative connotations, regardless of whether the absolute value of the bias decreases getting closer to zero.

4.7.1 Influence of module inclination angle in bias propagation

The influence of the module inclination angle in the propagation of the bias was analyzed performing simulations with an inclination angle varying from 0° to 65° by intervals of 5°. These simulations were conducted only in three of the locations included in the central part of the study: (i) BSRN CAR (Carpentras), a low-latitude station (44.08°N) situated in a sunny region with a high frequency of clear-sky days, (ii) DWD 662 (Braunschweig), a mid-latitude station (52.29°N) located in a cloudy region, and (iii) FMI 4714 (Sotkamo), a high-latitude station (64.11°N) located in a region with seasonal snow and low sun elevations during winter.

4.7.2 Uncertainty of the reference simulation

The uncertainty of each variable analyzed (G_H, B_H, D_H, G_{POA}, and P_{DC}) in the reference simulation was estimated to evaluate the significance of the results. The uncertainty was smaller in irradiance variables (G_H, B_H, D_H), which were measurements, than in G_{POA} and P_{DC}, which included the uncertainty of measured irradiance plus that of the simulation models. This uncertainty can be reduced by using G_{POA} and P_{DC} measurements, which is the standard approach for validating PV simulation models, but those are available only at a few sites. On the contrary, our goal is to analyze the suitability of different radiation databases for PV simulations under a common simulation framework. Thus, having a spatially uniform database from weather stations to feed the simulations and evaluate the radiation databases across Europe was more important than having high-quality but sparsely distributed G_{POA} and P_{DC} measurements. The expanded uncertainty with a 95% confidence level (u_{95}) was estimated from the values reported by previous studies applying the uncertainty propagation rules due to the lack of high-quality collocated data to calculate u statistically.

The uncertainty of measured variables (G_H and D_H) depends on the quality of the sensor and the operating conditions at the stations. In the present study, most stations use secondary standard pyranometers (shaded and unshaded), which have a typical uncertainty of ±3% and ±2% for hourly and daily values, respectively [19]. These values do not include additional uncertainties due to incorrect calibrations and operational defects, but the existence of significant operational errors in the current set of weather stations is unlikely. All stations are maintained by organizations that implement strict operating procedures. For instance, the BSRN, which follows the strictest guidelines among all the networks used, has an accuracy target of ±2% for G_H and D_H (1-min values) [41]. Besides, all measurements have passed the BQC and the BSRN tests.

Based on this, we assumed a u_{95} in annual G_H and D_H of ±2% for stations below 55° N, and of ±3.5% for stations above 55° N. Annual uncertainties are lower than the daily uncertainties due to the compensation of seasonal deviations. The larger uncertainty at high-latitude stations is due to the extreme weather conditions and to the high frequency of hours with low sun elevation angle that aggravates the cosine error of pyranometers, among others. These values are rough estimates just for the analysis of uncertainty propagation through the simulations. A more detailed analysis similar to those made by Reda [39], Vuilleumier et al. [41], and Habte et al. [40] would require the evaluation of the particular conditions at the stations such as the pyranometer model and dates of sensor replacement or re-calibrations. Besides, the uncertainty also varies spatially with latitude and temporally from season to season due to changes in the incoming irradiance and sun elevation angles [40]. Uncertainty fluctuations due to changes in either the equipment or the operating conditions are more likely in FMI and DWD networks than in the BSRN. A couple of DWD stations were temporally equipped with SCAPP sensors, which simultaneously measure B_N and D_H using a silicon detector. The uncertainty of SCAPP measurements is higher due to the limited spectral response of silicon and the cosine error, among other issues. In the FMI network, the uncertainty in D_H is not homogeneous between stations due to variations in the equipment (sorted by increasing accuracy): (i) shading ring (before 2012), (ii) Delta-T SPN1 multi-pyranometer (since 2012), (iii) shading ball on a solar tracker.

The uncertainty increases for B_H because this variable was not measured but calculated as the difference between G_H and D_H. As aforementioned, the absolute uncertainty adds in quadrature in sums and differences (Eq. 4.18), so the uncertainty in B_H is:

$$G_H = B_H + D_H \quad \rightarrow \quad U(B_H) = \sqrt{U^2(G_H) + U^2(D_H)} \tag{4.31}$$

Absolute uncertainties were transformed into relative ones and vice versa by using the annual average values for each variable: $\overline{G_H}$ = 130 W/m^2, $\overline{B_H}$ = 66 W/m^2 and $\overline{D_H}$ = 64 W/m^2, for stations below 55°N, and $\overline{G_H}$ = 104 W/m^2, $\overline{B_H}$ = 56 W/m^2, $\overline{D_H}$ = 48 W/m^2, for all stations above 55°N.

The uncertainty propagation through the simulations was made assuming that the PV simulation model is a series of multiplicative factors that transform the G_H into P_{DC}. The total uncertainty in multiplications is obtained by adding in quadrature the relative individual uncertainties:

$$\begin{aligned} u(G_{\mathrm{POA}}) &= \sqrt{u^2(B_H) + u^2(\mathrm{trans.\,model})} \\ u(P_{\mathrm{DC}}) &= \sqrt{u^2(B_H) + u^2(\mathrm{trans.\,model}) + \mathrm{u}^2(\mathrm{PVmod.\,model})} \end{aligned} \tag{4.32}$$

where $u(B_H)$ was considered the overall uncertainty of horizontal irradiance data because B_H had the largest uncertainty among the three horizontal irradiance variables. An annual uncertainty of 3% was assumed for both, transposition and PV module models, based on the studies made by Müller et al. [10] and Thevenard and Pelland [11].

FIGURE 4.7: Estimated annual uncertainty in the reference simulation.

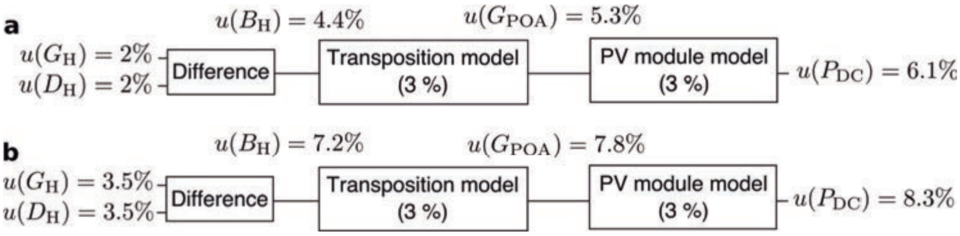

(**a**) Locations below 55°N. (**b**) Locations above 55°N.

Chapter 5

Results and Discussion

First, the different types of defects detected with the BQC at the European and Spanish weather stations are analyzed in Section 5.1. Several satellite-based and reanalysis databases are validated over Europe and also worldwide in Section 5.2. The uncertainty of both, solar radiation measurements and estimations, is evaluated in Section 5.3 using the dense network of Spanish weather stations. Finally, the propagation of the uncertainty in solar radiation data through PV simulations is assessed in Section 5.4.

5.1 Quality control of solar radiation measurements

The BQC was used to quality control all European and Spanish weather stations. Stations flagged were visually inspected using the two plots generated by the BQC and classified into the following categories:

- Operational errors: snow or frost accumulation, shading, soiling, time lags, large errors, diurnal $G_H = 0$, and incorrect leveling.
- Equipment errors: incorrect calibration of the sensor.
- Doubtful cases: potential errors of unknown cause.
- False alarms.

The tuning process of the window function used in the BQC is described in Subsection 5.1.1. Subsection 5.1.2 shows how the BQC plots (daily deviations and instantaneous irradiance) look like for each type of defect. The duration of each defect is depicted in Fig. 5.2. The quality of the monitoring networks is evaluated in Subsection 5.1.3. Finally, the strengths and limitations of the BQC are discussed in Subsection 5.1.4.

5.1.1 Setting up the BQC

The best configuration of the window function was determined by analyzing the precision-recall (PR) curves (Fig. 5.1) obtained with different combinations of w (window width) and n (CI width). w varied within 5, 10, 15, 20, 30, 40, 60, 90, and 120, whereas n ranged from 0.2 to 3.5 in intervals of 0.1. PR curves evaluate precision, i.e., the percentage of flags showing true defects, versus recall, i.e., the percentage of true defects found. The PR curves in Fig. 5.1 showed if the BQC was able to find the different types of defects at each station with erroneous data, independently of whether the BQC flagged the exact days when defects occur.

FIGURE 5.1: Precision-recall (PR) curves obtained for different combinations of n and w.

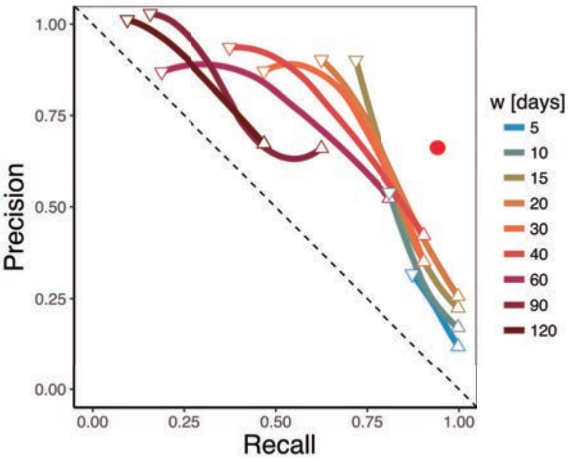

n goes from 0.2 (up-pointing triangle) to 3.5 (down-pointing triangle) in intervals of 0.1. The red dot represents the results obtained with the chosen configuration based on two runs of the window function: (i) w = 20 d, n = 2.4, (ii) w = 90 d, n = 0.4.

The PR curves showed similar patterns with decreasing n, i.e., narrowing the CI, and reducing w, i.e., analyzing fewer days with the window function. The number of defects detected increased at the expense of obtaining more false alarms. Conversely, false alarms decreased by increasing either n or w, but the number of defects found diminished as well. The best configuration may be an intermediate solution that balances the number of true positives and false alarms, somewhat around w = 30 d and n = 1.5. However, from the users' perspective, it is more useful to find all existing defects (high recall) rather than having few false alarms (high precision). This is even more clear in the BQC because it includes two plots that speed up the detection of false alarms. Thus, w and n should be tuned prioritizing the attainment of a high recall.

Besides, the characteristics of the defects vary with their duration. Defects introducing high deviations such as electronic shutdowns or equipment failures typically last from few hours to few days because they can be easily detected and corrected. Conversely, low-magnitude defects such as shading or calibration drifts often pass unnoticed and may last several months. Hence, defects detected with narrow windows ($w < 20$ d) are not the same as those found with wide ones ($w > 30$ d), so the use of an intermediate solution is not sufficient to detect all types of defects.

Based on the previous observations, the best results were obtained by running the window function with two different configurations. The first run looked for short-lived defects ($w = 20$ d), relaxing the CIs ($n = 2.4$) to reduce the number of false alarms. The second run searched long-living defects ($w = 90$ days) using more restrictive CIs ($n = 0.4$) to detect low-magnitude deviations. This design based on two configurations of the window function to detect different types of defects was possible thanks to the flexibility of the method, i.e., the trade-off between w and n. This configuration led to a precision of 66% and a recall of 92%, improving configurations based on a single run of the window function (Fig. 5.1).

5.1.2 Visual inspection of quality flags

FIGURE 5.2: Duration of defects detected at European and Spanish weather stations.

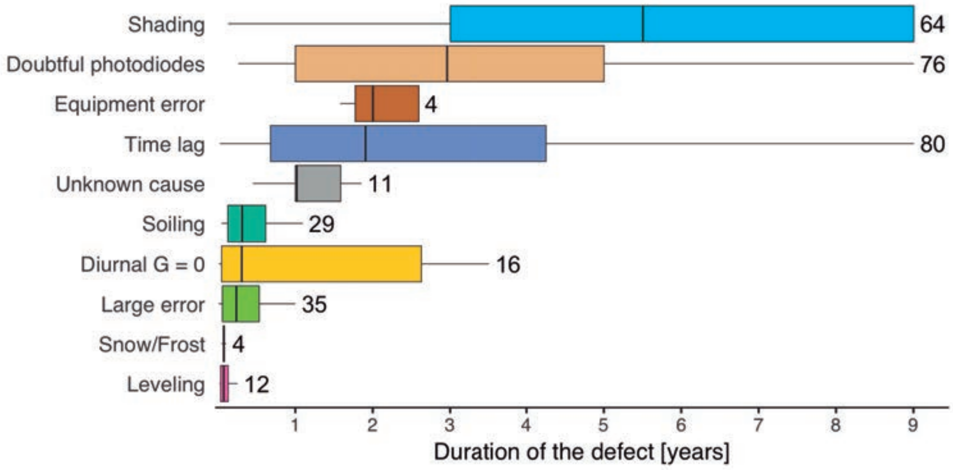

The label depicts the total number of stations showing each type of defect.

True errors

Snow or frost accumulation on pyranometers is an operational error characteristic of places with seasonal snow such as high-latitude regions or high-elevation mountains. Dew formation in the mornings may also be a problem in areas with enough humidity to produce water vapor condensation. Dew typically lasts few hours and causes smaller deviations in the readings than snow or frost, being undetected with the BQC because it is based on daily deviations. Ventilation units are installed in the pyranometers to prevent the accumulation of snow, frost, and dew. This is a common practice in high-quality networks such as the BSRN and national meteorological agencies. Some ventilators even integrate heaters to help in melting snow and ice. Therefore, snow accumulation is more likely in non-ventilated pyranometers than in ventilated ones. However, it may also affect ventilated stations if sensors are not regularly cleaned or in case of extreme weather conditions.

FIGURE 5.3: Operational error: snow or frost accumulation.

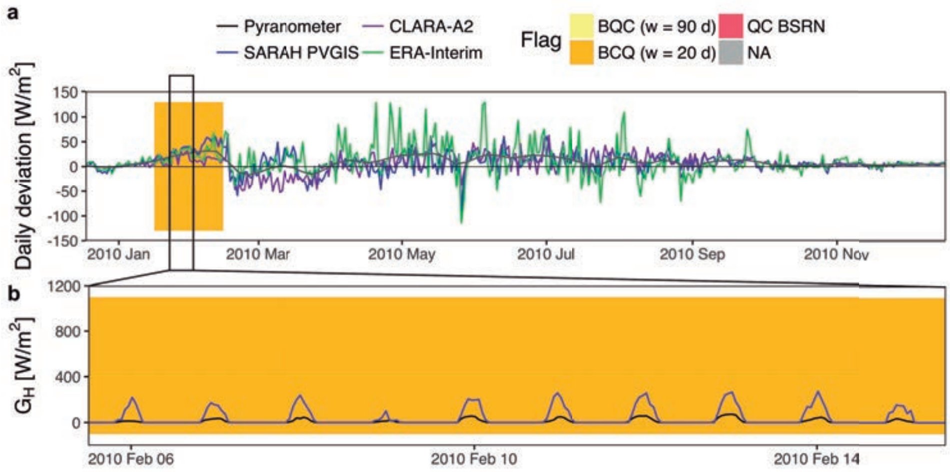

Station: LMT Apelsvoll.

Severe cases of snow or frost accumulation occur in regions with seasonal snow. Snow accumulation generally lasts from few days to few weeks and disappears when the pyranometer is cleaned, or the snow melts. This defect produces very low irradiance values detected by the BQC as a period of underestimated irradiance that leads to positive deviations for all radiation databases (Fig. 5.3a). The detection of this error is hindered by the low irradiance of these months, which leads to small deviations around 50 W/m^2. The deviations are particularly small in high latitudes because the irradiance is close to or even zero in winter. Snow or frost accumulations are not detected by traditional QC tests based on range or consistency checks because measurements obtained are plausible under cloudy conditions.

Soiling is caused by the accumulation of dust, pollen, pollution, or bird droppings on the sensor. This defect is also mitigated by installing ventilation units. A better solution for preventing soiling is to clean regularly the dome of the sensor, especially at locations with high aerosol loads. The BSRN measuring guidelines [17] recommend cleaning the instruments at least once per day, preferably before dawn.

FIGURE 5.4: Operational error: soiling (cleaned by rain).

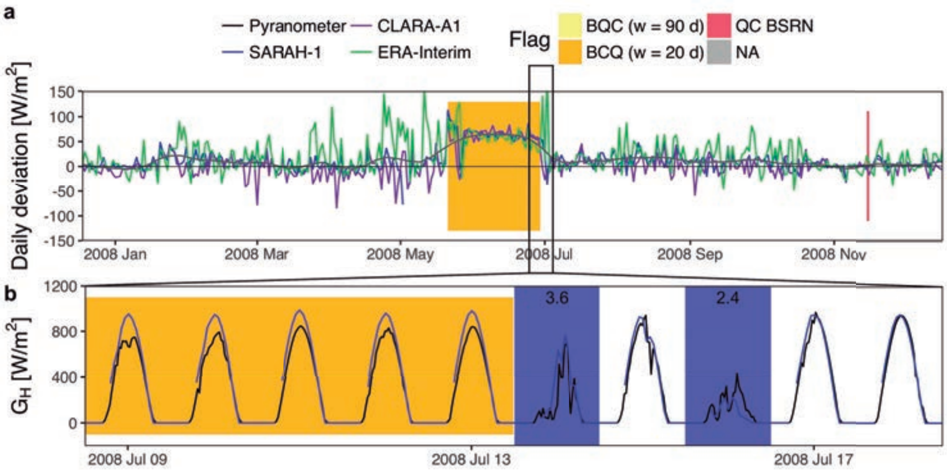

Station: SIAR A12. Days with precipitation are shaded in blue. The label shows the daily rainfall.

Soiling leads to underestimated irradiance values, but the magnitude of the deviations is very variable due to the different degrees of soiling. In most cases, daily irradiance values resemble those under cloudy conditions, which hinders the detection of soling by range checks that analyze each daily sample individually. The best approach to detect soiling is either by visual inspecting the time series or by analyzing if the underestimation prevails in time, as the BQC does. Soiling duration can also be very variable. The severity of the error generally increases with time until it rains (Fig. 5.4) or until cleaning the sensor manually (Fig. 5.5). Soiling may last several months at remote stations in arid climates, such as those located in desserts. Care must be taken when analyzing potential soiling cases with low-magnitude deviations because the deviations can be caused either by soling or by an overestimation in the radiation database. In these cases, checking the precipitation data if available can help in the detection of soiling cases.

Figure 5.5: Operational error: soiling (manually cleaned).

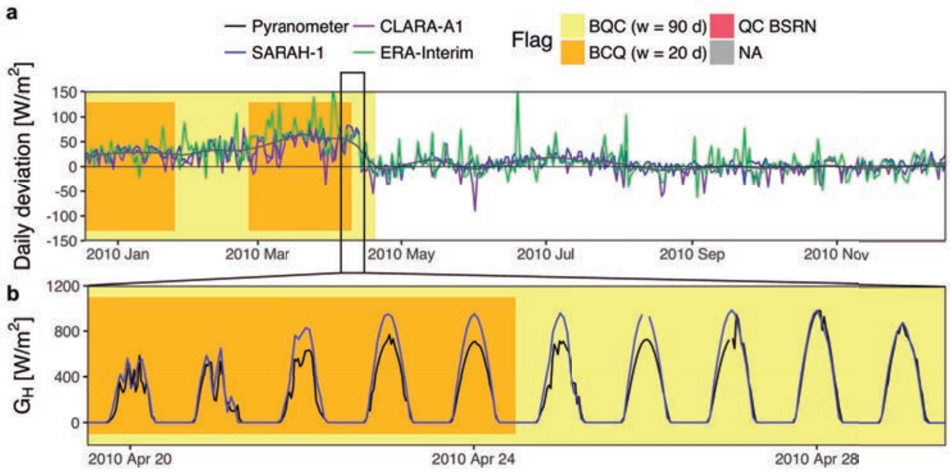

Station: SIAR AL02.

Shading is another defect that leads to the underestimation of irradiance because the sun is being blocked by artificial or natural objects around the station. Shadows typically appear in the morning or the afternoon because low solar elevation angles favor horizon blocking (Fig. 5.6). Occasionally, shadows may affect not only the pyranometer but also the surrounding region. This happens in high-latitude regions, where the sun elevation angle is low during winter, or deep valleys, where the surrounding mountains block the sun at sunrise and sunset. Here, the user has to decide whether to keep or remove the shadows depending on the end-use of the records. For instance, shadows should be kept in the datasets for an evaluation of the solar power capacity of the region, because they also reduce the energy yield obtained with PV panels. Contrary, shadows are generally removed for validating radiation databases, because these models are usually focused on global atmospheric processes.

Shadows can also occur around noon if a surrounding object such as trees or buildings directly blocks the sun (Fig. 5.7). Sometimes, even the components or the own weather station may cause the shadows (self-shading). Shading duration is usually long, typically spanning several years of the time series (Fig. 5.2). Shading may even affect the whole time series if the station was inadequately placed, or emerge during the operational stage due to low maintenance and changes in the surrounding area, which is an indirect consequence of an incorrect site selection as well. Similarly to soiling and snow, shading is hardly detected by conventional QC methods because the daily means obtained are physically possible under overcast conditions.

Figure 5.6: Operational error: shading (sunrise shadow).

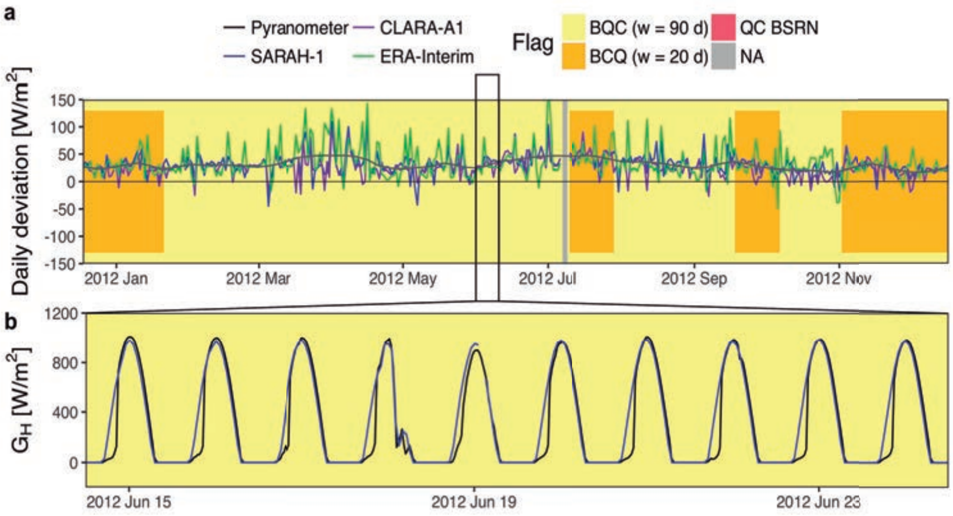

Station: SIAR A102.

Figure 5.7: Operational error: shading (midday shadow).

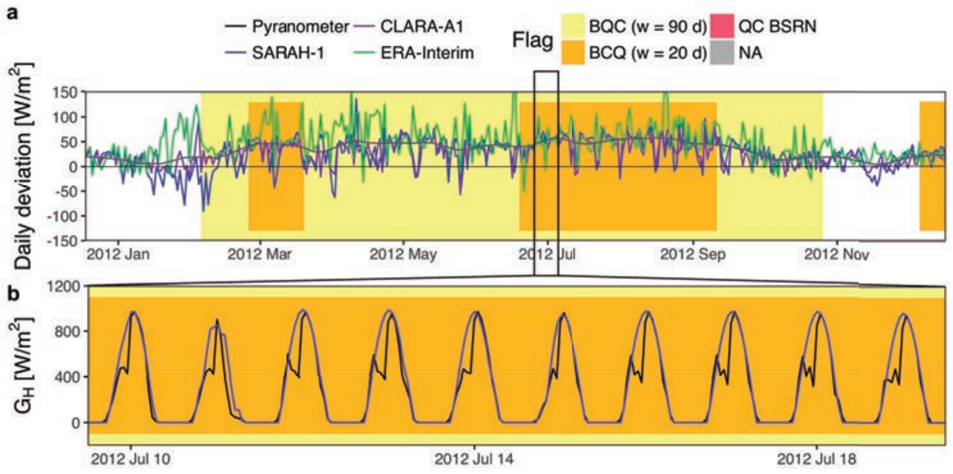

Station: SOS Rioja Urbaña.

The absolute time at high-quality weather stations is commonly measured in UTC or LST and set with one of the following methods [17]: (i) time-synchronization with GPS satellites, (ii) conversion of radio frequency time signals from national standards agencies, and (iii) time updates via the internet. *Time lags* are thus unusual in high-quality stations, and if they occur, they typically last few days and are usually related to an occasional failure in the data logger. However, time lags are common

FIGURE 5.8: Operational error: time lag.

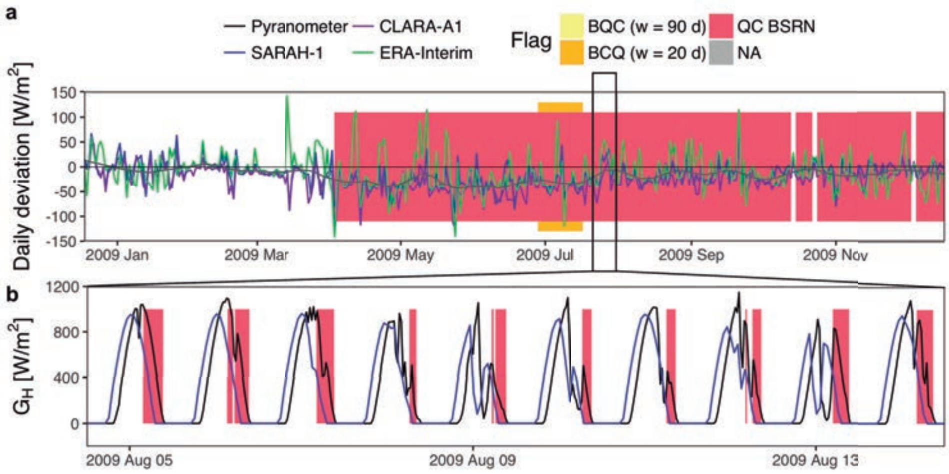

Station: SIAR AV101.

in low-quality monitoring networks that synchronize clocks manually or collect data in local time (LT). These time lags can span several months until the station is inspected again (Fig. 5.2). In some stations using LT, the time lag only appears either in winter or summer evidencing an inadequate correction for daylight saving time. These time lags are around ±1 h, but smaller time lags between 0-30 min may also occur due to an incorrect specification of the averaging intervals. The BQC cannot detect time lags because this defect gets masked in daily averages. Time lags were found by the BSRN checks included in the BQC, flagging either morning (forward time lag) or afternoon readings (backward time lag) if a time lag occurs (Fig. 5.8). Other tests have been specially tailored to detect this error, such as those based on the symmetry of the irradiance profiles [58].

Large errors include all types of equipment malfunctions and data processing errors that cause large deviations during short periods of few days or even less [33]. Large errors can be either positive or negative, and most of them are easily detected with basic range checks because the readings obtained are out of the physically possible limits. This was the case of the station in Fig. 5.9, with all measurements above the upper limit of physically plausible values, or station in Fig. 5.10, with night measurements above zero. These large errors were flagged by both the BSRN tests and the BQC. The inclusion of BSRN checks in the BQC assures the detection of too brief defects that do not produce sufficiently large deviations for being detected with a window of 20 days. The duration of large errors is generally very short (Fig. 5.2) because most stations implement automatic QC checks to detect these large deviations. In this sense, working with

FIGURE 5.9: Operational error: large error (values out of range).

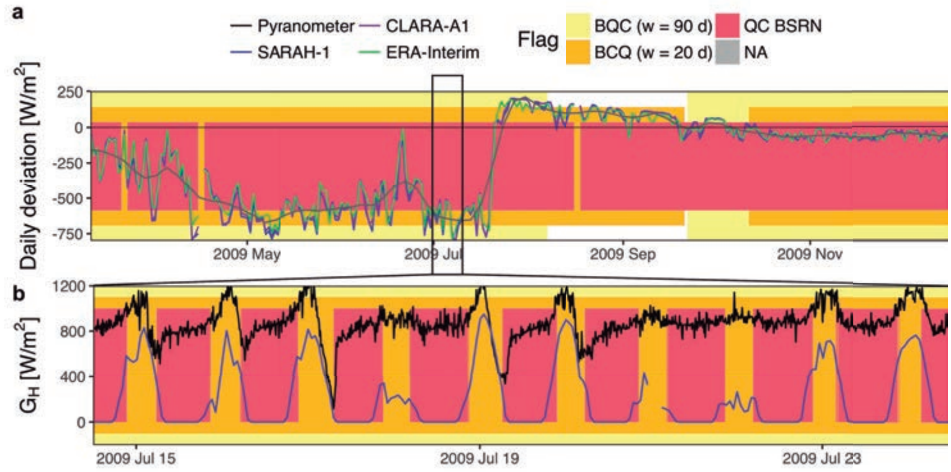

Station: MeteoGalicia 10800.

FIGURE 5.10: Operational error: large error (night values above zero).

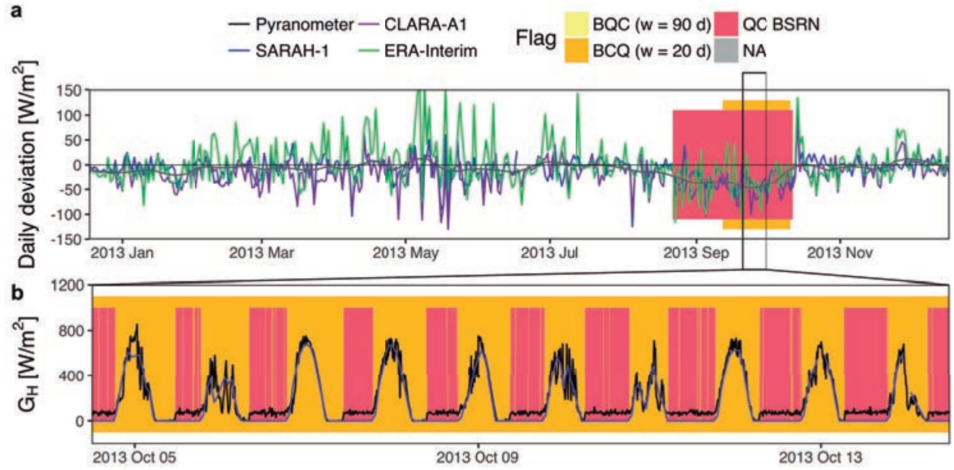

Station: Euskalmet 060.

sub-hourly data (1-min to 10-min) facilitates the detection of large errors because their magnitude can be mitigated after aggregating the data to hourly, daily, or monthly means. Some large errors generate physically possible measurements that still introduce significant deviations in the data. This was the case of the station shown in Fig. 5.11, whose records were around 2-3 W/m^2 during the whole year but passed the BSRN range tests. In this case, the error was straightforwardly detected by the window

FIGURE 5.11: Operational error: large error (values close to zero).

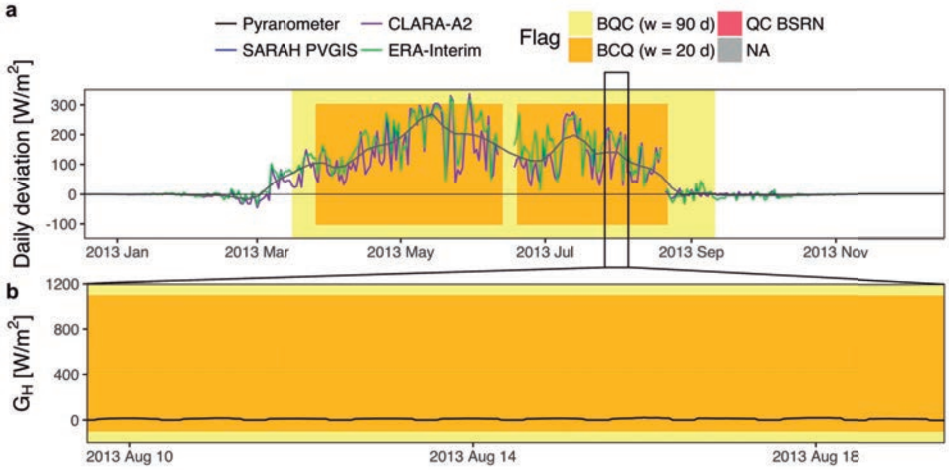

Station: LMT Sortland.

function as the deviations of the three radiation products were close to a 100%.

FIGURE 5.12: Operational error: diurnal $G_H = 0$ (constant).

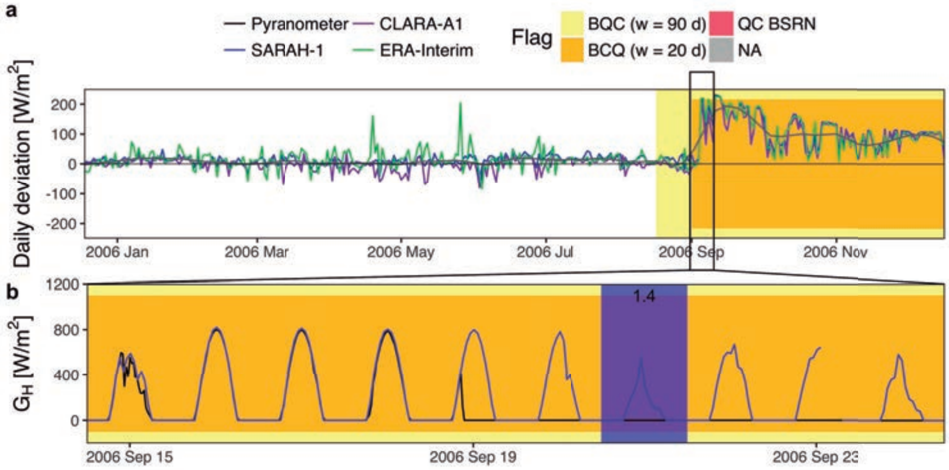

Station: SIAR M05.

Diurnal readings set to zero (*Diurnal* $G_H = 0$) are a particular case of large error. This defect can be easily detected when all diurnal values are zero (Fig. 5.12) because the daily mean is zero as well. However, some stations intermittently set diurnal readings to zero (Fig. 5.13), so the daily

FIGURE 5.13: Operational error: diurnal $G_H = 0$ (intermittent).

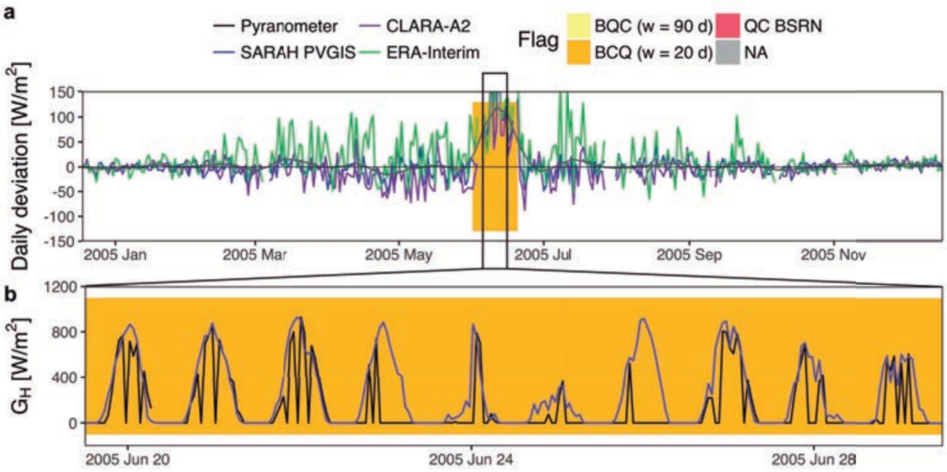

Station: Met Office 1302.

means resemble those of a cloudy day. The pyranometer produces acceptable records during the rest of the day. The most probable cause of the error may be a failure during the data processing or in the data logger, which integrates and saves the instantaneous records. Again, this error may pass unnoticed if working with temporally-aggregated data. Quality checks should be applied to high-resolution data whenever possible.

FIGURE 5.14: Operational error: incorrect leveling of the sensor.

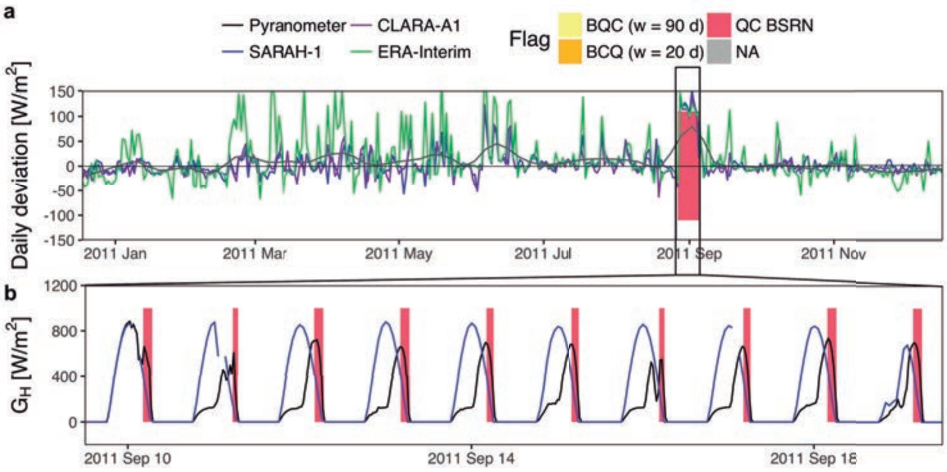

Station: SIAR MA04.

Pyranometers generally include a high-precision bubble level and adjustable screw legs to place the sensor horizontally (within ±0.1°). However, any failure in the mounting structure or the legs can result in an *incorrect leveling* of the sensor. It is an unusual defect that generally does not last too long because it can be detected either by visual inspecting the station or the time series. Deviations introduced in the measurements depend on the new angle of the pyranometer. Irradiance will be overestimated if the sensor is tilted towards the sun (south in the Northern hemisphere), while the opposite occurs if it tilts away from the sun. If the sensor tilts towards east or west, morning or afternoon measurements will be overestimated, respectively, while underestimating the rest of the day. This was the case of the station shown in Fig. 5.14, which depicts the time series of a pyranometer tilted towards west. The probability of detecting cases of incorrect leveling with the BQC increases with the duration of the defect, the inclination angle, and its direction. The daily global irradiance obtained at some inclinations can be similar to G_H, passing the BQC. Besides, the short duration of some defects (Fig. 5.14) hinders the detection of the error with the window function of 20 days. Similarly to time lags, this is another case for which the inclusion of the BSRN tests facilitates the detection of the defect. The BSRN range checks will flag all time slots with measurements above the physically possible limits for an horizontally-installed pyranometer.

All the defects described so far were operational errors. These defects generally introduce larger deviations than *equipment errors* and are more easily detected. However, the BQC found some equipment errors as well. The window function identified both positive and negative systematic deviations due to problems in the calibration of the pyranometers. These defects are more easily identified when the problem started or ended within the limits of the period under study because the difference between correctly and incorrectly calibrated sensors becomes more clear. This was the case of the station shown in Fig. 5.15, which presented a constant overestimation of the irradiance from 2005 to 2008 that suddenly disappeared in 2009. Checking the station metadata can help in the identification of the cause of equipment errors. In some stations, the systematic deviation ended/started with sensor replacements evidencing a problem in the calibration of the old/new sensor. For instance, this was observed at three MetOffice stations (326, 453, 586) that replaced second class sensors with secondary standard ones. In other stations such as the one shown in Fig. 5.15 the same sensor was used from 2005 to 2015, so the extinction of the bias was probably due to a re-calibration of the sensor.

FIGURE 5.15: Equipment error: inadequate calibration.

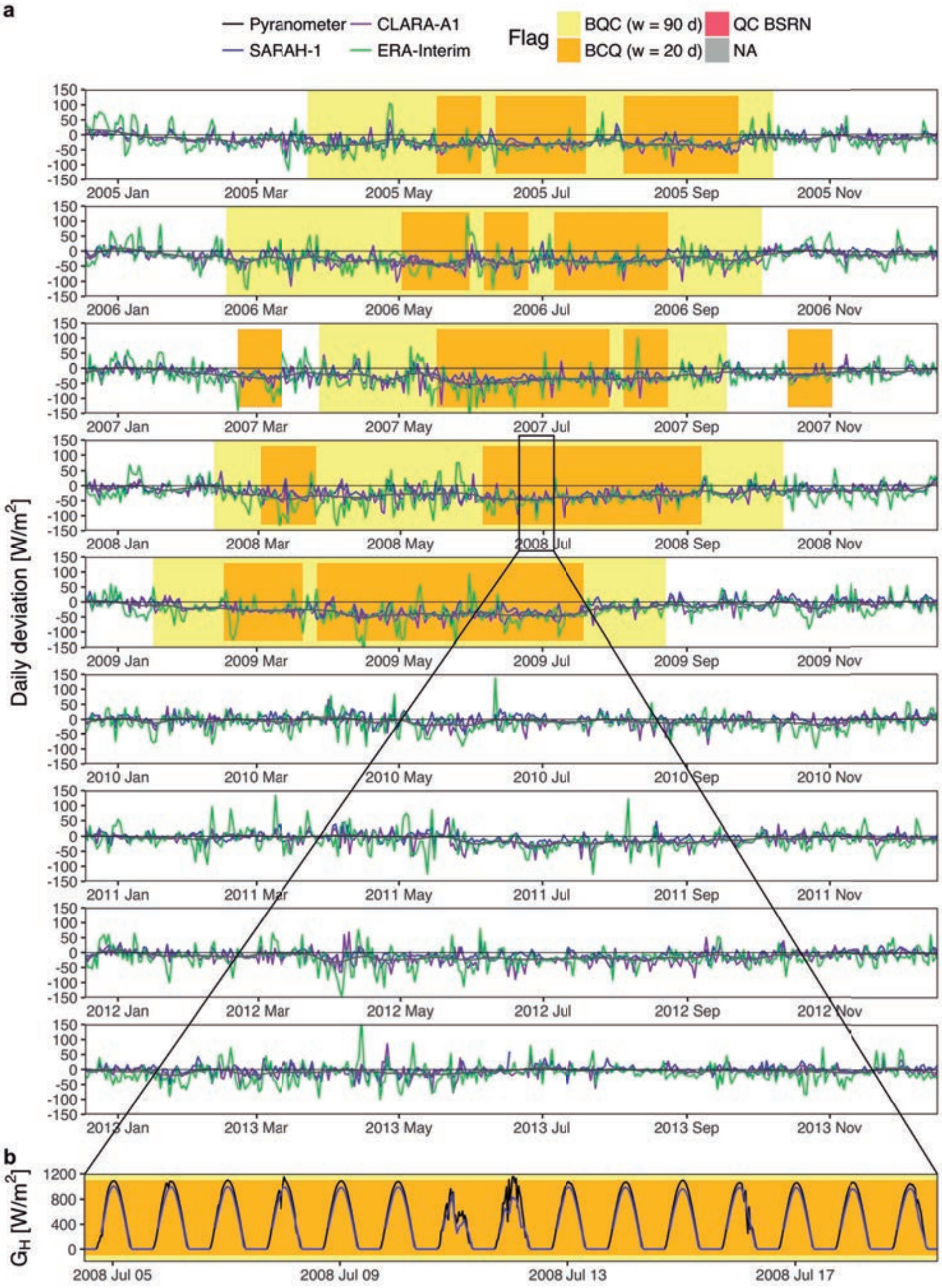

Station: SIAR ZA05.

False alarms

FIGURE 5.16: False alarms: snow-covered surfaces.

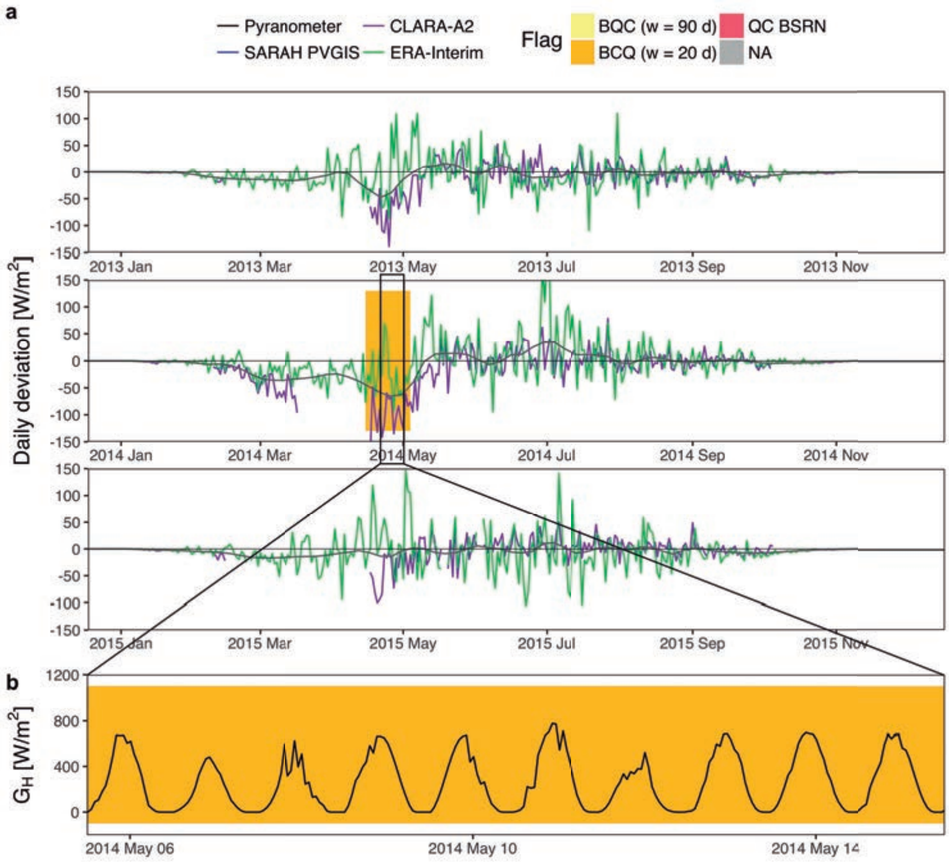

Station: FMI Utsjoki.

False alarms occur when all radiation databases fail inconsistently: if they fail just in one period of the time series (temporal inconsistency) or in one site of the spatial region defined to calculate the CIs (spatial inconsistency). An example of a temporal inconsistency is the presence of one month with snow cover in a region where snow rarely falls, whereas a case of a spatial inconsistency is filtering mountain stations with CIs calculated over a predominantly flat region. The window function flags inconsistent deviations because they are not included in the CIs.

False alarms were obtained at 1 station with seasonal snow and 5 mountain stations (Table 5.1). The station with seasonal snow was the highest-latitude station (FMI Utsjoki, 69.8°N). Satellite-based databases produce large deviations over snow-covered surfaces due to the similar reflectivity of snow and clouds. Even though FMI Utsjoki was filtered out with other

Figure 5.17: False alarms: mountains.

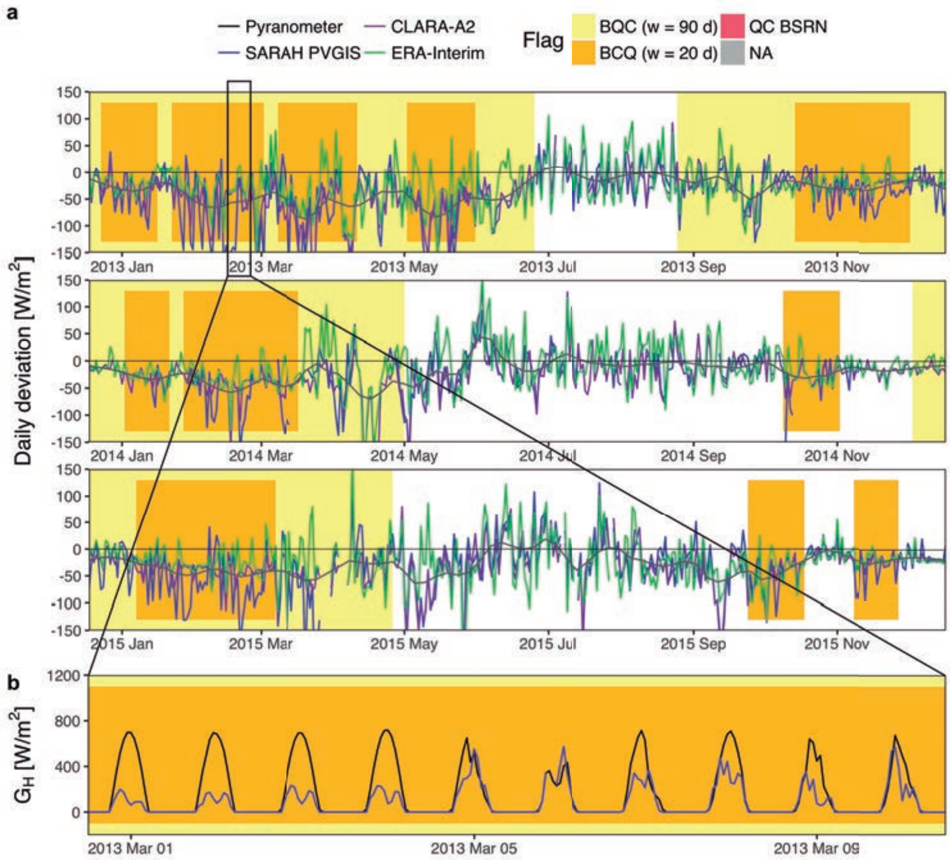

Station: DWD 5792 (Zugspitze - 2964 m).

high-latitude stations where the presence of snow is common, FMI Utsjoki is the station with the longest seasonal snow. The window function flagged just one month of the time series (April - May) where the snow still covers the ground, but the irradiance level is high increasing the magnitude of the deviations (Fig. 5.16). Thus, the BQC probably flagged the excessively large deviations during a year with abundant snow. The five mountain stations were located in the Alps (Météo France 5183001 - 1310 m, Météo France 6094002 - 1748 m, DWD 5792- 2964 m) and the Pyrenees (Météo France 9024004 - 1781 m, Météo France 64316003 - 1427 m). These stations were filtered out with the CIs calculated for all of France, so the BQC flagged the large deviations of solar radiation models in the mountains (Fig. 5.17). The limitations of solar radiation models in the mountains and over snow-covered surfaces are more extensively discussed in Section 5.2.

Doubtful cases

FIGURE 5.18: Doubtful cases: SIAR photodiodes.

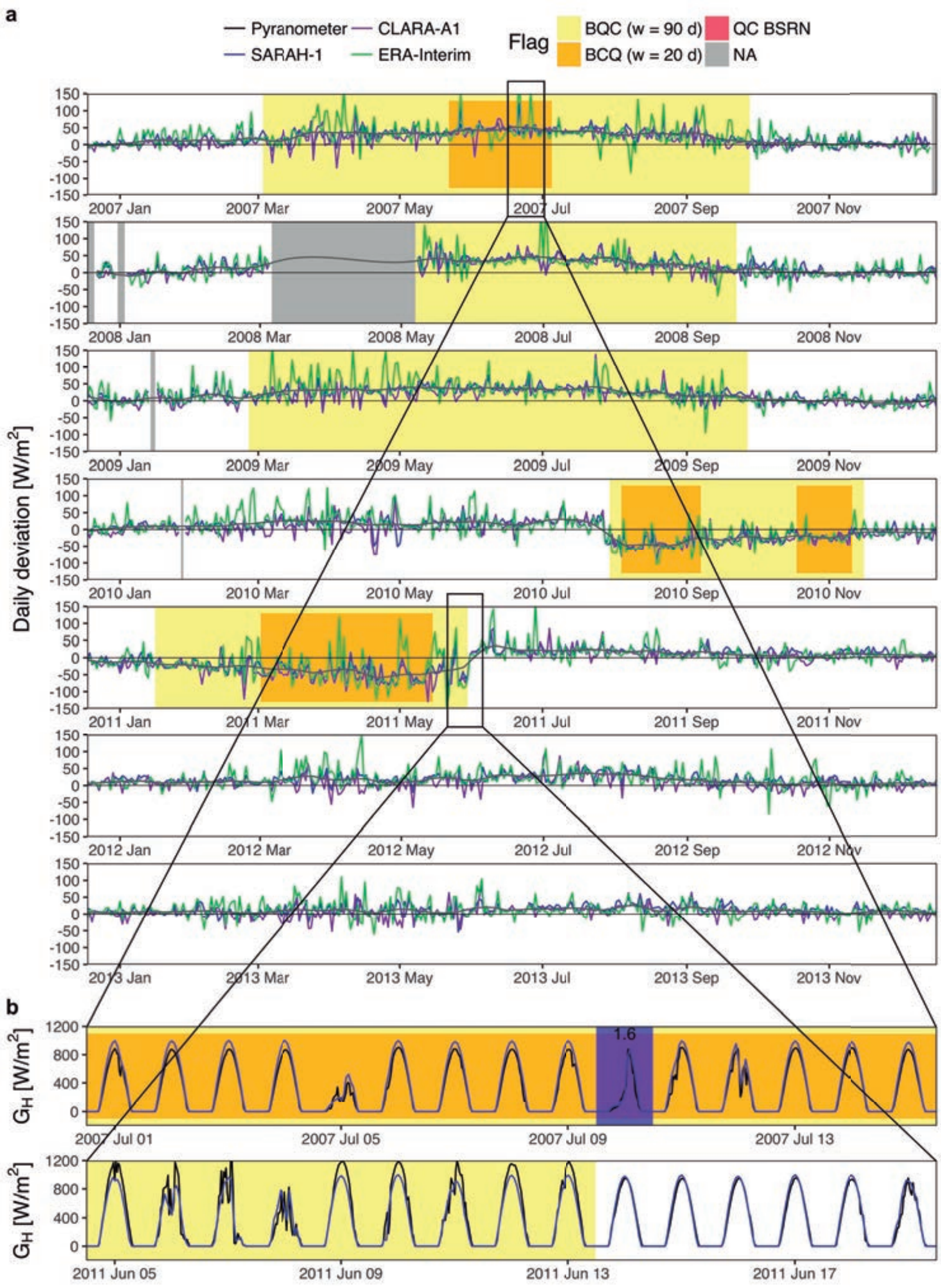

Station: SIAR A101.

There were some stations in which it was not possible to identify the cause of the deviation flagged after visual inspecting the time series. In some of them, the presence of defects was evident, but we could not determine their cause due to their low magnitude, the lack of metadata, and the lack of sub-daily data to generate the second plot of the BQC. These stations were included in the *Unknown cause* group.

There was an additional group of 60 stations in which the presence of an equipment error was highly likely. All of them were SIAR photodiode pyranometers, which have lower accuracy than thermopile pyranometers. The flags were long-term periods of at least 90 consecutive days with a small but persistent systematic deviation of around ±50 W/m^2 between measurements and the three radiation databases. The hypothesis of a simultaneous failure of all radiation databases, i.e., a false alarm of the BQC, was discarded because this type of error was only found in SIAR photodiodes. Further, although some of the negative biases (36 stations) could be caused by undetected operational errors such as small dust accumulations, these defects rarely produce long-term positive bias (24 stations). The bias in most of these stations followed random patterns spanning from 3 to 6 months at any season of the year and happening typically in just one year of the time series. Hence, these defects could be related to changes in temperature, aerosol, or water vapor accentuating temperature, linearity, and spectral errors [36]. On the other hand, some of the positive biases appeared for a consecutive number of years at the beginning of the time series (2005-2009) (Fig. 5.18). This suggests that the sensor was replaced or recalibrated, but SIAR did not provide the information required to verify this hypothesis. We assumed that photodiode-related errors caused the majority of these flags labeling them as *Doubtful photodiodes*. The analysis of equipment errors in SIAR photodiodes is discussed more extensively in Subsection 5.3.3.

5.1.3 Summary of the defects

European dataset

The QC method flagged suspect data at 29 out of the 335 European weather stations (Fig. 5.19). After visual inspecting the quality flags, we considered that defects indeed existed at 26 stations. False alarms were detected at the remaining 3 stations and at other 3 stations that have periods of both false alarms and true defects (Table 5.1). The majority of defects were operational errors (22 stations). Equipment errors were only found at 4 stations, and they were related to the use of low-quality or inadequately calibrated sensors at the beginning of the study period.

FIGURE 5.19: Summary of the defects found at the 335 European weather stations.

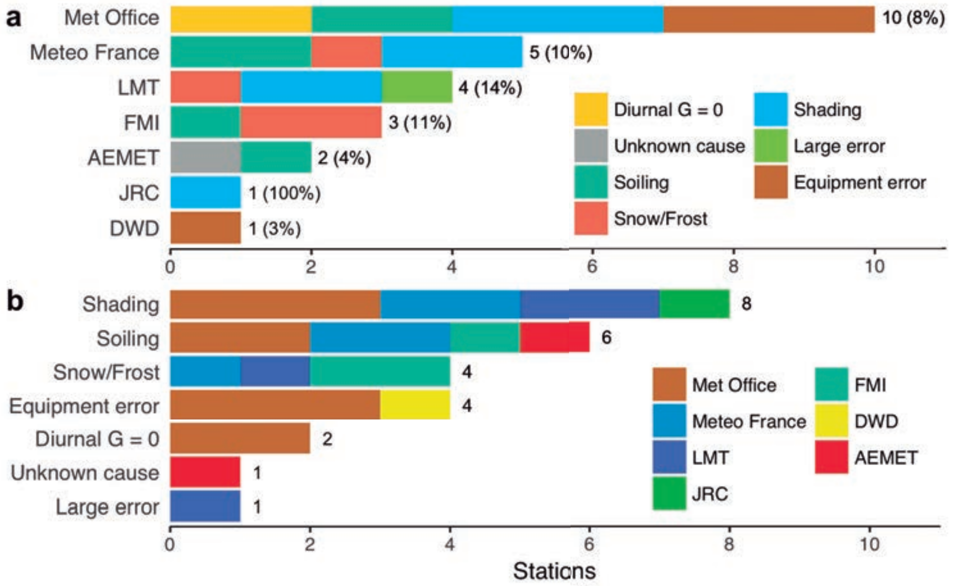

(**a**) Number of defects per network. The label shows the total number of defects in the network and the percentage of the stations with defects. (**b**) Number of stations showing each type of defect.

LMT was the European network with the highest percentage of defects (14% stations). LMT is a Norwegian network that covers the main agricultural districts of the country collecting data for research, forecast models, and alert services. LMT website indicates that stations are daily maintained, whereas measurements and equipment are quality controlled annually [163]. However, maintenance protocols of weather stations used for agricultural purposes are generally not so strict than those implemented by national meteorological agencies. This along with the extreme weather conditions in northern Norway (there are 6 stations from 65° to 70°N) may explain the high percentage of errors found in LMT stations.

Met Office, which is the British meteorological service and the most extensive network of the European dataset (121 stations), was the network with the largest number of defects (10 stations). Three of these stations presented systematic deviations at the beginning of the time series that were classified as equipment errors. These stations were initially equipped with second class pyranometers CM3 or CM5 (Kipp & Zonen). In 2005 and 2008, Met Office replaced all second class sensors by the secondary standard CMP11 (Kipp & Zonen), which is currently the standard pyranometer of Met Office. The systematic deviations occurred during the operation of

Table 5.1: List of stations flagged at the 335 European weather stations.

Network	Type of defect	Stations
FMI	Soiling	Ilomantsi
	Snow/Frost	Rautavaara, Siikajoki
	False alarm	Utsjoki
Met Office	Shading	918, 56424, 57250
	Soiling	370, 1352
	Diurnal $G_H = 0$	708, 1302
	Equipment error	326, 534, 586
DWD	Equipment error	3028
	False alarm	5792
Météo France	Shading	5183001, 27056003
	Soiling	58218006, 64316003
	Snow/Frost	6094002
	False alarm	5183001, 6094002, 64316003, 9024004
AEMET	Soiling	5402
	Unknown cause	6325O
LMT	Shading	Kise, Maere
	Snow/Frost	Apelsvoll
	Large error	Sortland
-	Shading	JRC Ispra

second class sensors and disappeared after replacing the sensor. This confirms that these deviations were caused either by the limitations of second class pyranometers or by an inadequate calibration of these sensors. Another particular defect found at Met Office stations was the presence of periods with diurnal readings intermittently set to zero. This defect could have been identified with range or persistence tests, questioning the automatic quality checks implemented by Met Office.

A relatively high number of defects (5 stations) were also found at Météo France compared to other meteorological agencies. All these defects occurred at type 1 stations, which are automatic "Radome-Resome" stations maintained by non-Météo France staff. On the other hand, no defects were found at type 0 stations, which are synoptic stations supervised by Météo France personnel. The main differences between type 0 and type 1 stations are the expertise of the person in charge and the geographical distribution of the stations. The density of type 1 stations is higher than that of type 0 ones. Besides, type 1 stations are located in more remote areas hindering the station maintenance. In the present study, type 1 stations were only used in regions where the density of type 0 stations was low such as the Alps or the Pyrenees (5 stations). Hence, the extreme weather conditions at those stations may explain some of the defects found such is the case of snow accumulation or soiling. The 4 false alarms found in Météo France also occurred at those 5 mountain stations. Maintenance frequency at mountain stations should be increased to reach the quality levels exhibited by stations in low-lying areas.

The number of defects in the rest of national meteorological services was acceptable. We only found 3 operational defects at FMI stations, with two of them being caused by the accumulation of snow or frost. Despite keeping pyranometers ventilated, this type of defect is hardly avoidable at high-latitude stations in winter. Again, maintenance frequency should be as high as possible under extreme weather conditions to keep the pyranometers clean. Nonetheless, the influence of this defect in annual average irradiance is low due to the low irradiance values during months with snow or frost. AEMET and DWD presented just two and one defects, respectively, while no defects were found at SHMI stations. In AEMET, the cause of one of the defects could not be found due to the lack of sub-daily irradiance data to generate the second plot of the BQC. No defects were observed at BSRN stations as well. This was expected because the BSRN uses the highest-quality equipment. All BSRN sites are staffed and implement the most stringent protocols among the networks analyzed [50].

Spanish dataset

The number of defects found in the Spanish dataset was more significant than that of the European dataset (Fig. 5.20). While most European networks were national meteorological services, the Spanish dataset includes different types of weather stations collecting G_H data across Spain, from the national meteorological service to regional and agricultural networks. The BQC flagged suspect data at 264 out of the 732 Spanish stations (Table 5.2). The majority of these defects were solely detected with the BQC. On the contrary, the BSRN checks only flagged time lags, some cases of incorrect leveling, and some large errors. Most of the defects were operational errors (208 stations), and hence mostly related to the inadequate maintenance of the stations. However, the BQC also flagged deviations at 60 doubtful SIAR stations probably related to photodiode limitations and its incorrect calibration.

The majority of the defects were found in SIAR (166 stations, 35% of SIAR stations), which was the most extensive network with 468 stations.

FIGURE 5.20: Summary of the defects found at the 732 Spanish weather stations.

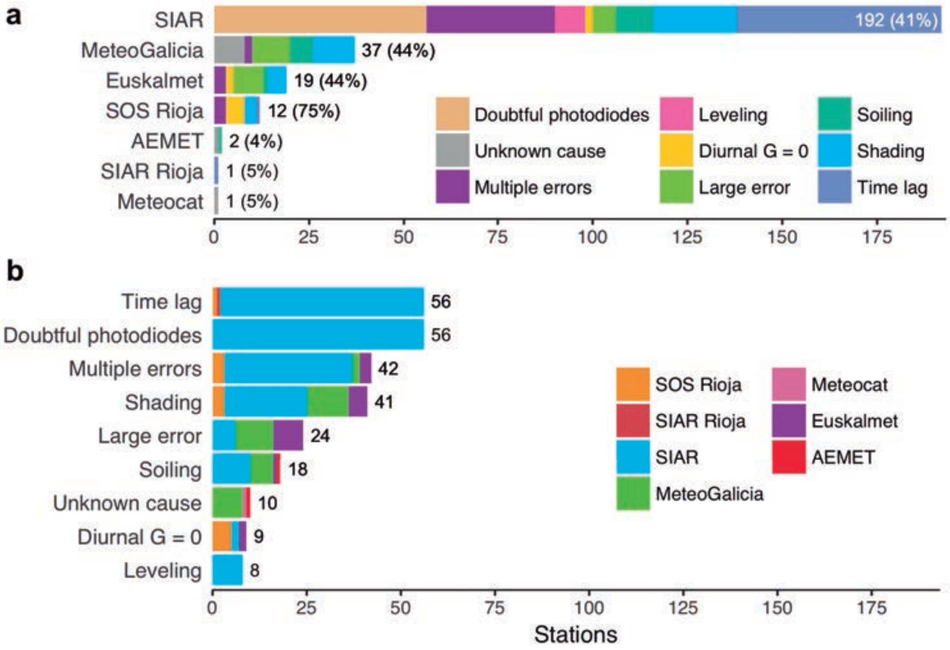

(**a**) Number of defects per network. The "Multiple error" group includes stations with two or more types of defects. The label shows the total number of defects in the network and the percentage of the stations with defects. (**b**) Number of stations showing each type of defect. Stations with multiple errors are accounted in each type of defect identified.

The Spanish Ministry of Agriculture created SIAR for irrigation planning, so most SIAR stations are located in agricultural regions such as Ebro and Guadalquivir Valleys or the Mediterranean Coast. Some locations were selected based on the proximity of other government facilities such as sewage-treatment plans to facilitate the station maintenance. By contrast, pyranometers must be installed in locations with a flat horizon and far from potential sources of contamination such as industrial areas, airports, or busy roads [17]. The inadequate location of some of the stations may explain the high amount of stations with shading (35 stations), due to horizon shadows, or soiling defects (14 stations), due to the proximity of sources of pollution. Besides, other variables such as temperature and precipitation are more critical than solar irradiance for agricultural purposes. The little interest on G_H along with the probably low maintenance of the stations may also explain the large number of large errors, time lags, or incorrect leveling cases identified. In this regard, most of these defects, such as time lags or some large errors, could have been prevented with the implementation of basic QC checks.

There were 60 additional SIAR stations classified as having doubtful photodiodes. Photodiodes are installed in agricultural weather stations due to their low-cost and because they require less maintenance than thermopile pyranometers. However, if they are not properly corrected for spectral response, cosine error, and temperature dependence, the uncertainty of the readings obtained may double that of adequately corrected sensors [26]. This suggests that most of SIAR photodiodes are incorrectly calibrated, or calibrated with general empirical corrections without accounting for the specific conditions at the station. Moreover, maintenance and calibration conditions may strongly vary between SIAR stations because some stations are maintained by the Spanish Ministry while others belong to the regional governments. Overall, the high number of operational errors and the likely presence of equipment errors make SIAR stations inadequate for solar radiation studies.

Table 5.2: List of stations flagged at the 732 Spanish weather stations.

Network	Type	Stations
AEMET	Soiling	5402
	Unknown cause	6325O
SIAR	Time lag	A09, A11, A16, AB07, AB08, AL01, AL05, AV01, AV101, AV102, BA01, BA07, BA104, BA205, BA207, BU102, CA07, CA10, CA101, CC04, CC09, CC102, CC13, CC16, CR01, CR02, CR03, CR10, CS11, GR09, GR10, H05, H06, H10, HU19, HU20, HU21, IB05, IB09, IB101, J102, J11, J15, LU02, M01, M102, MA09, MA10, MA101, NA09, NA101, NA102, NA103, NA104, NA105, NA106, NA107, NA108, NA109, NA110, NA111, SA03, SA101, SA102, SE101, SE12, SE13, SE17, TO10, TO11, TO12, V14, V26, VA06, VA102, ZA08
	Shading	A09, A10, A102, A1020, A13, AB01, AL10, BU101, CA05, CC10, CC14, CO04, CO08, CO102, GR03, GR09, GU07, IB04, IB07, IB08, IB09, J09, J102, MA09, MA10, MA101, V01, V101, V103, V104, V107, V19, V22, V24, VA05
	Soiling	A12, AL02, AL06, CA06, GR101, HU02, M01, MA06, MU03, MU11, TO03, TO09, V23, VA01
	Large error	A10, CR03, H101, J16, M04, MU10, MU17, NA14, SG01, V06, V104
	Diurnal $G_H = 0$	J15, M05, VA101
	Leveling	A02, A07, A11, CC17, CS04, MA04, TE05, TO08, V01, V23, Z08, Z11

	Doubtful photodiodes	A02, A03, A04, A08, A101, A11, AB01, AB02, AB05, AL08, AV101, BA101, BA102, BA203, C01, CC07, CC102, CC11, CC14, CC16, CO09, CR02, CS01, CS03, CS05, CS06, CS08, CS10, CS101, GR11, GU02, GU06, H01, H101, HU01, HU15, HU19, IB01, IB06, IB10, J01, J02, J03, J09, J12, LE01, M102, MA01, MA02, MA06, MU105, MU128, MU16, NA105, NA108, P02, P03, P07, SA03, SA101, SE02, SE08, SG02, V04, V05, V06, V07, V102, V14, V17, V20, V25, VA01, VA08, ZA05, ZA06
Meteocat	Unknown	DC
Euskalmet	Shading	023, 029, 051, 055, 058, 0DC
	Soiling	039, 047
	Large error	018, 026, 027, 030, 048, 054, 057, 060, 064, 0DC
	Diurnal $G_H = 0$	020, 040, 047, 057
MGalicia	Shading	10052, 10053, 10057, 10060, 10063, 10064, 10086, 10088, 10095, 10108, 19065
	Soiling	10045, 10099, 10125, 10126, 19068, 19070
	Large error	10047, 10091, 10093, 10104, 10105, 10112, 10114, 10119, 10121, 10131, 10132, 10800
	Diurnal $G_H = 0$	10105
	Unknown cause	10061, 10085, 10091, 10096, 10097, 10103, 10110, 10118, 10122
SIAR Rioja	Time lag	Albelda de Iregua
SOS Rioja	Time lag	Ezcaray, Santa Marina, Calahorra
	Shading	Urbaña, Moncalvillo, Calahorra, Villoslada
	Soiling	Ocón
	Large error	Ezcaray
	Diurnal $G_H = 0$	Haro, Arnedo, Nájera, Ocón, Yerga, Torrecilla

MeteoGalicia and Euskalmet are two regional meteorological agencies that provide high-resolution G_H data (10 min), but present an unusually high number of defects for a meteorological network (58% of Euskalmet stations, 49% of MeteoGalicia stations). This fact was especially alarming in Euskalmet, where all stations are equipped with the secondary standard pyranometers. The most common defect in both networks was large errors. Some of the defects identified, such as long nocturnal periods with physically impossible values (Euskalmet), evidence a deficient QC in both meteorological agencies. In this sense, Hérnandez et al. [193] described that the QC checks implemented at Euskalmet data center are composed by 5 levels of quality flags. This QC procedure should have eliminated some of the large errors found in this study, but Euskalmet data retrieved from `http://opendata.euskadi.eus` did not include any quality flag. This suggests that data provided by this website has not undergone the QC routines described in Hérnandez et al. [193].

Shading and soiling are also typical in both MeteoGalicia and Euskalmet, questioning again the maintenance protocols implemented by these networks. Mirás-Avalos et al. [194] also found several defects in MeteoGalicia and SIAR stations in Galicia with a QC procedure based on the one described in Younes et al. [34] and using additional spatial consistency tests. They suggested that certain defects were caused by the handling of data, whereas others were caused by a bad positioning of the sensors due to shading by nearby obstacles. Overall, G_H measurements from these two networks should be generally avoided despite the high-quality expected a priori from both meteorological agencies.

SOS Rioja stations presented the worst quality overall, with 79% of the stations showing defects (12 out of 16). The most common defect was the presence of diurnal periods with G_H equal 0, which is some cases extend the whole year indicating no maintenance in either the station or the processing center. Shading was another common defect in SOS Rioja (4 stations). Compared to other networks, the shadows were commonly visible around solar noon. This excludes the possibility of shadows being caused by obstacles on the horizon, such as mountains, trees, or buildings. SOS Rioja sensors are installed in lattice towers, so the most likely scenario is that the structure of the station is causing the shadows. This evidences inadequate planning during the installation phase. In addition, the lack of maintenance and quality checks ruins the high quality of the pyranometers (ISO 9060 first class). Similarly to Euskalmet, these results corroborate that the acquisition of high-quality equipment does not guarantee to collect high-quality records. Top-end pyranometers should be only installed if the adequate level of maintenance can be kept.

The number of defects in the remaining networks was low, with two defects in AEMET, one in SIAR Rioja and Meteocat, and no defects in Meteo Navarra and the BSRN. The good quality of the BSRN and AEMET was somehow expected. We recommend using these networks in applications requiring solar radiation data with low uncertainty. Besides, we also consider that Meteocat, Meteo Navarra, and SIAR Rioja present sufficient quality for being used for regional studies in Cataluña, Navarra, and La Rioja, respectively.

5.1.4 Strengths and limitations of the BQC

The majority of QC procedures described in Subsection 2.1.3 flag values that are implausible from a physical or a statistical perspective. The best example is the BSRN tests, which are the most common choice for quality control solar radiation data [45, 195, 82, 181, 196]. The main limitation of range checks is that the range of physically and statistically acceptable values for surface irradiance variables is very wide because the atmospheric transmissivity depends on different stochastic processes such as cloud formation or the concentration of aerosols, water vapor, and ozone, among others. Hence, these QC methods do not detect defects that introduce low-magnitude deviations, such as shading, soiling, or sensor miscalibrations. This fact was verified in the present study in which BSRN tests only detected time lags, some large errors, and some cases with incorrect leveling of pyranometers.

The strength of the BQC lies in its ability to detect low-magnitude operational errors. This is possible due to two main features of our method: (i) filter deviations of radiation databases (estimations - measurements) instead of irradiance measurements, and (ii) analyze periods of time with a window function instead of individual days/hours. Working with deviations reduces the acceptance ranges because the influence of stochastic atmospheric processes is eliminated, as these processes affect both measured and estimated values. The evaluation of several days all at once with a window function facilitates the detection of long-living errors because the BQC checks if low-deviations prevail in time. Still, the results show that the BSRN tests are a good complement to the BQC because they facilitate the detection of very short periods (few hours) of large deviations and errors that get masked in daily means such as time lags or incorrect leveling.

Another strength of the BQC is the two plots generated for the visual inspection of flagged stations. The two plots are useful in visually detecting false alarms and identifying the cause of the defects. The automatic generation of both plots for stations with flags speeds up the visual inspection and reduces the computation skills required. By contrast, the majority of the QC methods [52, 45, 51, 34] provide numerical flags and leave the user the decision of removing the samples. When working with large datasets, the visual inspection of numerical flags may become unfeasible from a practical point of view, so users may be tempted to remove all flagged samples without knowing the exact cause of the error and without discarding false alarms.

The use of radiation databases to detect errors in ground measurements entails some risks related to the uncertainty of estimation methods. The stability and variance of the estimations are the two most critical aspects. Regarding the temporal stability, our method flags inconsistent deviations of the radiation databases against station measurements. Systematic deviations are taken into account by the CIs, so the databases can overestimate or underestimate solar radiation as long as they do it consistently. However, inconsistent deviations can be caused either by a defect on the readings or by a failure in the radiation database. The use of three radiation databases derived with independent models increases the likelihood of errors in the recording process causing the deviations flagged. Besides, we observed that the number of false alarms decreased with the combination of the three databases. Still, the temporal stability of the model must be of critical importance when selecting the databases for the BQC.

All radiation databases used were designed for climate monitoring purposes, so the temporal stability of the data was one of the main concerns for their design. Even though both satellite-based databases are climatological datasets, their stability is not fully guaranteed because they are obtained by combining images from different satellite generations. Sometimes even the type of sensor is replaced, resulting in a potential introduction of artificial trends in the times series. Besides, satellite instruments degrade in time, so the calibration factors have to be continuously corrected to mitigate aging effects [197]. Nonetheless, the magnitude of these temporal instabilities is generally within the uncertainty of pyranometers and considerably smaller than the deviations caused by the equipment and operational errors, so they do not interfere in the BQC. The decadal trend of SARAH-1 was -1.1 W/m^2/decade [195], while that of CLARA-A2 showed a good agreement with the decadal trend from BSRN stations [176]. ERA-Interim used the same NWP model to derive the whole dataset including a bias correction scheme for long-term drifts and calibration errors [198]. In addition, we observed that the inter-annual stability of the three products was acceptable in the period studied (2005-2015), and none of the false alarms identified could be attributed to an artificial degradation of the products.

Based on the previous, the probability of false alarms in the BQC is low. False alarms can still occur when all models fail inconsistently at the same time. Inconsistent deviations are those that appeared just one year of the time series (temporal inconsistency) or at one location within the spatial region analyzed with the same CIs (spatial inconsistency). These deviations produce false alarms because they cannot be characterized by the CIs, but they only occurred at one station with seasonal snow and five stations located in the mountains. False alarms due to seasonal snow were minimized by filtering together stations above 65°N because the CIs already accounted for the large deviations of radiation databases during the snow season. False alarms at mountain stations could have been similarly reduced by grouping all mountain stations for calculating the CIs, but this option was discarded due to the few mountain stations available.

Another critical issue is the variance of radiation databases. As abovementioned, the bias (systematic errors) is not crucial because the CIs includes it. However, the variance (random errors) defines the width of the CIs and limits the magnitude of deviations flagged by the BQC. Random errors may be caused by limitations of the databases (low spatial and temporal resolution, low-quality ancillary products, or simple atmospheric models) and by the particular conditions of the region analyzed (mountains, snow-covered areas, coastlines, etc.) [199]. For instance, the high variance of the databases in the Nordic countries results in wider CIs than those in Southern Europe. This implies that low-magnitude defects such as shading or soiling are more easily detected in Southern Europe than in the Nordic countries. This problem was mitigated with the calculation of the CIs on a monthly basis (temporal averaging) and grouping stations that share similar characteristics (spatial averaging). This spatiotemporal averaging, along with the use of robust statistics, made the CIs more restrictive enhancing the detection of low-magnitude defects.

5.2 Validation of radiation databases

The main validation of satellite-based and reanalysis databases was made over Europe because the European dataset offers a dense network of weather stations to evaluate both types of modeling approaches (Subsection 5.2.1). A second validation was made against BSRN stations worldwide (Subsection 5.2.2) to verify globally the results obtained over Europe. The strengths and weaknesses of satellite-based and reanalysis models were summarized in Subsection 5.2.3.

5.2.1 Validation over Europe

Satellite-based models

The summary statistics showed in Table 5.3 were calculated by excluding stations located in the mountains and latitudes above 65°N. Solar radiation models typically present large deviations in the mountains, so including these results would have altered overall statistics. These stations are Météo France 5183001 (1310 m), Météo France 6094002, (1748 m), Météo France 9024004 (1781 m), Météo France 64316003 (1427 m), DWD 5792 (2964 m), and AEMET 2462 (1894 m). High-latitude stations were analyzed separately because the spatial coverage of models using images from geostationary satellites is limited to latitudes within ±65°. Mountain stations were excluded not only from the calculation of summary statistics but also from the different plots used in the evaluation. Contrary, results at high-latitude stations were kept in those plots. Note that the biases (MBD and $rMBD$) of SARAH PVGIS and CM SAF Operational product are negatively biased because missing hourly values at sunrise and sunset have been set to 0. Therefore, their actual bias should be somewhat larger.

TABLE 5.3: Summary statistics of daily G_H from satellite-based databases at European weather stations (2010-2014).

		MBD [W/m^2]	rMBD [%]	MAD [W/m^2]	rMAD [%]	RMSD [W/m^2]	rRMSD [%]
Lat. < 65°N 271 stations	SARAH PVGIS	0.07	-0.33	12.38	9.94	17.51	14.15
	SARAH-2	2.33	1.65	11.57	9.27	16.11	13.00
	CM SAF Oper.	4.63	3.96	12.73	10.35	17.57	14.28
	CLARA-A2	-2.18	-1.56	13.02	10.38	18.18	14.48
Lat. > 65°N 17 stations	CLARA-A2	-3.82	-3.97	13.23	14.87	20.30	22.98
Mountains 6 stations	SARAH PVGIS	-8.74	-5.05	34.56	21.30	48.28	29.85
	SARAH-2	-4.77	-2.62	28.59	17.95	40.55	25.56
	CM SAF Oper.	-6.09	-3.91	28.85	18.03	40.09	25.04
	CLARA-A2	-13.72	-8.40	27.85	17.34	37.00	23.09

The biases obtained by both SARAH versions are in line with previous validations made by CM SAF against BSRN stations: SARAH-E ($rMBD$ = +0.73%, MBD = +1.63 W/m^2) [21], SARAH-1 (MBD = +1.12 W/m^2) [195], and SARAH-2 (MBD = +1.7 W/m^2) [22]. In this study, SARAH-2 also obtained a positive $rMBD$ (+2.33 %), whereas the $rMBD$ of SARAH PVGIS, which is a combination of SARAH-1 and SARAH-E, was somewhat smaller (+0.07%). The increase of the bias from SARAH PVGIS to SARAH-2 is explained by the negative bias in SARAH PVGIS due to missing hourly values, along with a decreased underestimation in SARAH-2 due to an improved temporal stability and a reduced negative bias in high latitudes. CM SAF validations [22] revealed a decrease in the decadal trend from SARAH-1 (-1.7 W/m^2/decade) to SARAH-2 (-0.7 W/m^2/decade) due to an improved transition from MFG satellites (MVIRI instruments) to MSG satellites (SEVIRI instruments). Hence, SARAH-2 estimations are higher than those of SARAH-1 (and SARAH PVGIS) during the years validated in this study. Besides, SARAH PVGIS showed a stronger underestimation in high latitudes, even though both SARAH versions showed an increasing underestimation with increasing latitude (Fig. 5.21). The underestimation near the edge of satellite images is a known problem of SARAH-1 and SARAH-E [21, 195]. In those regions, satellites view clouds at very shallow angles overestimating cloud thickness and underestimating irradiance. This problem was addressed by SARAH-2 with a correction for the cloud index as a function of satellite zenith angle that minimized the underestimation of SARAH-2 in high latitudes [22].

Figure 5.21: Distribution of $rMBD$ in daily G_H from satellite-based databases over Europe.

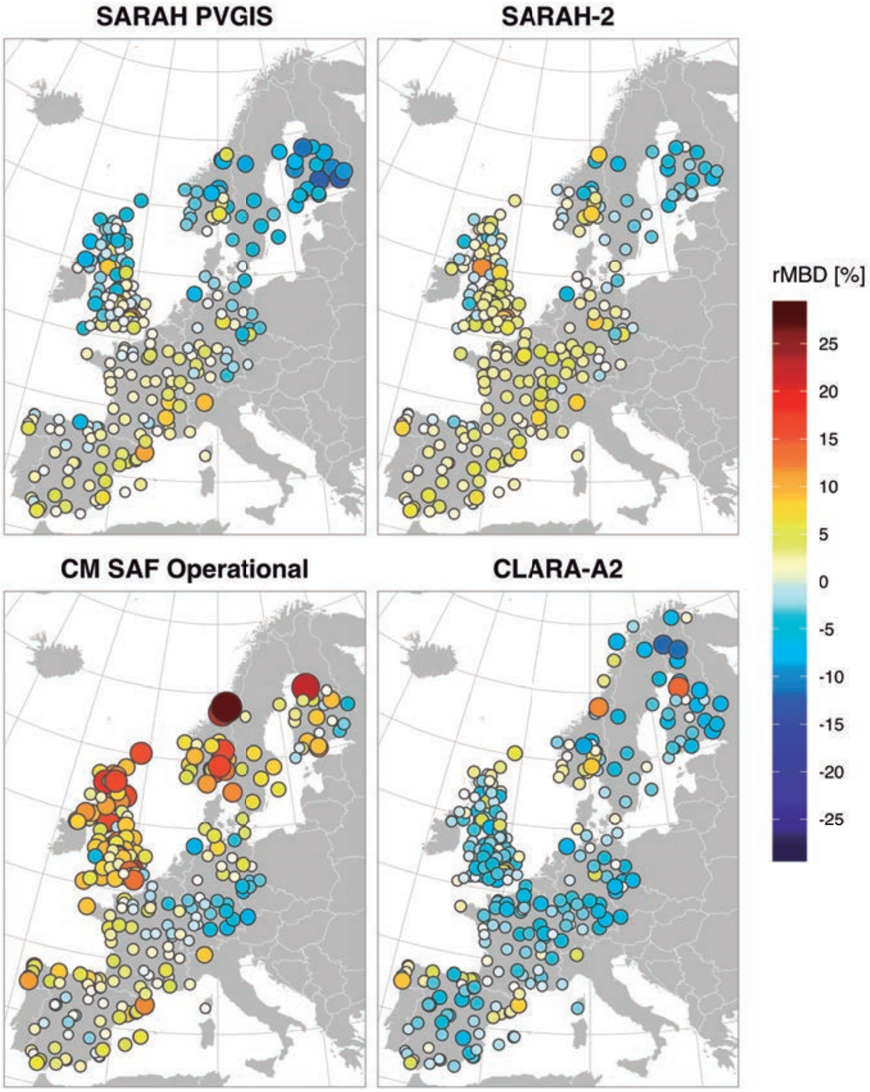

The magnitude of $rMBD$ is represented with both color and size.

The bias of both SARAH-2 and SARAH PVGIS was stronger in high latitudes during winter (Fig. 5.22). This was also observed by Riihelä et al. [102] in a validation of SARAH-1 over Finland and Sweden (MBD = -4.72 W/m^2). SARAH detects clouds solely with images from the visible channels of radiometers onboard geostationary satellites. These images are not sufficient to robustly differentiate between the high reflectivity of snow and that of clouds, leading to an over-prediction of clouds over snow-covered surfaces [22]. CM SAF is working on an improved snow detection algorithm [22]. In this respect, newest algorithms use infrared channels to detect clouds, but CM SAF cannot exploit all channels of SEVIRI instruments (2006-present) because it has to keep consistency with MVIRI data (1982-2005) to produce long-term homogeneous climate data records.

Excluding high latitude locations, both versions underestimate in summer and overestimate in winter (Fig. 5.22). This pattern is common among solar radiation models, and it may be related to an incorrect cloud prediction. Even the best algorithms will show clouds through random chance under clear conditions, which are more frequent in summer, while the opposite will occur under cloudy conditions in winter. These random errors typically average out and do not interfere in the annually-aggregated bias.

CLARA-A2 obtained the most homogeneous spatial distribution of the bias over Europe (Fig. 5.21), though it systematically underestimated G_H ($rMBD$ = -1.56%). CM SAF validations against BSRN stations also found negative biases for CLARA-A1 (MBD = -4.7 W/m^2) [200] and CLARA-A2 (MBD = -1.7 W/m^2) [103]. The decrease of the bias from CLARA-A1 to CLARA-A2 is most likely due to an improved cloud detection algorithm [103]. CLARA-A2 still underestimates in summer and overestimates in winter, which similarly to SARAH may be due to random errors in cloud prediction. This pattern changed in high latitudes where CLARA-A2 underestimates in winter and overestimates in summer. Negative biases in winter may be related to the same snow detection problems than those discussed for SARAH. Indeed, the actual bias of CLARA-A2 in winter may be even larger because daily samples showing strong deviations due to snow-related issues were set to missing by CM SAF [176]. The positive bias from May to September was also observed in the validation of CLARA-A1 made by Riihelä et al. [102] over Finland and Sweden. In that case, the overestimation in summer led to an overall positive MBD of +2.79 W/m^2 because CLARA-A1 coverage over snow-covered areas was even lower than that of CLARA-A2. Riihelä et al. [102] also reported a reducing variance from 1983 to 2009 due to an increasing satellite coverage. In this study, we have just evaluated the last years covered by CLARA-A2 (2010-2014) where the availability of polar-orbiting satellites is the highest (from 3 to 5). This increases the number of sub-daily satellite images used to calculate the daily atmospheric transmissivity reducing the uncertainty of daily estimates.

The CM SAF operational product showed the largest bias overall ($rMBD$ = +3.96%), which is especially alarming given the fact that its daily means were negatively biased due to missing values at low solar elevation angles. These systematic deviations ranged from +1 to +2 W/m^2 in Central

FIGURE 5.22: Heatmap of monthly-aggregated $rMBD$ in daily G_H from satellite-based databases at European stations.

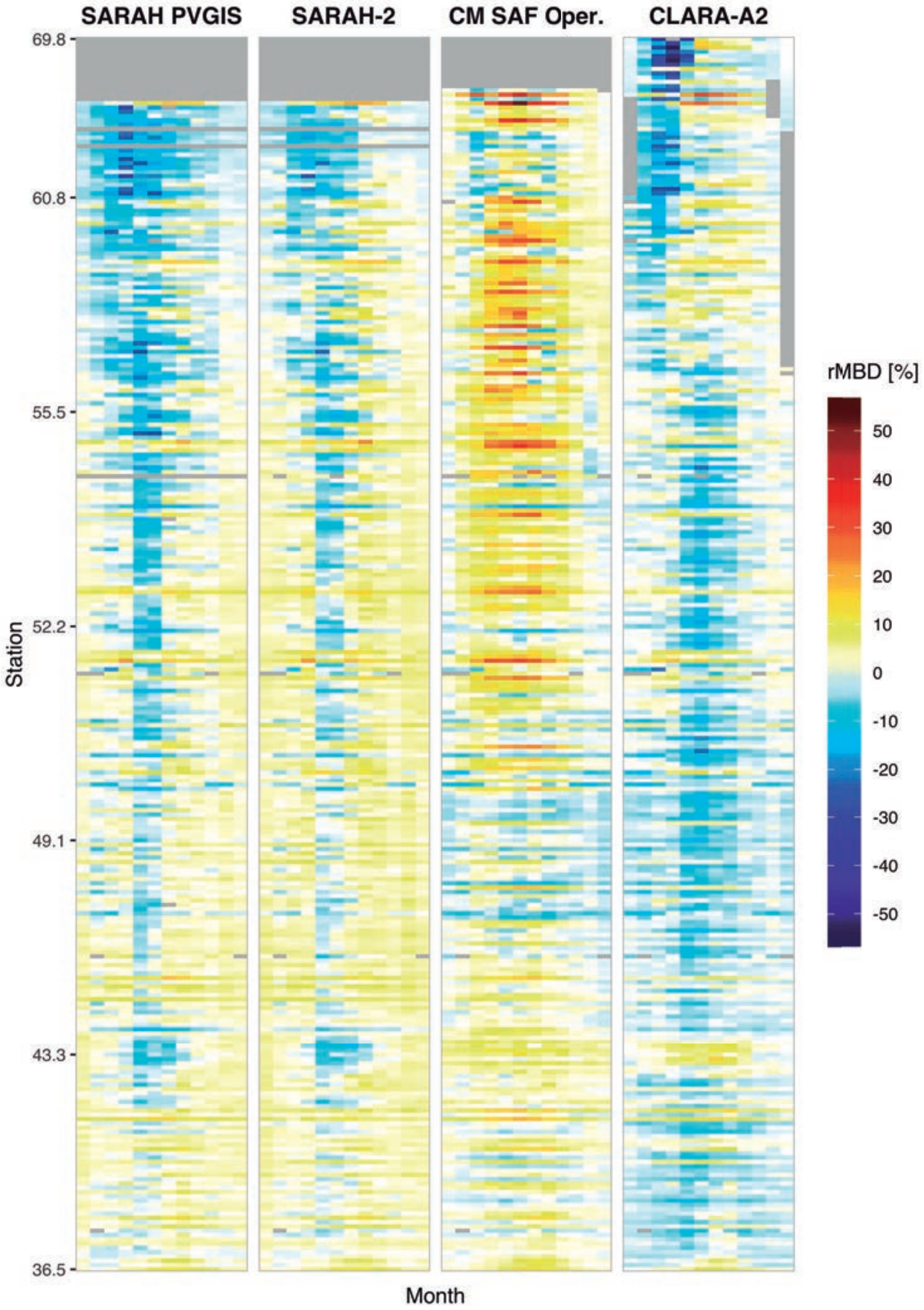

Stations are sorted from bottom to top by increasing latitude. Y-axis labels show the station latitude.

and Southern Europe, and from +3 to +4 W/m^2 in Northern Europe, before 2012. Since then, the number of missing values decreased, and these systematic deviations fell below +1 W/m^2. This validation includes years from 2010 to 2014, so the actual bias of the operational product may be around +2 W/m^2 larger due to missing values from 2010 to 2012. The overestimation of the operational product is more prominent on the coast ($rMBD = [+10, +20]\%$) (Fig. 5.21), which may be related to the coarser grid of the operational product (∼25 km) compared to other satellite databases. CLARA has a similar resolution, but the calculations are made in a grid of ∼5 km and then averaged. The quality of solar radiation models using coarse spatial grids degrades on the coasts because large portions of land and sea fall in the same pixel while irradiance shows a steep gradient. This issue is further discussed in the analysis of reanalysis databases (Subsection 5.2.1).

Compared to SARAH and CLARA, the bias of the operational product was more positive in summer than in winter (Fig. 5.22). Random errors due to cloud prediction show the opposite pattern. Hence, the overestimation in summer may be related to the quality of the aerosol climatology. The operational product uses the GADS/OPAC climatology whereas SARAH and CLARA take aerosol data from MACC reanalysis and Aerocom model median merged with Aeronet data, respectively. CM SAF has just updated its operational product implementing the modeling approach and input data used by SARAH-2, so most of the issues in the operational product mentioned above may have been corrected in the new version.

FIGURE 5.23: 2D density plots of relative deviations of daily G_H (satellite-based data minus measurements) against K_T at European stations.

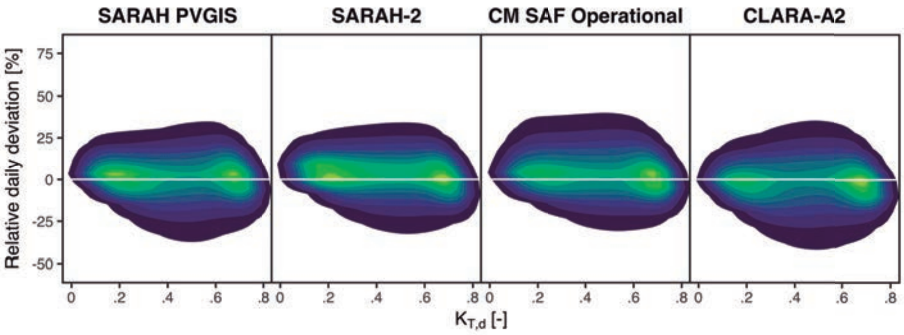

Density plots are generated with a 2D binned kernel density estimate.

Clouds are not only the most dominant factor in surface incoming irradiance but also the one most difficult to predict. Thus, errors in cloud placement produce the most significant deviations in solar radiation models. The quality of cloud predictions can be evaluated with the distribution of deviations against K_T (Fig. 5.22). In this case, any particular pattern was observed, and all databases showed a homogeneous performance against atmospheric transmissivity. Aerosol and water vapor data may also cause deviations at high K_T, but none of the satellite-based databases showed any particular systematic deviation under clear conditions.

SARAH-2 (MAD = 9.27%) and SARAH PVGIS ($rMAD$ = 9.94%) showed the smallest absolute errors. The reduction of the absolute error from SARAH-1 (MAD = 12.1 W/m^2) [195] to SARAH-2 (MAD = 11.8 W/m^2) [22] was also reported by CM SAF. The absolute error of CLARA-A2 was somewhat larger ($rMAD$ = 10.35 %), which could be related to the lower temporal resolution of polar-orbiting satellites. While SARAH-1 and SARAH-2 use hourly or half-hourly satellite images to calculate the cloud index, CLARA-A2 only has 3-5 diurnal images in mid and low latitudes. The temporal resolution of polar-orbiting satellites increases near the poles, but it is still lower than that of geostationary satellites. The absolute error of the CM SAF operational product ($rMAD$ = 10.38%) was comparable to those of SARAH-2 and SARAH-PVGIS, but similarly to the bias, it significantly increased in coastal regions as well (Fig. 5.24).

The validation metrics of all databases substantially worsened in the mountains (Table 5.3). All models tend to underestimate G_H ($rMBD$ = [-2, -8]%), which may be related to the presence of snow in winter. The absolute error increases even more, and both $rMAD$ (17-21 %) and $rRMSD$ (23-30%) in the mountains double those in low-lying areas. SARAH-2 showed the smallest degradation in mountain regions. The CM SAF validations [22] reported that SARAH-2 irradiance increased in mountainous areas (Alps or Pyrenees) and decreased in the valleys reducing the estimation errors due to the use of a downscaled water vapor based on a topographic correction. The low bias of the operational product was just a fortuitous value due to the compensation of the discussed overestimation of this product in low-lying areas with the underestimation of satellite-based models over snow-covered surfaces. These deviations are not compensated for absolute errors, so the operational product showed a large $rMAD$ in the mountains as well.

Solar radiation models typically produce large deviations in the mountains because they do not have a sufficiently high temporal and spatial resolution to model the particular atmospheric conditions in mountainous areas. This is complicated even more by terrain shading and the presence of snow in winter. Validation statistics in the mountains also worsen due to the comparison of spatial estimates against point measurements in a region with a steep gradient in solar irradiance. This also occurs in other

FIGURE 5.24: Distribution of *rMAD* in daily G_H from satellite-based databases over Europe.

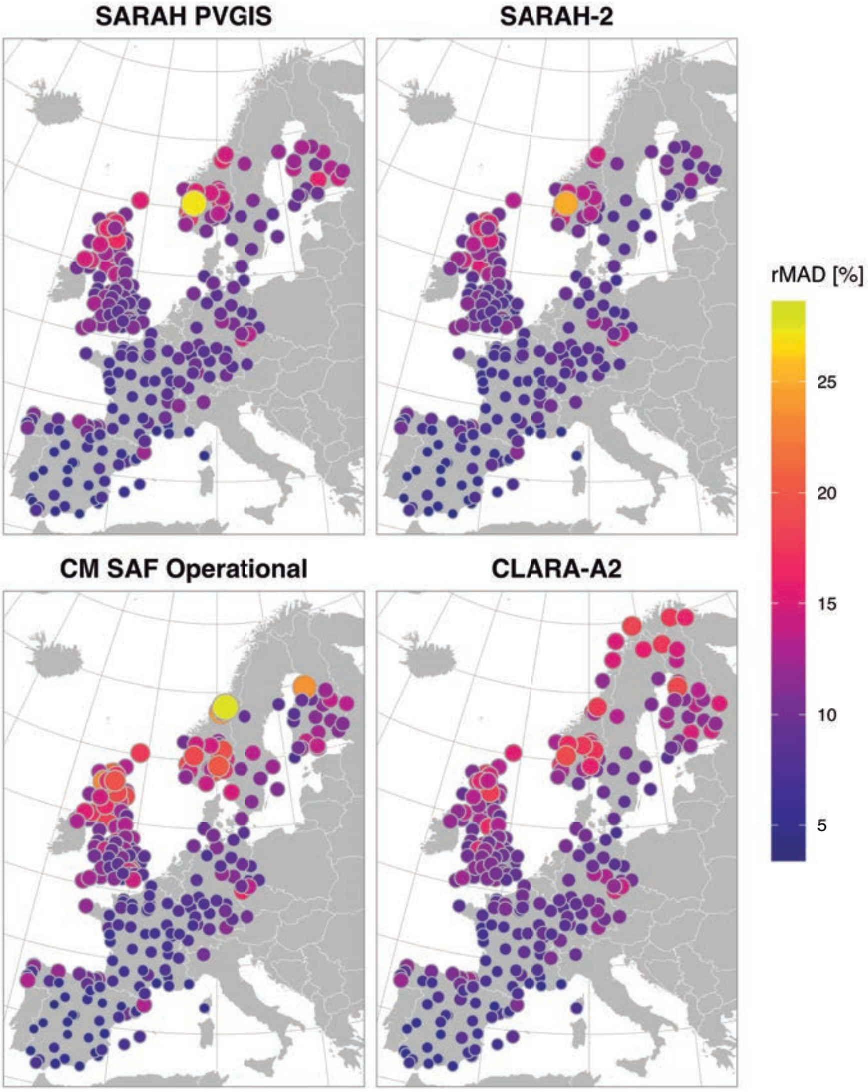

The magnitude of *rMAD* is represented with both color and size.

regions such as coastal areas, as observed in the results of the operational product. The representativeness of stations decreases in rough terrains, whereas the resolution of the spatial grids is too large to account for the high spatial variability [201]. We will further discuss these issues in the evaluation of reanalyses (Subsection 5.2.1).

Reanalysis databases

Reanalyses were evaluated based on the same groups of stations defined to validate satellite-based databases for comparability purposes (Table 5.4), although both global and regional reanalyses cover latitudes above 65°N.

TABLE 5.4: Summary statistics of daily G_H from reanalysis databases at European stations (2010-2014).

		MBD [W/m^2]	rMBD [%]	MAD [W/m^2]	rMAD [%]	RMSD [W/m^2]	rRMSD [%]
Lat.< 65°N 271 stations	ERA-Interim	11.67	9.24	24.18	19.19	35.57	28.29
	MERRA-2	18.66	15.02	26.59	21.29	39.15	31.41
	ERA5	3.75	3.18	19.48	15.48	28.08	22.36
	COSMO-REA6	-6.00	-3.72	22.56	17.57	31.84	25.13
Lat.> 65°N 17 stations	ERA-Interim	2.05	2.65	17.54	19.89	28.79	32.76
	MERRA-2	6.82	7.96	19.09	21.61	31.19	35.42
	ERA5	0.81	1.42	15.49	17.53	25.78	29.27
	COSMO-REA6	-1.96	-1.87	16.22	18.28	27.15	30.75
Mountains 6 stations	ERA-Interim	13.40	8.78	38.08	24.00	52.56	33.10
	MERRA-2	22.78	14.34	36.17	22.69	51.28	32.21
	ERA5	8.24	5.18	31.21	19.46	42.72	26.66
	COSMO-REA6	-1.44	-0.84	31.17	19.45	42.36	26.46

MERRA and ERA-Interim have probably been the two most widely used global reanalysis in the last years. In this study, we have validated MERRA-2 which is the successor of MERRA but still shares most of its main features. Both ERA-Interim and MERRA-2 strongly overestimate G_H over Europe, with a $rMBD$ of of +9.24% and +15.02%, respectively. The overestimation of both reanalyses in Europe and also globally has been reported in previous validations. Positive biases for ERA-Interim were found in Germany by Träger-Chatterjee et al. [120] (MBD = +5.2 W/m^2), in France ($rMBD$ = [-4, +14]%) and in the Baltic region ($rMBD$ = [+2, +17]%) by Boilley and Wald [24], in Europe by Bojanowski et al. [23] ($rMBD$ = +9.08%) and Zhang et al. [109] (MBD = +4.64 W/m^2), and globally by Zhang et al. [109] (MBD = +11.25 W/m^2) and Posselt et al. [202] (MBD = +5.64 W/m^2). Positive biases were for MERRA-2 were also found in France ($rMBD$ = [-5, +21]%) and in the Baltic region ($rMBD$ = [+7, +16]%) by Boilley and Wald [24], in Czech Republic by Jurůs et al. [122] (MBD = +23.4 W/m^2), in Europe by Zhang et al. [109] (MBD = +19.80 W/m^2), in North America by Zhao et al. [111] (MBD = +20.2 W/m^2), and globally by Zhang et al. [109] (MBD = +22.36 W/m^2) and Yi et al. [121] (MBD = +16.55 W/m^2). The overestimation of MERRA was stronger that that of ERA-Interim in most regions. We observed the same trend in this study, despite validating MERRA-2 instead of MERRA. This suggests that the upgrades of MERRA-2 have not solved the bias problems of its predecessor.

In this line, one of the first validations of MERRA-2 by the own NASA's GMAO [124] confirmed that MERRA-2 kept a positive bias of around [+5, +10] W/m^2 globally. Pfenninger and Staffell [125] also used both MERRA and MERRA-2 for simulating PV systems over Europe and obtained a similar overestimation in yield predicted from both versions.

ERA-Interim and MERRA-2 overestimated G_H across all Europe (Fig. 5.25). MERRA-2 obtained a larger average positive bias because it overestimated at almost all European stations and particularly in regions with high-cloudiness such as Central Europe or the British Islands. The overestimation of ERA-Interim was somehow mitigated in the Nordic countries, but it substantially increased in coastal regions of northern Spain, the British Islands, and Norway. The stronger overestimation at coastal locations is related to the above-mentioned errors due to comparing coarse spatial estimates against point values in regions with steep irradiance gradients. ERA-Interim (~81 km) and MERRA-2 (~50 km) pixels include large portions of both water and land whereas irradiance sharply changes in few km. Particularly, both products strongly overestimated in the Spanish, Norwegian, and British coasts because the average irradiance received by the sea is greater than that received by the land in these regions (Fig. 5.26). Thus, the spatial average provided by these pixels is greater the point value measured by inland stations. The increase of the bias at coastal locations was more accentuated in ERA-Interim than in MERRA-2 due to the coarser grid of the prior. Note that the irradiance estimates from both reanalyses were interpolated using IDW, eliminating some systematic deviations in the comparison against point values such as those caused by latitude effects [201]. Therefore, the bias may be even higher if the pixel values are directly compared to ground measurements.

The source of these biases was analyzed with the distribution of monthly-aggregated biases (Fig. 5.27) and with the distribution of daily deviations against K_T (Fig. 5.28). The overestimation of G_H under cloudy conditions (Fig. 5.28) drove the positive bias in both ERA-Interim and MERRA-2. This is probably caused by an underestimation of the cloud fraction due to predicting too few clouds, optically too thin clouds, or incorrect cloud properties (cloud phase or liquid/ice water content), among others. In this line, Träger-Chatterjee et al. [120] observed significant positive biases for ERA-Interim in cloudy regions and winter, when the frequency of clouds is high. Zhang et al. [109] and Zhao et al. [111] also suggested that an underestimation of clouds probably caused the overestimation of both ERA-Interim and MERRA-2. The performance of ERA-Interim and MERRA-2 differed under clear sky. ERA-Interim underestimated G_H averaging out the large overestimation under cloudy conditions and reducing the overall bias of ERA-Interim [24]. This compensation of the bias

FIGURE 5.25: Distribution of *rMBD* in daily G_H from reanalysis databases over Europe.

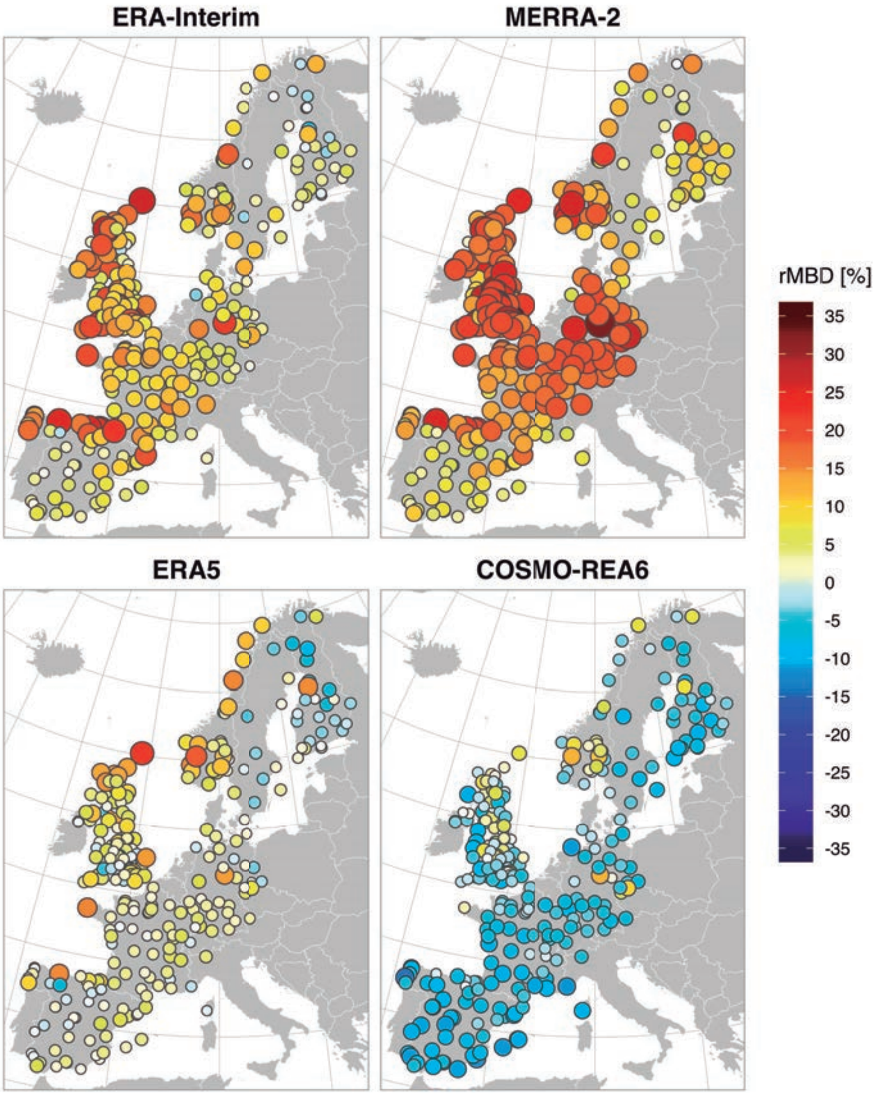

The magnitude of the *rMBD* is represented with both color and size.

may be related to random errors in cloud prediction. These random errors do not completely cancel out because the overestimation under cloudy conditions was more significant than that under clear sky resulting in the overall positive bias of ERA-Interim. Excluding coastal locations, the overestimation decreased in summer and regions with low-cloudiness such as Spain or southern France (Fig. 5.27). On the other hand, MERRA-2 slightly overestimated G_H under clear conditions as well, aggravating the strong overestimation under cloudy conditions and leading to the large average positive bias shown by MERRA-2. Therefore, MERRA-2 bias was positive in every month of the year (Fig. 5.27). The positive biases of MERRA2 under clear conditions cannot be caused by random errors in cloud prediction and may be related to aerosol errors.

FIGURE 5.26: Map of mean G_H form SARAH PVGIS (2010-2016).

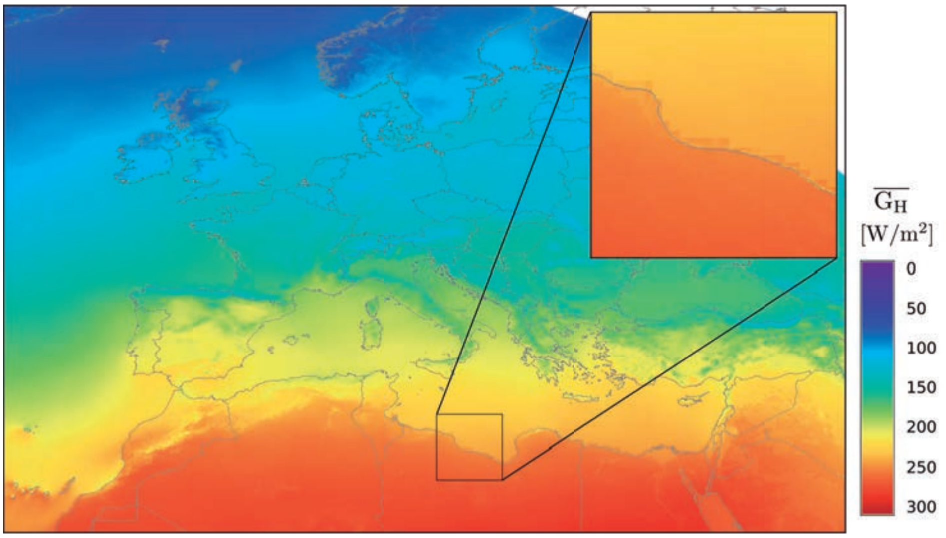

The inset shows the irradiance gradient on the Mediterranean coast of North Africa.

ERA5 is the newest global reanalysis produced by the ECMWF. Contrary to MERRA-2, ERA5 entails a significant improvement over ERA-Interim as it includes an increased horizontal, vertical, and temporal resolution, among other features. All these upgrades led to a notable reduction in the average *rMBD* shown by ERA-Interim over Europe from +11.67% to +3.75%, mainly due to a decreased overestimation at all European stations (Fig. 5.25). The bias reduction was driven by a reduced overestimation under cloudy conditions (Fig. 5.28). The bias of ERA5 still showed a similar dependence on the atmospheric transmissivity to that of ERA-Interim, but the magnitude of positive and negative biases under cloudy and clear conditions in ERA5 was comparable. Thus, both effects averaged out leading to a moderate average positive bias over Europe. Similarly to ERA-Interim, the dependence of the bias on K_T may be related to random errors in cloud prediction that lead to predicting clouds under clear sky and vice versa. Negative biases were stronger in summer when the frequency of clear conditions is higher, and positive biases were more accentuated in winter when cloudy conditions predominate (Fig. 5.27). The reduction of the bias was also very notable in coastal regions (Fig. 5.25) mainly due to the finer grid of ERA5 (~31 km) compared to that of ERA-Interim (~81 km). Nonetheless, moderate positive biases remained in the Norwegian, British and Spanish coasts, suggesting that the spatial grid of ERA5 is still inadequate to model the steep solar irradiance gradients of coastal regions.

COSMO-REA6 was the only regional reanalysis evaluated, which are characterized by using finer spatial grids and regional NWP models specially designed for the region covered by the reanalysis. In this regard, COSMO-REA6 presented the most homogeneous spatial distribution of the bias over Europe, being the only reanalysis that did not deteriorate in coastal regions (Fig. 5.25). This is most likely due to the fine spatial grid of COSMO-REA6 (~6.2 km) that is comparable to that used by most satellite-based products. Still, COSMO-REA6 systematically underestimates G_H over Europe ($rMBD$ = -5.30 W/m^2) and showed the same bias dependency on K_T as global reanalyses, though in this case, the dominant effect was the underestimation under clear condition (Fig. 5.28). Similar results were obtained by the HErZ-DWD when validating COSMO-REA6 against European BSRN stations (MBD = -9.2 W/m^2) [181, 203]. They found large negative biases at locations with low cloudiness such as Sede Boqer (MBD = -49.7 W/m^2) and positive biases at locations with high cloudiness such as Lerwick (MBD = +12.6 W/m^2). Frank et al. [181] investigated the source of the bias with collocated measurements from ceilometers. Positive biases under low K_T corresponded to cases with low (cloud base < 2 km) and medium-height clouds (2 km < cloud base < 5 km) and were caused by predicting by optically too thin or too few clouds. This effect was mainly observed in winter (Fig. 5.27) and in cloudy regions such as Scotland (Fig. 5.25). On the other hand, positive deviations under high K_T corresponded to clear conditions and were probably caused by a too strong aerosol extinction. The overestimation of the aerosol content was a known problem of the Tanré aerosol climatology [204] when producing COSMO-REA6, but this climatology was kept because it was the standard input for COSMO NWP model. Due to this excess of aerosols, the underestimation of COSMO-REA6 increased in summer (Fig. 5.27) and sunny regions such as Spain where the $rMBD$ exceeded -20 W/m^2 (Fig. 5.25).

The previous results suggest that the incorrect prediction of clouds is the primary source of error in reanalysis models. As above-mentioned, this type of error causes the under-prediction of clouds under cloudy conditions and vice versa, leading to positive and negative bias in G_H under overcast and clear conditions, respectively. These deviations averaged out in annually-aggregated biases, but they do not cancel out in annually-aggregated absolute errors, leading to large $MADs$ and $RMSDs$ for all reanalyses (Table 5.4). Therefore, models such as ERA5 can show a moderate

FIGURE 5.27: Heatmap of monthly-aggregated $rMBD$ in daily G_H from reanalysis databases at European stations.

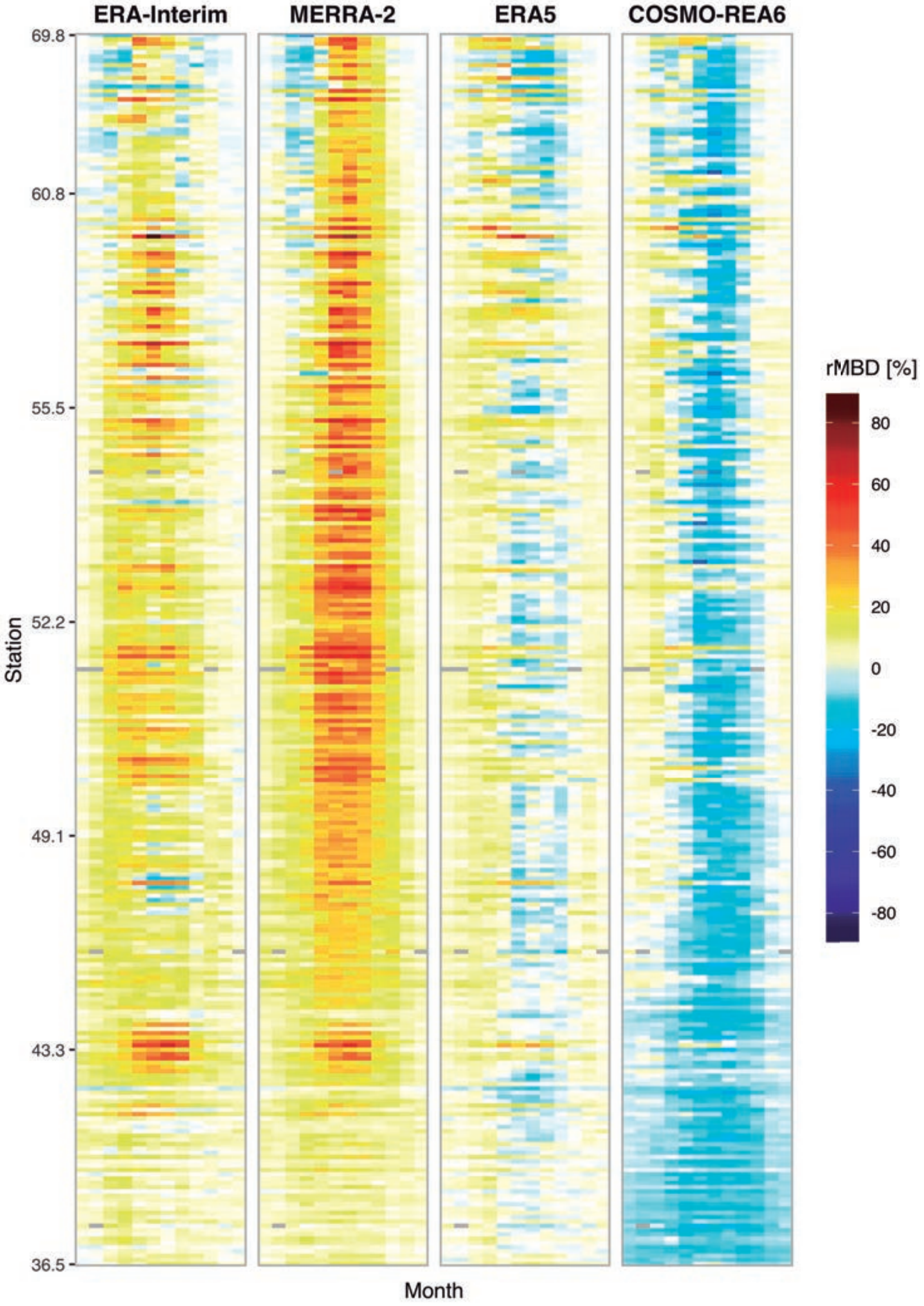

Stations are sorted from bottom to top by increasing latitude. Y-axis labels show the station latitude.

FIGURE 5.28: 2D density plot of relative deviations of daily G_H (reanalysis minus measurements) against K_T at European stations.

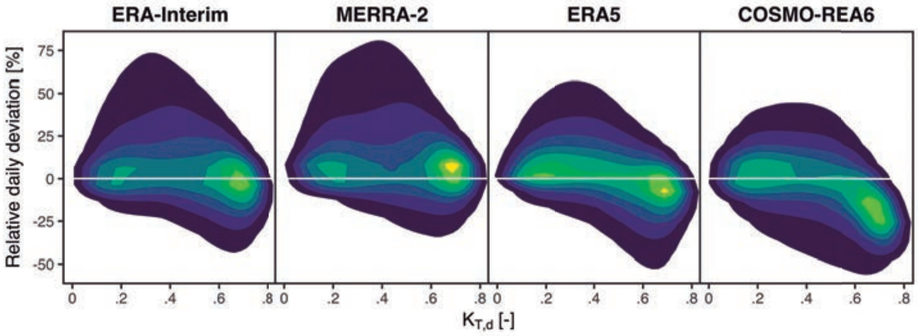

Plots are generated with a 2D binned kernel density estimate.

bias but a large absolute error because the low bias is a result of the compensation of seasonal deviations.

MERRA-2 and ERA-Interim presented the largest *rMAD* among the databases evaluated (21.29% and 19.12%, respectively). The *rMAD* of both products increased on the coast and in Central Europe (Fig. 5.29), a region characterized by high cloudiness. On the other hand, both MERRA-2 and ERA-Interim showed a moderate *rMAD* around 9-15 W/m^2 in regions with a high frequency of clear skies such as Spain. The *rMAD* also decreased from ERA-Interim (19.12%) to ERA5 (15.48%) confirming the improvement of ERA5. Although ERA5 showed the smallest *rMAD* among reanalyses over Europe, the reduction in the *rMAD* was less significant than that in the bias because ERA5 deviations also vary with atmospheric conditions. The *rMAD* of ERA5 was below 15% at most European locations excluding the coasts, the Alpine region, and the British Islands. The lowest absolute errors were obtained in Spain as well (*rMAD* = 8-12%). COSMO-REA6 obtained a very homogeneous spatial distribution of the *rMAD* (Fig. 5.29), with the *rMAD* slightly increasing in Scotland and Norway. The average *rMAD* was small but somewhat larger than that of ERA5 (17.57%), most likely due to the strong underestimation of COSMO-REA6 under clear conditions due to an excess of aerosol. This problem was aggravated in low-cloudiness regions of Southern Europe, where COSMO-REA6 obtained the greatest *rMAD* (12-15%) between the reanalyses evaluated. Besides, the differences between ERA5 and COSMO-REA6 on the coast were not as large for the *rMAD* as they were for the bias, suggesting that the use of coarse grids may have a greater impact on the bias than on the absolute error.

FIGURE 5.29: Distribution of *rMAD* in daily G_H from reanalysis databases over Europe.

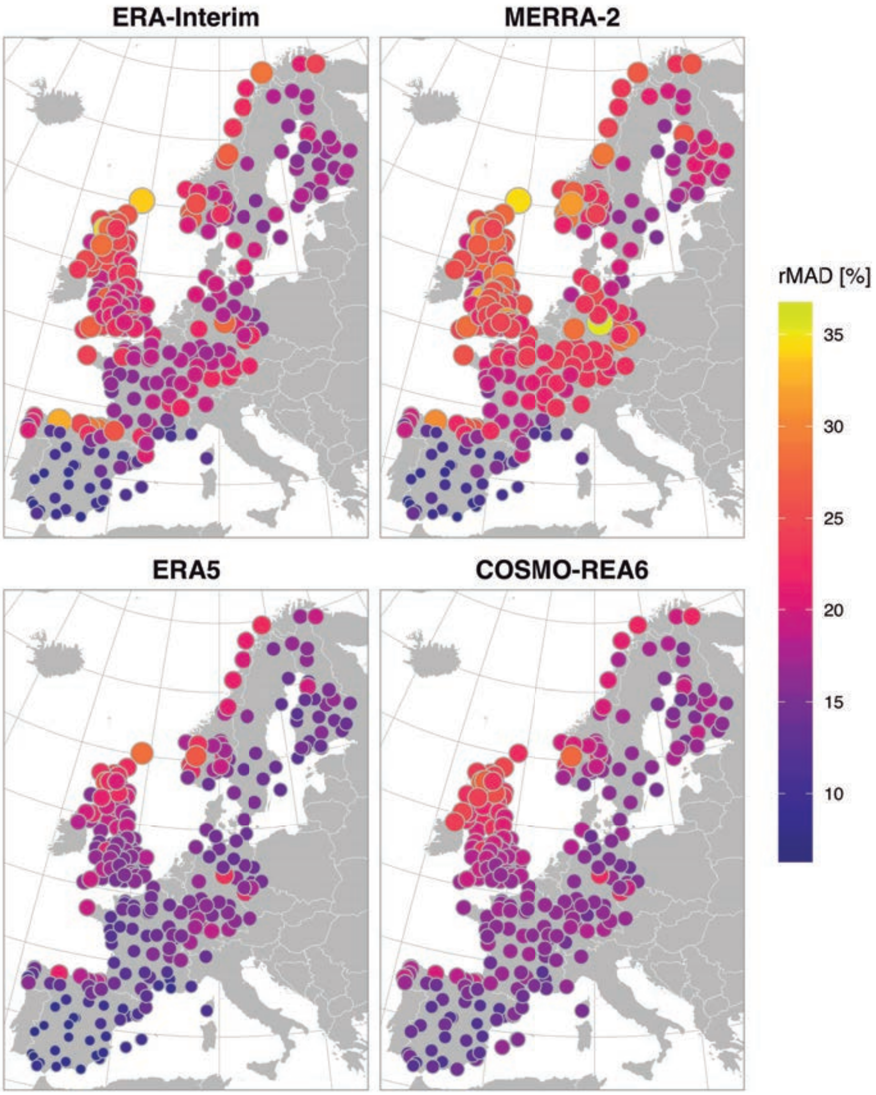

The magnitude of the *rMAD* is represented with both color and size.

All reanalyses showed a strong degradation in the mountains (Table 5.4). Similarly to the degradation on the coast, this was caused by using coarse spatial grids (30-80 km) that are inadequate to model local climates. Contrary to satellite-based products, reanalyses showed strong positive biases in mountainous areas. This was probably caused by an increased overestimation under cloudy conditions due to the characteristic high-cloudiness of mountains. Besides, the coarse grids of global reanalyses make that both, mountains and the surrounding flat regions, were included within the same pixel. Thus, the spatial average given by the pixel overestimates the irradiance compared to measurements made in the mountains, where the irradiance is typically lower than in flat areas.

Comparison of irradiance maps

As above-mentioned, the comparison of spatial estimates against ground measurements has several limitations. Large deviations may be obtained by databases with coarse grids over areas with steep irradiance gradients such as mountains or coastal regions. These uncertainties cannot be attributed to the underlying physics of reanalysis models. Thus, a second evaluation was made by directly comparing raster files from reanalyses against those from satellite-based products. Specifically, SARAH PVGIS was used as the reference over Europe due to its superior quality compared to reanalyses. Besides, this comparison allows evaluating databases in regions with low density of ground stations. The differences between gridded products were calculated at the original horizontal resolution of each product. Other authors remapped the product with higher resolution to the coarser spatial grid [120]. However, we intended to show the variation of the irradiance within a single pixel of coarse grids emphasizing the limitations of these grids in some particular regions.

In Europe, SARAH PVGIS showed a fairly low bias within ±5 W/m^2 at 74 % of European stations (Fig. 5.21). Therefore, if the difference between a reanalysis product and SARAH (Fig. 5.30) is outside this range, it is an indication that the accuracy of said product is low in that region. ERA5 exhibited the lowest deviations with values within ±5 W/m^2 in most of Europe, while the negative deviations observed in Southern Europe suggest that ERA5 is even able to correct the overestimation of SARAH there. Overall, the annual biases of both products were comparable in flat and cloudless European regions. Deviations were larger and generally positive in coastal regions due to the coarse resolution of reanalyses, and in the mountains, but here the bad performance of SARAH hinders an adequate analysis of ERA5. The underestimation of COSMO-REA6 increased with decreasing latitude exceeding -20 W/m^2 in Spain and Italy and is even higher in the southern edge of the grid. This is most likely caused by the underestimation under clear conditions caused by the excess of aerosols mentioned above. However, the differences between COSMO-REA6 and SARAH did not increase on the coast, while deviations remain within ±5 W/m^2 in Northern Europe and are comparable to those of ERA5.

FIGURE 5.30: Map of the difference in mean G_H between reanalysis databases and SARAH PVGIS (2010-2014).

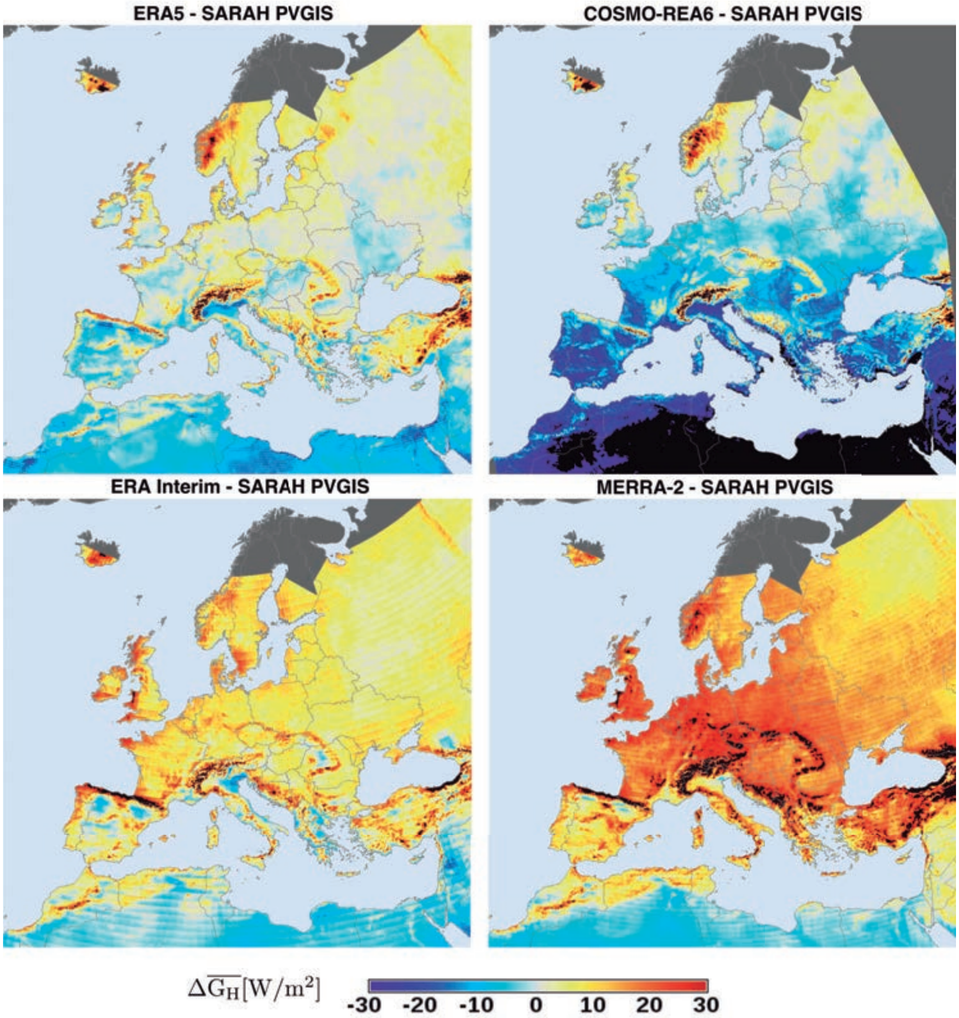

The color scale is limited to ±30W/m^2; larger differences are shown as black. Areas not covered by SARAH PVGIS are shown as dark grey.

Fig. 5.30 also evidences the significant reduction of the bias from MERRA-2 and ERA-Interim to ERA5. MERRA-2 showed the most substantial differences overall, especially in Central and Northern Europe with positive differences around +20 W/m^2. These positive differences were smaller in ERA-Interim, being around +10 W/m^2 for most of Europe, but these values are still considerably larger than those of ERA5. Besides, the increase of the differences in coastal areas of northern Spain, Wales, Scotland, and southern Sweden, was more pronounced for ERA-Interim than for ERA5. This moderate improvement on the coast proves the benefits of the finer grid used by ERA5 (~31 km) compared to that of ERA-Interim (~81 km).

5.2.2 Worldwide validation

The worldwide dataset of BSRN stations was used to compare satellite-based and reanalysis databases over a wider region. BSRN stations cover all continents and climatic regions, and some of them are located at particular areas such as high mountains, extreme latitudes, small islands, or arid regions, where solar radiation models typically present larger uncertainties. Therefore, the performance statistics at BSRN stations (Table 5.5) were generally worse than those at European stations (Table 5.3 and 5.4). Similarly to the validation over Europe, the statistics for stations located in the mountains were reported separately. In this case, only Izaña (IZA, 2373 m) was located in high mountains. The statistics for the stations covered by NSRDB PSM and SARAH PVGIS were also calculated for benchmarking against these databases.

TABLE 5.5: Summary statistics of daily G_H at BSRN stations (2010-2014).

		MBD [W/m^2]	rMBD [%]	MAD [W/m^2]	rMAD [%]	RMSD [W/m^2]	rRMSD [%]
All 40 stations	MERRA-2	11.34	7.12	30.17	18.37	43.12	26.79
	ERA-Interim	10.04	6.12	28.29	17.32	40.58	25.38
	ERA5	4.52	2.96	23.13	14.19	33.06	20.76
SARAH coverage 13 stations	MERRA-2	17.49	11.81	27.75	18.15	40.77	27.00
	ERA-Interim	8.88	6.70	24.45	16.12	35.89	23.96
	ERA5	0.80	1.31	20.99	13.57	30.47	19.88
	SARAH PVGIS	0.74	-0.17	13.46	8.55	19.74	12.74
NSRDB coverage 13 stations	MERRA-2	15.56	8.18	30.42	16.19	42.72	22.79
	ERA-Interim	14.14	7.77	29.26	15.71	41.79	22.43
	ERA5	6.30	3.43	22.36	11.93	31.56	16.82
	NSRDB-PSM	1.76	0.61	17.46	9.38	24.68	13.33
Mountains 1 station	MERRA-2	-33.63	-11.91	46.15	16.37	53.28	18.90
	ERA-Interim	-47.76	-16.92	60.51	21.46	70.17	24.89
	ERA5	-43.11	-15.27	51.93	18.41	58.88	20.88
	SARAH PVGIS	-72.24	-25.67	75.25	26.75	100.09	35.58

Overall, the statistics at BSRN stations were in concordance with those over Europe. Satellite-based databases showed both the smallest annually-aggregated bias (Table 5.5) and the most homogeneous distribution of the bias (Fig. 5.31) worldwide as well. The bias was also low for ERA5 ($rMBD$ = +4.52%) corroborating its improvement over previous global reanalyses. ERA5 showed a spatially homogeneous bias, with an average $rMBD$ comparable to that of SARAH PVGIS (1.31% vs. -0.17%) and NSRDB PSM

(3.43% vs. 0.61%) in the areas covered by Meteosat and GOES satellites, respectively. ERA5 only showed large positive deviations in coastal regions and small islands. This was the case of Lerwick ($rMBD$ = +19.2%) and Ny-Ålesund ($rMBD$ = +24.2%), two high-latitude islands, and Kwajalein ($rMBD$ = +18.9%), a coral atoll comprising 97 islands and islets with a total land area of 16 km^2.

FIGURE 5.31: Distribution of $rMBD$ in daily G_H at BSRN stations.

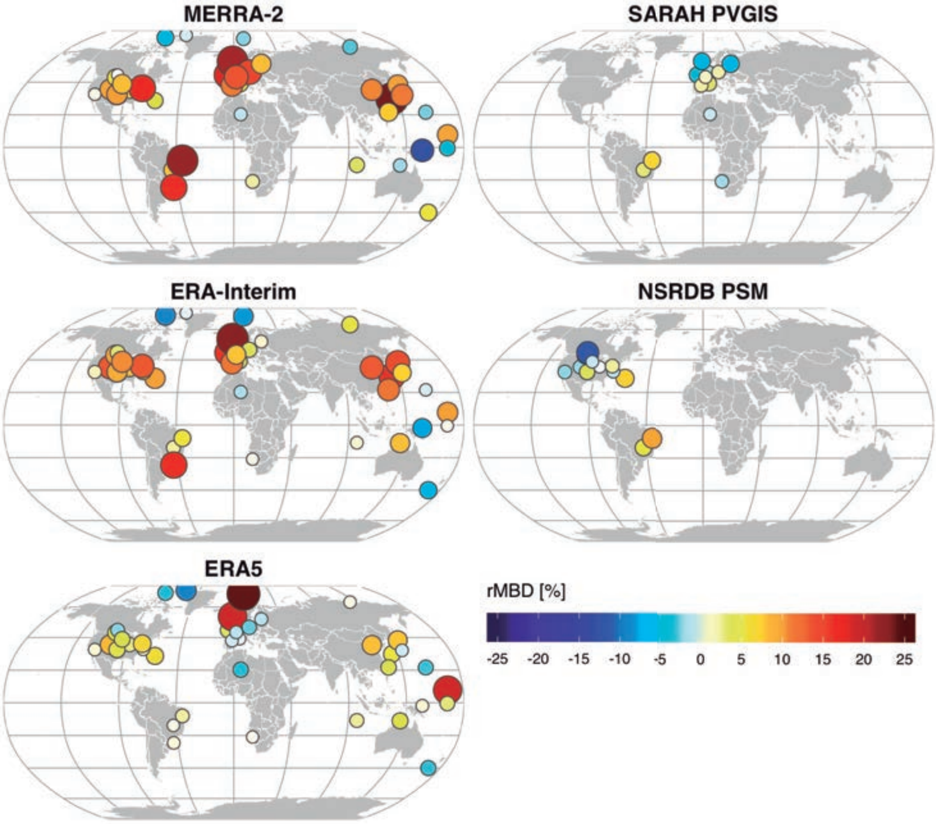

The magnitude of $rMBD$ is represented with both color and size.

The validation against BSRN stations confirmed that ERA-Interim and MERRA-2 present strong positive biases not only over Europe but also globally. ERA-Interim and MERRA-2 obtained the largest bias (+14.14% and +15.56% respectively) and the most heterogeneous distribution of the bias (Fig. 5.31). Similarly to ERA5, the overestimation increased in coastal regions and small islands due to the coarse spatial grids of global reanalyses. However, both ERA-Interim and MERRA-2 systematically overestimate G_H also over flat areas in North America, Europe, South America, and China. The source of the positive biases may vary for each database and region, but the most likely cause may be an underestimation of cloud coverage in regions with high cloudiness, e.g., South America, and the prediction of too few aerosols in regions with high aerosol contents, e.g., China.

FIGURE 5.32: 2D density plot of relative deviations of daily G_H (estimations minus measurements) against K_T at BSRN stations.

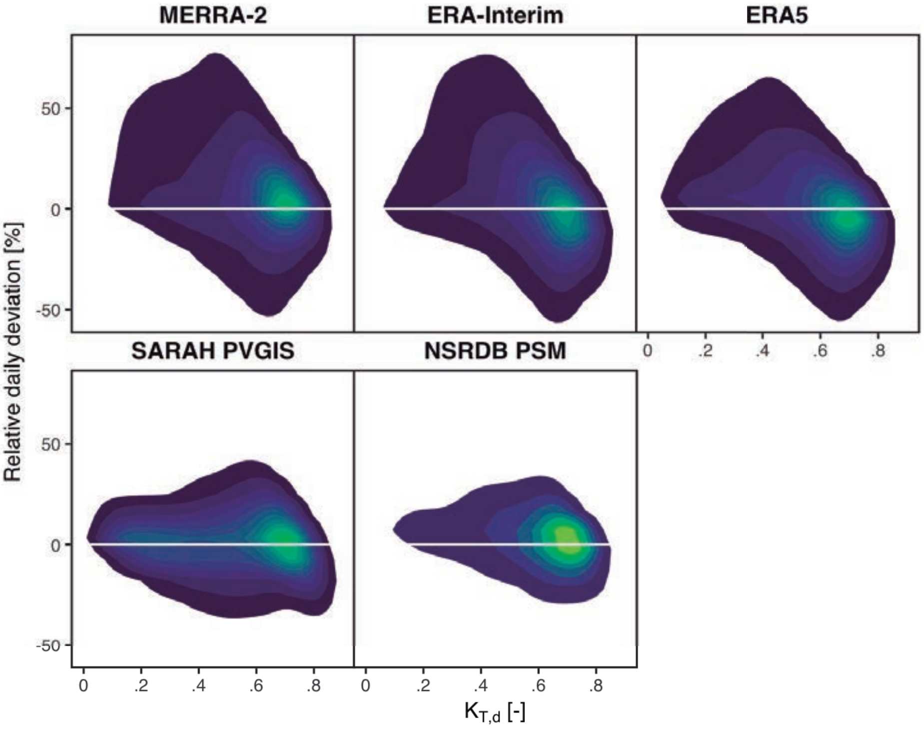

Plots are generated with a 2D binned kernel density estimate.

The distribution of daily deviations against K_T (Fig. 5.32) corroborated that the main difference between satellite-based and reanalysis models is the quality of cloud predictions. Note that the density plots of satellite-based products were calculated only with the stations covered by the product. Nonetheless, all reanalyses presented a similar distribution of the deviations against K_T, with positive and negative deviations under cloudy and clear conditions, respectively. On the other hand, deviations of both satellite-based products did not show any specific dependence with atmospheric transmissivity. In ERA5, these deviations average out in annually-aggregated bias, leading to a moderate *rMBD* worldwide. In ERA-Interim and MERRA-2, positives biases under cloudy conditions caused by an underestimation of clouds were stronger, causing the strong positive biases obtained by these products. These deviations did not cancel out in annually-aggregated absolute errors leading to substantially larger *MADs* and *RMADs* in the three reanalyses than in satellite-based databases (Fig. 5.31). These differences are expected to increase even more for sub-daily estimations.

FIGURE 5.33: Distribution of *rMAD* in daily G_H at BSRN stations.

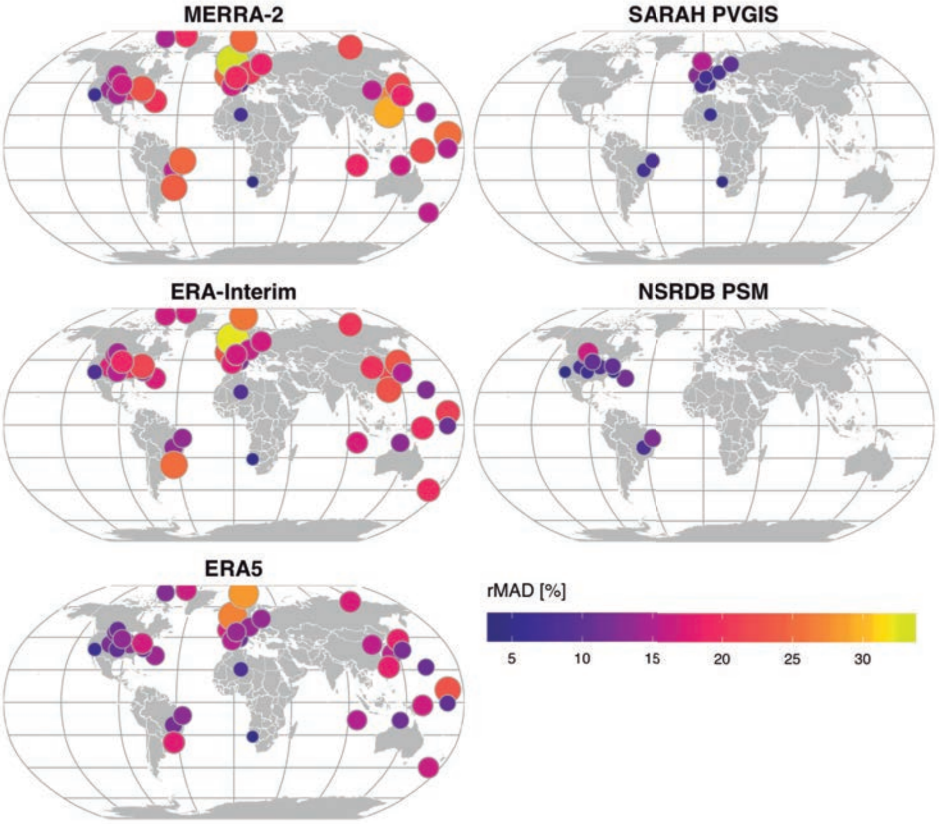

The magnitude of *rMAD* is represented with both color and size.

All databases showed a striking underestimation at Izaña (IZA), which was the only BSRN station in the mountains. Izaña is located in the Tenerife island (2034 km^2) at 2373 m, in the surroundings of Teide volcano (3718 m). The station is above the subtropical temperature inversion layer and affected by a quasi-permanent subsidence regime [205], so clouds typically affect the lower part of the island (below 2000 m) while clear conditions prevail in the upper area. These particular conditions aggravate the underestimation of satellite-based products. SARAH PVGIS pixels may include both lower and upper parts of the island, underestimating the irradiance of the upper parts, where IZA is located, due to the presence of clouds in the lower parts.

Maps of average irradiance were compared using SARAH PVGIS and NSRDB as the reference in areas covered by Meteosat and GOES satellites, respectively. Differences between global reanalyses and NSRDB (Fig. 5.34) shared a similar pattern, with positive deviations in North America and high negative differences in Central and South America. In North America, NSRDB biases at BSRN stations were the smallest overall. Thus, positive differences observed are most likely the consequence of the overestimation of the three reanalyses. The smallest deviations were obtained by ERA5 with values generally within ±5 W/m^2 except for the Rocky Mountains and the Great Lakes. The differences between ERA5 and NSRDB are particularly low in flat regions such as the Great Plains and the West Coast.

The deviations of all products were higher in the area covered by GOES West than in the area covered by GOES East. The maps show a clear discontinuity along the 105°W longitude line, which lies between the nadir points of the two satellites used to calculate the NSRDB. The magnitude of this discontinuity is substantially smaller than that of the reanalysis validation errors, making its impact on the results negligible. However, it serves to illustrate that the deviations shown here are not exclusively due to the reanalysis products. This discontinuity may be related to the degradation of models derived from geostationary satellite images near the edge of the images. The most likely cause of NSRDB discontinuity is the parallax effect, which makes that clouds appear displaced when viewed from shallow angles [81].

The differences became more complex in Central and South America due to the uncertain performance of NSRDB in this region. The number of BSRN stations to validate the databases was too low. Besides, NSRDB showed strong positive biases in the few BSRN stations available, while NSRDB and SARAH PVGIS estimations differed in the South American region covered by both databases. Hence, differences against NSRDB in South America should be interpreted with caution. The negative differences obtained by ERA5 in western Brazil then indicate that ERA5 has a smaller bias than NSRDB there, as it occurs at Brazilian BSRN stations.

FIGURE 5.34: Map of the difference in annual G_H (2010-2014) between reanalyses and NSRDB PSM (GOES coverage area) and SARAH PVGIS (Meteosat coverage area).

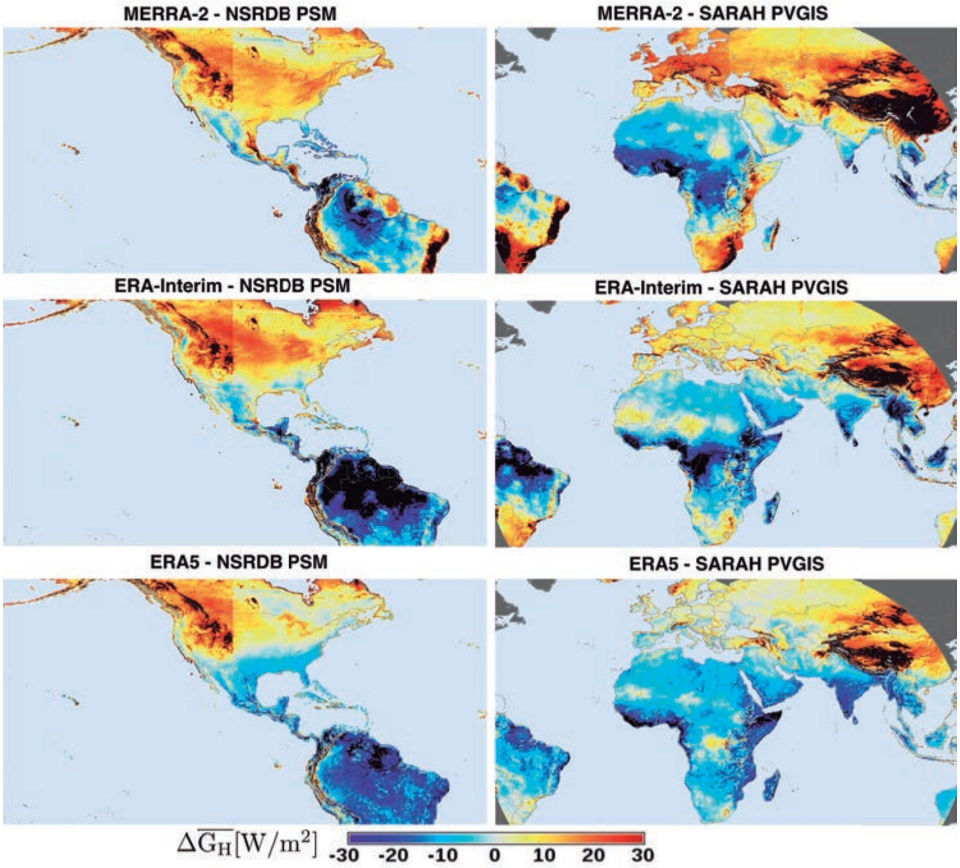

The color scale is limited to ±30W/m^2; larger differences are shown as black. Areas not covered by SARAH PVGIS are shown as dark grey.

However, this cannot be extrapolated to all of South America due to the lack of ground data. A pattern shared by differences with respect SARAH and NSRDB in South America is the strong negative deviations exceeding -20 W/m^2 in the Amazon Basin. This area belongs to the Inter Tropical Convergence Zone (ITCZ), which is a belt that encircles the Earth near the equator. The most likely cause of these negative deviations is the overestimation of the clouds in the ITCZ, a region that already has a high frequency of clouds [109]. Fig. 5.34 also depicts a discontinuity in the set of pixels that cover both water and land. For instance, high negative differences are observed in MERRA-2 on the coasts of Central America, while ERA5 shows a positive deviation on the West coast of North America. These discontinuities caused the high bias obtained at coastal stations and corroborate the limitations of reanalysis in those regions.

The differences between reanalyses and SARAH PVGIS also showed a discontinuity at the border between METEOSAT Prime and METEOSAT East, though it is somewhat less pronounced than in NSRDB PSM. ERA5 presented again the smallest deviations within ±5 W/m^2 over most of Europe, Central Asia, and South Africa. The most considerable differences were obtained in regions of the ITCZ such as the Guinean Gulf, West Africa, and India. This corroborates the limitations of reanalysis models in the ITCZ in particular, and in regions with frequent occurrence of clouds in general. On the other side, largest positive deviations were observed in the Tibetan Plateau and China. The positive bias for the Tibetan Plateau agrees with the ones obtained in other mountain ranges such as the Alps, the Pyrenees, the Rocky Mountains, or the Andes, while the overestimation over China may be related to the underestimation of clouds and anthropogenic aerosols reported by Zhang et al. [109]. In general, the maps evidence that the average irradiances from ERA5 and SARAH are comparable mostly for flat regions with a low occurrence of clouds.

5.2.3 Strengths and weaknesses of satellite-based and reanalysis databases

Databases derived from geostationary satellites are the best alternative to ground measurements for assessing the solar resource when long-term data are required. They provide spatially continuous estimates since the 1980s with a high spatiotemporal resolution (~3-5 km, ~15-30 min). Besides, they present the lowest uncertainty among estimation methods. Compared to reanalyses, their strength lies in their accurate prediction of clouds from geostationary satellites images. Clouds were traditionally predicted with empirical corrections using images from visible channels; such is the case of Heliosat-based models. However, new satellite-based models are replacing empirical corrections by RTM calculations making possible to exploit data from infrared channels, as well as to estimate the radiation components and spectral irradiance. Besides, this evolution towards physical modeling approaches enables future improvements such as including more detailed data of atmospheric constituents, which may bring the quality of satellite-based data even closer to that of ground measurements.

One of the main limitations of databases based on geostationary satellites is their spatial coverage. This is primarily a problem in high latitudes because none geostationary satellite covers latitudes above ±65°. Other minor limitations are their large uncertainties over bright surfaces, near the edge of satellite images, and in mountainous regions. Satellite-based models show large errors over bright surfaces, and particularly over snow-covered areas, because both clouds and snow have similar reflectivities leading to the over-prediction clouds. In this respect, the latest snow detection algorithms are including thermal data from infrared channels to better differentiate between clouds and snow. Uncertainties of satellite-based models also increase at the edge of satellite images due to the shallow viewing geometries. Empirical corrections based on the satellite viewing angle such as the one included by SARAH-2 can mitigate these deviations. The performance of satellite-based models also deteriorates in the mountains because their spatiotemporal resolution is not enough for modeling the steep irradiance gradients in rough terrains. The spatiotemporal resolution of the databases is limited by that of geostationary satellites, so the solution might be to increase the resolution of ancillary datasets such as aerosols or water vapor. In this line, SARAH-2 improved from SARAH-1 in the Alps and Pyrenees due to the use of a downscaled water vapor dataset.

Estimations based on polar-orbiting satellites may be a valid alternative to those based on geostationary satellites in high latitudes because they have global coverage and acceptable quality. However, their global coverage comes at the expense of a lower temporal resolution because each polar-orbiting satellite passes over a specific equatorial region just twice a day. Currently, from 4 to 6 polar-orbiting satellites are distributed at different equatorial crossing times, but the number of satellite images available each day to calculate cloud coverage is substantially lower than that from a single geostationary satellite. This is why the temporal resolution of databases based on polar-orbiting satellites is limited to daily values making them inadequate to applications requiring sub-daily data, such as the simulation of PV systems. This low temporal resolution also explains why the absolute error and uncertainty of polar-orbiting databases are higher than those of geostationary databases, especially at a daily level. Nonetheless, databases based on polar-orbiting satellites are the best alternative to those based on geostationary satellites if sub-daily data is not a requirement.

Global atmospheric reanalyses are another alternative to satellite-based models that provide hourly irradiance globally, including the poles, and estimate many other climatic variables such as temperature, wind speed, or humidity. Moreover, global reanalyses are developed by meteorological agencies and are generally free, in contrast to some satellite-based databases produced by private companies. This makes reanalyses an attractive option for applications such as the simulation of PV systems that require temperature and wind speed data in addition to surface irradiance. However, the accuracy of reanalyses is substantially lower than that of satellite-based models. This is mainly caused by their coarse spatial resolution and inadequate modeling of clouds. Global reanalyses have resolutions of around 30-80 km producing large uncertainties in regions with high irradiance variability such as coastal regions, small islands, and mountains. Besides, their main difference compared to satellite-based models is that they tend to overestimate under overcast conditions and underestimate under clear conditions due to cloud-related errors. Whereas satellite-based models specifically use satellite images each 15-30 min to predict clouds, cloud predictions in reanalysis are one of the many outputs that the NWP model produces after assimilating different sources of satellite and ground observations. However, reanalyses do not assimilate irradiance observations, so irradiance estimations are pure predictions from the NWP model. These limitations are particularly accentuated in reanalyses such as MERRA and ERA-Interim, where a significant under-prediction of clouds under cloudy conditions led to positive annual biases worldwide. ERA5 partly corrects this issue because it showed a similar overestimation and underestimation under cloudy and clear conditions, respectively, which average out leading to moderate annual biases similar to those of satellite-based databases. However, these intra-annual deviations do not cancel out when calculating absolute errors. Thus, the absolute error of ERA5 is still substantially larger than those of satellite-based databases.

Regional reanalyses correct some of the limitations of global reanalyses due to their high spatial resolution, which is similar to that of geostationary satellites, and the use of NWP models tailored for the specific area covered by the database. This results in a decreased degradation of the estimations in coastal or mountainous regions, but it comes at the expense of losing the global coverage. Besides, COSMO-REA6 has the same cloud-related errors as global reanalyses. Overall, COSMO-REA6 had a similar performance to ERA5 in Europe with a moderate annual bias and a large absolute error. However, COSMO-REA6 showed a negative bias in G_H driven by the strong underestimation under clear conditions caused the overestimation of aerosols.

Different a posteriori corrections of reanalysis databases have been developed to address the dependence of their deviations on cloudiness. Zhao et al. [111] corrected MERRA and NARR against ground measurements as a function of K_T and surface elevation. Jones et al. [128] corrected ERA-Interim against the satellite-based database Helioclim 3v5 using quantile mapping, which consists on adjusting the cumulative distribution function of ERA-Interim to that of Helioclim. Frank et al. [181] corrected COSMO-REA6 against ground measurements as a function of K_T, α_s, and the month of the year. They developed specific corrections for low ($K_T > 0.5$) and high ($K_T < 0.5$) cloudiness. All these corrected versions showed a substantial reduction of the bias. However, absolute errors barely decreased, even worsening at some locations because an incorrect cloud prediction cannot be fully corrected a posteriori. Bias-corrected databases might be a temporary solution to mitigate the impact of data with high bias, but the ultimate solution should be the improvement of cloud predictions.

Overall, former global reanalyses such as MERRA, MERRA-2, and ERA-Interim should be generally avoided and only used to fill gaps in ground measurements or satellite-based databases [23]. New reanalyses such as ERA5 and COSMO-REA6 have substantially improved former versions and are a valid alternative to satellite-based models in regions where those are missing. Still, these databases must be used knowing their limitations [24]; primarily their large uncertainties in regions with high cloudiness and places with steep irradiance gradients such as mountains, coasts, or small islands.

5.3 Uncertainty in annual global horizontal irradiance

After the evaluation of measured and estimated G_H data separately, the bias and annual uncertainty (u_{95}) in both sources of data were quantified under a common framework. The Spanish dataset was used because it is composed of a dense and diverse network of pyranometers to calculate the uncertainty statistically.

5.3.1 Uncertainty of estimations (radiation databases)

In general, the performance of radiation databases over Spain was similar to that observed over Europe. The main difference was that the validation in Spain includes an estimation of the annual uncertainty, giving an idea of the dispersion of deviations. Satellite-based products exhibited both the smallest bias and uncertainty (Fig. 5.35), with mean biases of +1.4 and -1.6% for SARAH-1 and CLARA-A1, respectively. The bias of ERA5 was similar to those of satellite-based databases (+1.3%), but ERA5 showed a greater annual variability ($^{+10.6}_{-5.5}$%). This is because ERA5 had positive and negative deviations under cloudy and clear conditions, respectively, due to a deficient modeling of clouds. These deviations cancel out in the

FIGURE 5.35: Relative deviations in annual G_H between radiation databases and AEMET secondary standard pyranometers.

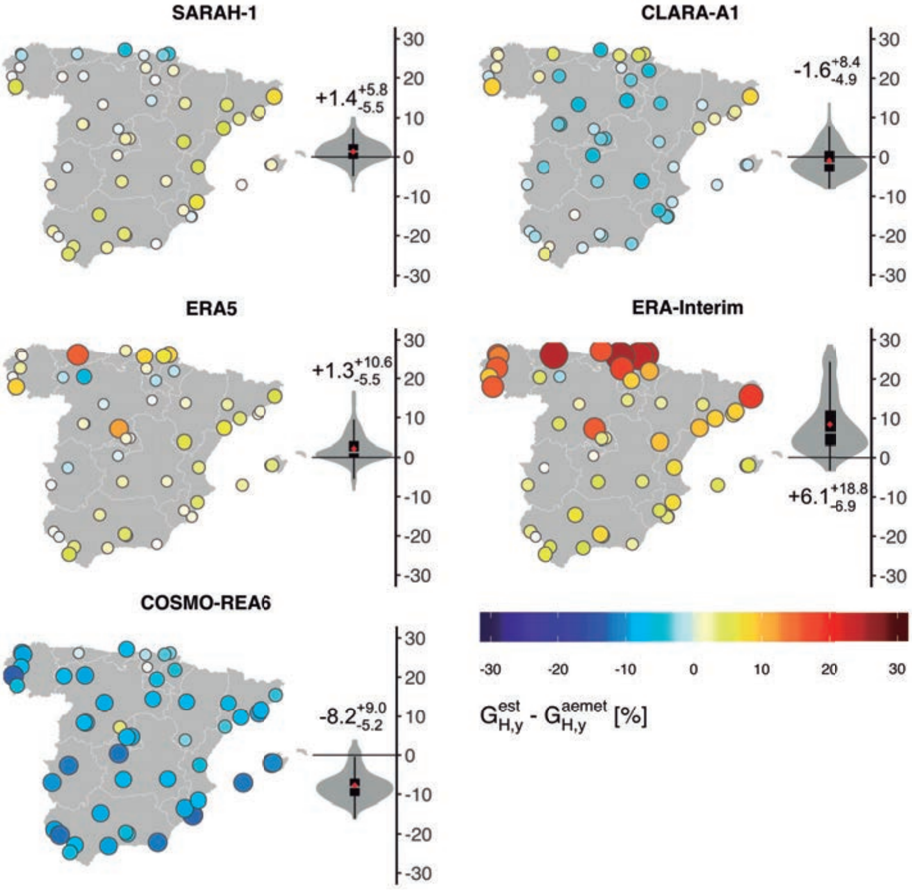

Violin plots outline the kernel probability density. Boxplots visualize the lower quartile, median and upper quartile. The red diamond represents the mean.

annual bias but increase the uncertainty of annual estimations. This increase will be even more significant for daily or hourly estimates. COSMO-REA6 showed a somewhat smaller uncertainty than ERA5, probably due to the attenuation of errors at coastal and mountain locations thanks to the higher resolution of COSMO-REA6. However, COSMO-REA6 had the largest bias over Spain (-8.2%) because the high frequency of clear conditions aggravates the underestimation due to the excess of aerosols. ERA-Interim exhibited a large positive bias and the most significant variability, with annual biases exceeding +20% on the Atlantic coast. The overall positive bias of +6.1% was driven by the underestimation of clouds under overcast conditions, whereas the large uncertainty was attributed to the coarse resolution of ERA-Interim (~81 km).

Uncertainties in estimated irradiance depend on the characteristics of the database. The strongest influencing factor is the type of modeling approach, with reanalyses showing larger uncertainties than satellite-based models. Another critical factor is the quality of estimations of the atmospheric components, mainly clouds, but also aerosols and water vapor. For example, the positive bias of ERA-Interim and the large variability of all reanalyses were driven by the incorrect modeling of clouds, whereas the underestimation of COSMO-REA6 was caused by the use of a deficient aerosol climatology. Significant differences were also observed between databases using similar models. For instance, the increase in the spatiotemporal resolution from ERA-Interim to ERA5 led to a substantial reduction in the bias and uncertainty.

The uncertainty of a particular database also changes spatially. This is one of the main differences between measurements and estimations. Despite some measuring errors aggravate under specific climatic conditions, the uncertainty of pyranometers varies spatially significantly less than that of radiation databases, especially if the sensor is properly calibrated and maintained. On the contrary, all regions covered by a database do not show the same uncertainty. Satellite-based models have large uncertainties in the mountains, over bright surfaces, and near the edge of satellite images [199], whereas the uncertainty of reanalyses increases in the mountains, coastal regions, and areas with high cloudiness.

5.3.2 Uncertainty added by operational defects

The bias and uncertainty added by operational defects were calculated based on the differences between measurements from stations showing defects and SARAH-1 (Fig. 5.36). Note that these differences are negatively biased because they include the bias and uncertainty of SARAH-1 ($+1.4^{+5.6}_{-5.3}\%$). The exact magnitude of operational defects is shown in Subsection 5.3.4 after removing the bias and uncertainty of SARAH-1. In any case, deviations added by operational errors are substantially larger than those of SARAH-1, justifying the use of SARAH-1 as the reference.

The annual bias added by operational defects increased with the duration of the defect and its intensity. Most operational failures introduced large annual differences around ±10%, while some severe cases exceeded ±30%. Differences were generally negative except for some stations with an incorrect leveling of the pyranometer or large errors. Shading, which was the most common defect at Spanish weather stations, resulted in negative differences (bias = -9.4%) that exceeded -30% in extreme cases. Stations with soiling and defects of unknown cause, which most likely are

FIGURE 5.36: Relative deviations in annual G_H between measurements with operational defects and SARAH-1.

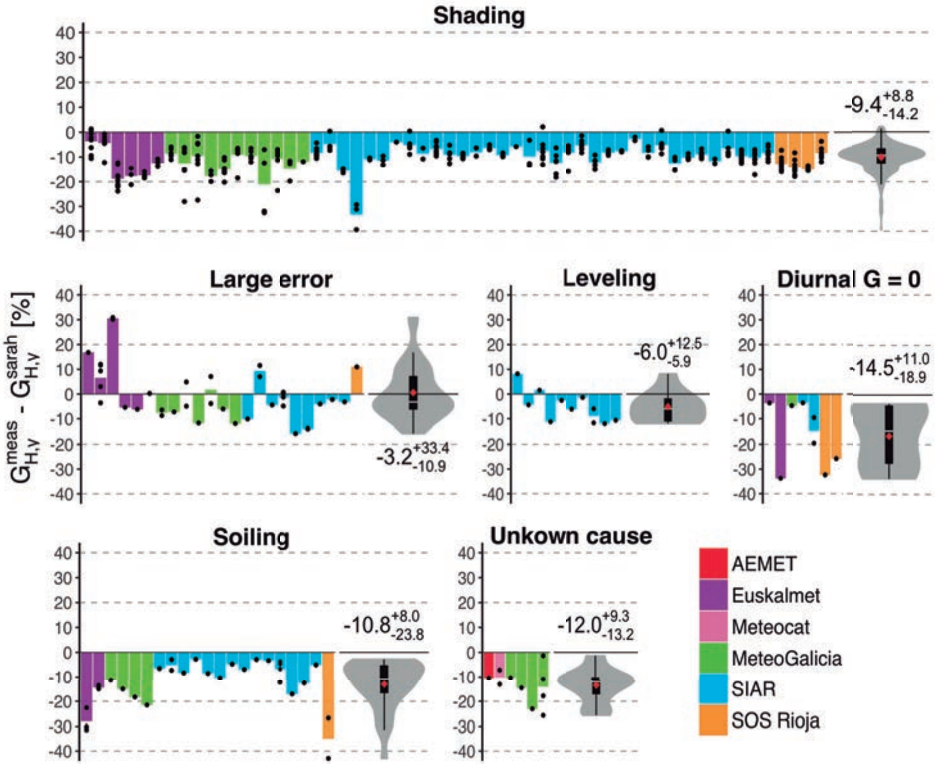

Deviations were calculated in stations and years with defects. Violin plots outline the kernel probability density. Boxplots visualize the lower quartile, median and upper quartile. The red diamond represents the mean.

low-intensity soiling errors, also showed similar negative biases (-10.8% and -12%, respectively). Large errors produced either positive or negative deviations, explaining the high variability obtained in these stations ($^{+33.4}_{-10.9}$%). Large errors shown in Fig. 5.36 only included stations with daily values within $-200 < G_H < 500$ W/m^2, but more extreme values were obtained at some Euskalmet stations. An incorrect leveling of the sensor can also lead to positive differences when the pyranometer is tilted towards the sun. The largest negative bias was introduced by diurnal periods with $G_H = 0$ (-14.5%), which is a particular case of large error. This value was calculated without taking into account two SOS Rioja stations with $G_H = 0$ all year round. All defects showed a high variability as a consequence of the different severity and duration of the defects. While the whole year was typically affected in the case of shading, some cases of electronic errors lasted just a few days or hours, having different impacts in the annual G_H.

5.3.3 Uncertainty of pyranometers (equipment errors)

The direct comparison of SIAR photodiodes against AEMET secondary standard pyranometers showed that significant differences exist between the annual G_H provided by both types of sensors (Fig. 5.37). The deviations showed high variability ($^{+7.1}_{-5.6}$%), with 56% of annual differences out of the ±1.5% uncertainty interval of secondary standards, while 15.3% of annual differences exceeded ±5%. The bias was predominantly positive (+0.7%) though some photodiodes also showed negative biases. However, the most relevant aspect was the high inter-annual variation of the bias (Fig. 5.38). A sharp change was observed in many photodiodes from 2009 to 2011: photodiodes overestimated annual G_H by around +2.5% from 2007 to 2009, and they underestimated it by around -1% from 2011 to 2013. A recalibration of SIAR photodiodes most likely caused this sharp decrease in annual G_H. Note that some SIAR stations are maintained by the central government and some others by each regional government, so calibration procedures and dates may differ between groups of stations. Some of the inter-annual variations might also be caused by the different performance of photodiodes with the amount and type of irradiance received each year, but they have a smaller order of magnitude than changes in the calibration constant.

FIGURE 5.37: Comparison between SIAR photodiodes and AEMET secondary standards separated by less than 20 km.

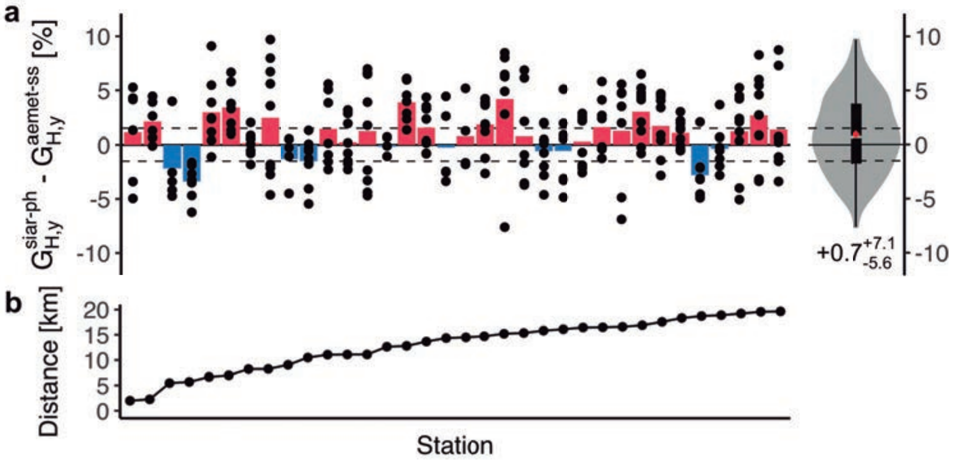

(a) Relative deviation in annual G_H between SIAR photodiodes and AEMET secondary standards. (a) Distance from SIAR photodiodes to the closest AEMET station. The dashed line depicts the uncertainty of secondary standard pyranometers. Violin plots outline the kernel probability density. Boxplots visualize the lower quartile, median and upper quartile. The red diamond represents the mean.

Differences in Figs. 5.37 and 5.38 included the uncertainty of secondary standard pyranometers and additional uncertainties because the sensors compared are not exactly in the same place. The uncertainty of secondary standard pyranometers was removed in Subsection 5.3.4 observing small changes from the values reported in the current section. This suggests that the use of AEMET stations as the reference is acceptable. Besides, no trend, neither in the bias nor the variance, was observed with increasing distance. Some of the largest differences were actually obtained between pairs of sensors closer than 8 km (Fig. 5.37). In addition, agricultural stations are typically installed in low-lying areas with a low spatial variability of irradiance, which means that the spatial representativeness of these stations is high. This suggests that the uncertainty of the comparison is low so the differences observed between photodiodes and secondary standards actually exist.

FIGURE 5.38: Inter-annual variation of the relative deviations in annual G_H between SIAR photodiodes and AEMET secondary standards separated by less than 20 km.

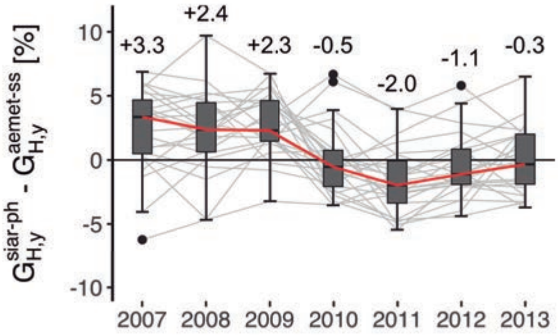

The 24 pairs of stations visualized have valid annual values for all the years in the period 2007-2013. Grey lines show the inter-annual variation for each pair of stations. The red line visualizes the median. The black dots are extreme cases lying beyond 1.5 times the interquartile range (length of the whiskers).

Different factors could be behind the differences observed in photodiodes. The main sources of uncertainty in photoelectric detectors are the spectral response, cosine error, temperature dependence, and linearity. Reda [39] estimated that the contributed uncertainty of each of these defects was 5%, 2%, 1%, and 1%, respectively. Driesse et al. [36] analyzed the individual impact of linearity, spectral response, temperature, and the angle of incidence on photodiode and thermopile pyranometers. They found positive errors up to +2% for high temperatures, up to +3% for medium and low angles of incidence, and up to +2% for high irradiances, while negative errors up to -3% were observed only for low irradiances. Similarly, Sengupta et al. [38] found an overprediction of photodiode pyranometers when compared to secondary standard sensors in the morning and the afternoon. Both studies emphasized the spectral limitations of photodiodes. The spectral response of silicon is limited to the range 350-1100 nm, which includes about 70-75% of the total energy [206], whereas 96% of broadband irradiance is received from 300 to 3000 nm. Thus, photodiodes include empirical corrections to estimate the broadband irradiance from the narrowband measurement, but problems arise when the part of the spectrum not seen by the sensors varies non-linearly. This occurs with changes in aerosol and water vapor concentrations, as well as with intra-daily and intra-annual variations of the sun elevation angle that modify the dominant scattering process in the atmosphere.

Previous defects introduce systematic deviations that can be mitigated using empirical correction functions. Ideally, these corrections should be applied individually per defect, type of sensor, and location after side-by-side comparisons with a reference radiometer. The calibration should last at least 1-2 months [42, 44] to include different atmospheric conditions. Photodiodes should be recalibrated every 2 years to mitigate the effects of sensitivity drifts [19]. Previous studies have reported that the uncertainty of uncorrected photodiodes oscillates within 5-10% for 1-min values, doubling that of corrected ones that are generally below 5% [44]. Al-Rasheedi et al. [44] obtained 91% of G_H measurements within ±5%, Vuilleumier et al. [186] reported an uncertainty of ±10% for presumably uncorrected photodiodes installed at Payerne, and Wilbert et al. [43] found that the uncertainty was reduced from 5.2% to 2.2% using empirical corrections [43]. All these values refer to 1-min records of G_H, which hinders the comparison with our study where only daily and annual uncertainties are reported. Besides, we did not carry a side-by-side validation against a reference instrument, which increases the uncertainty in our results.

Nonetheless, annual deviations obtained in this study are clearly larger than those reported in previous works. This may be partly explained by the distance between the SIAR and AEMET stations compared and the own uncertainty of AEMET stations, but these two factors alone cannot explain the large deviations obtained. The presence of undetected operational errors in SIAR photodiodes is also unlikely because the comparison was made after excluding the group of 56 doubtful photodiodes flagged by the BQC. Therefore, the high uncertainty of SIAR photodiodes compared to the values reported in previous studies may indicate that they are probably uncorrected. If corrected, it is likely to believe that general empirical corrections were applied to most SIAR sensors without taking into account the particular climatic conditions of each site. This would explain the abrupt inter-annual changes observed in several SIAR photodiodes from 2009 to 2011 and the remaining bias since then. Besides, the large deviations obtained in this group of quality-controlled SIAR photodiodes leads to the conclusion that equipment errors may also be behind most of the 56 doubtful photodiodes flagged by the BQC. Therefore, the real uncertainty of SIAR photodiodes may be even higher.

5.3.4 Comparison of the different sources of uncertainty

The uncertainty associated to radiation databases, operational errors, and equipment errors (Fig. 5.39) was calculated from the annual differences shown in previous subsections by removing the uncertainty of the reference irradiance, i.e., the uncertainty of secondary standards in the analysis of estimations and photodiodes, and the uncertainty of SARAH-1 in the analysis of operational defects. The expected uncertainty of secondary standards was used (±1.5%) [19], while the annual uncertainty of SARAH-1 was estimated from the validation against AEMET stations ($+1.4^{+5.6}_{-5.3}$%). The uncertainty of daily values was also reported, with the uncertainty of secondary standards and SARAH-1 increasing to ±2% and $^{+14.7}_{-14.9}$%, respectively. Note that the field uncertainty of secondary standards could be somewhat larger due to the presence of operational failures or an inadequate calibration. However, AEMET stations are strictly maintained and have passed the two QC tests. Besides, previous studies conducted by Vuilleumier et al. [41] and Reda [39] reported even lower field uncertainties of ±1.8% and ±2.6%, respectively, for 1-min records obtained with adequately calibrated and maintained secondary standards. Therefore, the uncertainty assumed for secondary standard seems reasonable. Besides, the changes from annual differences to annual uncertainties after removing the uncertainty in reference values were negligible, corroborating the adequacy of the reference values for each analysis.

When using solar radiation measurements, operational errors produced the largest uncertainties among all the factors analyzed. The impact of these defects should be smaller from the users' perspective because we have only used the years in which an operational error occurred. Annual biases of -8.0% and -9.4% were obtained for shading and soiling, respectively, which were widespread defects in agricultural and regional monitoring networks. These errors were mainly caused by the incorrect placement and low maintenance of the stations. What is worse, many of these errors occurred in networks with top-end pyranometers. Using high-quality pyranometers does not guarantee to obtain accurate measurements. These sensors should be only bought if strict maintenance routines can be maintained. More importantly, operational errors are generally caused by low-magnitude deviations that introduce large annual uncertainties because they persist in time. Thus, these low-magnitude defects usually pass the

FIGURE 5.39: Bias ± uncertainty (u_{95}) in annual and daily G_H.

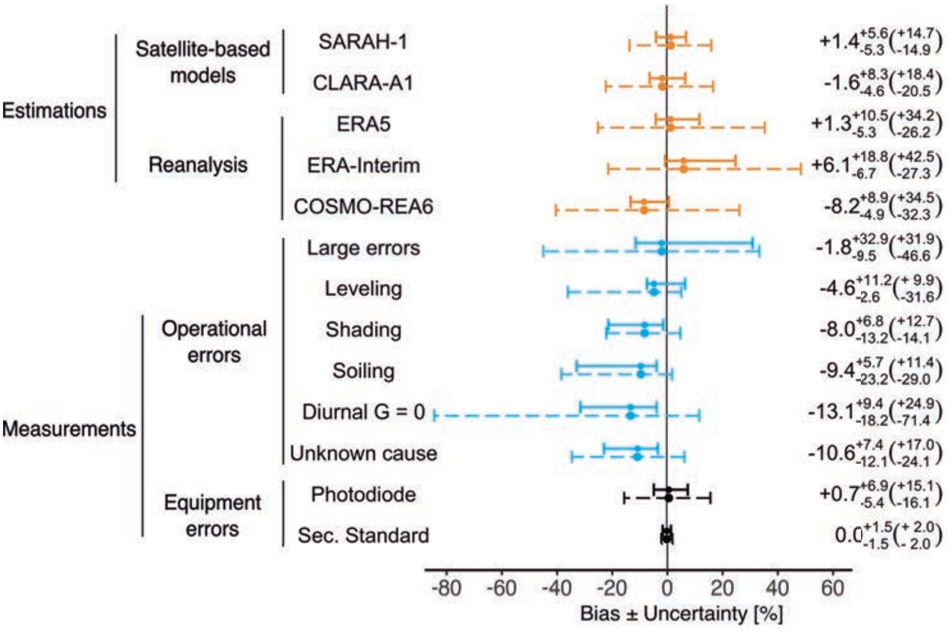

Annual and daily values are depicted with solid and dashed lines, respectively. Uncertainties for daily values are shown between parentheses.

automatic QC methods implemented by the monitoring networks and external QC procedures such as the BSRN tests. Therefore, operational errors can substantially skew solar radiation studies if the data is not quality controlled correctly.

The second largest source of uncertainty in annual G_H was due to solar radiation estimations. We observed considerable differences between reanalyses such as ERA-Interim and COSMO-REA6 (bias = +6.1 and -8.2%) and satellite-based products such as SARAH-1 and CLARA-A1 (bias = +1.4 and -1.6%). The gap between reanalysis and satellite-based products increased even more for daily estimations because the dependence of errors with cloudiness averaged out in annual values. These systematic errors in reanalysis are primarily caused by the incorrect prediction of clouds (ERA-Interim, ERA5) and aerosols (COSMO-REA6). The daily uncertainty also increased more in CLARA-A1 ($^{+18.4}_{-20.5}$%) than in SARAH-1 ($^{+14.7}_{-14.9}$%), probably due to the lower temporal resolution of polar-orbiting satellites. We confirm that satellite-based products using images from geostationary satellites, such as SARAH-1, provide the estimations with the lowest bias, uncertainty, and the most homogeneous spatial performance. New reanalysis such as ERA5 or COSMO-REA6 can be used when satellite-based data is missing but accounting for their limitations, such as their large errors in cloudy regions. Former reanalysis such as ERA-Interim or MERRA should be avoided for assessing the solar resource.

Uncertainties due to equipment errors were the smallest among all the factors compared. However, significant deviations were observed in low-cost photodiodes. The annual uncertainty of SIAR photodiodes ($^{+6.9}_{-5.4}\%$) was significantly higher than that of AEMET secondary standard (±1.5%) and similar to that of SARAH-1 ($^{+5.6}_{-5.3}\%$). The uncertainty in photodiodes would be even higher from the users' perspective because operational defects and 56 doubtful photodiodes were removed from this analysis. The daily ($^{+15.1}_{-16.1}\%$) and annual ($^{+6.9}_{-5.4}\%$) uncertainties obtained were larger than the values reported in previous studies made with photodiodes. Although part of this uncertainty could be attributed to the validation procedure, the inadequate calibration of SIAR photodiodes is the most likely cause of this high uncertainty. This suggests that poorly maintained and incorrectly calibrated photodiodes could obtain similar uncertainties than satellite-based databases such as SARAH-1. We recommend using secondary standard pyranometers when the accuracy of the results is critical, such as the validation of satellite-based products or the analysis of climate trends. If photodiodes have to be used, special care must be taken if they belong to low-quality monitoring networks because the probability of having operational errors and uncorrected sensors substantially increases.

5.3.5 Impact of measuring errors on solar radiation studies

Solar radiation measurements present the lowest uncertainty if strict measuring guidelines are followed, being therefore customarily used for applications such as analyzing climate trends, validating solar radiation models and correcting their biases, and assessing the solar resource, among others. Users sometimes take for granted the high-quality of measurements. However, previous sections evidenced that operational errors are frequent in some monitoring networks. These defects introduce significant biases and uncertainties, while photodiode pyranometers may increase this uncertainty even more. Therefore, studies based on stations showing defects might be substantially affected by the low quality of the measurements.

Validations of radiation databases are one example of a study strongly influenced by measuring errors. We have observed that the bias and uncertainty added by operational errors and some photodiodes can be similar or even higher than those of satellite-based databases. This prevents the accurate validation of the models because deviations added by defects can be mistaken for deviations of the model. Validations are made against high-quality networks such as the BSRN when low uncertainty is critical [21, 195]. However, the inclusion of data from national services and regional networks is customary to increase the density of stations for evaluating databases over specific regions. This increases the chances of introducing operational errors in the reference dataset.

FIGURE 5.40: Influence of operational defects on the annually-aggregated *rMBD* and *rMAD* of SARAH PVGIS at European stations with defects.

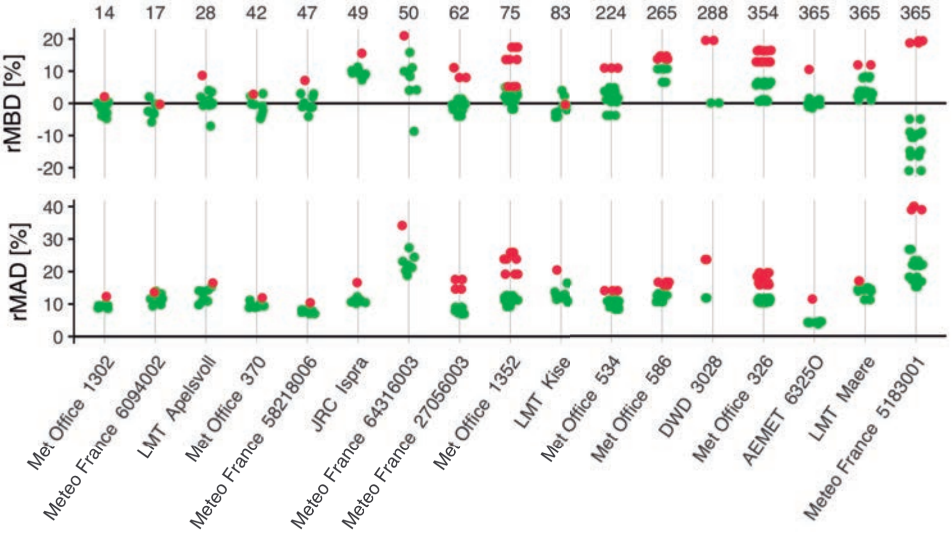

Stations are sorted from left to right by increasing number of daily samples removed per year (values shown at top). Red and green dots show the years with and without defects, respectively.

By way of example, we have quantified the effects of measuring errors on the evaluation of radiation databases by validating SARAH PVGIS against the European stations with defects (Fig. 5.40). The annual bias was used to evaluate the results to prevent that short defects got masked in long time series spanning several years. The reduction in both *rMBD* and *rMAD* from the years containing defects to those with acceptable data was around 2-10% at most stations. Differences up to a 20% were obtained at DWD 3028 (equipment error) and Météo France 5183001 (shading), values which were greater than the own *rMBD* and *rMAD*. The sign of the bias even changed at Météo France 5183001, altering the analysis of SARAH PVGIS performance completely. The impact of the defects on annually-aggregated statistics increased with its duration as expected, but significant deviations of around 2-3% were still obtained at stations with defects shorter than one month. Overall, these results evidence that using measurements from high-quality networks and applying a strict quality control of the data should be mandatory to perform an adequate evaluation of radiation databases. The progress of solar modeling techniques is accentuating this issue because the magnitude of modeling errors is getting closer, and sometimes smaller, than that of operational defects.

The previous was an extreme example because only stations with defects were used. However, the use of measurements from networks with a high number of operational errors or low-quality sensors is not unusual, partly because most widely used QC procedures cannot detect equipment or operational defects. In Spain, several studies have been published based on data from monitoring networks with a high number of operational failures such as Euskalmet [193, 207], MeteoGalicia [194], or SOS Rioja [131]. Studies based on SIAR stations, whose uncertainty is larger due to the presence of incorrectly calibrated photodiodes, are even more common [129, 208, 209, 130, 69, 210, 211, 212, 59]. This is because SIAR provides high-resolution (30-min) G_H data at no cost over a dense network of more than 500 stations. By contrast, the national meteorological service, AEMET, currently charges for sub-daily radiation data. Studies using SIAR data typically assumed the uncertainty reported in the pyranometer datasheet (±5%), but previous results have evidenced that this uncertainty may be substantially larger even after removing operational defects. Most of published studies applied basic range or consistency tests to quality control the data [129, 212] and did not discuss SIAR quality. Only Ruiz-Arias et al. [130] removed 14 SIAR stations in Andalucia after inspecting the data and observing suspicious inter-annual trends likely caused by deficient maintenance.

The consequences of using measurements with high uncertainty can be observed in some of the published validations of solar radiation models against SIAR stations. Besides obtaining large errors at some particular stations most likely due to operational defects, the biases obtained can be partly explained by the trends observed when comparing SIAR photodiodes against AEMET pyranometers (Fig. 5.38): SIAR photodiodes tend to overestimate before 2010 and underestimate since then. Antonanzas-Torres et al. [131] validated a CM SAF SIS product against SIAR stations during 2010-2011 obtaining a bias of +3.41%. The underestimation of SIAR photodiodes in 2010 and 2011 may explain this large positive bias for a satellite-based database in Spain. Urraca et al. [59] compared SARAH-1 against SIAR stations in Castilla la-Mancha from 2001 to 2013 obtaining a mean bias of +0.22%, which is lower than that obtained in Section 5.38 when validating SARAH-1 against AEMET stations (+1.4%). The overestimation of SIAR photodiodes before 2010 may also explain this difference. Besides, both studies obtained particularly large biases at locations where the BQC identified operational defects. Rodriguez-Amigo et al. [212] interpolated measurements from SIAR stations in Castilla y Leon from 2007 to 2013, validating them against four AEMET stations. Most interpolation techniques showed a positive bias, which agrees with the positive difference of +0.7% obtained in our comparison between SIAR and AEMET stations in the same period (Fig. 5.38). Ruiz-Arias et al. [210] corrected the WRF NWP model against AEMET stations during 2003-2012 and validated it against several SIAR stations. They observed an increasing bias in the corrected dataset that was attributed to the increasing number of AEMET stations after 2007. However, this trend also agrees with the decreasing bias observed in SIAR photodiodes from 2007 to 2013 (Fig. 5.38). Our comparison of SIAR and AEMET stations was made with a constant number of stations having data during all the years in the study period, so the trend observed by Ruiz-Arias et al. [210] was most likely due to the uncertainty and re-calibrations of SIAR photodiodes rather than to the increasing number of AEMET stations.

Uncertainties in solar radiation measurements did not directly affect the validation of locally-calibrated models, such as those based on empirical correlations with meteorological variables [209, 69, 79]. However, they did affect these studies when locally-calibrated models were benchmarked against satellite-based or NWP models. For instance, the CM SAF SIS database obtained strong positive biases at mountain stations of SOS Rioja (Urbaña and Moncalvillo) [69], which are explained by the shadows detected by the BQC at those stations. Conversely, empirical models showed moderate errors because they were able to "learn" the shading patterns. Interpolation techniques are another type of locally-calibrated models that have exploited the high-density of SIAR stations [129, 130, 212]. The consequences of interpolating data with measuring errors may be visible in the irradiance maps obtained, which presented "spotty" distributions with sharp irradiance gradients around the stations. This was attributed to particular model configurations or the presence of anomalies in the explanatory variables [129]. However, systematic deviations of photodiodes or operational errors in SIAR stations may also contribute to these "spotty" distributions, and this possibility was not discussed in any of the previous studies.

Patterns observed in the previous studies evidence the critical importance of using solar radiation measurements with low uncertainty since this is the foundation where the conclusions of these studies are built. The quality of the sensors and the maintenance protocols of the stations should always be checked. Besides, the use of advanced QC procedures such as the BQC is strongly recommended to identify any operational or equipment failure, which can occur even in high-quality networks such as national services. In the specific case of Spain, these results also highlight the necessity of making freely available AEMET data to improve the quality of solar radiation studies in Spain.

5.4 Propagation of the bias in G_H through PV simulations

The propagation of the bias in G_H through PV simulations was analyzed by comparing simulations made with SARAH PVGIS, COSMO-REA6, and ERA5 against a simulation based on station measurements. The annual bias in G_H and G_{POA} was analyzed separately below and above 55°N (Fig. 5.41) because the performance of radiation databases changes in high latitudes due to seasonal snow, low solar elevation angles, and low satellite viewing angles.

SARAH PVGIS obtained the smallest annual bias in G_H below 55°N ($bias_y = -0.06\%$). It showed a decreasing bias with increasing latitude, obtaining negative biases in northern Germany and particularly in the Nordic countries ($bias_y = -4.87\%$). SARAH PVIGS underestimate near the edge of satellite images due to an overestimation of cloud thickness because satellites view clouds at very shallow angles [195, 21]. This issue has been addressed in SARAH-2 with an empirical correction of the cloud index as a function of the satellite zenith angle, but it has not been implemented in SARAH PVGIS yet. The negative bias was stronger in winter (Fig. 5.45) probably due to the over-prediction of clouds over snow-covered surfaces [195]. COSMO-REA6 showed the largest bias by underestimating G_H across all latitudes (-4.99% and -5.98%) due to the overestimation of aerosols mentioned above. The most homogeneous distribution of the annual bias in G_H across Europe corresponded to ERA5, with a moderate overestimation of G_H below 55°N ($bias_y = +1.67\%$) and a low underestimation in high latitudes ($bias_y = -1.43\%$). Thus, ERA5 was the database with the smallest bias above 55°N, while the smallest bias below 55°N corresponded to SARAH PVGIS.

Annual biases in P_{DC} differed from those obtained in G_H at some locations. SARAH PVGIS obtained the most stable bias through simulations (Fig. 5.42), with $\Delta bias_y$ within ±1.8% in the transposition model and a negligible $\Delta bias_y$ within ±0.1% in the PV module model. In the transposition model, the bias got more positive below 55°N ($\Delta bias_y = +1.8\%$) and more negative in the Nordic countries ($\Delta bias_y$ = -1.46%). COSMO-REA6 presented a similar propagation pattern to that of SARAH PVGIS in the transposition model, but COSMO-REA6 obtained a non-negligible $\Delta bias_y$ of +0.92% in the PV module model. The increase in bias below 55°N canceled out the negative bias in G_H leading to a moderate bias in

FIGURE 5.41: Distribution of *rMBD* in G_H and P_{DC} for simulations using radiation databases.

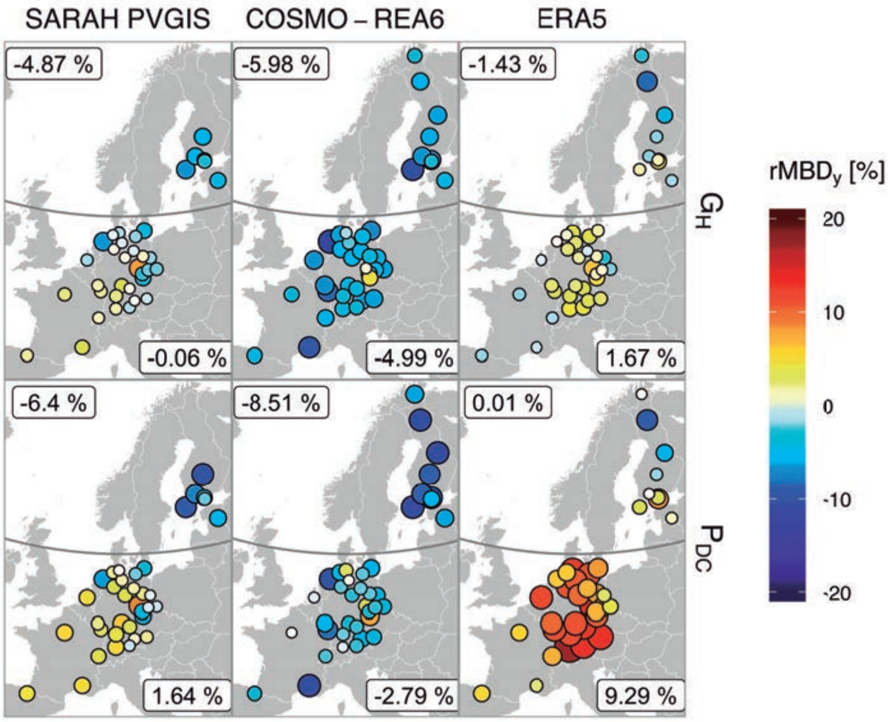

Values in the boxes represent the mean bias at locations over and under 55°N.

P_{DC}, whereas the decrease of bias in high latitudes accentuated the negative bias in P_{DC}. The largest change in the bias through the simulations was obtained by ERA5 below 55°N, with $\Delta bias_y$ = +6.09% in the transposition model and $\Delta bias_y$ = +1.52% in the PV module model. This led to a large bias in P_{DC} (+9.29%) despite the moderate bias in G_H (+1.67%) obtained by ERA5. ERA5 performance sharply changed in Northern Europe becoming the best radiation database in terms of G_H and the one showing the most stable bias through simulations ($\Delta bias_y$ = +1.44%). Therefore, ERA5 was the best performing database in high latitudes with an annual bias in P_{DC} of +0.01%, whereas SARAH PVGIS remained as the database with the smallest annual bias in P_{DC} below 55°N (+1.64 %).

These results evidence that, despite the bias in G_H is the primary driver of the bias in P_{DC}, the bias significantly changes through the simulations. Deviations observed were exclusively due to the source of radiation data, so changes in the bias through the simulations were caused by secondary

FIGURE 5.42: Propagation of *rMBD* in the transposition and PV module model.

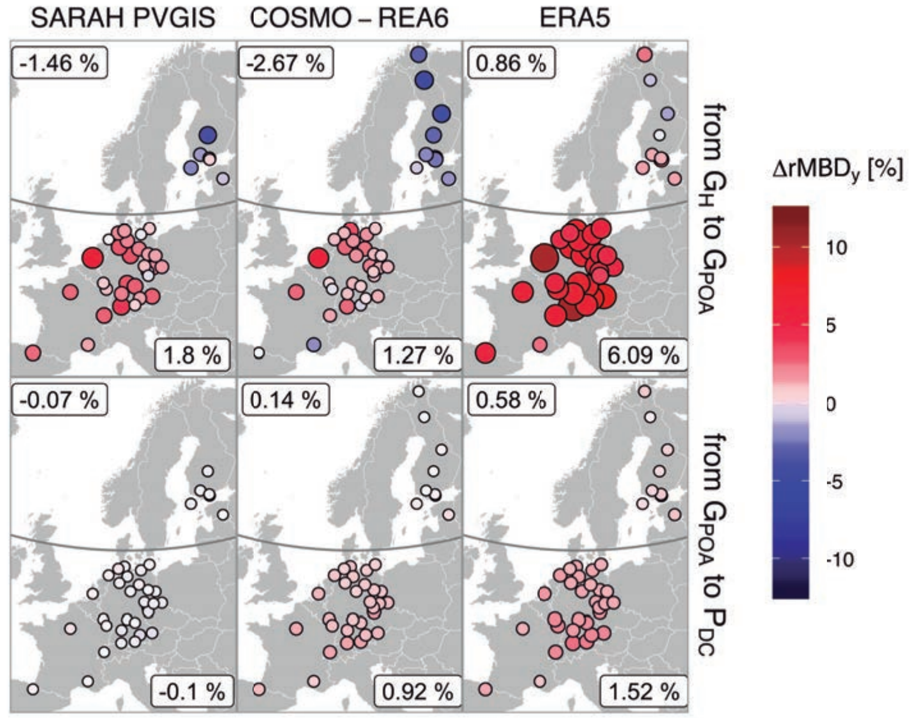

Values in the boxes represent the mean bias at locations over and under 55°N.

effects of uncertainties in estimated irradiance on the modeling chain. The magnitude and sign of these changes varied between databases and locations, and in some cases, they were even higher than the magnitude of the annual bias in G_H. For example, the annual bias in G_H of ERA5 was smaller than that of COSMO-REA6 (+1.67 vs. -4.99%), but the amplification of ERA5 bias through the simulations made that its annual bias in P_{DC} was greater than that of COSMO-REA6 (+9.29 vs. -2.79%). In the following sections, we analyze the root of these variations by studying independently the bias propagation through the transposition model (Subsection 5.4.1) and the PV module model (Subsection 5.4.2).

5.4.1 Bias propagation in the transposition model

The propagation of the bias in the transposition model was studied based on the distribution of daily deviations against K_T (Fig. 5.44), the deviations

FIGURE 5.43: Validation of B_H and D_H from radiation databases.

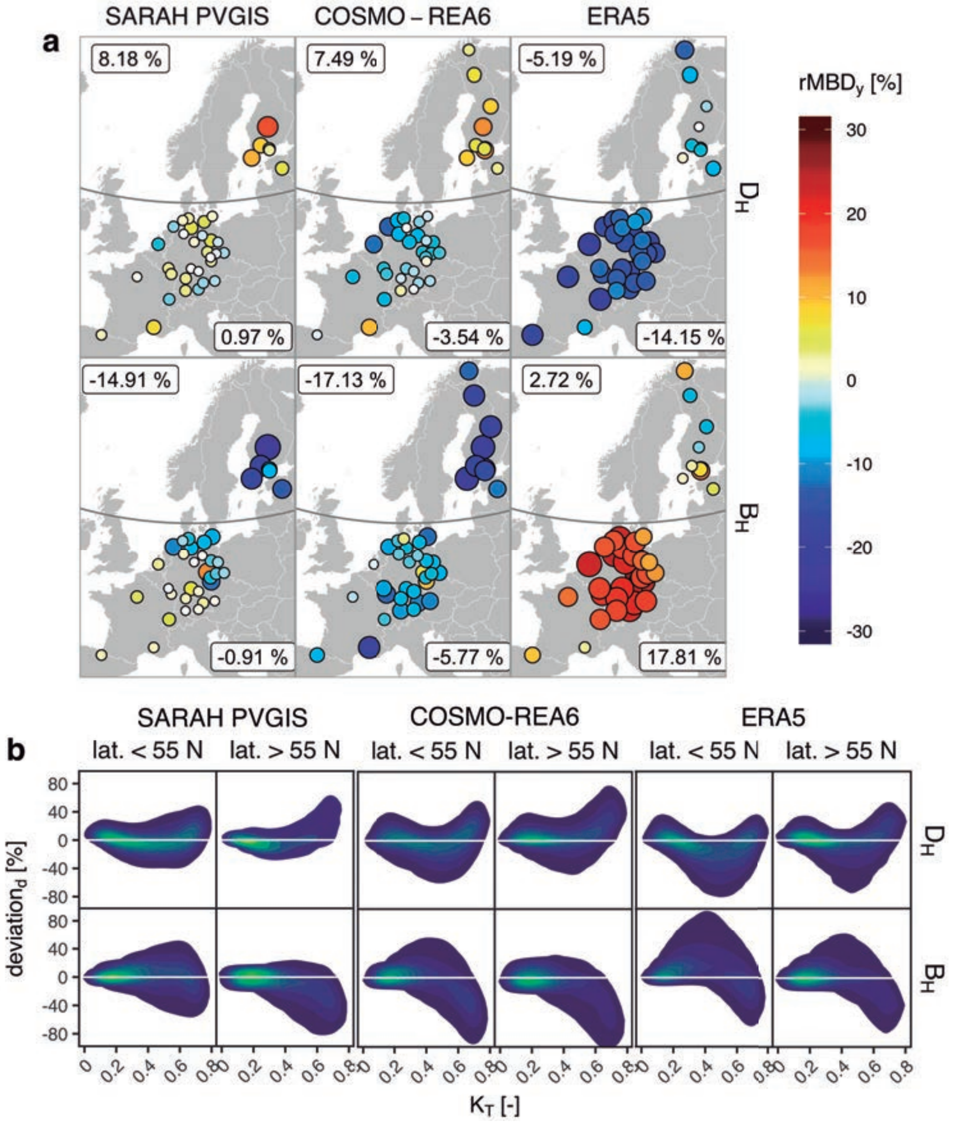

(**a**) Distribution of *rMBD* in D_H and B_H from radiation databases. (**b**) Daily deviations in B_H and D_H between radiation databases and station measurements. Values in the boxes represent the bias at locations over and under 55°N.

of B_H and D_H (Fig. 5.43), and the intra-annual distribution of these deviations (Fig. 5.45). The role of radiation components in the transposition model is essential because they are transposed separately and the contribution of each component varies with the inclination angle: the contribution of beam irradiance increases up to the optimum inclination angle whereas the contribution of diffuse irradiance decreases. Therefore, an unbalanced estimation of radiation components ($bias_y(G_H) \neq bias_y(D_H) \neq bias_y(B_H)$) will be accentuated through the transposition model leading to large errors in G_{POA}. The bias in G_{POA} will get more negative when B_H is underestimated ($bias_y(B_H) < bias_y(G_H)$) and will get more positive when B_H is overestimated ($bias_y(B_H) > bias_y(G_H)$) because beam irradiance plays a dominant role close to the optimum inclination angle. Regarding reflected irradiance, the relative bias in R_{POA} will be equal to that in G_{H} because R_{POA} was calculated from G_{H} assuming an istropic distribution and a constant ρ_g. Therefore, R_{POA} is not analyzed in this section because the bias of R_{POA} does not change through the transposition model.

Figure 5.44: Propagation of the bias in the transposition model (from G_H to G_{POA}).

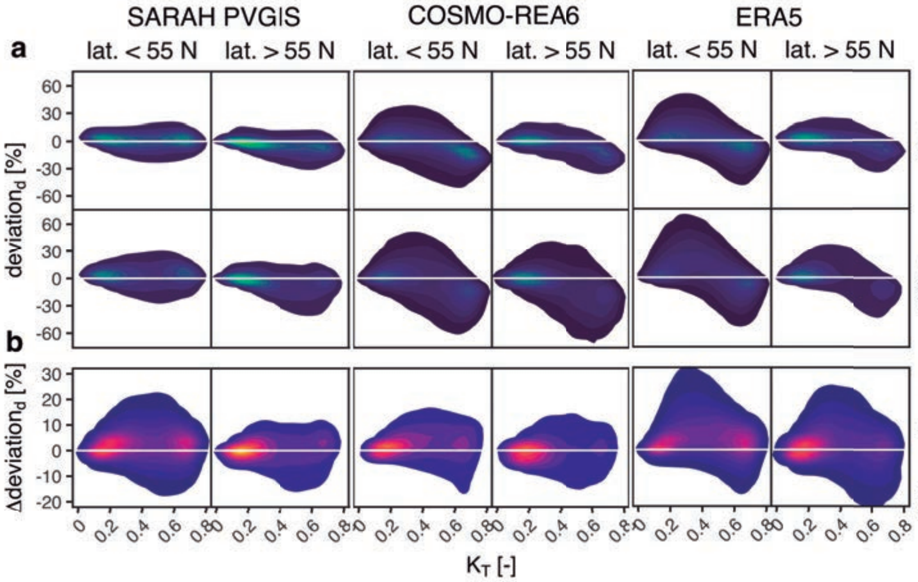

(**a**) Daily deviations in G_H and G_{POA} between radiation databases and station measurements. (**b**) 2D density plot of the variation of the daily deviations against the K_T.

The bias of SARAH slightly changed through the transposition model below 55°N ($\Delta bias_y = +1.8\%$) because of a balanced estimation of the radiation components ($bias_y(B_H) = -0.91\%$, $bias_y(D_H) = +0.97\%$) (Fig. 5.43). The increase of the bias may be partly explained by the presence of missing values at low solar elevations. These values were set to 0 for the validation of horizontal irradiance while they were reconstructed for PV simulations, introducing a small negative bias in G_H, B_H, and D_H when compared to

G_{POA} and P_{DC}. The $\Delta bias_y$ was more negative with an increasing latitude (Fig. 5.42b) due to the greater underestimation of B_H (Fig. 5.43a) that canceled out the overestimation caused by missing values. Therefore, $\Delta bias_y$ was -1.46% above 55°N driven by the strong imbalance between the radiation components ($bias_y(B_H)$ = -14.91%, $bias_y(D_H)$ = +8.18%). The underestimation of SARAH in G_H and G_{POA} was stronger under clear conditions in winter and spring (Fig. 5.45), so this effect may be related to the known limitations of SARAH over snow-covered surfaces [195]. In high latitudes, the imbalance between B_H and D_H (positive bias in D_H, negative bias in B_H) was also large in summer under clear conditions (Fig. 5.45), which may be related to other issues such as aerosols modeling.

The bias of COSMO-REA6 got more positive through the transposition model below 55°N ($\Delta bias_y$ = +1.27%) and more negative in high latitudes ($\Delta bias_y$ = -2.67%). Compared to SARAH, COSMO-REA6 presented an uneven intra-annual distribution of the deviations (Fig. 5.44), strongly underestimating under clear sky due to an excess of aerosols, and overestimating under cloudy conditions due to the under-prediction of clouds. Negative deviations under clear conditions were the dominant effect leading to the underestimation of G_H, D_H and B_H in mid and low latitudes. These deviations were particularly visible in central months of the year (Fig. 5.45). Below 55°N, both effects virtually balanced each other (Fig. 5.43b) and the bias of COSMO-REA6 slightly got more positive due to the overestimation of B_H under cloudy conditions and the predominantly high-cloudiness at the sites evaluated. Above 55°N, the overestimation of B_H under cloudy conditions was somehow mitigated. Therefore, the underestimation of B_H under clear conditions prevailed leading to a negative $\Delta bias_y$ through the transposition model of -2.67%. The bias became more negative as well at southern locations because the underestimation of B_H was accentuated by the high frequency of clear conditions (Fig. 5.43). Overall, both SARAH PVGIS and COSMO-REA6 presented a similar propagation pattern in the transposition model, with a moderate positive $\Delta bias_y$ below 55°N and a large negative $\Delta bias_y$ in high latitudes, though the causes of these changes differed in each database.

ERA5 showed a significantly positive $\Delta bias_y$ of +6.09% through the transposition model below 55°N, which may be explained by the great imbalance between beam and diffuse irradiance ($bias_y(B_H)$ = +17.81%, $bias_y(D_H)$ = -14.15%) (Fig. 5.43). Similarly to COSMO-REA6, ERA5 overestimated G_H under overcast conditions and underestimated it under clear skies. However, the overestimation of G_H under cloudy conditions was substantially more accentuated in ERA5 than in COSMO-REA6 (Fig. 5.44a) due to different failures in the prediction of clouds. The under-prediction of clouds led to an overestimated B_H for $K_T < 0.5$ (Fig. 5.44b), and thus, to

FIGURE 5.45: Heatmap of monthly-aggregated *rMBD* in G_H, D_H and B_H.

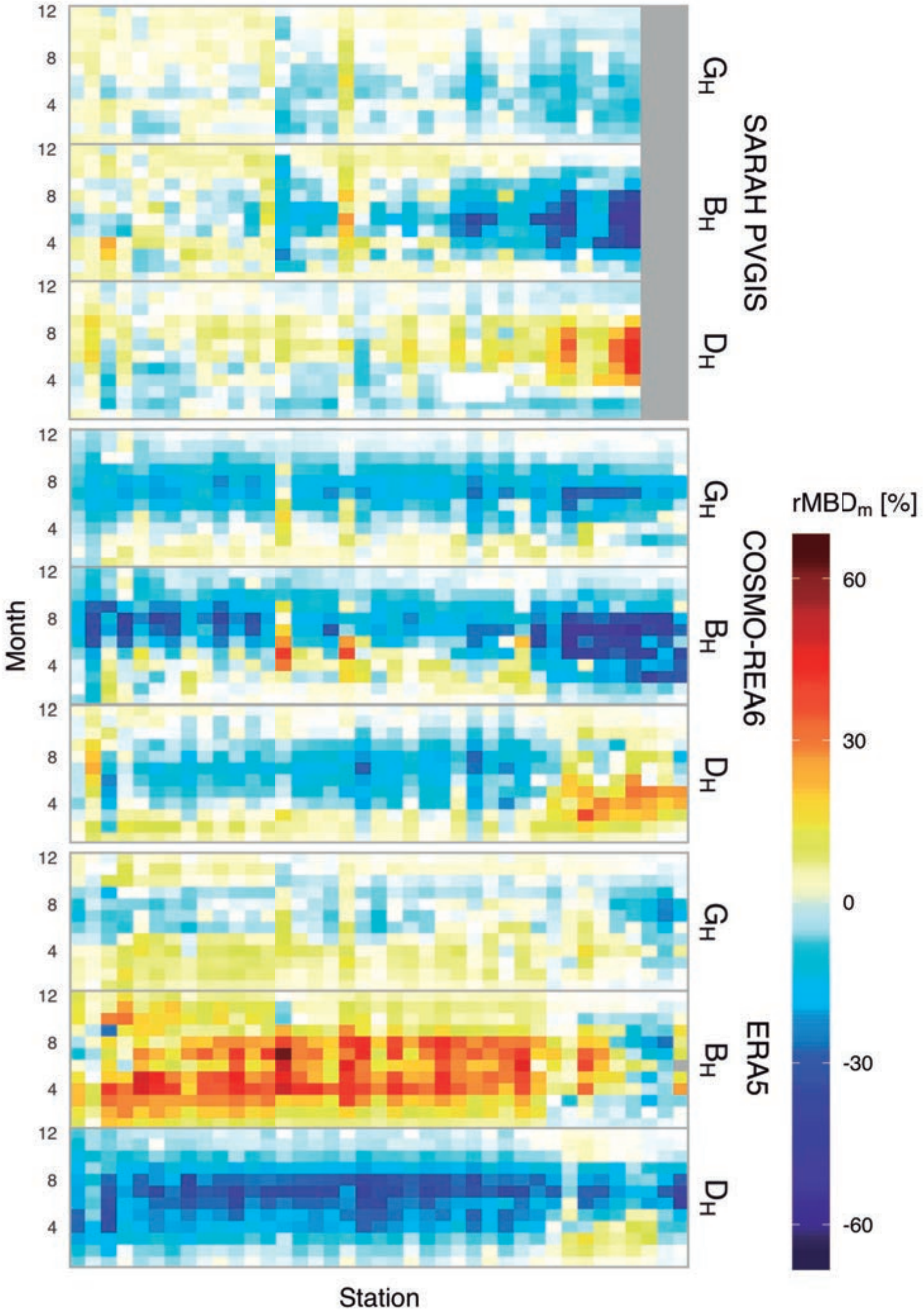

Stations are sorted from left to right by increasing latitude.

an overestimated G_{POA}. The performance of ERA5 completely changed in the Nordic countries because of a reduced overestimation of B_H under cloudy conditions, leading to a better balanced estimation of radiation components (Fig. 5.43). The overestimation of B_H for $K_T < 0.6$ canceled the underestimation of B_H for $K_T > 0.6$, producing a moderate $\Delta bias_y = +0.86\%$. Thus, ERA5 presented the smallest $\Delta bias_y$ through the transposition model above 55°N, which contrasts with its poor performance below 55°N where it obtained the largest $\Delta bias_y$ overall.

5.4.2 Bias propagation in the PV module model

The PV module model comprises the estimation of G_{eff} from G_{POA}, and the estimation of η' for temperature and irradiance values different from those under STC. In this study, the estimation of G_{eff} only accounted for AOI losses, which depend on solar geometry and are virtually independent of the radiation database. Therefore, variations of the bias through the PV module model primarily occurred in the estimation of η' and they were caused by second-order effects of irradiance errors on the model that calculates η'. These effects are two-fold because η' depends on irradiance directly (Fig. 5.46a) and indirectly via module temperature (Fig. 5.46b). Irradiance and temperature were the predominant factors at low and high irradiances, respectively. Therefore, η' increases with irradiance until a value of around 400 W/m^2, after which the heating of the cell by the radiation causes efficiency to decrease again (Fig. 5.46c) [213].

Figure 5.46: Variation of the relative module efficiency (η') of c-Si modules under conditions different from STC.

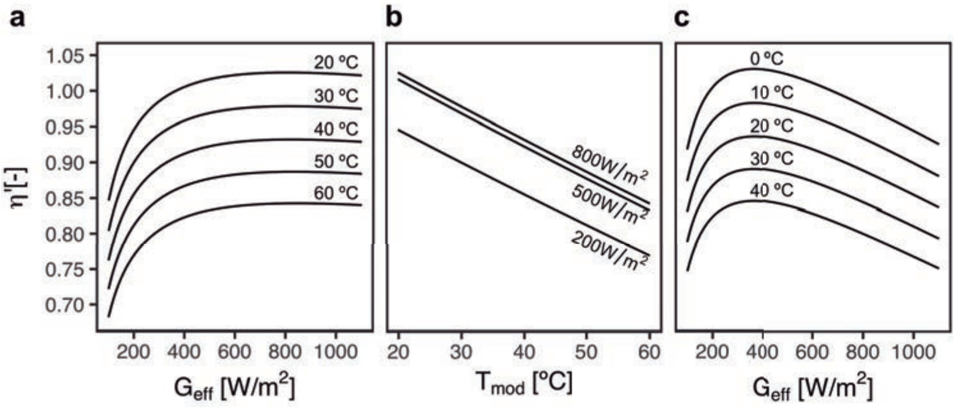

(a) η' as a function of irradiance for constant module temperature, **(b)** as a function of module temperature for constant irradiance, and **(c)** and as a function of irradiance for constant ambient temperature.

Figure 5.47: Propagation of the bias in the PV module model (from G_H to G_{POA}).

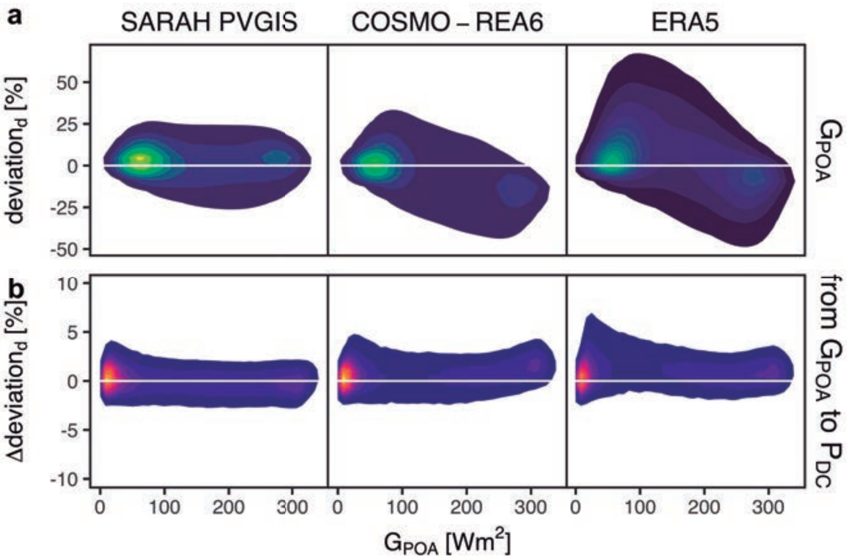

(**a**) 2D density plot of the daily deviations in G_{POA} between simulations using radiation databases and that using station measurements against G_{POA}. (**b**) 2D density plot of the variation of the daily deviations against G_{POA}.

The $\Delta bias_y$ through the PV module model can be explained by the interaction of curves shown in Fig. 5.46c with the distribution of daily deviations with irradiance (Fig. 5.47a). SARAH PVGIS exhibited a negligible $\Delta bias_y$ in the PV module model within ±0.1% because its deviations were evenly distributed with irradiance (Fig. 5.47a). Conversely, a positive $\Delta bias_y$ was obtained in the PV module model with both reanalyses: +0.92% and +0.14% for COSMO-REA6, and +1.52% and +0.58% for ERA5, for locations below and above 55°N, respectively. This is because both products present an unbalanced error distribution with positive deviations under cloudy conditions (low irradiance days) and negative deviations under clear conditions (primarily high irradiance days). Irradiance effects dominate η' in low irradiance days, so an overestimated irradiance led to an overestimated η', and hence to a positive $\Delta bias_y$. On the other hand, temperature effects dominate η' in high irradiance days. Here an underestimated irradiance led to a too low module temperature, and as a consequence, to an overestimated η' that resulted in a positive $\Delta bias_y$ as well. The combination of both effects results in the banana-shaped curves obtained in Fig. 5.47b, explaining why the bias got more positive in the PV module model. In COSMO-REA6, the positive $\Delta bias_y$ was mostly driven by an underestimated temperature in days with high irradiance due to the excess of aerosols (Fig. 5.47b). The positive $\Delta bias_y$ of ERA5 was primarily caused by an overestimated irradiance in days with low irradiance due to the underestimation of clouds (Fig. 5.47b). In summary, the bias was amplified through the PV module model in simulations based on reanalyses due to the intra-annual variations of the deviations with the atmospheric transmissivity.

5.4.3 Influence of module inclination angle on bias propagation

FIGURE 5.48: Influence of module inclination angle on bias propagation.

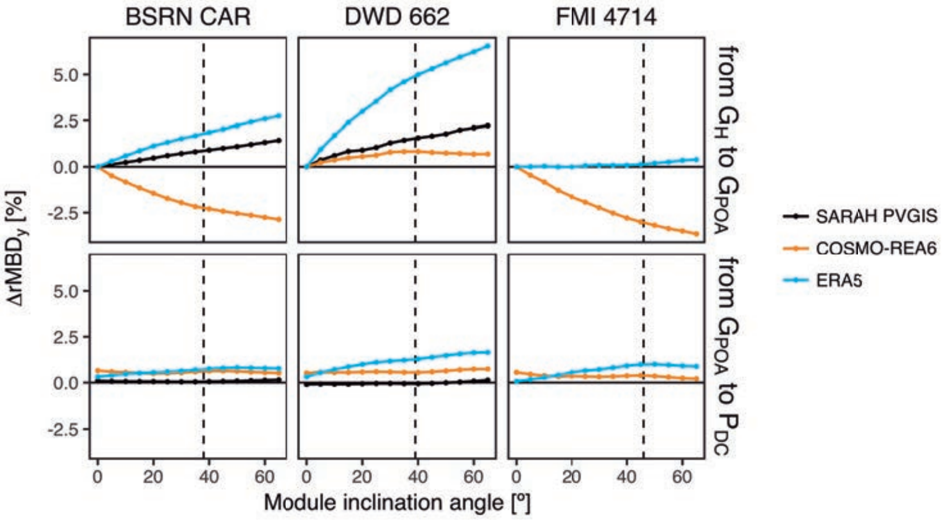

The dashed line shows the optimum inclination angle at each location.

The propagation of the bias through the transposition model showed a clear dependence on the module inclination angle. The $\Delta bias_y$ grew linearly with the inclination angle up to the optimum inclination at each location (Fig. 5.48). This trend was common to all databases and locations regardless of the sign of the $\Delta bias_y$, and it was caused by the increasing contribution of beam irradiance with the inclination angle. $\Delta bias_y$ increased more rapidly for databases with an imbalanced estimation of beam and diffuse components, such as ERA5 in Germany (DWD-662) and COSMO-REA6 in high latitudes (FMI-4714). In general, the trend in bias continued at a smaller rate beyond the optimum angle. This may be related to the fact that for an interval above the optimum angle B_{POA} still increases while D_{POA} continues to fall. Thus, the trend in bias caused by an imbalance of B and D will continue.

The $\Delta bias_y$ in the PV module model was small and virtually constant along different inclination angles because the inclination angle does not directly affect the PV module model. The changes of the bias observed were side effects of the propagation of the bias in the transposition model. A large $\Delta bias_y$ in the transposition model accentuates the defects in the radiation databases, leading to a more irregular distribution of errors in G_{POA}. This alters the calculation of the energy conversion efficiency of the module, explaining the amplification of the bias in the PV module model.

5.4.4 Selection of solar radiation databases for yield predictions

FIGURE 5.49: Summary of the annual relative deviations between the simulations using radiation databases and the one using solar radiation measurements.

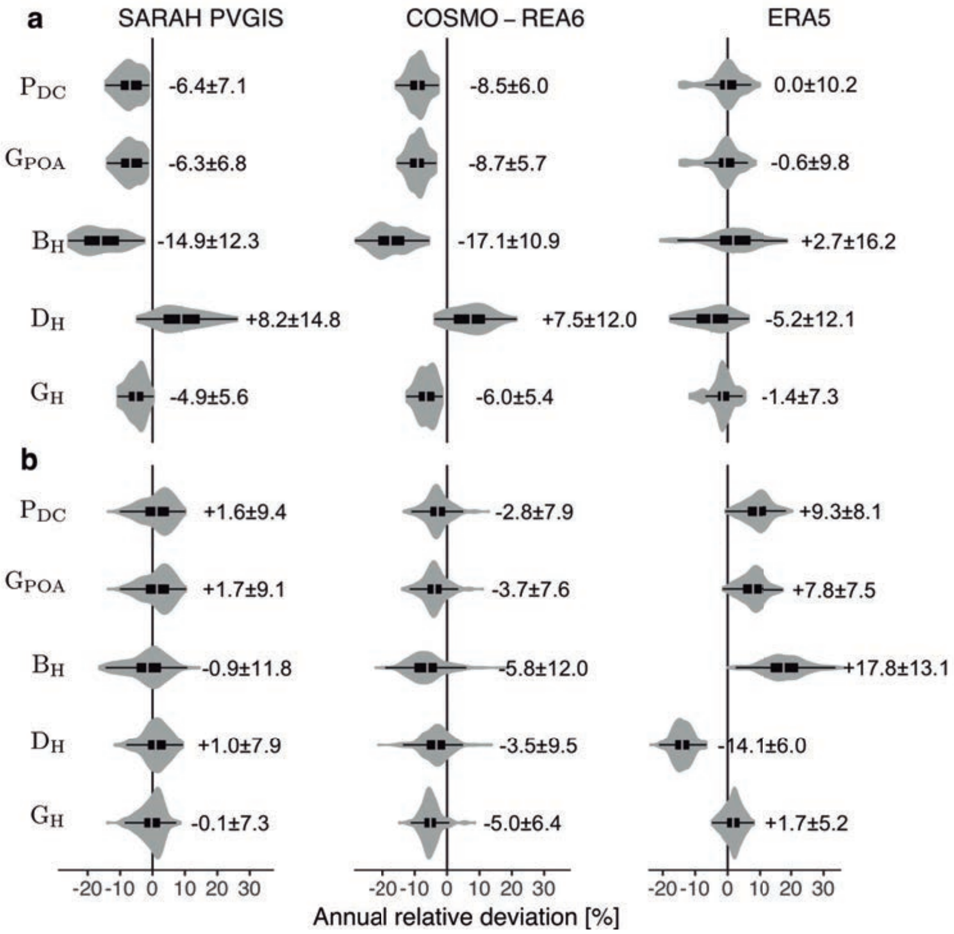

(**a**) Latitude > 55°N. (**b**) Latitude < 55°N. The labels represent the bias ± 95% CI.

We compared PV simulations made with SARAH PVGIS, ERA5, and COSMO-REA6 against a simulation based on station measurements to analyze the propagation of the bias in G_H through the PV modeling chain. The bias in G_H is the traditional metric for selecting radiation databases because it propagates proportionally to the bias in P_{DC}, and thus to the bias in Y_{AC} [157, 10]. The uncertainty in annual G_H is also considered because it is the main driver of the uncertainty in Y_{AC} and sets the risk and financial cost of the investment [10, 11, 13]. However, our results evidenced that these two indicators alone are insufficient to select solar radiation databases because the bias in G_H may get amplified through the modeling chain, as also suggested by Cole et al. [25]. These changes are most likely caused by the source of solar radiation data used because the remaining parameters were similar between simulations. In particular, the bias is amplified due to the effect of large intra-annual deviations in G_H and an incorrect prediction of radiation components on sub-models depending on the irradiance level. Cole et al. [25] estimated that these effects may change the bias about a ±2% using satellite-based data, but substantially larger changes were obtained in the present study with both satellite-based and reanalysis databases.

The most significant changes occurred through the transposition model ranging from ±1% up to +6%. Their magnitude increased linearly with the inclination angle, and they are related to the incorrect estimation of beam and diffuse irradiance. The amplification of the bias through the PV module model was smaller (around +1%). It was also caused by the effects of high intra-annual errors in G_H on module efficiency, which depends on irradiance directly, and indirectly via module temperature. These results suggest that these second-order effects cannot be neglected when selecting a radiation database for simulating PV systems, because databases showing the smallest bias in G_H may not always provide the least biased yield predictions (Fig. 5.49). The amplification of the bias also affects energy rating studies used to assess the performance of PV materials in a specific region because they alter the estimated real efficiency of the modules, and hence the performance ratio.

The interpretation of the results is constrained by the uncertainty in the reference simulation (Subsection 4.7.2). The annual bias of horizontal irradiance variables was higher than the uncertainty of the reference simulation at the majority of stations (Table 5.6). The exceptions were SARAH PVGIS below 55°N and ERA5 above 55°N, where around half of the stations were within the uncertainty limits due to the low deviations of both databases in those regions. The patterns showed by SARAH and ERA5 at those locations should be interpreted cautiously. For G_{POA} and P_{DC}, the number of stations within the uncertainty limits increased because both variables were not measured but estimated by feeding horizontal irradiance measurements to the simulation model. The uncertainty ranges of simulations using estimated and measured radiation increasingly overlap through the modeling chain, explaining the decrease of the uncertainty in G_{POA} and P_{DC} (Fig. 5.49). Therefore, the effects of high intra-annual errors and an incorrect estimation of radiation components on the annual uncertainty could not be evaluated due to the lack of measurements of G_{POA} and P_{DC}.

TABLE 5.6: Percentage of annual biases greater than the annual uncertainty of the reference simulation.

	Database	G_H	B_H	D_H	$G_{POA}{}^*$	$P_{DC}{}^*$
Latitude < 55°	SARAH	57	42	62	30	24
	COSMO-REA6	91	75	74	34	20
	ERA5	60	96	100	73	77
Latitude > 55°	SARAH	62	91	81	38	34
	COSMO-REA6	82	95	75	70	52
	ERA5	30	34	64	11	11

[*] In the reference simulation, G_{POA} and P_{DC} are estimated using the irradiance measurements as inputs to the PV simulation model.

Values shown in Table 5.6 are the worst-case scenario. The true number of biases greater than the uncertainty in the reference simulation should be considerably larger because test and reference simulations used the same transposition and PV module model. Thus, systematic deviations introduced by these models cancel out. Nonetheless, G_{POA} and P_{DC} deviations were significant for ERA5 below 55°N and for COSMO-REA6 above 55°N, even in this worst-case scenario. Concerning the uncertainties at DWD and FMI stations, we did not observe any significant difference between the results obtained at BSRN stations and those obtained at FMI or DWD. This suggests that the variation of uncertainty between stations was negligible and did not interfere significantly with the interpretation of the results.

5.4.5 Performance of PVGIS radiation databases in Europe

We have evaluated the performance of the three radiation databases currently implemented by PVGIS for simulating PV systems over Europe. PVGIS includes a fourth database, the CM SAF Operational product, but this database was excluded because its spatial coverage overlaps with that of SARAH PVGIS while it has a larger uncertainty than SARAH PVGIS (Section 5.2). The CM SAF operational is kept in PVGIS for historical reasons to keep consistency with the results produced by the initial PVGIS versions, but SARAH PVGIS should be preferred. The study was particularly focused on the analysis of ERA5 and COSMO-REA6 performance in Northern Europe. Both reanalyses were included in PVGIS to complement SARAH in high latitudes after their promising results in the validation against the European and Global datasets. However, their suitability for simulating PV systems had not been assessed yet.

Figure 5.50: Solar radiation databases included in PVGIS below 65°N.

Selected: 42.294, -2.620

Elevation (m): 1341

Solar radiation database*: PVGIS-CMSAF

Source: http://re.jrc.ec.europa.eu/pvg_tools/en/tools.html#PVP.

Significant differences were observed between geographic areas and databases. In mid and low European latitudes, the bias of reanalyses was substantially amplified through the simulations, especially that of ERA5. COSMO-REA6 showed a strong negative bias in G_H (-5.0%) due to an overestimation of aerosols. The bias of COSMO-REA6 got more positive through the simulation (+2.2%) reducing by chance the bias in P_{DC} (-2.8%). ERA5 showed a moderate bias in G_H (+1.7%) that was sharply amplified through the modeling chain leading to a bias in P_{DC} of +9.3%. These amplifications were most likely caused by the incorrect modeling of clouds that led to a substantial variation of daily deviations in G_H with the atmospheric transmissivity and an incorrect estimation of the radiation components. The strong variation of deviations with atmospheric conditions limits the capacity of reanalyses to produce accurate yield predictions despite showing moderate biases and uncertainties in annual G_H. On the contrary, SARAH showed the smallest bias in G_H (-0.1%) and the most stable bias through the simulations (+1.7%). These results corroborate that SARAH is the best database to simulate PV systems in most European regions below 55°N. Even though PVGIS offers reanalysis data to assess PV systems within the region covered by SARAH (Fig. 5.50), the use of these databases should be avoided.

FIGURE 5.51: Solar radiation databases included in PVGIS above 65°N.

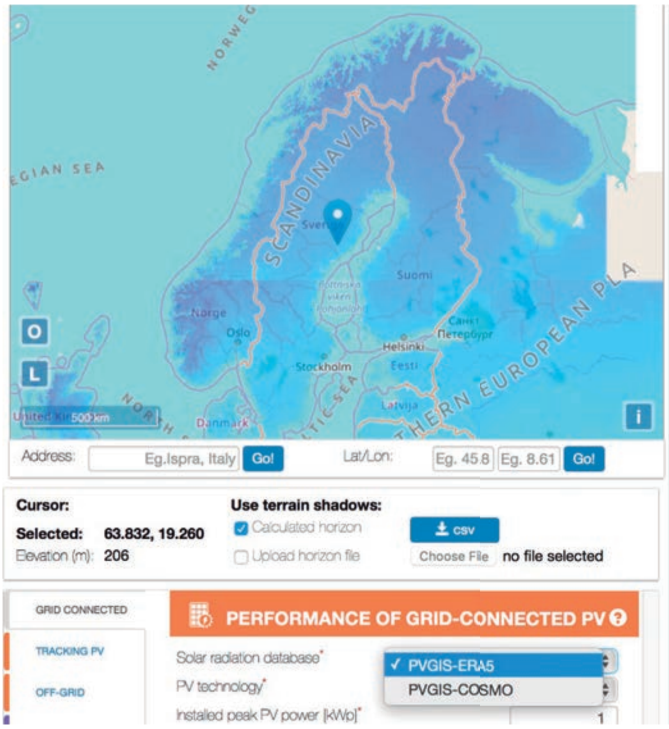

Cursor:
Selected: 63.832, 19.260
Elevation (m): 206

Use terrain shadows:
☑ Calculated horizon
☐ Upload horizon file

no file selected

Solar radiation database*: ✓ PVGIS-ERA5 / PVGIS-COSMO
PV technology*
Installed peak PV power [kWp]*: 1

Source: http://re.jrc.ec.europa.eu/pvg_tools/en/tools.html#PVP.

The performance of SARAH PVGIS sharply changed in Northern Europe. The annual bias became more negative through the transposition model caused by an underestimation of beam irradiance ($\Delta bias_y$ = -1.46%), aggravating the underestimation in G_H, and leading to significant negative biases in P_{DC}. This may be related to the above-discussed underestimation caused by shallow viewing geometries at the edge of satellite images and snow-detection problems. Thus, replacing SARAH PVGIS by SARAH-2 may partly correct these issues. COSMO-REA6 showed a similar propagation to that of SARAH PVGIS in high latitudes ($\Delta bias_y$ = -2.67%) that accentuated its underestimation in G_H over Europe. Conversely, ERA5 showed the smallest $\Delta bias_y$ and the best annual bias in both G_H (-1.4%) and P_{DC} (+0.0%) due to a reduced overestimation of clouds under overcast conditions. Therefore, ERA5 not only complements SARAH above 65°N but also outperforms it between 55°N and 65°N. These promising results validate the inclusion of ERA5 in PVGIS to assess PV systems in Northern Europe. Nonetheless, ERA5 still shows large intra-annual deviations in high latitudes due to cloud-related errors. PVGIS users should keep in mind that the uncertainty of yield predictions from ERA5 in high latitudes may be larger than that from SARAH in Central Europe, and substantially larger than that from station measurements in both regions. The uncertainty may increase even more at coastal locations due to the coarse resolution of ERA5 (31 km). Therefore, the uncertainty of the yield predictions obtained with ERA5 may be too high for the financial analysis of utility-scale plants. However, it is acceptable for preliminary assessments of the solar resource or planning residential PV systems in Northern Europe, which is indeed one of the main goals of PVGIS.

Chapter 6

Conclusions and Future work

6.1 Conclusions

The estimation of the total energy yield produced by a PV system is one of the most critical stages when planning new installations since it serves to identify the best sites, dimension their size, and analyze the financial viability of the project. The uncertainty of yield predictions is driven by that of solar radiation data, which currently accounts for around 50% of total uncertainty because it depends on stochastic atmospheric processes that are not easily predictable. The objectives of this thesis are to quantify the uncertainty in G_H measurements and estimations and analyze the propagation of this uncertainty through the modeling chain for reducing the uncertainty in PV system simulations.

Solar radiation measurements are the most accurate source of data when following strict measuring guidelines. The top-end secondary standard pyranometers have uncertainties in annual G_H below ±2% if they are correctly calibrated and maintained. However, we found substantially higher uncertainties in the low-cost photodiodes of SIAR when comparing them with nearby AEMET secondary standards (less than 20 km). After removing the uncertainty of secondary standards and operational defects, the uncertainty in annual G_H of SIAR photodiodes ($+0.7^{+6.9}_{-5.4}\%$) was even higher than that of the best satellite-based databases. Although part of this uncertainty may be attributed to the validation procedure, most of it is probably due to equipment errors such as cosine error, spectral response, or linearity, and the incorrect correction of these defects. This uncertainty will be even higher for daily or hourly G_H. Special attention must be paid to the calibration of the sensors when developing applications based on data from photodiode pyranometers because their equipment errors can skew the results obtained. We recommend to use data from secondary standards when the quality of solar radiation measurements is crucial; such is the case of the analysis of climate trends or the validation of radiation databases.

The uncertainty of solar radiation measurements increased even more due to operational defects caused by the poor placement of stations or low maintenance. We estimated that common defects such as soiling, shading, or large errors introduced annual biases around ±9%. We found operational defects at 29 out of the 335 European stations and at 264 out of the 732 Spanish weather stations. Some agricultural (SIAR) and regional networks (SOS Rioja, MeteoGalicia, Euskalmet) presented defects in more than 50% of their stations. Operational errors occurred equally in photodiode or thermopile pyranometers. In stations with photodiodes, such as those from SIAR, operational defects further increased the equipment uncertainty. In stations with thermopiles, such as those from Euskalmet or MeteoGalicia, operational errors ruined the high quality of sensors. Top-end sensors should be only installed if the adequate level of maintenance can be kept.

We observed that most operational defects produced low-magnitude deviations that introduced large annual biases because they persisted in time. However, the values obtained were physically plausible, and they easily pass common QC procedures such as the BSRN tests, which only detect time lags and some large errors. We developed and validated a new QC procedure, referred to as the Bias-based QC (BQC) method, to detect low-magnitude defects by analyzing the stability of deviations between several radiation databases and ground measurements. Specifically, the BQC flags groups of consecutive days when the deviations of all radiation databases differ statistically from the typical value for that region and time of the year. Compared to the BSRN tests, the BQC detected all operational defects identified in the European and Spanish networks, and it also found some equipment errors related to systematic deviations in photodiodes and incorrectly calibrated pyranometers. The use of advanced QC methods such as BQC is strongly recommended to avoid the inclusion of measuring errors in solar radiation studies.

The extensive validation performed of several radiation databases over Europe and worldwide confirmed the high-quality of satellite-based models, with most of them showing biases below ±3% over most of Europe. Databases derived from geostationary satellites, such as SARAH or NSRDB, should be preferred as they show the lowest uncertainty with spatiotemporal resolutions up to 15 min and 3 km. Their uncertainty increases in the mountains, over snow-covered surfaces, and at the border of satellite images. However, their main limitation is that their spatial coverage is limited to latitudes within ±65°. Hence, we explored the use of atmospheric reanalyses, which have global coverage and predict many other variables besides G_H, as an alternative to satellite data to assess the solar resource. We confirmed that former ERA-Interim and MERRA2 reanalyses should be avoided due to their low accuracy. Both reanalyses showed biases above +10% over Europe caused by cloud-related errors and their coarse spatial resolution. However, we discovered that the new ERA5 and COSMO-REA6 substantially improved former reanalyses showing a reduced bias of +3.75% and -6.00% over Europe, respectively. Their main limitation is that their moderate biases are a result of the compensation of large intra-annual deviations that vary with the atmospheric conditions due to cloud-related errors. This leads to absolute errors and uncertainties still larger than those of satellite-based models. Hence, both reanalyses should be used by taking into account their limitations; ERA5 still mispredicts clouds limiting its accuracy in regions with high cloudiness, whereas COSMO-REA6 overestimates aerosols underestimating G_H in sunny regions. However, both ERA5 and COSMO-REA6 are valid complements to satellite-based databases in regions where those are missing. Indeed, based on these results the online simulator PVGIS included ERA5 and COSMO-REA5 to assess PV systems in Northern Europe.

Solar radiation databases used for yield predictions are typically selected based on the bias and uncertainty in annual G_H. The prior propagates proportionally to the bias in Y_{AC} whereas the latter drives the uncertainty in Y_{AC}. However, we found that the bias in G_H may be substantially amplified through the PV modeling chain after comparing simulations based on the radiation databases implemented by PVGIS against a simulation based on station measurements. These amplifications are caused by the effects of large intra-annual deviations in G_H and an incorrect estimation of the radiation components on sub-models that depend on the irradiance level. The bias was amplified around ±6% in the transposition model and ±1% in the PV module. The amplification at some locations was higher than the bias of solar radiation measurements, so these effects have to be accounted for selecting radiation databases to simulate PV systems.

We also confirmed that SARAH generates the best yield predictions in Central and South Europe. By contrast, the large intra-annual deviations of COSMO-REA6 and ERA5 caused by cloud-related errors amplified their biases through the simulation, making them inadequate to simulate PV systems despite showing moderate biases in G_H. Importantly, the performance of ERA5 improved in Northern Europe. ERA5 not only complements SARAH above 65°N but also outperforms it between 55°N and 65°N because SARAH is affected by snow issues and shallow viewing geometries. These promising results validate the inclusion of ERA5 in PVGIS to complement SARAH in Northern Europe.

6.2 Future work

We developed the BCQ during the initial stage of this thesis using SARAH-1/SARAH PVGIS, CLARA-A1, and ERA-Interim. However, we later verified the improvement of SARAH-2, CLARA-A2, and ERA5 over their predecessors. It would be interesting to update the BQC using the newest version of each database, mainly by replacing ERA-Interim with ERA5. The reduction in the variance of the estimations would increase the robustness of the confidence intervals. This may allow finding currently undetected defects such as low-magnitude equipment errors. We could also test if adding a fourth database, such as COSMO-REA6, increases the number of defects identified and reduces the number of false alarms. Replacing ERA-Interim with ERA5 would also improve the graphical analysis of the BQC because there would be a second database with an intra-daily resolution to generate the plot of instantaneous irradiance. This will also enable to create this plot at high-latitudes, which currently is not possible due to the lack of coverage of SARAH above 65°N.

The principal obstacle to implementing the BQC is the requirement of solar radiation databases. Even though all databases used in this thesis are free, retrieving and processing the raster files requires minimum computational skills, especially if we want to implement the BQC over broad regions. Therefore, it would be interesting to develop an online implementation of the BQC that integrates the solar radiation databases, as online PV simulators do. In this way, users would only have to enter their G_H records and analyze the plots generated. The application would automatically compare the measurements against radiation databases, flag the data, and produce the two plots used to inspect the flags visually. This application may be extrapolated to other radiation and meteorological variables. For instance, the BQC could be used to quality control diffuse and beam irradiance thanks to the increasing number of satellite-based databases estimating the radiation components. Besides, it could be used to detect errors in temperature or wind speed by comparing measurements against estimations from different NWP models. The BQC could be even integrated into online PV simulators to automatically quality control irradiance, temperature, and wind speed measurements when provided by users.

Concerning the quality of pyranometers, we found that photodiodes may have substantially larger annual uncertainties than thermopile sensors, but we could not identify the exact cause of these deviations. We assumed that most of them were caused by equipment errors such as spectral effects, linearity, or temperature dependence, and by the use or incorrect empirical corrections for these errors. It would be interesting to make a detailed analysis of these errors using sub-daily collocated data from high-quality pyranometers at the stations showing defects. At least one year of data would be needed. Another option would be to use satellite-based models as the reference, but even the uncertainty of the most accurate databases might be too high for analyzing equipment errors. Finding the exact cause of photodiode deviations would provide a better understanding of their limitations facilitating their correction. This would allow exploiting the advantages of photodiode pyranometers, such as their low cost of quick response time.

Finally, we observed that the bias in G_H may be amplified through PV simulations due to high intra-annual deviations in G_H and the incorrect estimation of beam and diffuse irradiances. However, we could not evaluate the consequences of these errors in the uncertainty of annual yield predictions due to the lack of G_{POA} and P_{DC} measurements. It would be interesting to repeat the same analysis in a set of locations monitoring both G_{POA} and P_{DC} to evaluate whether the annual uncertainty in yield predictions is amplified as well.

6.3 Contributions

6.3.1 Main contributions

The main results of the thesis have been published in the following international journals and conferences.

International journals

- Urraca, R., Martinez-de-Pison, E., Sanz-Garcia, A., Antonanzas, J., Antonanzas-Torres, F.J.. Estimation methods for global solar radiation: Case study evaluation of five different approaches in central Spain. *Renewable and Sustainable Energy Reviews* 2017;77:1098-1113. URL: `http://dx.doi.org/10.1016/j.rser.2016.11.222`

  This publication was our first evaluation of solar radiation databases using SIAR data as the reference in Castilla-La Mancha. This study motivated most of the work presented in this thesis; such is the case of the analysis of photodiode pyranometers or the development of the BQC.

- Urraca, R., Gracia-Amillo, A.M., Huld, T., Martinez-de-Pison, F.J., Trentmann, J., Lindfors, A.V., Riihelä, A., Sanz-Garcia, A.. Quality control of solar radiation data with satellite-based products. *Solar Energy* 2017;158:49-62. URL: `http://dx.doi.org/10.1016/j.solener.2017.09.032`

  This study describes the BQC and its implementation at European weather stations.

- Urraca, R., Gracia-Amillo, A.M., Koubli, E., Huld, T., Trentmann, J., Riihelä, A., Lindfors, A.V., Palmer, D., Gottschalg, R., Antonanzas-Torres, F.. Extensive validation of CM SAF surface radiation products over Europe. *Remote Sensing of Environment* 2017;199:171-186. URL: `http://dx.doi.org/10.1016/j.rse.2017.07.013`

  This publication presents the validation of the CM SAF satellite-based databases used in this thesis.

- Urraca, R., Huld T., Gracia-Amillo, A., Martinez-de-Pison, F.J., Kaspar, F., Sanz-Garcia, A.. Evaluation of global horizontal irradiance estimates from ERA5 and COSMO-REA6 reanalyses using ground and satellite-based data. *Solar Energy* 2018;164:339-354. URL: `https://doi.org/10.1016/j.solener.2018.02.059`

  This study shows the evaluation of ERA5 and COSMO-REA6 in Europe and worldwide. Both reanalyses were benchmarked against former reanalysis versions (MERRA-2 and ERA-Interim) and satellite-based databases (SARAH and NSRDB). It was the first publication evaluating ERA5 and COSMO-REA6 surface irradiance estimates.

- Urraca, R., Huld, T., Martinez-de-Pison, F.J., Sanz-Garcia, A.. Sources of uncertainty in annual global horizontal irradiance data. *Solar Energy* 2018;170:873-884. URL: `https://doi.org/10.1016/j.solener.2018.06.005`

  This study shows the analysis of the uncertainty in solar radiation measurements and estimations over Spain presented in Section 5.3.

- Urraca, R., Huld, T., Lindfors, A.V., Riihelä, A., Martinez-de-Pison, F.J., Sanz-Garcia, A.. Uncertainties in estimated irradiance amplify bias propagation in PV simulations. *Solar Energy* 2018 (under review).

  This publication summarizes the analysis of the uncertainty propagation through PV simulations presented in Section 5.4.

International conferences

- Urraca, R., Antonanzas, J., Sanz-Garcia, A., Aldama, A., Martinez-de-Pison, F.J.. An algorithm based on satellite observations to quality control ground solar sensors: Analysis of Spanish meteorological networks. In: *International Conference on Hybrid Artificial Intelligence Systems, Oviedo, Spain, June 20-22*. 2018. URL: `https://doi.org/10.1007/978-3-319-92639-1_51`

  This contribution presents the implementation of the BQC at Spanish weather stations.

- Huld, T., Urraca, R., Gracia-Amillo, A., Trentmann, J.. A global hourly solar radiation data set using satellite and reanalysis data. In: *33rd European Photovoltaic Solar Energy Conference and Exhibition (EU PVSEC), Amsterdam, 25-29 September*. 2017. `https://doi.org/10.4229/EUPVSEC20172017-6BV.3.4`

  This contribution presents the combination of satellite-based (SARAH) and reanalysis (ERA5 and COSMO-REA6) databases for assessing the solar resource at any European location.

- Huld, T., Pinedo Pascua, I., Gracia-Amillo, A. Urraca, R., Dunlop, E.. PVGIS version 5: improvements to models and features. In: *33rd European Photovoltaic Solar Energy Conference and Exhibition (EU PVSEC), Amsterdam, 25-29 September*. 2017. `https://doi.org/10.4229/EUPVSEC20172017-6DO.6.1`

  This contribution presents PVGIS version 5. One of the new features is the inclusion of ERA5 and COSMO-REA6 for simulating PV systems in Northern Europe.

6.3.2 Other related contributions

International journals

- Urraca, R., Antonanzas, J., Martinez-de-Pison, F.J., Antonanzas-Torres, F.. Estimation of solar global irradiation in remote areas. *Journal of Renewable and Sustainable Energy* 2015;7: 023136. URL: `https://doi.org/10.1063/1.4919084`
- Urraca, R., Antonanzas, J., Alia-Martinez, M., Martinez-de-Pison, F.J., Antonanzas-Torres, F.. Smart baseline models for solar irradiation forecasting. *Energy Conversion and Management* 2016;108:539-548. URL: `https://doi.org/10.1016/j.enconman.2015.11.033`
- Antonanzas, J., Urraca, R., Martinez-de-Pison, F.J., Antonanzas, F.. Optimal solar tracking strategy to increase irradiance in the plane of array under cloudy conditions: A study across Europe. *Solar Energy* 2018;163:122-130. URL: `https://doi.org/10.1016/j.solener.2018.01.080`.

International conferences

- Urraca, R., Antonanzas-Torres, F., Martinez-de-Pison, F.J., Perpiñan-Lamigueiro, O., Antonanzas J.. Irradiation forecasting using genetic algorithms and random forests. In: *XIV World Renewable Energy Congress, Bucarest, June 8-12*. 2015.
- Urraca, R., Antonanzas, J., Antonanzas-Torres, F., Martinez-de-Pison, F.J.. Estimation of daily global horizontal irradiation using extreme gradient boosting machines. In: *International Joint Conference SOCO'16-CISIS'16-ICEUTE'16. San Sebastián, Spain, October 19-21*. 2016. `https://doi.org/10.1007/978-3-319-47364-2_11`

Bibliography

[1] Huld, T., Bodis, K., Pinedo Pascua, I., Dunlop., E., Taylor, N., Jäger-Waldau, A.. The rooftop potential for PV systems in the European Union to deliver the Paris Agreement. *European Energy Innovation* 2018;Spring 2018:12–15. URL: http://www.europeanenergyinnovation.eu/PDF-Publications.

[2] Arantegui, R., Jäger-Waldau, A.. Photovoltaics and wind status in the European Union after the Paris Agreement. *Renewable and Sustainable Energy Reviews* 2018;81:2460–2471. URL: http://dx.doi.org/10.1016/j.rser.2017.06.052.

[3] Jäger-Waldau, A.. PV status report 2017. European Comission; 2017. URL: https://ec.europa.eu/jrc/en/publication/eur-scientific-and-technical-research-reports/pv-status-report-2017.

[4] EUROSTAT. Renewable energy statistics. 2018. URL: http://ec.europa.eu/eurostat/statistics-explained/index.php/Renewable_energy_statistics; [accessed 26.04.18].

[5] Comisión de Expertos de Transición Energética. Análisis y propuestas para la descarbonización. Ministerio de Energía, Turimso y Agenda Digital (MINETAD); 2018. URL: http://www.minetad.gob.es/es-ES/GabinetePrensa/NotasPrensa/2018/Documents/Resumen%2020180402%20Veditado.pdf.

[6] MIT. The future of solar energy. An interdisciplinary MIT study; 2015. URL: http://energy.mit.edu/research/future-solar-energy/.

[7] IRENA. Renewable power generation costs in 2017. International Renewable Energy Agency, Abu Dhabi.; 2018. URL: http://www.irena.org/publications/2018/Jan/Renewable-power-generation-costs-in-2017.

[8] DG Energy. Quarterly Report on European electricity markets. Directorate General for Energy. Volume 10 (issue 4; fourth quarter of 2017); 2018. URL: https://ec.europa.eu/energy/en/data-analysis/market-analysis.

[9] Kougias, I., Szabo, S., Monforti-Ferrario, F., Huld, T., Bodis, K.. A methodology for optimization of the complementaritiy between small-hydropower plants and solar PV systems. *Renewable Energy* 2016;87:1023–1030. URL: http://dx.doi.org/10.1016/j.renene.2015.09.073.

[10] Müller, B., Hardt, L., Armbruster, A., Kiefer, K., Reise, C.. Yield predictions for photovoltaic power plants: empirical validation, recent advances and remaining uncertainties. *Progress in Photovoltaics* 2016;24:570–583. URL: http://dx.doi.org/10.1002/pip.2616.

[11] Thevenard, D., Pelland, S.. Estimating the uncertainty in long-term photovoltaic yield predictions. *Solar Energy* 2013;91:432–445. URL: http://dx.doi.org/10.1016/j.solener.2011.05.006.

[12] GeoModel Solar. Solargis pvPlanner. User manual; 2016. URL: https://solargis2-web-assets.s3.eu-west-1.amazonaws.com/public/doc/e9989f5001/Solargis-pvPlanner-user-manual.pdf.

[13] Richter, M., De Brabandere, K., Kalisch, J., Schmidt, T., Lorenz, E.. Best Practice Guide On Uncertainty in PV Modelling. 3E – University of Oldenburg; 2015. URL: http://www.perfplus.eu/frontend/files/userfiles/files/308991_PerfPlus_Deliverable_D2_4_20150205.pdf.

[14] Müller, B., Reise, C., Heydenreich, W., Kiefer, K.. Are yield certificates reliable? A comparison to monitored real world results. In: *22nd European Photovoltaic Solar Energy Conference and Exhibition, September 3–7, 2007, Milan, Italy*. 2007:1–4. URL: http://dx.doi.org/10.13140/2.1.3209.4405.

[15] Müller, B., Bostock, P., Farnung, B., Reise, C.. A framework to calculate uncertainties for lifetime energy yield predictions of PV systems. In: *IEEE PV Specialist Conference (PVSC), 25-30 June 2017, Washington, USA*. 2017:1–5.

[16] Müller, B., Wild, M., Driesse, A., Behrens, K.. Rethinking solar resource assessments in the context of global dimming and brightening. *Solar Energy* 2014;99:272–282. URL: http:

//dx.doi.org/10.1016/j.solener.2013.11.013.

[17] McArthur, L.J.B.. World Climate Research Programme - Baseline Surface Radiation Network (BSRN) - Operations Manual Version 2.1. Downsview, Ontario, CANADA, Experimental Studies Division, Atmospheric Environment Service; 2005. URL: http://epic.awi.de/30644/.

[18] Polo, J., Wilbert, S., Ruiz-Arias, J.A., Meyer, R., Gueymard, C., Súri, M., Martín, L., Mieslinger, T., Blanc, P., Grant, I., Boland, J., Ineichen, P., Remund, J., Escobar, R., Troccoli, A., Sengupta, M., Nielsen, K.P., Renne, D., Geuder, N., Cebecauer, T.. Preliminary survey on site-adaptation techniques for satellite-derived and reanalysis solar radiation datasets. *Solar Energy* 2016;132:25–37. URL: http://dx.doi.org/10.1016/j.solener.2016.03.001.

[19] Sengupta, M., Habte, A., Gueymard, C., Wilbert, S., Renné, D.. Best practices handbook for the collection and use of solar resource data for solar energy applications: Second edition. NREL technical report, NREL/TP-5D00-68886; 2017. URL: https://www.nrel.gov/docs/fy18osti/68886.pdf.

[20] Wild, M.. Global dimming and brightening: A review. *Journal of Geophysical Research* 2009;11:1–31. URL: httpx://doi.org/10.1029/2008JD011470.

[21] Gracia Amillo, A., Huld, T., Müller, R.. A new database of global and direct solar radiation using the Eastern Meteosat satellite, models and validation. *Remote Sensing* 2014;6:8165–8189. URL: http;//dx.doi.org/10.3390/rs6098165.

[22] Pfeifroth, U., Kothe, S., Trentmann, J.. Validation report Meteosat solar surface SARAH-2. CM SAF; 2016. URL: https://dx.doi.org/10.5676/EUM_SAF_CM/SARAH/V002.

[23] Bojanowski, J.S., Vrieling, A., Skidmore, A.K.. A comparison of data sources for creating a long-term time series of daily gridded solar radiation for Europe. *Solar Energy* 2014;99:152–71. URL: http://dx.doi.org/10.1016/j.solener.2013.11.007.

[24] Boilley, A., Wald, L.. Comparison between meteorological re-analyses from ERA-Interim and MERRA and measurements of daily solar irradiation at surface. *Renewable Energy* 2015;75:135–43. URL: http://dx.doi.org/10.1016/j.renene.2014.09.042.

[25] Cole, I., Palmer, D., Goss, B., Gottschalg, R.. Impact analysis of irradiance dataset selection on photovoltaic system energy yield modeling. In: *1st International Conference on Large-Scale Grid Integration of Renewable Energy in India, 6-8 September 2017, New Delhi, India*. 2017:1–10.

[26] Gueymard, C.A., Ruiz-Arias, J.A.. Extensive worldwide validation and climate sensitivity analysis of direct irradiance predictions from 1-min global irradiance. *Solar Energy* 2016;128:1–30. URL: https://doi.org/10.1016/j.solener.2015.10.010.

[27] WMO. Guide to meteorological instruments and methods of observation: WMO No. 8. Geneva, Switzerland; 2014. URL: https://library.wmo.int/opac/doc_num.php?explnum_id=4147; updated 2017.

[28] ISO. ISO 9060:1990: Specification and classification of instruments for measuring hemispherical solar and direct solar radiation. Geneva, Switzerland; 1990. URL: https://www.iso.org/obp/ui/#iso:std:iso:9060:ed-1:v1:en.

[29] Becker, R., Behrens, K.. Quality assessment of heterogeneous surface radiation network data. *Advances in Science & Research* 2012;8:93–97. URL: http://dx.doi.org/10.5194/asr-8-93-2012.

[30] Huld, T., Gracia Amillo, A.M.. Estimating PV module performance over large geographical regions: The role of irradiance, air temperature, wind speed and solar spectrum. *Energies* 2015;8:5159–5181. URL: http://dx.doi.org/10.3390/en8065159.

[31] Moradi, I.. Quality control of global solar radiation using sunshine hours. *Energy* 2009;34(1):1–6. URL: http://dx.doi.org/10.1016/j.energy.2008.09.006.

[32] Journée, M., Bertrand, C.. Quality control of solar radiation data within the RMIB solar measurements network. *Solar Energy* 2011;85:72–86. URL: http://dx.doi.org/10.1016/j.solener.2010.10.021.

[33] Zahumenský, I.. Guidelines on quality control procedures for data from automatic weather stations. World Meteorological Organization; Geneva, Switzerland; 2004. URL: https://www.wmo.int/pages/prog/www/OSY/Meetings/ET-AWS3/Doc4(1).pdf.

[34] Younes, S., Claywell, R., Muneer, T.. Quality control of solar radiation data: Present status and proposed new approaches. *Energy* 2005;30:1533–1549. URL: http://dx.doi.org/10.1016/j.energy.2004.04.031.

[35] Driesse, A., Zaaiman, W., Riley, D., Taylor, N., Stein, J.S.. Investigation of pyranometer and photodiode calibrations under different conditions. In: *Photovoltaic Specialist Conference (PVSC), 5-10 June 2016, Portland, USA*. 2016:1–6. URL: http://dx.doi.org/10.1109/PVSC.2016.7749562.

[36] Driesse, A., Zaaiman, W., Riley, D., Taylor, N., Stein, J.S.. Indoor and outdoor evaluation of global irradiance sensors. In: *31st European Photovoltaic Solar Energy Conference, 14-18 September 2015, Hamburg, Germany*. 2015:1704–1709. URL: http://dx.doi.org/10.4229/EUPVSEC20152015-5CO.5.3.

[37] Driesse, A., Zaaiman, W.. Characterization of global irradiance sensors. In: *Photovoltaic Specialist Conference (PVSC), 14-19 June 2015, New Orleans, USA*. 2015:1–5. URL: http://dx.doi.org/10.1109/PVSC.2015.7356004.

[38] Sengupta, M., Gotseff, P., Stoffel, T.. Evaluation of photodiode and thermopile pyranometers for photovoltaic applications. NREL technical report, NREL/CP-5500-56540; 2012. URL: http://www.nrel.gov/docs/fy15osti/63112.pdf.

[39] Reda, I.. Method to calculate uncertainties in measuring shortwave solar irradiance using thermopile and semiconductor solar radiometers. NREL technical report, NREL/TP-3B10-52194; 2012. URL: https://www.nrel.gov/docs/fy11osti/52194.pdf.

[40] Habte, A., Wilcox, S., Stoffel, T.. Evaluation of radiometers deployed at the National Renewable Energy Laboratory's Solar Radiation Research Laboratory. NREL technical report, NREL/TP-5D00-60896; 2015. URL: https://www.nrel.gov/docs/fy14osti/60896.pdf.

[41] Vuilleumier, L., Hauser, M., Félix, C., Vignola, F., Blanc, P., Kazantzidis, A., Calpini, B.. Accuracy of ground surface broadband shortwave radiation monitoring. *Journal of Geophysical Research: Atmospheres* 2014;119:838–860. URL: http://dx.doi.org/10.1002/2014JD022335.

[42] Geuder, N., Affolter, R., Krass, B., Wilbert, S.. Long-term behavior, accuracy and drift of LI-200 pyranometers as radiation sensors in Rotating Shadowband Irradiometers (RSI). *Energy Procedia* 2014;49:2330–2339. URL: http://dx.doi.org/10.1016/j.egypro.2014.03.247.

[43] Wilbert, S., Kleindiek, S., Nouri, B., Geuder, N., Habte, A., Schwandt, M., Vignola, F.. Uncertainty of rotating shadowband irradiometers and Si-pyranometers including the spectral irradiance error. *AIP Conference Proceedings* 2015;1734(1):150009. URL: http://dx.doi.org/10.1063/1.4949241.

[44] Al-Rasheedi, M., Gueymard, C., Ismail, A., Hussain, T.. Comparison of two sensor technologies for solar irradiance measurement in a desert environment. *Solar Energy* 2018;161:194–2016. URL: https://doi.org/10.1016/j.solener.2017.12.058.

[45] Roesch, A., Wild, M., Ohmura, A., Dutton, E.G., Long, C.N., Zhang, T.. Assessment of BSRN radiation records for the computation of monthly means. *Atmospheric Measurement Techniques* 2011;4:339–354. URL: http://dx.doi.org/10.5194/amt-4-339-2011.

[46] NREL. Users manual for SERI QC software - Assessing the quality of solar radiation data. Tech. Rep.; National Renewable Energy Laboratory (NREL), Golden, CO; 1993. URL: http://www.nrel.gov/docs/legosti/old/5608.pdf.

[47] Molineaux, B., Ineichen, P.. Automatic quality control of daylight measurement: software for IDMP stations; 2003. URL: http://idmp.ente.fr.

[48] Geiger, M., Diabatè, L., Mènard, L., Wald, L.. Controlling the quality of solar irradiation data by means of a web service. In: *European Geophysical Society, 27th General Assembly, April 2002, Nice, France*. 2002:A–03419. URL: https://hal-mines-paristech.archives-ouvertes.fr/hal-00465569.

[49] Hoyer-Klick, C., Beyer, H.G., Dumortier, D., Schroedter-Homscheidt, M., Wald, L., Martinoli, M., Schilings, C., Gschwind, B., Menard, L., Gaboardi, E., Ramirez-Santigosa, L., Polo, J., Cebecauer, T., Huld, T., Súri, M., de Blas, M., Lorenz, E., Pfatischer, R., Remund, J., Ineichen, P., Tsvetkov, A., Hofierka, J.. MESOR. Management and Exploitation of Solar Resource Knowledge. In: *Proceeding of the EUROSUN 2008, 1st International Conference on Solar Heating, Cooling and Buildings, Lisbon, Portugal, October 2008*. 2008:7–10. URL: http://proceedings.ises.org/paper/eurosun2010/eurosun2010-0245-HoyerKlick.pdf.

[50] Ohmura, A., Dutton, E.G., Forgan, B., Fröhlich, C., Gilgen, H., Hegner, H., Heimo, A., König-Langlo, G., McArthur, B., Müller, G., Philipona, R., Pinker, R., Whitlock, C.H., Dehne, K., Wild, M.. Baseline Surface Radiation Network (BSRN/WCRP): New precision radiometry for climate research. *Bulletin of the American Meteorological Society* 1998;79:2115–2136. URL: https://doi.org/10.1175/1520-0477(1998)079<2115:BSRNBW>2.0.CO;2.

[51] Long, C.N., Dutton, E.G.. BSRN Global Network recommended QC tests, V2.0. *BSRN Technical Report* 2002;URL: http://ezksun3.ethz.ch/bsrn/admin/dokus/qualitycheck.pdf.

[52] Long, C.N., Shi, Y.. An automated quality assessment and control algorithm for surface radiation measurements. *The Open Atmospheric Science Journal* 2008;2:23–27. URL: http://dx.doi.org/10.2174/1874282300802010023.

[53] Perez, R., Ineichen, P., Seals, R., Zelenka, A.. Making full use of the clearness index for parameterizing hourly insolation conditions. *Solar Energy* 1990;45(2):111–114. URL: https:

//doi.org/10.1016/0038-092X(90)90036-C.

[54] Pashiardis, S., Kalogirou, S.A.. Quality control of solar shortwave and terrestrial longwave radiation for surface radiation measurements at two sites in Cyprus. *Renewable Energy* 2016;96:1015–1033. URL: http://dx.doi.org/10.1016/j.renene.2016.04.001.

[55] Tang, W., Yung, K., J., H., Qin, J.. Quality control and estimation of global solar radiation in China. *Solar Energy* 2010;84:466–475. URL: http://dx.doi.org/10.1016/j.solener.2010.01.006.

[56] Schwandt, M., Chhatbar, K., Meyer, R., Mitra, I., Vashistha, R., Giridhar, G., Gomathinayagam, S., Kumar, A.. Quality check procedures and statisitcs for the Indian SRRA solar radiation measurement network. *Energy Procedia* 2014;57:1227–1236. URL: http://dx.doi.org/10.1016/j.egypro.2014.10.112.

[57] Moreno-Tejada, S., Ramírez-Santigosa, L., Silva-Pérez, M.A.. A proposed methodology for quick assessment of timestamp and quality control results of solar radiation data. *Renewable Energy* 2015;78:531–537. URL: https://doi.org/10.1016/j.renene.2015.01.031.

[58] Ineichen, P.. Solar radiation resource in Geneva: measurements, modeling, data quality control, format and accessibility. Université de Gèneve, ID: unige:29599; 2013. URL: http://archive-ouverte.unige.ch/unige:29599.

[59] Urraca, R., Martinez-de Pison, E., Sanz-Garcia, A., Antonanzas, J., Antonanzas-Torres, F.. Estimation methods for global solar radiation: Case study evaluation of different approaches in central Spain. *Renewable & Sustainable Energy Reviews* 2017;77:1098–1113. URL: http://dx.doi.org/10.1016/j.rser.2016.11.222.

[60] Besharat, F., Dehghan, A.A., Faghih, A.R.. Empirical models for estimating global solar radiation: A review and case study. *Renewable & Sustainable Energy Reviews* 2013;21:798–821. URL: http://dx.doi.org/10.1016/j.rser.2012.12.043.

[61] Angstrom, A.. Solar and terrestrial radiation. report to the international commission for solar research on actinometric investigations of solar and atmospheric radiation. *Quarterly Journal of the Royal Meteorological Society* 1924;50(210):121–5. URL: http://dx.doi.org/10.1002/qj.49705021008.

[62] Prescott, J.. Evaporation from water surface in relation to solar radiation. *Transactions of the Royal Society of South Australia* 1940;64:114–8.

[63] Black, J.N.. The distribution of solar radiation over the Earth's surface. *Archiv f́ur Meteorologie, Geophysik und Bioklimatologie* 1956;7(2):165–89. URL: http://dx.doi.org/10.1007/BF02243320.

[64] Supit, I., van Kappel, R.R.. A simple method to estimate global radiation. *Solar Energy* 1998;63(3):147–60. URL: http://dx.doi.org/10.1016/S0038-092X(98)00068-1.

[65] Bristow, K.L., Campbell, G.S.. On the relationship between incoming solar radiation and daily maximum and minimum temperature. *Agricultural and Forest Meteorology* 1984;31(1):41–59. URL: http://dx.doi.org/10.1016/0168-1923(84)90017-0.

[66] Hargreaves, G.H., Samani, Z.A.. Estimating potential evapotranspiration. *Journal of Irrigation and Drainage Engineering* 1982;108:223–30.

[67] de Jong, R., Stewart, D.W.. Estimating global solar radiation from common meteorological observations in western Canada. *Canadian Journal of Plant Science* 1993;73(2):509–18. URL: http://dx.doi.org/10.4141/cjps93-068.

[68] Liu, D.L., Scott, B.J.. Estimation of solar radiation in Australia from rainfall and temperature observations. *Agricultural and Forest Meteorology* 2001;106(2):159–66. URL: http://dx.doi.org/10.1016/S0168-1923(00)00173-8.

[69] Antonanzas-Torres, F., Sanz-Garcia, A., Martínez-de Pisón, F.J., Perpiñán-Lamigueiro, O.. Evaluation and improvement of empirical models of global solar irradiation: Case of study northern Spain. *Renewable Energy* 2013;60:604–14. URL: http://dx.doi.org/10.1016/j.renene.2013.06.008.

[70] Siqueira, A.N., Tiba, C., Fraidenraich, N.. Generation of daily solar irradiation by means of artificial neural net works. *Renewable Energy* 2010;35(11):2406–14. URL: http://dx.doi.org/10.1016/j.renene.2010.03.019.

[71] Martí, P., Gasque, M.. Improvement of temperature-based ANN models for solar radiation estimation through exogenous data assistance. *Energy Conversion and Management* 2011;52(2):990–1003. URL: http://dx.doi.org/10.1016/j.enconman.2010.08.027.

[72] Dahmani, K., Notton, G., Voyant, C., Dizene, R., Nivet, M.L., Paoli, C., Tamas, W.. Multilayer perceptron approach for estimating 5-min and hourly horizontal global irradiation from exogenous meteorological data in locations without solar measurements. *Renewable Energy* 2016;90:267–82. URL: http://dx.doi.org/10.1016/j.renene.2016.01.013.

[73] Benghanem, M., Mellit, A., Alamri, S.N.. ANN-based modeling and estimation of daily global solar radiation data: A case study. *Energy Conversion and Management* 2009;50(7):1644–55. URL: `http://dx.doi.org/10.1016/j.enconman.2009.03.035`.

[74] Antonanzas-Torres, F., Urraca, R., Fernandez-Ceniceros, J., Martinez-de Pison, F.J.. Generation of daily global solar irradiation with support vector machines for regression. *Energy Conversion and Management* 2015;96:277–86. URL: `http://dx.doi.org/10.1016/j.enconman.2015.02.086`.

[75] Antonanzas, J., Urraca, R., Martinez-de Pison, F.J., Antonanzas-Torres, F.. Solar irradiation mapping with exogenous data from support vector regression machines estimations. *Energy Conversion and Management* 2015;100:380–90. URL: `http://dx.doi.org/10.1016/j.enconman.2015.05.028`.

[76] Chen, J.L., Li, G.S., Wu, S.J.. Assessing the potential of support vector machine for estimating daily solar radiation using sunshine duration. *Energy Conversion and Management* 2013;75:311–8. URL: `http://dx.doi.org/10.1016/j.enconman.2013.06.034`.

[77] Urraca, R., Antonanzas, J., Alia-Martinez, M., Martinez-de Pison, F.J., Antonanzas-Torres, F.. Smart baseline models for solar irradiation forecasting. *Energy Conversion and Management* 2016;108:539–48. URL: `http://dx.doi.org/10.1016/j.enconman.2015.11.033`.

[78] Kisi, O.. Modeling solar radiation of Mediterranean region in Turkey by using fuzzy genetic approach. *Energy* 2014;64:429–36. URL: `http://dx.doi.org/10.1016/j.energy.2013.10.009`.

[79] Urraca, R., Antonanzas, J., Martinez-de Pison, F.J., Antonanzas-Torres, F.. Estimation of solar global irradiation in remote areas. *Journal of Renewable and Sustainable Energy* 2015;7(2):1–14. URL: `http://dx.doi.org/10.1063/1.4919084`.

[80] Salcedo-Sanz, S., Casanova-Mateo, C., Pastor-Sánchez, A., Sanchez-Girón, M.. Daily global solar radiation prediction based on a hybrid Coral Reefs Optimization - Extreme Learning Machine approach. *Solar Energy* 2014;105:91–8. URL: `http://dx.doi.org/10.1016/j.solener.2014.04.009`.

[81] Sengupta, M., Xie, Y., Lopez, A., Habte, A., Maclaurin, G., Shelby, J.. The National Solar Radiation Database (NSRDB). *Renewable and Sustainable Energy Reviews* 2018;89:51–60. URL: `https://doi.org/10.1016/j.rser.2018.03.003`.

[82] Qu, Z., Oumbe, A., Blanc, P., Espinar, B., Gesell, G., Gschwind, B., Klüser, L., Lefèvre, M., Saboret, L., Schroedter-Homscheidt, M., Wald, L.. Fast radiative transfer parameterisation for assessing the surface solar irradiance: The Heliosat-4 method. *Meteorologische Zeitschrift* 2017;26(1):33–57. URL: `http://dx.doi.org/10.1127/metz/2016/0781`.

[83] Müller, R.W., Matsoukas, C., Behr, H.D., Gratzki, A., Hollmann, R.. The CM-SAF operational scheme for the satellite based retrieval of solar surface irradiance - a LUT based eigenvector hybrid approach. *Remote Sensing of Environment* 2009;113:1012–24. URL: `http://dx.doi.org/10.1016/j.rse.2009.01.012`.

[84] SOLARGIS. SolarGIS Solar Resource Database. Description and accuracy. SOLARGIS; 2016. URL: `https://solargis.info.`

[85] Inman, R., Pedro, H., Coimbra, C.. Solar forecasting methods for renewable energy integration. *Progress in Energy and Combustion Science* 2013;39:535–576. URL: `http://dx.doi.org/10.1016/j.pecs.2013.06.002`.

[86] Gueymard, C.A.. Clear-sky irradiance predictions for solar resource mapping and large-scale applications: Improved validation methodology and detailed performance analysis of 18 broadband radiative models. *Solar Energy* 2012;86:2145–2169. URL: `http://dx.doi.org/10.1016/j.solener.2011.11.011`.

[87] Lefèvre, M., Oumbe, A., Blanc, P., Espinar, P., Gschwind, B., Qu, Z., Wald, L., Schroedter-Homscheidt, M., Hoyer-Klick, C., Arola, A., Benedetti, A., Kaiser, J.W., Morcrette, J.. McClear: a new model estimating downwelling solar radiation at ground level in clear-sky conditions. *Atmospheric Measurements Technology* 2013;6:2403–2418. URL: `https://doi.org/10.5194/amt-6-2403-2013`.

[88] Müller, R.W., Dagestad, K.F., Ineichen, P., Schroedter-Homscheidt, M., Cros, S., Dumortier, D., Kuhlemann, R., Olseth, J.A., Piernavieja, G., Reise, C., Wald, L., Heinemann, D.. Rethinking satellite-based solar irradiance modelling: The SOLIS clear-sky module. *Remote Sensing of Environment* 2004;91(2):160–174. URL: `http://dx.doi.org/10.1016/j.rse.2004.02.009`.

[89] Mayer, B., Kylling, A.. Technical note: The libRadtran software package for radiative transfer calculations - description and examples of use. *Atmospheric Chemistry and Physics* 2005;5(7):1855–77. URL: `http://dx.doi.org/10.5194/acp-5-1855-2005`.

[90] Cano, D., Monget, J.M., Albuisson, M., Guillard, H., Regas, N., Wald, L.. A method for

the determination of the global solar radiation from meteorological satellite data. *Solar Energy* 1986;37(1):31–39. URL: `http://dx.doi.org/10.1016/0038-092X(86)90104-0`.

[91] Beyer, H.G., Costanzo, C., Heinemann, D.. Modifications of the Heliosat procedure for irradiance estimates from satellite images. *Solar Energy* 1996;56:207–12. URL: `http://dx.doi.org/10.1016/0038-092X(95)00092-6`.

[92] Hammer, A., Heinemann, D., Hoyer, C., Kuhlemann, R., Lorenz, E., Müller, R., Beyer, H.G.. se assessment using remote sensing technologies. *Remote Sensing of Environment* 2003;86:423–32. URL: `http://dx.doi.org/10.1016/S0034-4257(03)00083-X`.

[93] Rigollier, C., Lefèvre, M., Wald, L.. The method Heliosat-2 for deriving shortwave solar radiation from satellite images. *Solar Energy* 2004;77(2):159–69. URL: `http://dx.doi.org/10.1016/j.solener.2004.04.017`.

[94] Polo, J., Bernardos, A., Navarro, A.A., Fernandez-Peruchena, C.M., Ramirez, L., Guisando, V., Martinez, S.. Solar resources and power potential mapping in Vietnam using satellite-derived and GIS-based information. *Energy Conversion and Management* 2015;98:348–58. URL: `http://dx.doi.org/10.1016/j.enconman.2015.04.016`.

[95] Polo, J.. Solar global horizontal and direct normal irradiation maps in Spain derived from geostationary satellites. *Journal of Atmoshperic and Solar-Terrestrial Physics* 2015;130-31:81–88. URL: `http://dx.doi.org/10.1016/j.jastp.2015.05.015`.

[96] Sanchez-Lorenzo, A., Enriquez-Alonso, A., Wild, M., Trentmann, J., Vicente-Serrano, S., Sanchez-Romero, A., Posselt, R., Hakuba, M.. Trends in downward surface solar radiation from satellite and ground observations over Europe 1983-2010. *Remote Sensing of Environment* 2017;189:108–117. URL: `https://doi.org/10.1016/j.rse.2016.11.018"`.

[97] CM SAF. The Satellite Application Facility on Climate Monitoring. 2015. URL: `http://www.cmsaf.eu/EN/Home/home_node.html`; [accessed 20.10.16].

[98] SoDa. Solar radiation Data. 2016. URL: `http://www.soda-is.com/eng/index.html`; [accessed 20.10.16].

[99] Castelli, M., Stöckli, R., Tetzlaff, A., Wagner, J.E., Belluardo, G., Zebisch, M., Petitta, M.. The HelioMont method for assessing solar irradiance over complex terrain: Validation and improvements. *Remote Sensing of Environment* 2014;152:603–613. URL: `http://dx.doi.org/10.1016/j.rse.2014.07.018`.

[100] DLR. Deutsches zentrum für Luft- und Raumfahrt - German Aerospace Center. 2016. URL: `http://www.dlr.de/dlr/en/desktopdefault.aspx/tabid-10002/`; [accessed 20.10.16].

[101] NASA/GEWEX. Surface radiation budget SRB. 2016. URL: `https://gewex-srb.larc.nasa.gov`.

[102] Riihelä, A., Carlund, T., Trentmann, J., Müller, R., Lindfors, A.V.. Validation of CM SAF surface solar radiation datasets over Finland and Sweden. *Remote Sensing* 2015;7(6):6663–82. URL: `http://dx.doi.org/10.3390/rs70606663`.

[103] Trentmann, J., Kothe, S.. Validation Report Surface Radiation CLARA-A2. CM SAF; 2016. URL: `https://dx.doi.org/10.5676/EUM_SAF_CM/CLARA_AVHRR/V002`.

[104] Thomas, C., Wey, E., Blanc, P., Wald, L., Lefèvre, M.. Validation of HelioClim-3 version 4, HelioClim-3 version 5 and MACC-RAD using 14 BSRN stations. *Energy Procedia* 2016;91:1059–1069. URL: `http://dx.doi.org/10.1016/j.egypro.2016.06.275`.

[105] Vernay, C., Pitaval, S., Blanc, P.. Review of satellite-based surface solar irradiation databases for the engineering, the financing and the operating of photovoltaic systems. *Energy Procedia* 2014;57:1383–91. URL: `http://dx.doi.org/10.1016/j.egypro.2014.10.129`; 2013 {ISES} Solar World Congress.

[106] Ineichen, P.. Long term satellite global, beam and diffuse irradiance validation. *Energy Procedia* 2014;48:1586–1596. URL: `http://dx.doi.org/10.1016/j.egypro.2014.02.179`.

[107] Sengupta, M., Habte, A., Kurtz, S., Dobos, A., Wilbert, S., Lorenz, E., Stoffel, T., Renné, D., Gueymard, C., Myers, D., Wilcox, S., Blanc, P., Perez, R.. Best practices handbook for the collection and use of solar resource data for solar energy applications. NREL technical report; 2015. URL: `http://www.nrel.gov/docs/fy15osti/63112.pdf`.

[108] Reanalyses.org. Advancing in Reanalysis. 2017. URL: `http://reanalyses.org`; [accessed 10.09.17].

[109] Zhang, X., Liang, S., Wang, G., Yao, Y., Jiang, B., Cheng, J.. Evaluation of reanalysis surface incident shortwave radiation products from NCEP, ECMWF, GSFC, and JMA, using satellite and surface observations. *Remote Sensing* 2016;8(3):225. URL: `http://dx.doi.org/10.3390/rs8030225`.

[110] You, Q., Sanchez-Lorenzo, A., Wild, M., Folini, D., Fraedrich, K., Ren, G., Shichang, K.. Decadal variation of surface solar radiation in the Tibetean Plateau from observations,

reanalysis and model simulations. *Climate Dynamics* 2013;40(7-8):2073–2086. URL: `http://dx.doi.org/10.1007/s00382-012-1383-3`.

[111] Zhao, L., Lee, X., Liu, S.. Correcting surface solar radiation of two data assimilation systems against FLUXNET observation in North America. *Journal of Geophysical Research: Atmospheres* 2013;118:9552–9564. URL: `http://dx.doi.org/10.1002/jgrd.50697`.

[112] Dee, D.P., Uppala, S.M., Simmons, A.J., Berrisford, P., Poli, P., Kobayashi, S., Andrae, U., Balmaseda, M.A., Balsamo, G., Bauer, P., Bechtold, P., Beljaars, A.C.M., van de Berg, L., Bidlot, J., Bormann, N., Delsol, C., Dragani, R., Fuentes, M., Geer, A.J., Haimberger, L., Healy, S.B., Hersbach, H., Hólm, E.V., Isaksen, L., Kållberg, P., Köhler, M., Matricardi, M., McNally, A.P., Monge-Sanz, B.M., Morcrette, J.J., Park, B.K., Peubey, C., de Rosnay, P., Tavolato, C., Thépaut, J.N., Vitart, F.. The ERA-Interim reanalysis: configuration and performance of the data assimilation system. *Quarterly Journal of the Royal Meteorological Society* 2011;137(656):553–97. URL: `http://dx.doi.org/10.1002/qj.828`.

[113] Harada, Y., Kamahori, H., Kobayashi, C., Endo, H., Kobayashi, S., Ota, Y., Onoda, H., Onogi, K., Miyaoka, K., Takahasi, K.. The JRA-55 reanalysis: Representation of atmospheric circulation and climate variability. *Journal of the Meteorological Society of Japan Ser II* 2016;94(3):269–302. URL: `https://dx.doi.org/10.2151/jmsj.2016-015`.

[114] Saha, S., Moorthi, S., Pan, H.L., Wu, X., Wang, J., Nadiga, S., Tripp, P., Kistler, R., Woollen, J., Behringer, D., Liu, H., Stokes, D., Grumbine, R., Gayno, G., Wang, J., Hou, Y.T., Chuang, H.Y., Juang, H.M.H., Sela, J., Iredell, M., Treadon, R., Kleist, D., Delst, P.V., Keyser, D., Derber, J., Ek, M., Meng, J., Wei, H., Yang, R., Lord, S., Dool, H.V.D., Kumar, A., Wang, W., Long, C., Chelliah, M., Xue, Y., Huang, B., Schemm, J.K., Ebisuzaki, W., Lin, R., Xie, P., Chen, M., Zhou, S., Higgins, W., Zou, C.Z., Liu, Q., Chen, Y., Han, Y., Cucurull, L., Reynolds, R.W., Rutledge, G., Goldberg, M.. The NCEP climate forecast system reanalysis. *Bulletin of the American Meteorological Society* 2010;91(8):1015–1057. URL: `https://doi.org/10.1175/2010BAMS3001.1`.

[115] ECMWF. ERA5 data documentation. European Centre for Medium-range Weather Forecast (ECMWF); 2017. URL: `https://software.ecmwf.int/wiki/display/CKB/ERA5+data+documentation`.

[116] Bollmeyer, C., Keller, J., Ohlwein, C., Wahl, S., Crewell, S., Friederichs, P., Hense, A., Keune, J., Kneifel, S., Pscheidt, I., Redl, S., Steinke, S.. Towards a high-resolution regional reanalysis for the European CORDEX system. *Quarterly Journal of the Royal Meteorological Society* 2015;141:1–15. URL: `https://dx.doi.org/10.1002/qj.2486`.

[117] Messinger, F., DiMego, G., Kalnay, E., Mithcell, K., Shafran, P., Ebisuzaki, W., Jović, J., Woolen, J., Rogers, E., Berbery, E., Ek, M., Grumbine, R., Higgins, W., Li, H., Lin, Y., Mankin, G., Parrish, D., Shi, W.. North America Regional Reanalysis. *Bulletin of the American Meteorological Society* 2006;87:343–360. URL: `http://dx.doi.org/10.1175/BAMS-87-3-343`.

[118] NCEP/UCAR, PMG. Arctic System Reanalysis version 2. National Center for Atmospheric Research/University Corporation for Atmospheric Research and Polar Meterology Group/Byrd Polar Research Center/The Ohio State University. Research Data Archive at the National Center for Atmospheric Research Computational and Information Systems Laboratory; 2017. URL: `http://rda.ucar.edu/datasets/ds631.1/`.

[119] Alexandri, G., Georgoulias, A., Meleti, C., Balis, D., Kourtidis, K., Sanchez-Lorenzo, A., Trentmann, J., Panis, P.. A high resolution satellite view of surface solar radiation over the climatically sensitive region of Eastern Mediterranean. *Atmospheric Research* 2017;188:107–121. URL: `http://dx.doi.org/10.1016/j.atmosres.2016.12.015`.

[120] Träger-Chatterjee, C., Müller, R.W., Trentmann, J., Bendix, J.. Evaluation of ERA-40 and ERA-interim re-analysis incoming surface shortwave radiation datasets with mesoscale remote sensing data. *Meteorologische Zeitschrift* 2010;19(6):631–640. URL: `https://dx.doi.org/10.1127/0941-2948/2010/0466`.

[121] Yi, Y., Kimball, J., Jones, L., Reichle, R., McDonald, K.. Evaluation of MERRA land surface estimates in preparation for the soil moisture active passive mission. *Journal of Climate* 2011;24:3797–3816. URL: `http://dx.doi.org/10.1175/2011JCLI4034.1`.

[122] Jurůs, P., Eben, K., Resler, J., Krč, P., Kasanickỳ, I., Pelikan, E., Brabec, M., Hosek, J.. Estimating climatological variability of solar energy production. *Solar Energy* 2013;98:255–264. URL: `http://dx.doi.org/10.1016/j.solener.2013.10.007`.

[123] Rienecker, M.M., Suarez, M.J., Gelaro, R., Todling, R., Bacmeister, J., Liu, E., Bosilovich, M.G., Schubert, S.D., Takacs, L., Kim, G.K., Bloom, S., Chen, J., Collins, D., Conaty, A., da Silva, A., Gu, W., Joiner, J., Koster, R.D., Lucchesi, R., Molod, A., Owens, T., Pawson, S., Pegion, P., Redder, C.R., Reichle, R., Robertson, F.R., Ruddick, A.G.,

Sienkiewicz, M., Woollen, J.. MERRA: NASA's Modern-Era Retrospective analysis for Research and Applications. *Journal of Climate* 2011;24(14):3624–48. URL: http://dx.doi.org/10.1175/JCLI-D-11-00015.1.

[124] Draper, C., Reichle, R.H., Koster, R.D.. Assessment of MERRA-2 Land Surface Energy Flux Estimates. NASA Global Modeling and Assimilation Office, Greenbelt, MD, USA; 2017. URL: ftp://gmaoftp.gsfc.nasa.gov/pub/data/csdraper/Draper_M2_sub2_DRAFT.pdf.

[125] Pfenninger, S., Staffell, I.. Long-term patterns of European PV output using 30 years of validated hourly reanalysis and satellite data. *Energy* 2016;114:1251–1265. URL: http://dx.doi.org/10.1016/j.energy.2016.08.060.

[126] Wang, A., Zeng, X.. Evaluation of multireanalysis products with in situ observations over the Tibetan Plateau. *Journal of Geophyiscal Research* 2012;117. URL: http://dx.doi.org/10.1029/2011JD016553.

[127] Decker, M., Brunke, M., Wang, Z., Sakaguchi, K., Zeng, X., Bosilovich, M.. Evaluation of the reanalysis products from the GSFC, NCEP, and ECMWF using flux tower observations. *Journal of Climate* 2012;25:1916–1944. URL: https://dx.doi.org/10.1175/JCLI-D-11-00004.1.

[128] Jones, P.D., Harpham, C., Troccoli, A., Gschwind, B., Ranchin, T., Wald, L., Goodess, C.M., Dorling, S.. Using ERA-Interim reanalysis output for creating datasets of energy-relevant climate variables. *Earth System Science Data* 2017;9:471–495. URL: https://dx.doi.org/10.5194/essd-2016-67.

[129] Alsamamra, H., Ruiz-Arias, J.A., Pozo-Vázquez, D., Tovar-Pescador, J.. A comparative study of ordinary and residual kriging techniques for mapping global solar radiation over southern Spain. *Agricultural and Forest Meteorology* 2009;149(8):1343–57. URL: http://dx.doi.org/10.1016/j.agrformet.2009.03.005.

[130] Ruiz-Arias, J.A., Pozo-Vázquez, D., Santos-Alamillos, F.J., Lara-Fanego, V., Tovar-Pescador, J.. A topographic geostatistical approach for mapping monthly mean values of daily global solar radiation: A case study in southern Spain. *Agricultural and Forest Meteorology* 2011;151(12):1812–22. URL: http://dx.doi.org/10.1016/j.agrformet.2011.07.021.

[131] Antonanzas-Torres, F., Cañizares, F., Perpiñán, O.. Comparative assessment of global irradiation from a satellite estimate model (CM SAF) and on-ground measurements (SIAR): A Spanish case study. *Renewable & Sustainable Energy Reviews* 2013;21:248–61. URL: http://dx.doi.org/10.1016/j.rser.2012.12.033.

[132] Park, J.K., Das, A., Park, J.H.. A new approach to estimate the spatial distribution of solar radiation using topographic factor and sunshine duration in South Korea. *Energy Conversion and Management* 2015;101:30–39. URL: http://dx.doi.org/10.1016/j.enconman.2015.04.021.

[133] Chelbi, M., Gagnon, Y., Waewsak, J.. Solar radiation mapping using sunshine duration-based models and interpolation techniques: Application to Tunisia. *Energy Conversion and Management* 2015;101:203–15. URL: http://dx.doi.org/10.1016/j.enconman.2015.04.052.

[134] Evrendilek, F., Ertekin, C.. Statistical modeling of spatio-temporal variability in monthly average daily solar radiation over Turkey. *Sensors* 2007;7(11):2763 – 78. URL: http://dx.doi.org/10.3390/s7112763.

[135] Ertekin, C., Evrendilek, F.. Spatio-temporal modeling of global solar radiation dynamics as a function of sunshine duration for Turkey. *Agricultural and Forest Meteorology* 2007;145(1-2):36–47. URL: 10.1016/j.agrformet.2007.04.004.

[136] Moreno, A., Gilabert, M.A., Martínez, B.. Mapping daily global solar irradiation over Spain: A comparative study of selected approaches. *Solar Energy* 2011;85(9):2072–84. URL: http://dx.doi.org/10.1016/j.solener.2011.05.017.

[137] Antonanzas-Torres, F., Martinez-de Pison, F.J., Antonanzas, J., Perpiñán, O.. Downscaling of global solar irradiation in complex areas in R. *Journal of Renewable and Sustainable Energy* 2014;6:063105. URL: http://dx.doi.org/10.1063/1.4901539.

[138] Huld, T., Pinedo, I.. Spatial downscalling of 2-meter air temperature using operational forecast data. *Energies* 2015;8(4):2381–2411. URL: http://dx.doi.org/10.3390/en8042381.

[139] Antonanzas, J., Osorio, N., Escobar, R., Urraca, R., Martinez-de Pison, F., Antonanzas-Torres, F.. Review of photovoltaic power forecasting. *Solar Energy* 2016;136:78–111. URL: http://dx.doi.org/10.1016/j.solener.2016.06.069.

[140] Goss, B., Gottschalg, R., Betts, T.. Uncertainty analysis of photovoltaic energy yield prediction. In: *8th Photovoltaic Science Application and Technology (PVSAT-8) Conference and Exhibition,2-4 April 2012, Newcastle, England*. 2012:157–160.

[141] Reise, C., Müller, B., Moser, D., Belluardo, G., Ingenhoven, P.. Uncertainties in PV system yield predictions and assessments. International Energy Agency (IEA). Report IEA-PVPS T13-12:2018; 2018. URL: http://iea-pvps.org/index.php?id=477.

[142] European Commission JRC. PVGIS: Photovoltaic Geographical Information System. 2018. URL: `http://re.jrc.ec.europa.eu/pvgis.html`; [accessed 15.01.18].

[143] NREL. PVWatts Calculator. 2018. URL: `http://pvwatts.nrel.gov`; [accessed 10.01.18].

[144] GeoModel Solar. SOLARGIS pvPlanner. 2018. URL: `https://solargis.info/pvplanner/#tl=Google:hybrid&bm=satellite`; [accessed 10.01.18].

[145] Valentin Software. PV*SOL. 2018. URL: `http://pvsol-online.valentin-software.com/#/`; [accessed 10.01.18].

[146] Freeman, J., Whitmore, J., Blair, N., Dobos, A.P.. Validation of multiple tools for flat plate photovoltaic modeling against measured data. NREL technical report; 2014. URL: `https://www.nrel.gov/docs/fy14osti/61497.pdf`.

[147] Dirnberger, D., Müller, B., Reise, C.. PV module energy rating: opportunities and limitations. *Progress in Photovoltaics* 2015;23:1754–1770. URL: `http://dx.doi.org/10.1002/pip.2618`.

[148] Huld, T., Salis, E., Pozza, A., Herrmann, W., Müllejans, H.. Photovoltaic energy rating data sets for Europe. *Solar Energy* 2016;133:349–362. URL: `http://dx.doi.org/10.1016/j.solener.2016.03.071`.

[149] Liu, B., Jordan, R.. The interrelationship and characteristic distribution of direct, diffuse and total solar radiation. *Solar Energy* 1960;4:1–19. URL: `https://doi.org/10.1016/0038-092X(60)90062-1`.

[150] Liu, B., Jordan, R.. Daily insolation on surfaces tilted towards the equator. *Trans ASHRAE* 1962;53:526–541.

[151] Ineichen, P.. Global irradiance on tilted and oriented planes: model validations. University of Geneva; 2011. URL: `https://archive-ouverte.unige.ch/unige:23519`.

[152] Gracia, A.M., Huld, T.. Performance comparison of different models for the estimation of global irradiance on inclined surfaces. Validation of the model implemented in PVGIS. JRC Technical Report; 2013. URL: `https://publications.europa.eu/en/publication-detail/-/publication/4ef8c4e1-4397-4e27-8487-448786327f27`.

[153] Moretón, R., Lorenzo, E., Pinto, A., Muñoz, J., Narvarte, L.. From broadband horizontal to effective in-plane irradiation: A review of modelling and derived uncertainty for PV yield prediction. *Renewable and Sustainable Energy Reviews* 2017;78:886–903. URL: `https://dx.doi.org/10.1016/j.rser.2017.05.020`.

[154] de la Parra, I., Muñoz, M., Lorenzo, E., García, M., Marcos, J., Martínez-Moreno, F.. PV performance modeling: A review in the light of quality assurance for large PV plants. *Renewable and Sustainable Energy Reviews* 2017;78:780–797. URL: `http://dx.doi.org/10.1016/j.rser.2017.04.080`.

[155] Jerez, S., Tobin, I., Vautard, R., Montávez, J.P., López-Romero, J.M., Thais, F., Bartok, B., Christensen, O.B., Colette, A., Dèquè, M., Nikulin, G., Kotlarski, S., van Meijgaard, E., Teichmann, C., Wild, M.. The impact of climate change on photovoltaic power generation in Europe. *Nature Communications* 2015;6:10014:1–8. URL: `http://dx.doi.org/10.1038/ncomms10014`.

[156] Hansen, C.W., Martin, C.M.. Photovoltaic system modeling: uncertainty and sensitivity analyses. SANDIA Reports; 2015. URL: `http://prod.sandia.gov/techlib/access-control.cgi/2015/156700.pdf`.

[157] Müller, B., Heydenreich, W., Kiefer, K., Reise, C.. More insights from the monitoring of real world PV power plants - A comparison of measured to predicted performance of PV systems. In: *24th European Photovoltaic Solar Energy Conference, 21-25 September 2009, Hamburg, Germany*. 2009:3888–3892. URL: `http://dx.doi.org/10.4229/24thEUPVSEC2009-5AO.8.1`.

[158] BSRN. Baseline Surface Radiation Network. 2017. URL: `http://bsrn.awi.de`; [accessed 15.08.17].

[159] SMHI. Swedish Meteorological and Hydrological Institute. 2016. URL: `http://www.smhi.se/en`; [accessed 10.10.16].

[160] FMI. Finish Meteorological Institute. 2016. URL: `http://en.ilmatieteenlaitos.fi`; [accessed 10.10.16].

[161] DWD. Deutscher Wetterdienst. 2016. URL: `http://www.dwd.de/DE/Home/home_node.html`; [accessed 10.10.16].

[162] AEMET. Agencia Estatal de Meteorología. 2017. URL: `http://eportal.magrama.gob.es/websiar/Inicio.aspx`; [accessed 05.02.17].

[163] NIBIO-LMT. Norwegian Institute of Bioceonomy Research - Landbruksmeteorologisk Tjeneste. 2016. URL: `http://lmt.nibio.no/`; [accessed 10.10.16].

[164] JRC. Joint Research Centre, Ispra, ESTI meteo tower. 2016. URL: `http://iamest.jrc.it/meteo/meteo.php`; [accessed 10.10.16].

[165] SIAR. Servicio de Información Agroclimática para el Regadío. 2015. URL: `http://eportal.magrama.gob.es/websiar/Inicio.aspx`; [accessed 10.10.16].

[166] Meteo Navarra. Web de meteorología y climatología de Navarra. 2017. URL: `http://meteo.navarra.es`; [accessed 07.01.17].

[167] Meteocat. Servicio Meteorológico de Cataluña. 2017. URL: `http://www.meteo.cat`; [accessed 07.01.17].

[168] Euskalmet. Agencia vasca de meteorología. 2017. URL: `http://www.euskalmet.euskadi.eus`; [accessed 07.01.17].

[169] MeteoGalicia. Unidad de Observación y Predición Meteorológica de Galicia. 2017. URL: `http://www.meteogalicia.gal`; [accessed 07.01.17].

[170] SIAR La Rioja. Servicio de Información Agroclimático de La Rioja. 2017. URL: `http://www.larioja.org/agricultura/es/informacion-agroclimatica/datos-estaciones`; [accessed 07.01.17].

[171] SOS Rioja. Estaciones meteorológicas del Gobierno de La Rioja. 2017. URL: `http://www.larioja.org/emergencias-112/es/meteorologia`; [accessed 07.01.17].

[172] Müller, R., Behrendt, T., Hammer, A., Kemper, A.. A new algorithm for the satellite-based retrieveal of solar surface irradiance in spectral bands. *Remote Sensing* 2012;4:622–647. URL: `http://dx.doi.org/10.3390/rs4030622`.

[173] Müller, R., Pfeifroth, U., Träger-Chatterjee, C., Cremer, R., Trentmann, J., Hollmann, R.. Surface solar radiation data set - Heliosat (SARAH) - Edition 1. Satellite Application Facility on Climate Monitoring (CM SAF); 2015. URL: `http://dx.doi.org/10.5676/EUM_SAF_CM/SARAH/V001`.

[174] Pfeifroth, U., Kothe, S., Müller, R., Trentmann, J., Hollmann, R., Fuchs, P., Werscheck, M.. Surface Radiation Data Set - Heliosat (SARAH) - Edition 2. Satellite Application Facility on Climate Monitoring (CM SAF); 2017. URL: `http://dx.doi.org/10.5676/EUM_SAF_CM/SARAH/V002`.

[175] Karlsson, K., Riihelä, A., Müller, R., Meirink, J., Sedlar, J., Stengel, M., Lockhoff, M., Trentmann, J., Kaspar, F., Hollmann, R., Wolters, E.. CLARA-A1: CM SAF cLouds, Albedo and Radiation dataset from AVHRR data - Edition 1 - Monthly Means / Daily Means / Pentad Means / Monthly Histograms. Satellite Application Facility on Climate Monitoring (CM SAF); 2012. URL: `http://dx.doi.org/10.5676/EUM_SAF_CM/CLARA_AVHRR/V001`.

[176] Karlsson, K., Anttila, K., Trentmann, J., Stengel, M., Merinik, J., Devasthale, A., Hanschmann, T., Kothe, S., Jääskeläinen, E., Sedlar, J., Benas, N., van Zadelhoff, G., Schludnt, C., Stein, D., Finkensieper, S., Håkansson, N., Hollmann, R.. CLARA-A2: The second edition of the CM SAF cloud and radiation data record from 34 years of global AVHRR data. *Atmospheric Chemistry and Physics* 2016;:1–41URL: `http://dx.doi.org/10.5194/acp-2016-935`.

[177] Gelaro, R., McCarty, W., Suárez, M.J., Todling, R., Molod, A., Takacs, L., Randles, C.A., Darmenov, A., Bosilovich, M.G., Reichle, R., Wargan, K., Coy, L., Cullather, R., Draper, C., Akella, S., Buchard, V., Conaty, A., da Silva, A.M., Gu, W., Kim, G.K., Koster, R., Lucchesi, R., Merkova, D., Nielsen, J.E., Partyka, G., Pawson, S., Putman, W., Rienecker, M., Schubert, S.D., Sienkiewicz, M., Zhao, B.. The Modern-Era Retrospective Analysis for Research and Applications, version 2 (MERRA-2). *Journal of Climate* 2017;30(14):5419–5454. URL: `https://doi.org/10.1175/JCLI-D-16-0758.1`.

[178] Molod, A., Takacs, L., Suarez, L., Bacmeister, J.. Development of the GEOS-5 atmospheric general circulation model: evolution from MERRA to MERRA2. *Geoscientific Model Development* 2015;8:1339–1356. URL: `http://dx.doi.org/10.5194/gmd-8-1339-2015`.

[179] Wahl, S., Bollmeyer, C., Crewell, S., Figura, C., Friederichs, P., Hense, A., Keller, J.D., Ohlwein, C.. A novel convective-scale regional reanalysis COSMO-REA2: Improving the representation of precipitation. *Meteorologische Zeitschrift* 2017;:1–17URL: `http://dx.doi.org/10.1127/metz/2017/0824`.

[180] Schättler, U., Doms, G., Schraff, C.. A description of the non-hydrostatic regional model LM - Part VII: Users' guide, Technical report. Deutscher Wetterdienst: Offenbach, Germay; 2011.

[181] Frank, C., Wahl, S., Keller, J., Pospichal, B., Hense, A., Crewell, S.. Bias correction of a novel european reanalysis data set for solar energy applications. *Solar Energy* 2018;164:12–24. URL: `https://doi.org/10.1016/j.solener.2018.02.012`.

[182] Chen, Y., Bundy, D., Hoff, S.. Modeling the variation of wind speed with height for agricultural source pollution control. *Agricultural and Biosystems Engineering Publications* 1998;372. URL: `https://lib.dr.iastate.edu/abe_eng_pubs/372`.

[183] Leys, C., Ley, C., Klein, O., Bernard, P., Licata, L.. Detecting outliers: Do not use standard deviation around the mean, use absolute deviation around the median. *Journal of Experimental*

Social Psychology 2013;49(4):764–766. URL: http://dx.doi.org/10.1016/j.jesp.2013.03.013.

[184] Gueymard, C.. A review of validation methodologies and statistical performance indicators for modeled solar radiation data: Towards a better bankability of solar projects. *Renewable and Sustainable Energy Reviews* 2014;39:1024–1034. URL: http://dx.doi.org/10.1016/j.rser.2014.07.117.

[185] Farrance, I., Badrick, T., Sikaris, K.A.. Uncertainty in measurement and total error - are they so incompatible. *Clin Chem Lab Med* 2016;54(1):1309–1311. URL: http://dx.doi.org/10.1515/cclm-2016-0314.

[186] Vuilleumier, L., Félix, C., Vignola, F., Blanc, P., Badosa, J., Kazantzidis, A., Calpini, B.. Performance evaluation of radiation sensors for the solar energy sector. *Meteorologische Zeitschrift* 2017;26(5):485–505. URL: https://dx.doi.org/10.1127/metz/2017/0836.

[187] Muneer, T.. Solar radiation model for Europe. *Building Services Engineering Research & Technology* 1990;4:153–163. URL: http://dx.doi.org/10.1177/014362449001100405.

[188] Martin, N., Ruiz, J.. Calculation of the PV modules angular losses under field conditions by means of an analytical model. *Solar Energy Materials & Solar Cells* 2001;70(1):25–38. URL: http:dx.doi.org/10.1016/S0927-0248(00)00408-6.

[189] IEC. IEC 61853-2. Photovoltaic (PV) module performance testing and energy rating - Part 2: Spectral responsivity, incidence angle and module operating temperature measurements. International Electrotechnical Commission (IEC) Central Office; 2016. URL: https://webstore.iec.ch/publication/25811.

[190] Huld, T., Friesen, G., Skoczek, A., Kenny, R.P., Sample, T., Field, M., Dunlop, E.D.. A power-rating model for crystalline silicon PV modules. *Solar Energy Materials & Solar Cells* 2011;95:3359–3369. URL: 10.1016/j.solmat.2011.07.026.

[191] Faiman, D.. Assessing the outdoor operating temperature of photovoltaic modules. *Progress in Photovoltaics, Research and Applications* 2008;16:307–315. URL: http://dx.doi.org/10.1002/pip.813.

[192] Koehl, M., Heck, M., Wiesmeier, S., Wirth, J.. Modeling of the nominal operating cell temperature based on outdoor weathering. *Solar Energy Materials & Solar Cells* 2011;95:1638–1646. URL: http://dx.doi.org/10.1016/j.solmat.2011.01.020.

[193] Hérnandez, R., Maruri, M., Otxoa de Alda, K., Egaña, J., Gaztelumendi, S.. Quality control procedures at Euskalmet data center. *Advances in Science & Research* 2012;8:129–134. URL: http://dx.doi.org/10.5194/asr-8-129-2012.

[194] Mirás-Avalos, J., Rodríguez-Gomez, B., Meizoso-López, M., Sande-Fouz, P., González-García, M., Paz-González, A.. Data quality assessment and monthly stability of ground solar radiation in Galicia (NW Spain). *Solar Energy* 2012;86:2499–3511. URL: http://dx.doi.org/10.1016/j.solener.2011.09.017.

[195] Müller, R., Pfeifroth, U., Träger-Chatterjee, C., Trentmann, J., Cremer, R.. Digging the METEOSAT treasure - 3 decades of solar surface radiation. *Remote Sensing* 2015;7:8067–101. URL: http://dx.doi.org/10.3390/rs70608067.

[196] Riihela, A., Kallio, V., Devraj, S., Aharma, A., Lindfors, A.. Validation of SARAH-E satellite-based surface solar radiation estimates over India. *Remote Sensing* 2018;10(3):392. URL: http://dx.doi.org/doi:10.3390/rs10030392.

[197] Decoster, I., Clerbaux, N., Baudrez, E., Dewitte, S., Ipe, A., Nevens, S., Velazquez Blazquez, A., Cornelis, J.. Spectral aging model applied to Meteosat First Generation visible band. *Remote Sensing* 2014;6:2534–2571. URL: http://dx.doi.org/10.3390/rs6032534.

[198] Beyer, H., Costanzo, C., Heinemann, D.. Evaluation and assessment of the CM-SAF surface solar radiation climate data records. EUMETSAT Satelite Application Facility on Climate Monitoring, CDOP AS Study No 18; 2011. URL: http://www.cmsaf.eu/EN/Documentation/Reports/2007-now/CLM_AS10_P05.pdf?__blob=publicationFile&v=3.

[199] Suri, M., Cebecauer, T.. Satellite-based solar resource data: model validation statistics versus user's uncertainty. In: *ASES SOLAR 2014 Conference, San Francisco, 7-9 July 2014*. 2014:7–9.

[200] Trentmann, J., Müller, R.. Validation Report Surface Radiation CLARA-A1. CM SAF; 2012. URL: https://dx.doi.org/10.5676/EUM_SAF_CM/CLARA_AVHRR/V001.

[201] Hakuba, M., Folini, D., Sanchez-Lorenzo, A., M., W.. Spatial representativeness of ground-based solar radiation measurements. *Journal of Geophysical Research* 2013;88:8585–8597. URL: http://dx.doi.org/10.1002/jgrd.50673,2013.

[202] Posselt, R., Müller, R., Stöckli, R., Trentmann, J.. Remote sensing of solar surface radiation for climate monitoring - the CM SAF retrieval in international comparison. *Remote Sensing of Envirionment* 2012;118:186–198. URL: http://dx.doi.org/10.1016/j.rse.2011.11.016.

[203] Frank, C., Wahl, S., Keller, J., Pospihal, B., Hense, A., Crewell, S.. A novel data set for solar energy applications based on high resolution reanalysis COSMO-REA6. In: *5th International Conference on Reanalysis (ICR5), 13-17 November 2017, Rome, Italy*. 2017:URL: ftp://ftp.meteo.uni-bonn.de/pub/reana/presentations/Rome2017/radiation_bias_correction.pdf.

[204] Zubler, E.M., Lohmann, U., Lüthi, D., Schär, C.. Intercomparison of aerosol climatologies for use in a regional climate model over Europe. *Geophysical Research Letters* 2011;38(15):1–5. URL: http://dx.doi.org/10.1029/2011GL048081.

[205] García, R.D., García, O.E., Cuevas, E., Cachorro, V.E., Barreto, A., Guirado-Fuentes, C., Kouremeti, N., Bustos, J.J., Romero-Campos, P.M., de Frutos, A.M.. Aerosol optical depth retrievals at the Izaña Atmospheric Observatory from 1941 to 2013 by using artificial neural networks. *Atmospheric Measurement Techniques* 2016;9(1):53–62. URL: https://dx.doi.org/10.5194/amt-9-53-2016.

[206] Meyers, D.R.. Quantitative analysis of spectral impacts on silicon photodiode radiometers. NREL technical report, NREL/CP-5500-50936; 2011. URL: https://www.nrel.gov/docs/fy11osti/50936.pdf.

[207] Rodríguez, F., Fleetwood, A., Galarza, A., Fontán, L.. Predicting solar energy generation through artificial neural networks using weather forecasts for microgrid control. *Renewable Energy* 2018;126:855–864. URL: https://doi.org/10.1016/j.renene.2018.03.070.

[208] Pagola, I., Gastón, M., Fernández-Peruchena, C., Moreno, S., Ramírez, L.. New methodology of solar radiation evaluation using free access databases in specific locations. *Renewable Energy* 2010;35:2792–2798. URL: http://dx.doi.org/10.1016/j.renene.2010.04.034.

[209] Almorox, J., Hontoria, C., Benito, M.. Models for obtaining daily global solar radiation with measured air temperature data in Madrid (Spain). *Applied Energy* 2011;88:1703–1709. URL: http://dx.doi.org/10.1016/j.apenergy.2010.11.003.

[210] Ruiz-Arias, J., Quesada-Ruiz, S., Fernández, E., Gueymard, C.. Optimal combination of gridded and ground-observed solar radiation data for regional solar resource assessment. *Solar Energy* 2015;112:411–424. URL: http://dx.doi.org/10.1016/j.solener.2014.12.011.

[211] Rubio-Aliaga, A., Lozano-Sánchez, J., García-Cascales, M., Benhamou, M., Molina-García, A.. GIS based solar resource analysis for irrigation purposes: Rural areas comparison under groundwater scarcity conditions. *Solar Energy Materias & Solar Cells* 2016;156:128–139. URL: http://dx.doi.org/10.1016/j.solmat.2016.06.045.

[212] Rodriguez-Amigo, M., Diez-Mediavilla, M., Gonzalez-Peña, D., Perez-Burgos, A., Alonso-Tristan, C.. Mathematical interpolation methods for spatial esitmation of global horizontal irradiance in Castilla-León, Spain: A case of study. *Solar Energy* 2017;151:14–21. URL: http://dx.doi.org/10.1016/j.solener.2017.05.024.

[213] Huld, T., Suri, M., Dunlop, E.. Geographical variation of the conversion efficiency of crystalline silicon photovoltaic modules in Europe. *Progress in Photovoltaics: Research and Applications* 2008;16(7):595–607. URL: http://dx.doi.org/10.1002/pip.846.

Appendix A

List of weather stations

A.1 Global dataset

Table A.1: List of weather stations included in the global dataset.

Network	ID	Lon.[°]	Lat.[°]
BSRN	ALE	-62.42	82.49
BSRN	BER	-64.67	32.27
BSRN	BIL	-97.52	36.60
BSRN	BON	-88.37	40.07
BSRN	BOU	-105.01	40.05
BSRN	BRB	-47.71	-15.60
BSRN	CAB	4.93	51.97
BSRN	CAM	-5.32	50.22
BSRN	CAR	5.06	44.08
BSRN	CLH	-75.71	36.91
BSRN	CNR	-1.60	42.82
BSRN	COC	96.83	-12.19
BSRN	DAR	130.89	-12.43
BSRN	DRA	-116.02	36.63
BSRN	E13	-97.48	36.60
BSRN	EUR	-85.94	79.99
BSRN	FLO	-48.52	-27.60
BSRN	FPE	-105.10	48.32
BSRN	FUA	130.38	33.58
BSRN	GOB	15.04	-23.56
BSRN	ISH	124.16	24.34
BSRN	IZA	-16.50	28.31
BSRN	KWA	167.73	8.72
BSRN	LAU	169.69	-45.05
BSRN	LER	-1.18	60.14
BSRN	LIN	14.12	52.21
BSRN	MAN	147.43	-2.06
BSRN	MNM	153.98	24.29
BSRN	NAU	166.92	-0.52
BSRN	NYA	11.93	78.92
BSRN	PAL	2.21	48.71
BSRN	PSU	-77.93	40.72
BSRN	PTR	-40.32	-9.07
BSRN	REG	-104.71	50.20
BSRN	SAP	141.33	43.06
BSRN	SXF	-96.62	43.73
BSRN	TAM	5.53	22.79
BSRN	TAT	140.13	36.06
BSRN	TIK	128.92	71.59
BSRN	TOR	26.46	58.25
BSRN	XIA	116.96	39.75

A.2 European dataset

TABLE A.2: List of weather stations included in the European dataset.

Network	ID	Lon.[°]	Lat.[°]
BSRN	Ler	-1.18	60.14
BSRN	Cam	-5.33	50.22
BSRN	DWD_3015	14.12	52.21
BSRN	Car	5.06	44.08
BSRN	Pal	2.21	48.71
BSRN	Pay	6.94	46.81
BSRN	Cnr	-1.60	42.82
FMI	Parainen	21.37	59.78
FMI	Kaarina	22.55	60.39
FMI	Turku	22.18	60.45
FMI	Vantaa	24.96	60.33
FMI	Helsinki	24.96	60.20
FMI	Jokioinen	23.50	60.81
FMI	Asikkala	25.52	61.26
FMI	Lappeenranta	28.57	61.04
FMI	Parikkala	29.46	61.44
FMI	Kauhajoki	22.19	62.41
FMI	Virrat	23.55	62.33
FMI	Jyväskylä	25.68	62.40
FMI	Juva	27.89	61.89
FMI	Seinäjoki	22.49	62.94
FMI	Kuopio	27.32	63.14
FMI	Rautavaara	28.66	63.38
FMI	Ilomantsi	30.98	62.77
FMI	Toholampi	24.17	63.82
FMI	Pyhäjärvi	25.71	63.74
FMI	Sotkamo	28.34	64.11
FMI	Siikajoki	25.09	64.68
FMI	Oulu	25.40	65.01
FMI	Rovaniemi	25.84	66.56
FMI	Sodankylä	26.63	67.37
FMI	Rovaniemi_2	26.01	66.58
FMI	Muonio	24.12	67.97
FMI	Utsjoki	27.01	69.76
SMHI	Borlänge	15.43	60.48
SMHI	Göteborg	12.00	57.70
SMHI	Karlstad	13.47	59.37
SMHI	Kiruna	20.43	67.83
SMHI	Luleå	22.13	65.55
SMHI	Lund	13.22	55.72
SMHI	Norrköping	16.15	58.58
SMHI	Stockholm	18.07	59.35
SMHI	Umeå	20.25	63.82
SMHI	Växjö	14.73	56.93
SMHI	Visby	18.35	57.67
SMHI	Östersund	14.50	63.20
Met Office	23	-2.90	58.95
Met Office	44	-4.44	58.29
Met Office	48	-3.92	58.23
Met Office	54	-6.32	58.21
Met Office	66	-5.31	57.61
Met Office	67	-4.89	57.73
Met Office	79	-3.97	57.82
Met Office	105	-4.71	56.87
Met Office	113	-3.83	57.21
Met Office	132	-3.56	57.65
Met Office	161	-2.20	57.21
Met Office	163	-2.14	57.13
Met Office	177	-2.26	56.85
Met Office	212	-3.73	56.33
Met Office	235	-2.86	56.38
Met Office	268	-2.38	55.71
Met Office	315	-1.60	55.42
Met Office	326	-1.58	54.77
Met Office	370	-0.44	53.87
Met Office	384	-0.52	53.18
Met Office	395	0.14	52.87
Met Office	429	1.35	52.76
Met Office	435	0.57	52.26
Met Office	440	0.96	52.12
Met Office	456	-0.24	52.40
Met Office	458	-0.59	52.01
Met Office	461	-0.46	52.23
Met Office	471	-0.36	51.81
Met Office	533	-1.20	53.84
Met Office	534	-1.32	53.87
Met Office	535	-1.15	53.83
Met Office	554	-1.25	52.84
Met Office	556	-1.25	53.01
Met Office	583	-0.46	52.61
Met Office	586	-1.92	52.45
Met Office	587	-1.93	52.48
Met Office	595	-1.33	52.36
Met Office	643	-2.66	52.79
Met Office	669	-2.88	52.24
Met Office	676	-2.58	51.52
Met Office	692	-1.69	51.86
Met Office	708	-0.45	51.48

Network	ID	Lon.[°]	Lat.[°]
Met Office	1023	-3.21	55.31
Met Office	1033	-4.01	54.80
Met Office	1035	-3.95	54.93
Met Office	1046	-4.63	54.09
Met Office	1083	-2.68	54.50
Met Office	1125	-2.18	53.61
Met Office	1144	-2.98	53.18
Met Office	1145	-4.54	53.25
Met Office	1161	-4.74	52.79
Met Office	1190	-3.46	52.76
Met Office	1198	-4.57	52.14
Met Office	1205	-4.02	52.43
Met Office	1285	-3.61	51.09
Met Office	1302	-2.64	51.01
Met Office	1352	-3.90	50.77
Met Office	1378	-3.40	50.74
Met Office	1415	-4.67	50.50
Met Office	1450	-6.22	54.66
Met Office	1467	-6.15	55.18
Met Office	1568	-7.64	54.40
Met Office	4911	1.28	52.68
Met Office	17314	-1.53	54.30
Met Office	17346	-2.70	53.76
Met Office	18904	-2.25	53.47
Met Office	18905	-1.34	53.45
Met Office	18974	-6.88	56.50
Met Office	18993	0.12	52.21
Met Office	18995	-1.28	52.78
Met Office	19144	-0.11	51.52
Met Office	19187	-1.69	52.48
Met Office	19206	-3.44	51.40
Met Office	19260	-3.34	55.93
Met Office	24102	-1.53	52.42
Met Office	24125	-4.53	55.91
Met Office	24942	-1.12	52.62
Met Office	24948	-2.13	52.59
Met Office	25046	-2.98	53.41
Met Office	25054	-2.27	53.00
Met Office	25351	-1.22	54.57
Met Office	25727	-1.39	50.89
Met Office	30437	-7.57	54.15
Met Office	30620	-0.23	51.14
Met Office	55511	-2.15	53.34
Met Office	55827	-3.40	57.01
Met Office	56214	-0.66	51.49
Met Office	56286	-0.45	51.48
Met Office	56424	-1.93	52.46
Met Office	56471	-0.01	51.54
Met Office	56472	-0.02	51.54
Met Office	56963	-6.95	55.16
Met Office	57063	-7.59	54.33
Met Office	57199	-2.38	53.36
Met Office	57247	-1.42	50.78
Met Office	57250	-5.20	50.04
Met Office	57254	-2.50	55.30
Met Office	61843	0.49	52.83
Met Office	61844	-2.35	52.39
Met Office	61846	-1.92	50.97
Met Office	61847	-1.08	50.98
Met Office	61915	1.47	52.69
Met Office	61937	-2.37	54.18
Met Office	61938	-3.72	50.59
Met Office	61948	-2.32	52.78
Met Office	61949	-2.73	52.92
Met Office	61973	-1.73	53.26
DWD	183	13.43	54.68
DWD	656	10.60	51.72
DWD	662	10.45	52.29
DWD	691	8.80	53.05
DWD	853	12.87	50.79
DWD	1048	13.75	51.13
DWD	1358	12.95	50.43
DWD	1443	7.83	48.02
DWD	1580	7.95	49.99
DWD	1684	14.95	51.16
DWD	1957	11.95	51.51
DWD	1975	9.99	53.63
DWD	2290	11.01	47.80
DWD	2712	9.19	47.68
DWD	3028	8.84	51.79
DWD	3032	8.41	55.01
DWD	3098	7.64	51.25
DWD	3631	7.15	53.71
DWD	3668	11.05	49.50
DWD	3987	13.06	52.38
DWD	4271	12.08	54.18
DWD	4336	7.11	49.21
DWD	4466	9.55	54.53
DWD	4642	11.73	52.89
DWD	4928	9.20	48.83
DWD	5100	6.66	49.75
DWD	5404	11.69	48.40
DWD	5419	11.31	50.98
DWD	5440	10.93	49.01
DWD	5705	9.96	49.77
DWD	5779	13.75	50.73
DWD	5792	10.98	47.42
DWD	5856	13.35	48.55
DWD	5906	8.55	49.51
Meteo France	5183001	6.64	44.88
Meteo France	6088001	7.21	43.65
Meteo France	6094002	6.93	44.10

Network	ID	Lon.[°]	Lat.[°]
Meteo France	8401001	4.49	49.42
Meteo France	9024004	1.69	42.72
Meteo France	10228002	4.47	48.35
Meteo France	11069001	2.29	43.22
Meteo France	12145001	3.02	44.12
Meteo France	12254001	2.48	44.41
Meteo France	13054001	5.22	43.44
Meteo France	14066001	-0.43	49.33
Meteo France	14137001	-0.46	49.18
Meteo France	17300009	-1.19	46.18
Meteo France	18033001	2.36	47.06
Meteo France	20004002	8.79	41.92
Meteo France	21131001	5.17	47.03
Meteo France	21154001	4.58	47.85
Meteo France	21473001	5.09	47.27
Meteo France	25056001	5.99	47.25
Meteo France	26198001	4.73	44.58
Meteo France	27056003	0.56	49.10
Meteo France	29075001	-4.41	48.44
Meteo France	33281001	-0.69	44.83
Meteo France	34154001	3.96	43.58
Meteo France	35281001	-1.73	48.07
Meteo France	37179001	0.73	47.44
Meteo France	44020001	-1.61	47.15
Meteo France	47091001	0.59	44.17
Meteo France	49020001	-0.61	47.48
Meteo France	55386002	5.76	48.93
Meteo France	58218006	3.37	47.17
Meteo France	60175001	2.52	49.25
Meteo France	61169003	-0.59	48.75
Meteo France	61214002	0.66	48.76
Meteo France	62516002	2.50	50.58
Meteo France	63113001	3.15	45.79
Meteo France	64316003	-1.03	43.03
Meteo France	64549001	-0.42	43.38
Meteo France	66136001	2.87	42.74
Meteo France	67124001	7.64	48.55
Meteo France	68205001	7.41	47.93
Meteo France	69029001	4.94	45.73
Meteo France	71105001	4.80	46.30
Meteo France	73171002	6.05	45.49
Meteo France	75114001	2.34	48.82
Meteo France	80379002	2.38	49.87
Meteo France	85191003	-1.38	46.70
Meteo France	87085006	1.18	45.86
Meteo France	95527001	2.53	49.02
AEMET	B228	2.63	39.55
AEMET	B278	2.74	39.56
AEMET	B954	1.38	38.88
AEMET	0016A	1.16	41.14
AEMET	0076	2.07	41.29
AEMET	0201D	2.20	41.39
AEMET	0367	2.76	41.91
AEMET	1014A	-1.79	43.36
AEMET	1024E	-2.04	43.31
AEMET	1082	-2.91	43.30
AEMET	1111	-3.80	43.49
AEMET	1249X	-5.87	43.35
AEMET	1387	-8.42	43.37
AEMET	1387E	-8.37	43.31
AEMET	1428	-8.41	42.89
AEMET	1479I	-8.81	42.58
AEMET	1495	-8.62	42.24
AEMET	1549	-6.60	42.56
AEMET	1700X	-8.09	42.42
AEMET	2030	-2.48	41.77
AEMET	2422	-4.75	41.64
AEMET	2462	-4.01	40.79
AEMET	2661	-5.65	42.59
AEMET	2867	-5.50	40.96
AEMET	2871D	-5.67	40.96
AEMET	3129	-3.56	40.47
AEMET	3194U	-3.72	40.45
AEMET	3260B	-4.05	39.88
AEMET	3469A	-6.34	39.47
AEMET	4121	-3.92	38.99
AEMET	4478G	-7.01	38.88
AEMET	4642E	-6.91	37.28
AEMET	5402	-4.85	37.85
AEMET	5514	-3.63	37.14
AEMET	5530E	-3.79	37.19
AEMET	5783	-5.88	37.42
AEMET	5860E	-6.74	37.10
AEMET	5960	-6.06	36.75
AEMET	5973	-6.26	36.50
AEMET	6156	-4.48	36.72
AEMET	6325O	-2.36	36.85
AEMET	7031	-0.80	37.79
AEMET	7031X	-0.81	37.78
AEMET	7178I	-1.17	38.00
AEMET	8019	-0.57	38.28
AEMET	8178D	-1.86	39.01
AEMET	8368U	-1.12	40.35
AEMET	8414A	-0.47	39.48
AEMET	9091R	-2.73	42.87
AEMET	9170	-2.33	42.45
AEMET	9263D	-1.65	42.78
AEMET	9433	-1.07	41.68
AEMET	9443R	-0.91	41.63
AEMET	9771C	0.60	41.63
AEMET	9981A	0.49	40.82
LMT	Apelsvoll	10.87	60.70

Network	ID	Lon.[°]	Lat.[°]
LMT	Arnes	11.39	60.13
LMT	Åsbakk	10.77	59.67
LMT	Bø	9.03	59.42
LMT	Etne	5.95	59.66
LMT	Fåvang	10.19	61.46
LMT	Frosta	10.69	63.57
LMT	Fureneset	5.04	61.29
LMT	Gausdel	10.26	61.22
LMT	Gjerpen	9.58	59.23
LMT	Gran	10.56	60.36
LMT	Gvarv	9.21	59.38
LMT	Hjelmeland	6.15	59.23
LMT	Holt	18.91	69.65
LMT	Kise	10.81	60.77
LMT	Kvithamar	10.88	63.49
LMT	Landvik	8.52	58.34
LMT	Løken	9.06	61.12
LMT	Mære	11.43	63.94
LMT	Njøs	6.86	61.18
LMT	Osäker	11.04	59.32
LMT	Pasvik	30.04	69.46
LMT	Særheim	5.65	58.76
LMT	Sande	10.22	59.62
LMT	Sortland	15.28	68.65
LMT	Tjøtta	12.43	65.83
LMT	Ullensvang	6.65	60.32
LMT	Vagones	14.45	67.28
LMT	Valnesfjord	15.10	67.28
JRC	Ispra	8.61	45.81

A.3 Spanish dataset

TABLE A.3: List of weather stations included in the Spanish dataset.

Network	ID	Lon.[°]	Lat.[°]
SIAR	TO04	-4.66	39.72
SIAR	TO05	-5.14	39.81
SIAR	TO06	-3.77	39.68
SIAR	TO07	-3.98	40.06
SIAR	TO08	-3.33	40.03
SIAR	TO09	-4.40	39.83
SIAR	TO10	-3.14	39.61
SIAR	TO11	-3.94	39.94
SIAR	TO12	-3.77	39.66
SIAR	V01	-0.72	39.57
SIAR	V02	-0.63	39.69
SIAR	V03	-0.69	39.40
SIAR	V04	-0.46	39.28
SIAR	V05	-0.74	39.52
SIAR	V06	-0.24	39.10
SIAR	V07	-0.52	39.07
SIAR	V10	-0.22	39.73
SIAR	V101	-0.40	39.59
SIAR	V1010	-0.39	39.59
SIAR	V102	-0.45	39.11
SIAR	V1020	-0.45	39.12
SIAR	V103	-0.55	39.23
SIAR	V1030	-0.53	39.23
SIAR	V104	-0.36	38.94
SIAR	V106	-1.23	39.50
SIAR	V107	-0.49	39.48
SIAR	V14	-0.44	39.22
SIAR	V16	-0.47	39.60
SIAR	V17	-0.50	39.36
SIAR	V18	-0.64	38.95
SIAR	V19	-0.55	39.00
SIAR	V20	-0.29	39.65
SIAR	V21	-1.16	39.43
SIAR	V22	-0.20	38.89
SIAR	V23	-0.25	38.96
SIAR	V24	-0.36	39.19
SIAR	V25	-0.69	39.07
SIAR	V26	-0.47	39.60
SIAR	V27	-0.83	39.68
SIAR	VA01	-5.29	42.15
SIAR	VA02	-5.21	41.23
SIAR	VA03	-4.69	41.31
SIAR	VA05	-4.10	41.77
SIAR	VA06	-5.00	41.49
SIAR	VA07	-4.27	41.64
SIAR	VA08	-5.07	41.86
SIAR	VA101	-4.70	41.71
SIAR	VA102	-4.90	41.31
SIAR	VA103	-4.98	41.40
SIAR	Z01	-1.33	41.45
SIAR	Z02	-0.72	41.35
SIAR	Z03	-0.52	41.39
SIAR	Z04	0.15	41.17
SIAR	Z05	-1.28	41.58
SIAR	Z06	-1.20	42.10
SIAR	Z07	-1.31	42.27
SIAR	Z08	-0.94	42.10
SIAR	Z09	-1.33	41.92
SIAR	Z10	-0.75	41.60
SIAR	Z11	-0.82	41.71
SIAR	Z13	-1.66	41.33
SIAR	Z14	-1.51	41.86
SIAR	Z15	-1.75	41.92
SIAR	Z16	-0.07	41.30
SIAR	Z17	-0.54	41.55
SIAR	Z18	-1.42	41.11
SIAR	Z19	-0.75	41.87
SIAR	Z20	-1.25	42.18
SIAR	Z21	-1.14	42.00
SIAR	Z22	-1.25	41.84
SIAR	Z23	-0.73	41.59
SIAR	Z24	-1.61	41.36
SIAR	Z25	-1.31	41.91
SIAR	Z26	-0.77	41.89
SIAR	Z27	-1.06	41.76
SIAR	ZA01	-5.81	42.00
SIAR	ZA02	-5.65	41.48
SIAR	ZA04	-5.39	41.88
SIAR	ZA05	-5.90	41.78
SIAR	ZA06	-5.67	41.93
SIAR	ZA07	-5.52	41.50
SIAR	ZA08	-5.37	41.51
Meteocat	C8	1.30	41.68
Meteocat	CD	1.43	42.37
Meteocat	CT	0.74	42.40
Meteocat	D4	3.18	42.27
Meteocat	D9	1.52	41.22
Meteocat	DC	2.48	42.19

Network	ID	Lon.[°]	Lat.[°]
SIAR	BA06	-7.06	38.72
SIAR	BA07	-6.35	38.58
SIAR	BA08	-5.90	38.93
SIAR	BA09	-6.35	38.58
SIAR	BA101	-6.32	38.85
SIAR	BA102	-5.71	38.39
SIAR	BA103	-5.10	39.07
SIAR	BA104	-6.31	38.21
SIAR	BA105	-5.86	38.98
SIAR	BA106	-5.99	39.01
SIAR	BA201	-7.08	38.77
SIAR	BA202	-6.91	38.91
SIAR	BA203	-6.83	38.88
SIAR	BA204	-6.73	38.91
SIAR	BA205	-6.67	38.86
SIAR	BA206	-6.47	38.86
SIAR	BA207	-6.35	38.66
SIAR	BA209	-5.86	38.99
SIAR	BA210	-5.74	39.10
SIAR	BU01	-2.97	42.69
SIAR	BU02	-4.13	42.75
SIAR	BU03	-3.77	42.04
SIAR	BU04	-3.80	42.35
SIAR	BU05	-3.58	41.64
SIAR	BU07	-3.08	42.70
SIAR	BU101	-3.24	42.97
SIAR	BU102	-2.78	42.74
SIAR	C01	-8.05	43.45
SIAR	C02	-8.14	43.03
SIAR	CA01	-6.02	36.76
SIAR	CA02	-6.01	36.64
SIAR	CA04	-5.62	36.84
SIAR	CA05	-6.13	36.33
SIAR	CA06	-5.84	36.29
SIAR	CA07	-5.38	36.41
SIAR	CA08	-6.15	36.62
SIAR	CA09	-6.31	36.78
SIAR	CA10	-6.16	36.61
SIAR	CA101	-6.40	36.75
SIAR	CA11	-6.33	36.72
SIAR	CC01	-5.68	39.87
SIAR	CC03	-6.05	40.21
SIAR	CC04	-6.23	40.01
SIAR	CC05	-6.68	40.05
SIAR	CC07	-5.60	39.14
SIAR	CC08	-6.48	39.38
SIAR	CC09	-5.46	39.86
SIAR	CC10	-5.86	39.96
SIAR	CC101	-6.31	40.30
SIAR	CC102	-5.76	39.46
SIAR	CC103	-5.35	39.39
SIAR	CC104	-6.90	39.75
SIAR	CC105	-6.21	39.85
SIAR	CC106	-6.63	39.27
SIAR	CC11	-5.65	40.10
SIAR	CC12	-5.94	40.24
SIAR	CC13	-5.56	40.01
SIAR	CC14	-6.46	39.96
SIAR	CC15	-5.88	40.14
SIAR	CC16	-6.69	40.07
SIAR	CC17	-5.87	40.14
SIAR	CC18	-6.33	39.37
SIAR	CC19	-6.03	40.21
SIAR	CO01	-5.21	38.25
SIAR	CO02	-4.45	38.00
SIAR	CO03	-5.23	37.73
SIAR	CO04	-5.16	37.72
SIAR	CO05	-4.50	37.91
SIAR	CO06	-4.80	37.86
SIAR	CO07	-4.89	37.52
SIAR	CO08	-4.31	37.69
SIAR	CO09	-5.23	37.73
SIAR	CO101	-4.43	37.50
SIAR	CO102	-5.12	38.50
SIAR	CR01	-3.20	39.21
SIAR	CR02	-3.36	39.10
SIAR	CR03	-4.23	39.23
SIAR	CR04	-3.99	39.04
SIAR	CR05	-3.62	38.95
SIAR	CR06	-2.80	38.84
SIAR	CR07	-3.06	39.08
SIAR	CR08	-3.33	39.38
SIAR	CR09	-3.69	39.01
SIAR	CR10	-3.35	39.12
SIAR	CR101	-3.95	39.03
SIAR	CR11	-2.88	38.70
SIAR	CS01	-0.23	39.80
SIAR	CS03	0.37	40.59
SIAR	CS04	0.40	40.41
SIAR	CS05	-0.12	39.99
SIAR	CS06	-0.11	39.89
SIAR	CS07	0.15	40.13
SIAR	CS08	-0.17	39.88
SIAR	CS09	-0.48	39.82
SIAR	CS10	-0.21	39.97
SIAR	CS101	-0.14	39.94
SIAR	CS11	-0.19	39.97
SIAR	CU01	-2.30	39.36
SIAR	CU02	-2.76	39.47
SIAR	CU03	-2.09	39.45
SIAR	CU04	-2.94	40.11
SIAR	CU05	-1.65	40.03

Network	ID	Lon.[°]	Lat.[°]
SIAR	CU07	-2.32	40.41
SIAR	CU08	-1.85	39.40
SIAR	CU09	-2.14	40.15
SIAR	GR01	-2.77	37.56
SIAR	GR02	-2.38	37.88
SIAR	GR03	-4.14	37.17
SIAR	GR04	-3.77	37.26
SIAR	GR05	-3.55	37.42
SIAR	GR06	-3.15	37.19
SIAR	GR07	-3.18	36.92
SIAR	GR08	-4.15	36.99
SIAR	GR09	-3.68	36.74
SIAR	GR10	-3.60	37.02
SIAR	GR101	-3.64	37.17
SIAR	GR11	-3.68	36.75
SIAR	GU01	-3.17	40.66
SIAR	GU02	-2.95	40.93
SIAR	GU03	-3.01	40.53
SIAR	GU04	-3.25	40.59
SIAR	GU05	-1.80	40.80
SIAR	GU06	-2.99	40.21
SIAR	GU07	-3.17	40.66
SIAR	GU08	-3.25	40.59
SIAR	GU09	-3.21	40.68
SIAR	H01	-7.03	37.32
SIAR	H02	-7.24	37.30
SIAR	H03	-7.06	37.41
SIAR	H04	-6.79	37.15
SIAR	H05	-6.74	37.35
SIAR	H06	-6.94	37.96
SIAR	H07	-7.25	37.55
SIAR	H08	-6.60	37.66
SIAR	H09	-6.54	37.37
SIAR	H10	-6.48	37.15
SIAR	H101	-6.80	37.24
SIAR	HU01	-0.15	41.53
SIAR	HU02	0.29	41.64
SIAR	HU03	0.07	41.74
SIAR	HU04	0.38	41.78
SIAR	HU05	-0.34	41.79
SIAR	HU06	0.13	41.94
SIAR	HU07	0.11	42.01
SIAR	HU08	-0.18	41.77
SIAR	HU09	-0.38	42.11
SIAR	HU10	0.09	41.46
SIAR	HU11	-0.36	41.94
SIAR	HU12	-0.14	41.95
SIAR	HU13	-0.73	41.99
SIAR	HU14	0.17	42.39
SIAR	HU15	0.15	41.82
SIAR	HU16	-0.72	42.56
SIAR	HU17	0.35	41.50
SIAR	HU18	-0.51	41.97
SIAR	HU19	0.30	41.88
SIAR	HU20	0.23	41.74
SIAR	HU21	-0.26	41.88
SIAR	HU22	-0.71	42.58
SIAR	IB01	1.44	39.01
SIAR	IB02	2.94	39.68
SIAR	IB03	3.17	39.55
SIAR	IB04	2.73	39.56
SIAR	IB05	3.09	39.48
SIAR	IB06	3.04	39.80
SIAR	IB07	2.71	39.78
SIAR	IB08	4.10	40.00
SIAR	IB09	3.36	39.70
SIAR	IB10	2.46	39.55
SIAR	IB101	3.85	39.97
SIAR	IB11	1.40	38.73
SIAR	J01	-3.06	37.75
SIAR	J02	-2.93	37.67
SIAR	J03	-3.23	37.86
SIAR	J04	-3.24	38.08
SIAR	J05	-3.69	37.99
SIAR	J06	-4.08	37.58
SIAR	J07	-3.60	37.92
SIAR	J08	-3.30	37.94
SIAR	J09	-3.65	38.06
SIAR	J10	-4.13	38.06
SIAR	J101	-3.24	37.97
SIAR	J102	-3.20	38.06
SIAR	J103	-3.33	37.88
SIAR	J104	-3.79	37.94
SIAR	J11	-3.00	38.30
SIAR	J12	-4.01	37.95
SIAR	J14	-3.08	38.03
SIAR	J15	-3.77	37.89
SIAR	J16	-4.18	38.05
SIAR	LE01	-6.71	42.57
SIAR	LE02	-5.43	42.51
SIAR	LE03	-5.51	42.40
SIAR	LE04	-5.74	42.26
SIAR	LE05	-5.84	42.22
SIAR	LE06	-5.90	42.46
SIAR	LE07	-5.77	42.46
SIAR	LE08	-5.02	42.37
SIAR	LE09	-5.26	42.44
SIAR	LU01	-7.49	43.16
SIAR	LU02	-7.50	42.51
SIAR	M01	-3.50	40.41
SIAR	M02	-3.50	40.31
SIAR	M03	-3.63	40.04

Network	ID	Lon.[°]	Lat.[°]
SIAR	M04	-3.18	40.11
SIAR	M05	-3.56	40.23
SIAR	M06	-3.47	40.19
SIAR	M102	-4.27	40.25
SIAR	MA01	-4.54	36.76
SIAR	MA02	-4.13	36.80
SIAR	MA03	-4.56	37.06
SIAR	MA04	-5.21	36.44
SIAR	MA05	-4.43	37.08
SIAR	MA06	-4.84	37.14
SIAR	MA07	-4.50	36.67
SIAR	MA08	-4.72	36.77
SIAR	MA09	-4.68	36.72
SIAR	MA10	-4.56	37.03
SIAR	MA101	-4.56	36.73
SIAR	MU01	-1.59	37.42
SIAR	MU02	-1.51	37.73
SIAR	MU03	-1.13	37.75
SIAR	MU04	-1.05	37.80
SIAR	MU06	-1.07	37.68
SIAR	MU07	-0.92	37.63
SIAR	MU08	-1.82	37.86
SIAR	MU09	-1.63	37.60
SIAR	MU10	-1.15	38.16
SIAR	MU101	-1.42	37.79
SIAR	MU102	-1.69	38.25
SIAR	MU103	-1.22	38.13
SIAR	MU104	-0.98	37.98
SIAR	MU105	-1.36	37.57
SIAR	MU106	-1.78	38.10
SIAR	MU107	-1.24	37.70
SIAR	MU108	-1.68	38.11
SIAR	MU109	-1.73	37.59
SIAR	MU11	-1.30	38.01
SIAR	MU110	-1.31	38.24
SIAR	MU111	-1.50	38.29
SIAR	MU112	-1.24	38.39
SIAR	MU114	-1.11	38.56
SIAR	MU115	-1.42	38.39
SIAR	MU117	-0.90	37.77
SIAR	MU119	-0.93	37.82
SIAR	MU12	-1.33	38.13
SIAR	MU120	-0.82	37.79
SIAR	MU121	-1.13	37.94
SIAR	MU123	-1.47	38.04
SIAR	MU124	-1.99	38.04
SIAR	MU125	-1.33	38.32
SIAR	MU126	-1.05	38.17
SIAR	MU128	-0.99	37.75
SIAR	MU130	-0.88	37.85
SIAR	MU14	-1.81	38.20
SIAR	MU15	-1.34	37.90
SIAR	MU16	-1.69	37.50
SIAR	MU17	-1.00	38.03
SIAR	MU18	-1.19	38.66
SIAR	MU19	-1.12	37.83
SIAR	MU20	-1.26	38.19
SIAR	NA01	-1.57	42.07
SIAR	NA02	-1.84	42.05
SIAR	NA03	-1.72	42.03
SIAR	NA04	-1.64	42.00
SIAR	NA05	-1.32	42.56
SIAR	NA06	-1.61	42.51
SIAR	NA07	-1.49	42.38
SIAR	NA08	-1.75	42.69
SIAR	NA09	-1.79	42.58
SIAR	NA10	-1.81	42.51
SIAR	NA101	-1.72	42.21
SIAR	NA102	-1.66	42.26
SIAR	NA103	-2.05	42.36
SIAR	NA104	-1.66	42.42
SIAR	NA105	-1.62	42.36
SIAR	NA106	-1.72	42.81
SIAR	NA107	-1.28	42.67
SIAR	NA108	-2.17	42.66
SIAR	NA109	-1.84	42.12
SIAR	NA11	-1.79	42.41
SIAR	NA110	-1.81	42.29
SIAR	NA111	-1.98	42.50
SIAR	NA12	-1.89	42.34
SIAR	NA13	-2.30	42.48
SIAR	NA14	-1.52	42.30
SIAR	NA15	-2.18	42.54
SIAR	NA16	-2.13	42.47
SIAR	NA17	-1.90	42.36
SIAR	P01	-4.30	42.05
SIAR	P02	-4.49	41.95
SIAR	P03	-4.72	42.08
SIAR	P04	-4.59	42.27
SIAR	P05	-4.28	42.35
SIAR	P06	-4.25	42.49
SIAR	P07	-4.77	42.53
SIAR	P08	-4.28	42.35
SIAR	P101	-4.59	42.56
SIAR	SA01	-6.54	40.59
SIAR	SA02	-5.48	40.99
SIAR	SA03	-5.48	40.99
SIAR	SA101	-5.36	41.04
SIAR	SA102	-5.53	40.78
SIAR	SE01	-5.94	37.18
SIAR	SE02	-5.88	37.02
SIAR	SE03	-6.13	36.98

Network	ID	Lon.[°]	Lat.[°]
SIAR	SE05	-6.27	37.15
SIAR	SE07	-6.13	37.23
SIAR	SE08	-6.05	37.08
SIAR	SE09	-5.08	37.59
SIAR	SE10	-5.23	37.53
SIAR	SE101	-5.59	37.40
SIAR	SE11	-5.13	37.26
SIAR	SE12	-5.92	37.46
SIAR	SE13	-6.26	37.42
SIAR	SE14	-5.68	37.61
SIAR	SE15	-5.54	37.66
SIAR	SE16	-5.67	37.18
SIAR	SE17	-6.06	37.51
SIAR	SE18	-5.35	37.22
SIAR	SE19	-5.96	37.51
SIAR	SE20	-6.12	37.11
SIAR	SE21	-5.95	37.19
SIAR	SE22	-5.69	37.59
SIAR	SG01	-4.30	41.30
SIAR	SG02	-4.48	41.17
SIAR	SO01	-2.50	41.46
SIAR	SO02	-3.22	41.57
SIAR	SO03	-2.43	41.83
SIAR	SO101	-2.09	41.74
SIAR	TE01	-0.21	40.96
SIAR	TE02	-0.24	41.10
SIAR	TE03	-0.53	41.22
SIAR	TE04	-1.36	40.78
SIAR	TE05	-1.17	40.35
SIAR	TE06	-1.29	40.53
SIAR	TO01	-4.70	39.96
SIAR	TO03	-4.97	39.87
SIAR	TO04	-4.66	39.72
SIAR	TO05	-5.14	39.81
SIAR	TO06	-3.77	39.68
SIAR	TO07	-3.98	40.06
SIAR	TO08	-3.33	40.03
SIAR	TO09	-4.40	39.83
SIAR	TO10	-3.14	39.61
SIAR	TO11	-3.94	39.94
SIAR	TO12	-3.77	39.66
SIAR	V01	-0.72	39.57
SIAR	V02	-0.63	39.69
SIAR	V03	-0.69	39.40
SIAR	V04	-0.46	39.28
SIAR	V05	-0.74	39.52
SIAR	V06	-0.24	39.10
SIAR	V07	-0.52	39.07
SIAR	V10	-0.22	39.73
SIAR	V101	-0.40	39.59
SIAR	V1010	-0.39	39.59
SIAR	V102	-0.45	39.11
SIAR	V1020	-0.45	39.12
SIAR	V103	-0.55	39.23
SIAR	V1030	-0.53	39.23
SIAR	V104	-0.36	38.94
SIAR	V106	-1.23	39.50
SIAR	V107	-0.49	39.48
SIAR	V14	-0.44	39.22
SIAR	V16	-0.47	39.60
SIAR	V17	-0.50	39.36
SIAR	V18	-0.64	38.95
SIAR	V19	-0.55	39.00
SIAR	V20	-0.29	39.65
SIAR	V21	-1.16	39.43
SIAR	V22	-0.20	38.89
SIAR	V23	-0.25	38.96
SIAR	V24	-0.36	39.19
SIAR	V25	-0.69	39.07
SIAR	V26	-0.47	39.60
SIAR	V27	-0.83	39.68
SIAR	VA01	-5.29	42.15
SIAR	VA02	-5.21	41.23
SIAR	VA03	-4.69	41.31
SIAR	VA05	-4.10	41.77
SIAR	VA06	-5.00	41.49
SIAR	VA07	-4.27	41.64
SIAR	VA08	-5.07	41.86
SIAR	VA101	-4.70	41.71
SIAR	VA102	-4.90	41.31
SIAR	VA103	-4.98	41.40
SIAR	Z01	-1.33	41.45
SIAR	Z02	-0.72	41.35
SIAR	Z03	-0.52	41.39
SIAR	Z04	0.15	41.17
SIAR	Z05	-1.28	41.58
SIAR	Z06	-1.20	42.10
SIAR	Z07	-1.31	42.27
SIAR	Z08	-0.94	42.10
SIAR	Z09	-1.33	41.92
SIAR	Z10	-0.75	41.60
SIAR	Z11	-0.82	41.71
SIAR	Z13	-1.66	41.33
SIAR	Z14	-1.51	41.86
SIAR	Z15	-1.75	41.92
SIAR	Z16	-0.07	41.30
SIAR	Z17	-0.54	41.55
SIAR	Z18	-1.42	41.11
SIAR	Z19	-0.75	41.87
SIAR	Z20	-1.25	42.18
SIAR	Z21	-1.14	42.00
SIAR	Z22	-1.25	41.84

Network	ID	Lon.[°]	Lat.[°]
SIAR	Z23	-0.73	41.59
SIAR	Z24	-1.61	41.36
SIAR	Z25	-1.31	41.91
SIAR	Z26	-0.77	41.89
SIAR	Z27	-1.06	41.76
SIAR	ZA01	-5.81	42.00
SIAR	ZA02	-5.65	41.48
SIAR	ZA04	-5.39	41.88
SIAR	ZA05	-5.90	41.78
SIAR	ZA06	-5.67	41.93
SIAR	ZA07	-5.52	41.50
SIAR	ZA08	-5.37	41.51
Meteocat	C8	1.30	41.68
Meteocat	CD	1.43	42.37
Meteocat	CT	0.74	42.40
Meteocat	D4	3.18	42.27
Meteocat	D9	1.52	41.22
Meteocat	DC	2.48	42.19
Meteocat	DF	3.04	41.98
Meteocat	DQ	1.36	41.31
Meteocat	U7	0.51	40.86
Meteocat	UA	0.51	41.20
Meteocat	UU	0.63	40.71
Meteocat	V8	0.88	41.67
Meteocat	VK	0.45	41.68
Meteocat	W6	1.02	41.14
Meteocat	WA	1.15	41.88
Meteocat	WP	1.69	41.49
Meteocat	WS	2.42	41.84
Meteocat	X1	0.82	41.15
Meteocat	X4	2.17	41.38
Meteocat	XE	1.20	41.10
Euskalmet	001	-2.63	42.85
Euskalmet	001	-2.63	42.85
Euskalmet	002	-2.66	43.35
Euskalmet	003	-2.87	43.29
Euskalmet	007	-2.00	43.32
Euskalmet	017	-1.97	43.29
Euskalmet	018	-1.80	43.39
Euskalmet	019	-2.76	43.44
Euskalmet	020	-2.70	42.72
Euskalmet	022	-2.65	43.10
Euskalmet	023	-2.49	43.07
Euskalmet	024	-2.35	42.79
Euskalmet	026	-1.98	43.12
Euskalmet	027	-2.95	43.14
Euskalmet	029	-2.06	43.19
Euskalmet	030	-2.40	42.86
Euskalmet	033	-2.78	43.17
Euskalmet	034	-3.04	42.81
Euskalmet	035	-2.87	42.96
Euskalmet	036	-2.62	43.17
Euskalmet	039	-2.97	43.28
Euskalmet	040	-2.69	42.86
Euskalmet	042	-3.04	43.37
Euskalmet	043	-2.18	43.05
Euskalmet	047	-2.54	42.77
Euskalmet	048	-2.68	42.60
Euskalmet	050	-2.89	42.67
Euskalmet	051	-3.00	43.03
Euskalmet	053	-2.71	43.07
Euskalmet	054	-2.66	43.04
Euskalmet	055	-2.49	42.91
Euskalmet	056	-2.52	42.84
Euskalmet	057	-2.85	43.36
Euskalmet	058	-2.16	43.14
Euskalmet	059	-3.28	43.16
Euskalmet	060	-2.60	42.56
Euskalmet	061	-3.07	43.29
Euskalmet	064	-2.15	43.29
Euskalmet	065	-3.41	43.21
Euskalmet	069	-2.73	43.41
Euskalmet	0AA	-2.50	42.89
Euskalmet	0DC	-2.26	43.17
Euskalmet	0EC	-2.02	43.25
M. Navarra	Aguilar Codes	-2.40	42.61
M. Navarra	Aoiz	-1.37	42.79
M. Navarra	Aralar	-1.96	42.95
M. Navarra	Arangoiti	-1.20	42.64
M. Navarra	Bardenas (Yugo)	-1.58	42.20
M. Navarra	Bardenas (Loma)	-1.38	42.07
M. Navarra	Beortegi	-1.43	42.80
M. Navarra	Carcastillo	-1.46	42.37
M. Navarra	Carrascal	-1.66	42.68
M. Navarra	Doneztebe	-1.66	43.13
M. Navarra	El Perdon	-1.71	42.73
M. Navarra	Erremendia	-1.19	42.88
M. Navarra	Estella	-2.03	42.67
M. Navarra	Etxarri-Aranatz	-2.06	42.91
M. Navarra	Getadar	-1.47	42.62
M. Navarra	Gorramendi	-1.45	43.21
M. Navarra	Oskotz	-1.76	42.95
M. Navarra	Pamplona Upna	-1.63	42.79
M. Navarra	Pamplona	-1.64	42.82
M. Navarra	Tafalla	-1.69	42.52
M. Navarra	T. de Iturgoien	-1.98	42.81
M. Navarra	Tudela	-1.65	42.13
M. Navarra	Ujue	-1.51	42.51
M. Navarra	Urbasa	-2.18	42.85
M. Navarra	V. de Yerri	-1.95	42.74
M. Navarra	Yesa	-1.19	42.62
MeteoGalicia	10045	-8.26	43.24

Network	ID	Lon.[°]	Lat.[°]
MeteoGalicia	10046	-7.89	43.34
MeteoGalicia	10047	-7.08	43.54
MeteoGalicia	10048	-7.34	42.12
MeteoGalicia	10049	-9.03	42.56
MeteoGalicia	10050	-8.25	43.49
MeteoGalicia	10052	-8.77	42.75
MeteoGalicia	10053	-7.55	42.99
MeteoGalicia	10055	-7.78	43.23
MeteoGalicia	10056	-7.50	42.47
MeteoGalicia	10057	-7.59	42.30
MeteoGalicia	10058	-7.40	41.98
MeteoGalicia	10060	-8.68	42.08
MeteoGalicia	10061	-8.14	42.62
MeteoGalicia	10062	-6.92	42.82
MeteoGalicia	10063	-8.43	42.23
MeteoGalicia	10064	-8.66	42.41
MeteoGalicia	10067	-8.70	42.46
MeteoGalicia	10085	-8.80	42.58
MeteoGalicia	10086	-8.40	42.32
MeteoGalicia	10087	-8.87	42.97
MeteoGalicia	10088	-7.44	43.46
MeteoGalicia	10089	-7.98	42.91
MeteoGalicia	10091	-8.86	42.00
MeteoGalicia	10092	-8.05	43.71
MeteoGalicia	10093	-8.83	43.34
MeteoGalicia	10094	-8.28	43.13
MeteoGalicia	10095	-8.46	42.82
MeteoGalicia	10096	-8.69	43.10
MeteoGalicia	10097	-7.79	43.59
MeteoGalicia	10098	-7.25	42.75
MeteoGalicia	10099	-7.47	42.65
MeteoGalicia	10100	-7.27	42.49
MeteoGalicia	10101	-7.89	43.04
MeteoGalicia	10102	-7.19	42.60
MeteoGalicia	10103	-7.28	43.56
MeteoGalicia	10104	-7.56	43.66
MeteoGalicia	10105	-7.28	43.16
MeteoGalicia	10106	-7.17	43.34
MeteoGalicia	10107	-7.79	43.15
MeteoGalicia	10108	-7.62	42.81
MeteoGalicia	10109	-8.24	42.42
MeteoGalicia	10110	-7.71	41.95
MeteoGalicia	10111	-8.10	41.95
MeteoGalicia	10112	-7.97	42.17
MeteoGalicia	10113	-7.63	42.23
MeteoGalicia	10114	-6.93	42.46
MeteoGalicia	10115	-7.01	42.36
MeteoGalicia	10116	-7.09	42.16
MeteoGalicia	10117	-7.30	42.40
MeteoGalicia	10118	-7.37	43.65
MeteoGalicia	10119	-7.97	41.90
MeteoGalicia	10120	-8.32	42.63
MeteoGalicia	10121	-8.50	42.47
MeteoGalicia	10122	-7.93	42.58
MeteoGalicia	10124	-8.56	42.88
MeteoGalicia	10125	-8.90	42.22
MeteoGalicia	10126	-8.93	42.38
MeteoGalicia	10127	-8.62	42.60
MeteoGalicia	10128	-9.01	42.47
MeteoGalicia	10129	-8.80	42.40
MeteoGalicia	10130	-6.78	42.38
MeteoGalicia	10131	-7.30	42.26
MeteoGalicia	10132	-7.05	42.71
MeteoGalicia	10135	-9.12	42.80
MeteoGalicia	10136	-7.05	43.18
MeteoGalicia	10137	-6.91	42.96
MeteoGalicia	10138	-6.89	42.21
MeteoGalicia	10141	-8.13	43.56
MeteoGalicia	10143	-7.86	43.74
MeteoGalicia	10144	-8.17	42.93
MeteoGalicia	10146	-7.48	43.16
MeteoGalicia	10153	-9.06	43.11
MeteoGalicia	10154	-8.60	42.32
MeteoGalicia	10161	-8.68	42.17
MeteoGalicia	10162	-7.63	43.63
MeteoGalicia	10500	-7.44	41.95
MeteoGalicia	10800	-9.18	43.13
MeteoGalicia	19065	-8.73	42.51
MeteoGalicia	19066	-8.77	42.51
MeteoGalicia	19068	-8.77	42.44
MeteoGalicia	19069	-8.87	42.46
MeteoGalicia	19070	-8.74	42.47
MeteoGalicia	50500	-8.52	42.80
SIAR Rioja	Agoncillo	-2.29	42.47
SIAR Rioja	Albelda	-2.47	42.38
SIAR Rioja	Aldeanueva	-1.90	42.22
SIAR Rioja	Alfaro	-1.78	42.15
SIAR Rioja	Arenzana	-2.72	42.39
SIAR Rioja	Ausejo	-2.15	42.34
SIAR Rioja	Calahorra	-2.00	42.33
SIAR Rioja	Casalarreina	-2.90	42.54
SIAR Rioja	Cervera	-1.89	42.01
SIAR Rioja	Foncea	-3.04	42.61
SIAR Rioja	Igea	-1.99	42.06
SIAR Rioja	Leiva	-3.05	42.50
SIAR Rioja	Logroño	-2.51	42.44
SIAR Rioja	Pazuengos	-2.91	42.34
SIAR Rioja	Quel	-2.04	42.25
SIAR Rioja	Rincón Soto	-1.85	42.25
SIAR Rioja	San Vicente	-2.73	42.57
SIAR Rioja	Sta.Engracia	-2.26	42.37
SIAR Rioja	Sto.Domingo	-2.94	42.43

Network	ID	Lon.[°]	Lat.[°]	Network	ID	Lon.[°]	Lat.[°]
SIAR Rioja	Uruñuela	-2.71	42.46	SOS Rioja	Moncalvillo	-2.62	42.33
SIAR Rioja	Villar Torre	-2.86	42.38	SOS Rioja	Nájera	-2.72	42.42
SOS Rioja	Aguilar	-1.97	41.97	SOS Rioja	Ocón	-2.23	42.29
SOS Rioja	Alfaro	-1.74	42.18	SOS Rioja	San Román	-2.46	42.23
SOS Rioja	Arnedo	-2.09	42.23	SOS Rioja	Santa Marina	-2.37	42.24
SOS Rioja	Calahorra	-2.00	42.29	SOS Rioja	Torrecilla	-2.62	42.25
SOS Rioja	Ezcaray	-3.01	42.33	SOS Rioja	Urbaña	-2.85	42.17
SOS Rioja	Haro	-2.84	42.57	SOS Rioja	Villoslada	-2.67	42.12
SOS Rioja	Logroño	-2.47	42.46	SOS Rioja	Yerga	-1.97	42.14